UNIVERSITA' DEGLI STUDI DI PADOVA
FACOLTA' DI INGEGNERIA

DIPARTIMENTO DI INGEGNERIA IDRAULICA MARITTIMA AMBIENTALE E GEOTECNICA

SCUOLA DI DOTTORATO DI RICERCA IN SCIENZE DELL'INGEGNERIA CIVILE E AMBIENTALE
XXII CICLO

TESI DI DOTTORATO

MODELLAZIONE COSTITUTIVA DEL COMPORTAMENTO DIPENDENTE DAL TEMPO DEI LIMI ETEROGENEI DI VENEZIA

Constitutive modelling of the time-dependent behaviour of Venice heterogeneous silts

direttore della scuola: Ch.mo Prof. Stefano Lanzoni

supervisore: Ch.mo Prof. Paolo Simonini

dottoranda: Valentina Berengo

Summary

The topic of the thesis is the analysis of the Venice Lagoon soils' creep behaviour and its modelling. It therefore consists in two parts: a set of experimental tests on soils samples and the formulation of an improvement in an existing creep model in order to better reproduce unloading –reloading behaviour. The new formulation is then validate on experimental laboratory and in- situ measures.

The creep behaviour of soils has been investigated since long time and many models have already been formulated, but some basic characteristic (like the time reference for creep strain, or the isotache approach validity to every conditions) are still under debate. What has been recognize is the importance of viscous behaviour in terms of soil compressibility, especially for normally consolidated soils, while overconsolidated ones has a very low creep strain rates. Chapter 1 and Chapter 2, therefore, describe the state of arts in modelling soils' creep behaviour.

The analysis proposed in this thesis is based on settlement measures from an 40 m diameter embankment construction in the Venice Lagoon area, near the Lido inlet. As described in Chapter 6, the construction started in September 2002 and ended in March 2003. The final height was 6.7 m. It was kept constant for 4 years and then the embankment has been removed in three phases. Between one phase and the following three months went by, in order to get possible creep settlements. The subsoil was, in fact, instrumented with sliding deformeters capable to detect displacement at every meter depth, until 60 m and measurements taken along the whole process has revealed creep settlement during the 4 years at constant height and also after the first removal phase.

The complete analysis of the Venetian subsoil is described in Chapter 7: the grain size properties are obtained and the mechanical behaviour is described throughout primary and secondary compression coefficients from laboratory oedometer tests and in-situ settlement measurements. The main feature of Venetian soils is the presence of a predominantly silty fraction, being a consequence of mechanical degradation of the original sand particles. The silt is always combined with clay and/or sand, forming a chaotic interbedding of different sediments, whose mineralogic characteristic are, however, variable from site to site, in a relatively narrow range due to a unique geological origin and common depositional environment. Piezocone tests performed before the embankment construction and after the embankment removal have been used in order to retrace the soil profile and to validate the piezocone classification charts, as well.

Beside the extreme soil heterogeneity that makes difficult to compare laboratory tests on different soil specimens, one of the major problem in performing laboratory test was the sensitivity to stress-relief, since it makes almost impossible to retrace the preconsolidation pressure. Since it is very important in creep analysis, its profile has been deduced from in situ stress strain curves identifying it with the yielding point after that a steep reduction in stiffness can be observed. Secondary compression coefficient profile for normally consolidated states is obtained from in-situ measurements and it can reliably used in modelling while the primary consolidation coefficient profile from in- situ stress strain curves cannot be compared with those from oedometer laboratory tests. This is due to the absence of a rigorous loading sequence in embankment construction and also to the absence of a real constraint in lateral displacement, testimonied by the stiffness evolution, always decading and not increasing as in an oedometer test.

After the embankment removal, at the centerline an Osterberg sampling has been performed, whose samples has been used to perform a set of Constant Rate of Strain tests described in Chapter 8. The testing device is a rigid walls Rowe cell with two pressure-volume controllers to load the sample throughout a membrane full of water and impose a back pressure to the sample internal water respectively. At the cell base the pore pressure development is measured by an electric pressure transducer. The Constant Rate of Strain tests have been performed in order to verify the applicability of isotache theory to Venetian soils. It states that for a given material there is a unique relationship between effective stress and strain and strain rate. Different strain rates give a set of parallel curves in the semi-logarithmic compression plane. The higher the strain rate, the more the curve is translated on the right-side of the compression plane. As a consequence the preconsolidation pressure is strain rate dependent.

Due to Venetian soils heterogeneity, CRS tests results on different samples cannot be compared since the compression curve slope, that is an intrinsic material parameter, is different for each one. On the other hand, soil looses his "historical memory" (i.e. the preconsolidation pressure cannot be retrace) due to disturbance in sampling, so that the stress strain curves are not correctly positioned in the compression plane. As a solution, in order to verify the expected curves positioning, the strain rate has been changed during the same test. To overcome the sampling disturbance, besides, samples has been preconsolidated in laboratory before performing CRS tests to the same value. CRS tests at different strain rates have shown the expected strain rate dependency of the preconsolidation pressure shown by the compression curve.

In this thesis Venetian soils unloading behaviour has been carefully examined. After the first removal phase further creep settlements have been observed, since the OCR is still close to the unity, while in the following phases creep settlements have not been shown anymore, due to the high OCR values. In the third phase, on the contrary, a delayed swelling has been observed.

The OCR dependency of creep strains has been universally recognized and it is noticeable also in standard oedometer tests. Long term oedometer tests on Venetian soils have shown, indeed, that for overconsolidated step the creep slope (in strain-log(time) plane) is very flat at the beginning and then increases with time. This feature is well captured by the Soft Soil Creep model (SSC).
For this reason (and for many others, as for example the preconsolidation creep strain dependency, or the isotache approach) it was chosen to describe the creep behaviour of silty and clayey layers of Venetian soils. Its features are described in Chapter 3.

Its application to model the embankment trial overestimates the swelling response in unloading phase and also does not catch the hysteretic behaviour of unloading-reloading cycles performed in CRS tests. It has been chosen, therefore, to introduce in the SSC model a stiffness decay law that accounts for small strain behaviour.

It is well known, in fact, as described in Chapter 4, that stiffness decay with strain level from a high value characteristic of very small strain shown in in-situ structures (and evaluable by means of dynamic tests) until a lower value shown in ordinary laboratory tests. This is responsible for hysteretic behaviour and for stiffer response in unloading processes. The Hardin & Drnevich formulation for stiffness decay has been introduced in the model in order to take it into account. It allows to estimate the stiffness value at every strain level once one knows the initial value (at very small stiffness) and the reference strain amplitude (corresponding to a stiffness decay of 30%).

The introduction into the SSC model of the reduction law for elastic stiffness is described in Chapter 5. Basically there is a strain level check at each strain increment since the elastic volumetric stiffness has made be strain dependent. Beyond a reference value, to not superpose the imposed decay to plasticity decay, the constant stiffness value of the unmodified model is taken. To model unloading- reloading behaviour Masing rules are implemented. They state that the shear modulus on each loading reversal recovers the initial value and that in unloading or reloading the decay is slower than in primary loading.
The obtained formulation is absolutely general and it has been applied in modelling CRS tests on Venetian soils and also to model vertical displacements under the centreline during the entire embankment construction and removal process. The results (reported in Chapter 9) are very satisfactory since the improvement in catching unloading and reloading behaviour is noticeable.

La tesi è imperniata sullo studio e la modellazione costitutiva del comportamento viscoso dei terreni del sottosuolo della laguna di Venezia ed il lavoro è costituito da una parte sperimentale basata sull'analisi di misure effettuate in sito e da prove di laboratorio e una parte teorica di modellazione costitutiva validata sulle misure sperimentali.

Il comportamento viscoso dei terreni, noto in letteratura come creep è oggetto di studio della comunità scientifica già da diverso tempo e diversi modelli sono stati formulati, sebbene il dibattito risulti ancora aperto su alcuni dei punti cardine come l'identificazione di un tempo di riferimento cui far risalire l'origine delle deformazioni di natura viscosa o l'applicabilità del modello isotache (che costituisce la più recente generalizzazione della ricerca di una interrelazione tra cedimenti e tempo) ad ogni tipologia di terreno e ad ogni condizione di prova. Il fenomeno viscoso riveste infatti un ruolo non trascurabile nello studio della compressibilità dei terreni, specialmente se normalconsolidati, per i quali la velocità con cui il creep si manifesta è maggiore rispetto ai sovraconsolidati e non è pensabile, allo stato dell'arte, trascurarne gli effetti anche in sede ingegneristica di calcolo dei cedimenti. I primi due capitoli del presente elaborato pertanto vogliono brevemente illustrare quanto noto in letteratura sul fenomeno viscoso soprattutto dal punto di vista della sua modellazione costitutiva.

L'analisi proposta nella presente tesi muove da misure di cedimento effettuate nel corso del processo di costruzione di un rilevato in terre rinforzate nella zona lagunare di Treporti, a ridosso della Bocca di Porto di Lido. Il processo di costruzione (diffusamente descritto nel capitolo 6 dedicato ai terreni della Laguna di Venezia) è consistito in 14 fasi tra il Settembre del 2002 ed il Marzo del 2003 fino ad un'altezza finale del rilevato di 6.7m e per un diametro di 40 m. Il rilevato è stato lasciato insistere ad altezza invariata per i successivi 4 anni sul terreno di fondazione e quindi è stato rimosso in 3 fasi successive tra le quali sono intercorsi 3 mesi ciascuna. Scopo primario della sperimentazione è stata la rilevazione dei cedimenti del terreno di fondazione, preventivamente instrumentato per poter misurare con precisione gli spostamenti verticali ad ogni metro di profondità grazie ad una strumentazione innovativa costituita da assestimetri multibase inseriti nel terreno fino ad una profondità di 60 m. Quest'ultimi hanno permesso la lettura di cedimenti di puro creep nella fase di stazionarietà nei 4 anni che hanno seguito la costruzione ed anche nei 3 mesi a seguito del primo sbancamento. L'intero processo non ha eguali nella realizzazione di prove in vera grandezza nel suo genere, sia per durata che per complessità del terreno di fondazione.

All'analisi del terreno di fondazione è stato dedicato quindi il capitolo 7, sia dal punto di vista granulometrico che del suo comportamento meccanico, attraverso la disamina dei profili dei coefficienti di compressione meccanica, ottenuti sia da prove di laboratorio che da misure in sito.
Il terreno di fondazione della laguna di Venezia risulta essere costituito da una elevatissima alternanza di strati eterogenei di sabbie, limi e limi argillosi con la stessa matrice mineralogica e comune ambiente deposizionale ma diversa curva granulometrica ed inoltre la sequenza con cui la deposizione è avvenuta ha creato una stratificazione così fitta da rendere impossibile l'identificazione di strati omogenei. Le prove con piezocono effettuate in sito prima della costruzione e dopo la rimozione del rilevato sono state strumento di analisi per rintracciare una corretta stratigrafia e al contempo, essendo accompagnate da prove di classificazione di laboratorio su campioni prelevati da sondaggio, per validare l'applicabilità delle note carte di classificazione.

Una delle maggiori difficoltà nell'analisi del dato sperimentale affrontata nella presente tesi è stata quindi la necessità di individuare dei trend sulla base di dati appartenenti di fatto a campioni diversi, quantomeno granulometricamente, e di conseguenza anche dalle diverse proprietà meccaniche. Questo aspetto interessa non solo le misure in sito ma a maggior ragione anche gli esiti delle prove di laboratorio, in cui il terreno ha mostrato inoltre un'estrema sensibilità al campionamento, perdendo memoria della struttura in sito e della tensione di preconsolidazione. Essendo il grado di sovraconsolidazione un parametro basilare per la definizione del comportamento viscoso, tanto più rilevante quanto più vicino all'unità, se ne è ricavato il profilo direttamente dall'analisi delle curve di compressione in sito per ciascuno strato, considerando il processo di costruzione del rilevato assimilabile ad una prova di compressione in cui fosse possibile identificare una soglia di snervamento in corrispondenza della quale il modulo di rigidezza valutato per i successivi incrementi di carico dovuti alla costruzione del rilevato mostrano un netto decadimento. Per quanto riguarda il comportamento di creep il coefficiente di compressione secondaria relativo allo stato normalconsolidato è stato ricavato dalle curve degli spostamenti nel tempo per ogni strato di spessore 1 m e analogamente si è proceduto alla determinazione del coefficiente di compressione primaria. Nella tesi si evidenzia da un lato l'attendibilità del coefficiente di compressione secondaria come parametro per una possibile modellazione e dall'altro l'impossibilità di identificare propriamente il coefficiente di compressione primaria in sito con quello ottenibile da prove edometriche mancando completamente la rigorosità nella sequenza di carico. Il paragone con prove edometriche, inoltre, non risulta intrinsecamente corretto, mancando in sito la condizione di confinamento laterale propria della condizione edometrica, come d'altro canto testimonia l'evoluzione del modulo di rigidezza in sito, che decade nel tratto di compressione, pur considerando le misure di cedimento sotto il centro del rilevato. Ai fini di completezza nella tesi si è proceduto al confronto con i dati offerti da prove di laboratorio: il coefficiente di compressibilità primaria in sito è risultato mediamente maggiore dei quello ricavabile da prove edometriche standard sui campioni prelevati con carotaggio Osterberg effettuati lungo 4 verticali prima della costruzione del rilevato.

A seguito della rimozione un ulteriore carotaggio con campionatore Osterberg è stato effettuato in corrispondenza del centro, sui cui campioni è stata intrapresa una sperimentazione dedicata esclusivamente allo studio del comportamento meccanico dipendente dal tempo le cui modalità e gli esiti sono riportati nel capitolo 8 del presente elaborato. La strumentazione utilizzata e dettagliatamente descritta è costituita da una cella di Rowe, a pareti rigide, con trasmissione idraulica del carico mediante una membrana riempita d'acqua messa in pressione da un attuatore. Un secondo attuatore controlla la contro-pressione applicata all'acqua contenuta nel campione, portato a saturazione nella

prima fase di prova. Il drenaggio è permesso alla testa del campione mentre alla base un trasduttore di pressione permette la misura di eventuali sovrappressioni neutrali. Le prove sono state effettuate a velocità di deformazione costante (CRS) allo scopo di verificare l'applicabilità del modello isotache, secondo cui un'unica legge interrelaziona tensioni, deformazioni e velocità di deformazione, dando luogo ad un insieme di curve nel piano di compressione (parallele in scala semilog), traslate verso destra quanto più la velocità di prova è maggiore. La diretta conseguenza di tale approccio è la dipendenza della tensione di preconsolidazione dalla velocità di deformazione. Un discreto numero di prove a diverse velocità di deformazione sono state effettuate su provini provenienti da diverse profondità del carotaggio centrale.

Data l'estrema eterogeneità del materiale, il parallelismo tra le prove a diversa velocità (od anche alla stessa) sui diversi campioni non è stato sempre rintracciato, ed il posizionamento nel piano di compressione è risultato spesso sfalsato dalla perdita di struttura del terreno e quindi dalla conseguente perdita di memoria della storia di carico. Come soluzione è stata proposta la tecnica, già nota in letteratura, di variare la velocità di deformazione in corso di prova, ottenendo così l'atteso comportamento. Una soluzione originale è stata quella poi di preconsolidare meccanicamente i campioni ad un prefissato valore della tensione di preconsolidazione, e quindi di eseguire la prova CRS. Due coppie di campioni hanno mostrato pendenze analoghe, quindi è stato possibile rintracciare la supposta posizione reciproca nel piano di compressione e di apprezzare dunque la dipendenza della tensione di preconsolidazione dalla velocità di prova.

La tesi presenta oltre all'analisi dei dati in fase di carico e di stazionarietà, la disamina del comportamento in fase di scarico del terreno. Si registrano ancora cedimenti viscosi a seguito del primo sbancamento del rilevato (2 m circa), dal momento che il grado di sovraconsolidazione è ancora prossimo all'unità, mentre nelle fasi di sbancamento successive si osserva nel periodo a tensione costante un comportamento stazionario o addirittura un rigonfiamento ritardato nel tempo.

L'identificazione del profilo del coefficiente di compressione secondaria a seguito del primo sbancamento proposto nella tesi mostra come effettivamente l'influenza del grado di sovraconsolidazione porti ad una significativa riduzione del coefficiente di compressione secondaria, così come predetto dal modello Soft Soil Creep (Vermeer & Neher, 1999) noto in letteratura. Lo stesso fenomeno è stato evidenziato nell'analisi di prove edometriche standard di laboratorio. L'esecuzione di prove edometriche a lungo termine sul terreno di Treporti da parte della candidata in sede di tesi di laurea aveva già mostrato come, per lunghi tempi di carico, la pendenza del secondario tornasse ad aumentare, anche in stadi sovraconsolidati, fino idealmente a raggiungere il valore caratteristico di stati normalconsolidati. Questa caratteristica è prevista dal modello Soft Soil Creep (SSC) ed insieme ad altre (come ad esempio l'evoluzione della tensione di preconsolidazione per creep, o l'appartenenza all'approccio isotache) ha costituito motivo di scelta da parte della candidata nel fare del SSC il modello di base in cui introdurre la dipendenza della rigidezza dallo stato deformativo. Nella presente tesi le genesi e le peculiarità del modello base sono estesamente descritte nel capitolo 3 ad esso dedicato,dopo aver introdotto la teoria generale del creep e della modellazione costitutiva nei suoi principi base.

L'applicazione del modello SSC così come originariamente formulato al caso sperimentale del rilevato di Treporti ha mostrato una sovrastima della risposta in termini di spostamento verticale di rigonfiamento in scarico ed allo stesso tempo esso non è in grado di cogliere i cicli di isteresi riscontrati nell'ambito della sperimentazione CRS in cui un buon numero di

prove sono state effettuate con cicli di scarico e ricarico ad hoc per valutare l'evoluzione della rigidezza. Come riportato nel capitolo 4, è ampiamente noto nella letteratura geotecnica, infatti, che la rigidezza mostra un decadimento con lo stato deformativo, muovendo da un valore caratteristico delle piccolissime deformazioni valutabile principalmente da prove dinamiche e tipico di strutture poste in opera, fino ai valori decisamente inferiori per stati deformativi riproducibili dalle classiche prove di laboratorio. Il decadimento è sia micromeccanicamente che mascropicamente riconducibile a deformazioni di tipo deviatorico e la legge che si è scelta per la sua descrizione è quella sperimentale proposta da Hardin e Drnevich nel 1972 per la rigidezza secante opportunamente trasposta in termini di rigidezza tangente. Essa permette, noto il valore di rigidezza a piccolissime deformazioni ed il livello deformativo corrispondente ad una sua riduzione del 30% (detto 'deformazione di riferimento'), di stimare la rigidezza corrispondente ad un qualsiasi livello deformativo.

La candidata ha introdotto nell'equazione costitutiva del modello di creep SSC la dipendenza della rigidezza volumetrica elastica dallo stato deformativo così come descritto nel capitolo centrale dell'elaborato (5). Sostanzialmente si opera una valutazione preventiva dello stato di deformazione ad ogni incremento della stessa, ottenendo, di fatto, una rigidezza volumetrica dipendente sia dallo stato tensionale che deformativo. Oltre una certa soglia di deformazione, poi, si è scelto che il modello utilizzi un valore di rigidezza non più dipendente dallo stato deformativo ma il valore di rigidezza elastica che si sarebbe utilizzato nel modello non modificato di modo da non imporre, utilizzando la legge di decadimento sperimentale di Hardin e Drnevich, ad una grandezza elastica il decadimento dovuto a plasticità. La modellazione degli scarichi e ricarichi, inoltre, è stata effettuata tenendo conto del fatto che ad ogni cambio di direzione vi è un recupero della rigidezza iniziale (prima regola di Masing) e della minore rapidità con cui il decadimento avviene (seconda regola di Masing).

La formulazione così ottenuta e presentata nell'ambito della presente tesi è di carattere assolutamente generale. Essa mostra risultati decisamente buoni sia nella modellazione di prove di laboratorio (edometriche standard e CRS con scarico e ricarico) effettuate sui limi di Venezia che nella modellazione dell'evoluzione dei cedimenti nel sito sperimentale di Treporti in cui apporta un deciso miglioramento nella predizione del comportamento in scarico rispetto al modello senza implementazione della rigidezza a piccolissime deformazioni, come mostrato nel capitolo conclusivo (9).

Index

Chapter 1 - Soil behaviour modelling

Introduction

To describe a continuum state there are three relationship among stresses, called equilibrium equations, and six compatibility equations for which the continuum integrity is kept. These relationships are not enough to individuate exactly the 15 unknown quantities (6 stresses, 6 strains and 3 rigid displacements) involved in the equilibrium and compatibility expressions. The soil response is characterized, in fact, by a certain link between strain increments and stress increments, and these further conditions allow to determine all the unknowns. This link can be expressed in terms of stiffness or compliance depending on which kind of relationship is chosen and it is called *constitutive law*:

$$\sigma_{ij} = D_{ijhk}\varepsilon_{hk} \tag{1.1}$$

where D_{ijhk} is the stiffness matrix (or tensor) and

$$\varepsilon_{hk} = C_{hkij}\sigma_{ij} \tag{1.2}$$

where C_{hkij} is the compliance matrix (or tensor) and it is $C_{hkij} = D_{ijhk}^{-1}$.

A general three-dimensional stress state is defined by means of six independent stress tensor elements, similarly six components define the strain. The general relationship described above will be therefore:

$$\begin{bmatrix} \sigma_x \\ \sigma_y \\ \sigma_z \\ \sigma_{yz} \\ \sigma_{zx} \\ \sigma_{xy} \end{bmatrix} = \begin{bmatrix} D_{11} & D_{12} & D_{13} & D_{14} & D_{15} & D_{16} \\ D_{21} & D_{22} & D_{23} & D_{24} & D_{25} & D_{26} \\ D_{31} & D_{32} & D_{33} & D_{34} & D_{35} & D_{36} \\ D_{41} & D_{42} & D_{43} & D_{44} & D_{45} & D_{46} \\ D_{51} & D_{52} & D_{53} & D_{54} & D_{55} & D_{56} \\ D_{61} & D_{62} & D_{63} & D_{64} & D_{65} & D_{66} \end{bmatrix} \begin{bmatrix} \varepsilon_x \\ \varepsilon_y \\ \varepsilon_z \\ \gamma_{yz} \\ \gamma_{zx} \\ \gamma_{xy} \end{bmatrix} \tag{1.3}$$

and the stress-strain matrix contains 36 moduli, that depend on the basis chosen to define tension and stress.

.

Elastic constitutive law

A linear relationship between stress and strain is the simplest link that can be proposed, implying a constant proportionality between general stress increments and strain increments (see Figure 1.1). This is denoted as linear elasticity or as Hooke's law from the name of who first stated the relationship.

Hooke (1675) described his discovery in the anagram '*ceiiinosssttuv*', whose solution he published in 1678 as '*ut tensio, sic vis*' meaning 'as the extension, so the force'. This approach well represents a metal wire extension behaviour and he formula for the one-dimensional deformation gives:

$$\varepsilon_z = \frac{1}{E}\sigma_z \tag{1.4}$$

where E is called Young's modulus and it is a constant for the soil, in linear elasticity framework.

The equation means that the presence of a vertical stress causes a vertical strain. At the same time, indeed, it causes lateral deformation in the opposite direction. Defining Poisson's ratio as:

$$\nu = -\frac{\varepsilon_{lateral}}{\varepsilon_{vertical}} \tag{1.5}$$

also the lateral strain can be retraced as:

$$\varepsilon_{lateral} = -\frac{\nu}{E}\sigma_z \tag{1.6}$$

It is well known that in fully isotropic conditions Young's modulus and Poisson's ratio are sufficient to describe the linear elastic response of a material.

There are two types of elasticity indeed: the first involves constant moduli and it is called linear elasticity while the second (non linear elasticity) deals with stress dependent moduli so that there is no guarantee that the use of such moduli may cause thermodynamic problems like energy generation in closed loop cycles. The behaviour of an elastic material can be in general described by generalisations of Hooke's original statement that can be summarized in the existence of a one-to-one relationship between stress and strain. Such a relationship may be linear or non linear, but an essential feature is that the application and removal of a stress leaves the material in pristine conditions and no nett energy is dissipated. Under such conditions the material behaviour is fully reversible and the behaviour is defined as hyper-elastic where hyper-elasticity means elasticity of higher degree.

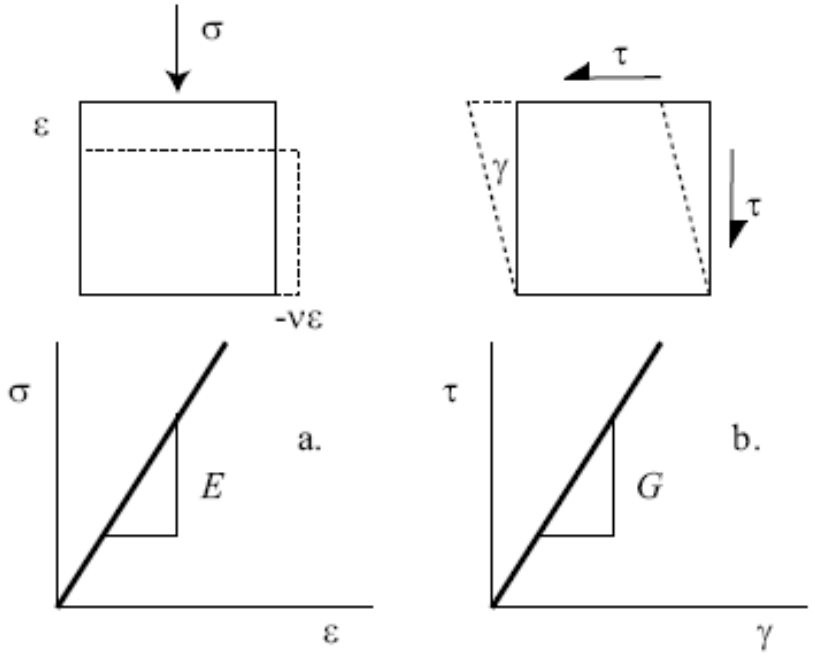

Figure 1.1: linear relationship between stress and strain for compression and shearing of elastic element

In order to describe a recoverable behaviour, in fact, the system has to be conservative (or path independent) which implies that the strains obtained are independent of the sequence in which the stresses are applied or removed and independent system of stresses can be superposed to deduce the results of applying combination of stresses.
As better described in Chapter 3, in fact, these conditions imply the existence of a unique energy function independent of load history and they give a symmetric stiffness matrix.

The elastic compliance matrix of a fully isotropic mean is therefore:

$$D^{-1} = \frac{1}{E}\begin{bmatrix} 1 & -\nu & -\nu & 0 & 0 & 0 \\ -\nu & 1 & -\nu & 0 & 0 & 0 \\ -\nu & -\nu & 1 & 0 & 0 & 0 \\ 0 & 0 & 0 & 2(1+\nu) & 0 & 0 \\ 0 & 0 & 0 & 0 & 2(1+\nu) & 0 \\ 0 & 0 & 0 & 0 & 0 & 2(1+\nu) \end{bmatrix} \tag{1.7}$$

and the stiffness matrix is the inverse matrix:

$$D = \frac{E}{(1+\nu)(1-2\nu)}\begin{bmatrix} (1-\nu) & \nu & \nu & 0 & 0 & 0 \\ \nu & (1-\nu) & \nu & 0 & 0 & 0 \\ \nu & \nu & (1-\nu) & 0 & 0 & 0 \\ 0 & 0 & 0 & \frac{1}{2}(1-2\nu) & 0 & 0 \\ 0 & 0 & 0 & 0 & \frac{1}{2}(1-2\nu) & 0 \\ 0 & 0 & 0 & 0 & 0 & \frac{1}{2}(1-2\nu) \end{bmatrix} \tag{1.8}$$

Instead of using the Young modulus and the Poisson's ratio, dealing with soils, it is more useful to use an alternative pair of elastic constants: the bulk modulus K and the shear modulus G, which divide the elastic deformation into a volumetric part (change of size at constant shape) and a distortional part (change of shape at constant volume) respectively.

In introducing appropriate quantities with which to describe these two parts separately axisymmetric conditions of the triaxial tests are chosen. The two degrees of deformational freedom for soil samples in the triaxial apparatus are compression and distortion. Defining the volumetric strain increment linked with compression first, as:

$$d\varepsilon_p = d\varepsilon_a + 2d\varepsilon_r = I_{1,\varepsilon} \tag{1.9}$$

where $I_{1,\varepsilon}$ is the first strain invariant and where a and r denote the axial and radial components respectively, the volumetric effective stress associated with it to get the work done in changing the volume of a unit element of soil as:

$$dW_p = p' d\varepsilon_p \tag{1.10}$$

it results to be:

$$p' = \frac{1}{3}\left(\sigma'_a + 2\sigma'_r\right) = \frac{1}{3} I_1 \tag{1.11}$$

where I_1 I is the first stress invariant.

Moving then from the definition of the deviator stress as:

$$q = \sigma'_a - \sigma'_r = F / A \tag{1.12}$$

that represents the amount by which the axial stress exceeds the radial stress and where F is the vertical force applied in a triaxial test, there are no remaining choice in the definition of the work-conjugate distortional strain increment that is therefore:

$$d\varepsilon_p = \frac{2}{3}\left(d\varepsilon_a - d\varepsilon_r\right) \tag{1.13}$$

since the increment of work required to change the shape of a unit element of soil is given by:

$$dW_q = q d\varepsilon_q \tag{1.14}$$

The total work done per unit volume during any strain increment is the sum of volumetric and distortional terms:

$$dW = dW_v + dW_q = p' d\varepsilon_p + q d\varepsilon_q = \sigma'_a \, d\varepsilon_a + 2\sigma'_r \, d\varepsilon_r \tag{1.15}$$

The elastic response expressed in terms of these stress and strain quantities and involves bulk modulus K and shear modulus G as both defined in the following:

$$K = \frac{E}{3(1-2\nu)} \tag{1.16}$$

$$G = \frac{E}{2(1+2\nu)} \tag{1.17}$$

and the constitutive law results to be:

$$\begin{bmatrix} d\varepsilon_p \\ d\varepsilon_q \end{bmatrix} = \begin{bmatrix} 1/K & 0 \\ 0 & 1/3G \end{bmatrix} \begin{bmatrix} dp' \\ dq \end{bmatrix} \tag{1.18}$$

in the compliance shape, and:

$$\begin{bmatrix} dp' \\ dq \end{bmatrix} = \begin{bmatrix} K & 0 \\ 0 & 3G \end{bmatrix} \begin{bmatrix} d\varepsilon_p \\ d\varepsilon_q \end{bmatrix} \tag{1.19}$$

in the stiffness shape.

It appears clearly the absence of any coupling between volumetric an distortional effects for the isotropic elastic model. Thus, if the mean effective stress is changed without change in distortional stress the shape of the soil elements remains unchanged and conversely, if the soil element is subjected to a distortional strain (change in shape) without change in volume (undrained deformation) then there will be no tendency for the effective mean stress to change.

Linear elasticity is a case of hyper-elastic behaviour, while hypo-elasticity ,on the other side, is a lower degree elasticity in which there is not a unique strain energy function to describe the material state. Hypo-elasticity indeed relates stress increments to strain increments by means of a modulus matrix in which the moduli may be stress dependent and obtained from curve fitting procedures on experimental data. The constitutive matrix will not be necessarily symmetric.
As a consequence the uniqueness of solution may be questioned and the calculated deformation may depend on the load history and not only the load condition.
Besides, thermodynamic problem like energy generation in closed loop cycles can be caused.

Let consider, for instance, the work related to change of shape and the change of volume for the stress cycle reported in Figure 1.2, supposing an elastic constitutive law with the following stress dependent moduli:

$$K = K_1 + K_2 p' \tag{1.20}$$

$$G = G_1 + G_2 p' \tag{1.21}$$

As observed, the energy entered by moving from a to b is returned when we unload from c to d. The energy used on shear deformation from b to c is however less than the energy returned when we unload with a lower stiffness from d to a. There something got back more than what is brought in and energy is generated in the loop that is unrealistic. This is an example of hypo-elastic constitutive law that brings thermodynamic problems.

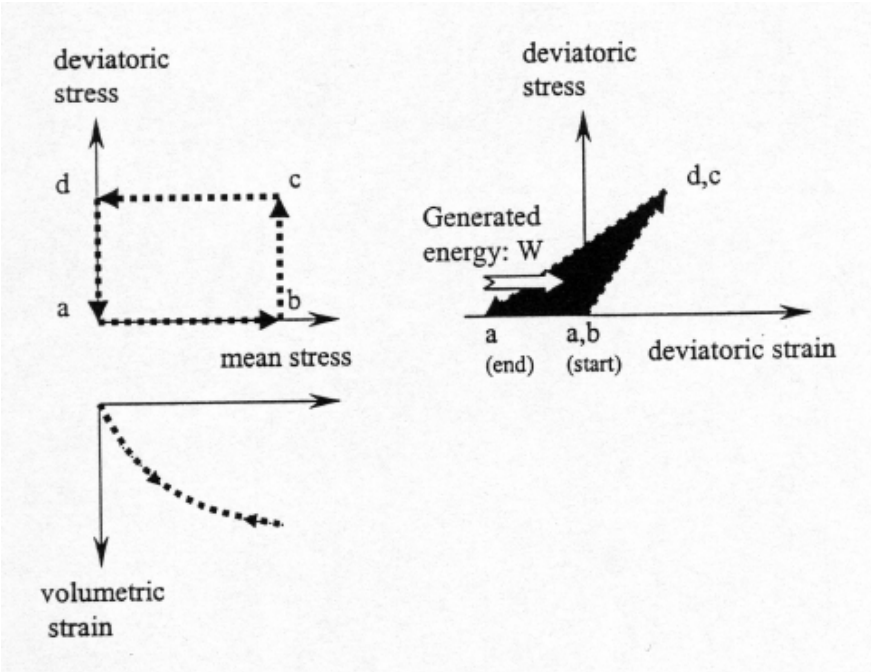

Figure 1.2: nett energy generation in a closed loops using stress dependent moduli (Nordal, 2004)

Elasto-plasticity theory: the four main ingredients

Elastic material models and solutions based on theory of elasticity may be directly applied in geotechnical engineering for problems where strains are very small.

Elastic strains are by definition recoverable and strains are again zero when the load causing them is removed. When involved strain is significant some of the strain will normally be permanent. Permanent strains are called irrecoverable or plastic, hence the name of *elasto-plasticity* associated to the constitutive law that accounts for irreversible behaviour of the material.

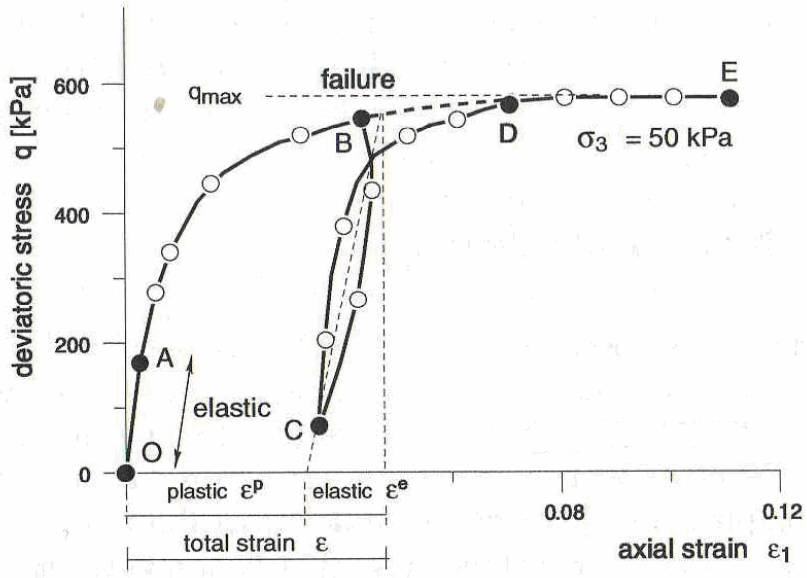

Figure 1.3: triaxial shear test with unloading –reloading cycle (Abed, 2008)

Figure 1.3 shows the result of a standard triaxial test with one unloading- reloading cycle. Up to some point A, the stress-strain relationship is more or less elastic and linear. If unloading takes place at any point along OA the material will follow the same path but in the opposite direction.

(1) The first ingredient of an elasto-plastic model is therefore the *elastic domain* in which the behaviour can be considered as elastic, and a related relationship that governs the elastic contribution:

$$d\varepsilon_{ij}^{\,e} = D^{-1} d\sigma_{ij} \tag{1.22}$$

Beyond point A unloading will not show full reversibility of strain, i.e. a return to point O. Such point A is known as the *yield point*. If the sample is loaded up to B and then unloaded to C, permanent deformations OC will occur. At point B the total axial strain can be expressed as the sum of an elastic and a plastic parts.
This decomposition of total strain into elastic and plastic components form one of the basic equations in elasto-plasticity. Hence:

$$d\varepsilon_{ij} = d\varepsilon_{ij}^{\,e} + d\varepsilon_{ij}^{\,p} \tag{1.23}$$

where ε_i denotes a strain component.

(2) The *yield point*, or more generically the *yield surface* in three-dimensional conditions, marks the boundary of the region of elastically attainable states of stress. It is described by an equation called *yield criterion*:

$$F(\sigma_{ij}, h) = 0 \tag{1.24}$$

where h represents a set of variables linked to the history of the process (hardening parameters), later described.

Whenever $F(\sigma_{ij}, h) < 0$ the soil state represented is inside the yield locus and the response is elastic. Whether $F(\sigma_{ij}, h) = 0$ the soil state is in an elasto-plastic condition.

The yield locus can represent either a failure situation (in case of elastic perfectly plastic materials) or simply a yielding condition. In the elastic-perfectly plastic model there is a region of stress space which can be reached elastically, without incurring any irrecoverable deformations, however, as soon as the boundary of this elastic region is reached then the material fails at constant stress as described in Figure 1.4. Stress points outside the yielding surface $(F(\sigma_{ij}, h) > 0)$ are not allowed. In the case of prefect plasticity the yield criterion coincides with a failure criterion. so one of the first yield criterion first assumed is the well known Mohr Coulomb frictional failure law (1773):

$$\tau_f = c' + \sigma' \tan\varphi \tag{1.25}$$

that expressed in terms of principal stresses gives:

$$\left|\sigma'_i - \sigma'_k\right| - \left(\sigma'_i + \sigma'_k\right)\sin\varphi - 2c\cos\varphi = 0 \tag{1.26}$$

where i and k has to be changed into 1,2,3 respectively in order to get six equation whose representation in principal stress space gives a pyramid with axis coinciding with hydrostatic axis ($\sigma'_1 = \sigma'_2 = \sigma'_3$) as in Figure 1.5a. Since soil does not bear extension stress a tension cut-off has to be applied:

$$\sigma'_1 \geq 0, \sigma'_2 \geq 0, \sigma'_3 \geq 0 \tag{1.27}$$

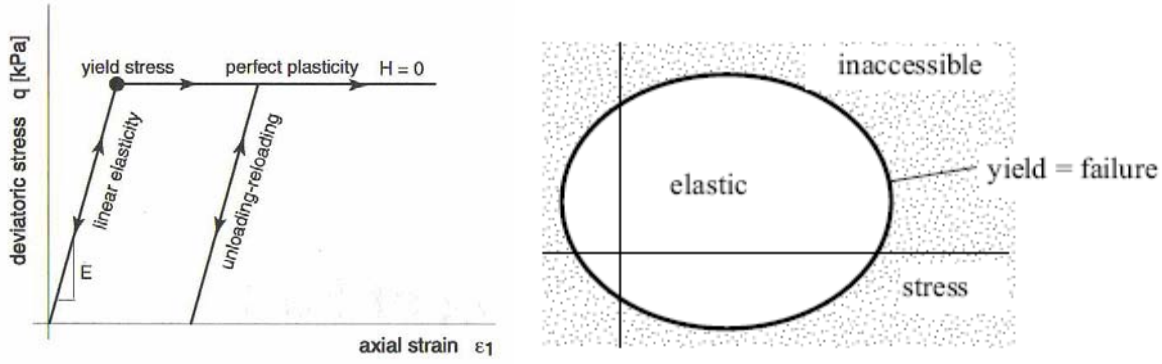

Figure 1.4: perfect plasticity

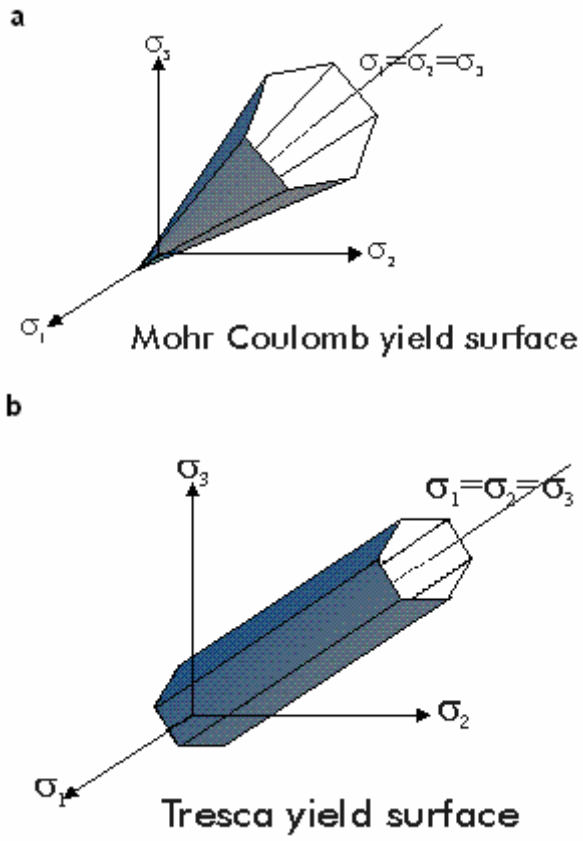

Figure 1.5: (a) Mohr Coulomb yield surface and (b) Tresca yield surface in principal stress state

The Mohr Coulomb failure (or yielding) criterion is a generalization of the Tresca criterion that is a prism in principal stress space whose expression is:

$$\left|\sigma'_i - \sigma'_k\right| - 2c = 0 \tag{1.28}$$

This failure criterion was first formulated for metals (1864), that show typically elastic perfectly plastic behaviour. Both of these failure criteria, together with many others (Von Mises, Drucker-Prager, Matsuoka-Nakai etc.), can be assumed in geotechnical modelling as failure criteria in elastic perfectly plastic models, or better as yielding surfaces, since soils do not behave as perfectly plastic materials.

On reloading starting from point C in Figure 1.3, in fact, the primary loading curve is reached at point D and then follows the primary loading curve up to a maximum value $q_{\max}$ at point E where the soil fails. Shear stress at point E is known as soil shear resistance under constant confining pressure σ_r.During primary loading along the path OABDE the so called yield point is gradually moved from A to E. This process of increasing the yielding point is known as *hardening*.

In an elastic perfectly plastic framework, such as depicted in Figure 1.4, the material shows no hardening and the stiffness H of the material reduces to zero. Another type of plastic behaviour is seen in Figure 1.6 where the linear stress-strain is continuous in the plastic range but with a lower stiffness H compared to the stiffness E in the elastic range. If the plastic stiffness $H > 0$ then the behaviour is referred to as *strain hardening* behaviour, otherwise for $H < 0$ it is called *strain softening* behaviour.

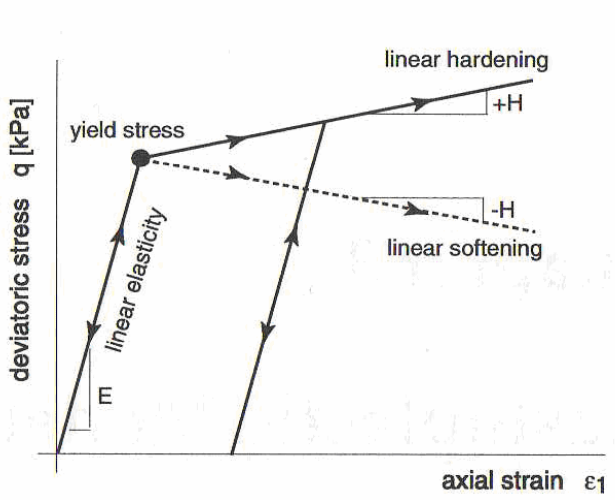

Figure 1.6: linear strain hardening or softening plasticity

For a hardening model the elastic boundary is then not fixed but will depend on the history of loading of the soil, that is accounted by the hardening parameter *h* included in the yield criterion. As for the perfect plasticity, there is the usual constraint that the current state of stress cannot lie outside the current yield surface but the yield surface is no longer of fixed size (as for perfectly plastic models is) but is able to expand in order to accommodate the imposed stress changes.
From the onset of yielding, the yield surface moves along with the stress state. The surface may expand keeping its shape (isotropic hardening), translate (kinematic hardening) or both (mixed hardening), as reported in Figure 1.7, if hardening causes yield surface rotation, it is called rotational hardening.

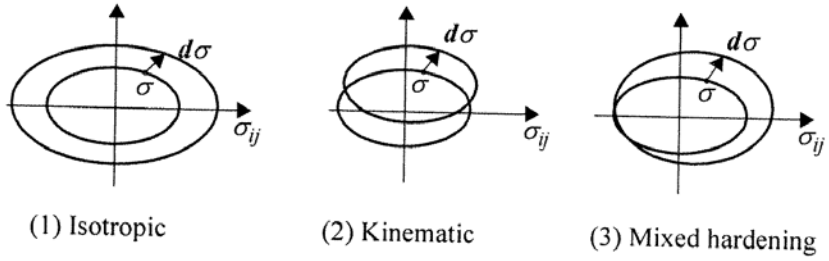

Figure 1.7: types of hardening during plastic loading

The condition that states that the stress state must remain on the yield surface when plastic strain are being generated is called *consistency condition* :

$$dF = 0 \tag{1.29}$$

Three are thus the possible soil states:

- $F(\sigma_{ij}, h) < 0$: the stress state is inside the yield locus and the response is taken as entirely elastic
- $F(\sigma_{ij}, h) = 0$ and $dF < 0$: the stress state is on the yield locus but there is a return inside the yield surface so that material response is elastic
- $F(\sigma_{ij}, h) = 0$ and $dF = 0$: the soil state is on the yield surface and plastic strains are occurring

(3) The increasing of yielding stress in one-dimensional process like that reported in Figure 1.3, or more in general the evolution of the yield surface during plastic loading, is usually related to the plastic deformation experienced by the soil and it is described by an equation called *hardening law* that is a further necessary ingredient to define an elasto-plastic model. It can be expressed in the form:

$$h = h(d\varepsilon_{ij}{}^{p}) \tag{1.30}$$

where h is the set of internal parameters called hardening parameters already mentioned and $d\varepsilon_{ij}{}^{p}$ are the plastic strain.

As already showed, the hardening rule is integrated into the yield function by writing the yield function in terms of hardening parameters: $F(\sigma_{ij}, h) = 0$. The consistency equation thus becomes:

$$dF(\sigma_{ij}, h) = \frac{\partial F}{\partial \sigma_{ij}} d\sigma_{ij} + \frac{\partial F}{\partial h}\frac{\partial h}{\partial \varepsilon_{hk}} d\varepsilon_{hk}{}^{p} = 0 \tag{1.31}$$

It provides the *loading criterion* reported in Figure 1.8: the definition of loading unloading for an applied stress increment is related to the direction of the stress increment relatively to the current yield function. A process of loading causes plastic strains to develop, unloading is assumed purely elastic in classical theory and the stress point leaves the yield surface F which stays fixed in stress space at its current position. If softening is modelled the inward stress increment in Figure 1.8 could result from a shrinking yield surface and it is necessary to use the strain increment to distinguish plastic softening from elastic unloading.

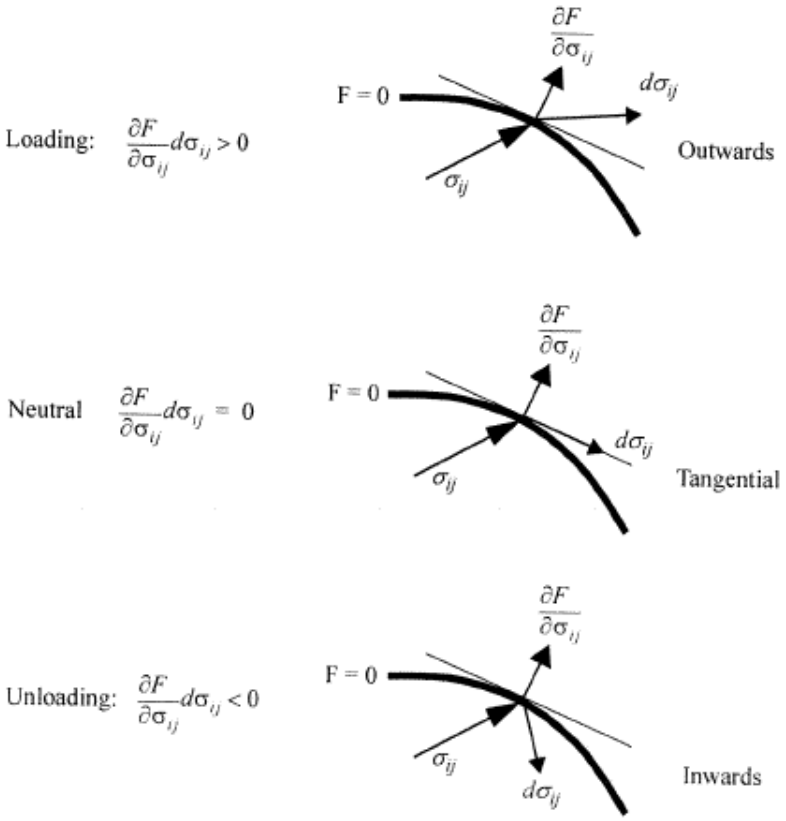

Figure 1.8:loading criterion (Nordal, 2008)

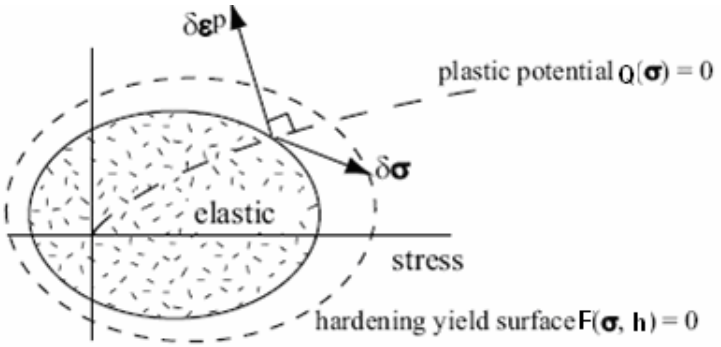

Figure 1.9: yield function and plastic potential

(4) There is a fourth element to complete the list of elasto-plastic model's list, that is the *flow rule*.
A first definition came up when researchers were dealing with metals and it represents a way of describing the mechanism of plastic deformation. The fundamental property of plastic strain increment originally postulated by St.Venant states that the direction of plastic strain increment $d\varepsilon_{ij}{}^{p}$ is uniquely given by the current stress state and consequently it is assumed to be independent of corresponding stress increments. Von Mises (1928) proposed the concept of a potential surface so that plastic strain can be related to the gradient of a potential function $Q(\sigma_{ij})$ to which it is orthogonal (see Figure 1.9):

$$d\varepsilon_{ij}{}^{p} = d\lambda \frac{dQ}{d\sigma_{ij}} \tag{1.32}$$

The formulation is known as the *flow rule* where $d\lambda$ is a scalar multiplier.

Drucker (1951) proposed his postulate by which for a stable material $Q(\sigma_{ij}) = F(\sigma_{ij})$ and the plastic strain is thus orthogonal to the yield surface. This gives an *associated flow rule* (also called *normality postulate*):

$$d\varepsilon_{ij}{}^{p} = d\lambda \frac{dF}{d\sigma_{ij}} \tag{1.33}$$

The validity of the associated flow is not always acceptable. It is commonly accepted that the Coulomb surface is a fairly good failure surface for frictional soils. However, associated flow predicts a plastic volume increase or plastic dilation far above the experimentally observed values. It would be in fact $\varphi \equiv \psi$, being ψ the dilation angle. Furthermore, the plastic volume increase would never stop as long as any plastic deformation takes place. Consequently, the soil would expand under a process of continuous shearing and this does not happen. A critical state may on the contrary develop where no further volume increase takes place.
The normality postulate therefore cannot be assumed as valid in modelling frictional material. Not the same happens for clays, for which the postulate reflects quite well the real behaviour.

By means of the hardening rule the scalar quantity $d\lambda$ can be determined. Substituting the flow rule equation (1.33) into the consistency equation (1.31), in fact, one gets:

$$dF(\sigma_{ij},h)=\frac{\partial F}{\partial \sigma_{ij}}d\sigma_{ij}+\frac{\partial F}{\partial h}\frac{\partial h}{\partial \varepsilon_{hk}}d\lambda\frac{\partial G}{\partial \sigma_{ij}}=0 \tag{1.34}$$

and thus:

$$d\lambda=-\frac{\dfrac{\partial F}{\partial \sigma_{ij}}d\sigma_{ij}}{\dfrac{\partial F}{\partial h}\dfrac{\partial h}{\partial \varepsilon_{hk}}\dfrac{\partial G}{\partial \sigma_{ij}}}=\frac{1}{H}\frac{\partial F}{\partial \sigma_{ij}}d\sigma_{ij} \tag{1.35}$$

where H is the plastic resistance number:

$$H=\frac{\dfrac{\partial F}{\partial \sigma_{ij}}d\sigma_{ij}}{d\lambda}=\frac{cause}{effect}=-\frac{\partial F}{\partial h}\frac{\partial h}{\partial \varepsilon_{hk}}\frac{\partial G}{\partial \sigma_{ij}} \tag{1.36}$$

The consistency condition can be write as:

$$dF(\sigma_{ij},h)=\frac{\partial F}{\partial \sigma_{ij}}d\sigma_{ij}-Hd\lambda=0 \tag{1.37}$$

In case of elastic conditions (for instance in unloading path for which it holds: $\frac{\partial F}{\partial \sigma_{ij}}d\sigma_{ij}<0$) there are no plastic strain so that $d\lambda=0$.

This condition allows to distinguish the case of softening for which still holds: $\frac{\partial F}{\partial \sigma_{ij}}d\sigma_{ij}<0$ but $H<0$ (see Figure 1.6). In order to fulfil the consistency condition it has to be then: $d\lambda>0$.

The four elements herein described as fundamental ingredients of elasto-plasticity theory will be pointed out in the next paragraph in the specific case of the Modified Cam Clay model, that is the base of the creep model described in Chapter 3.

The Modified Cam Clay model for clays

Historically it is probably reasonable to describe Cam clay as the first hardening plastic model that has become generally adopted for soils. It has formed a basis for much subsequent development of soil models. Originally developed in the early 1960s, models of the Cam clay form have been widely and successfully used for analysis of problems involving the loading of soft clays. It has been less successful in describing the behaviour of sands for which models it makes use of distortional hardening and non-associated flow.
Two versions have been formulated: the original Cam Clay (Schofield & Wroth, 1958) and the Modified Cam Clay (Roscoe & Burland, 1968). The latter is the basis of the creep model described in Chapter 3. The main ingredients of this elasto-plastic model will be presented in the following as described in the previous paragraph.

(1) *Elastic response*

Results of oedometer tests are typically presented in semi-logarithmic plots because it is found that

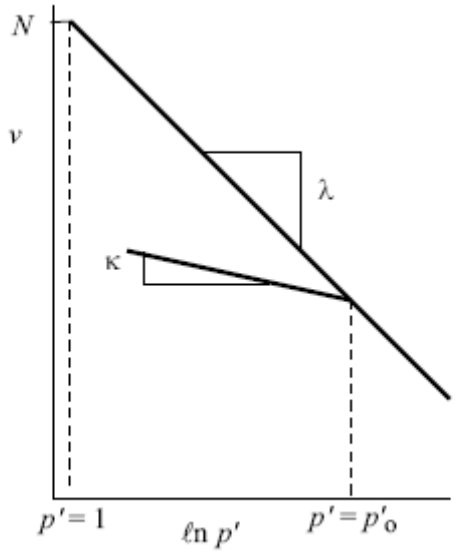

Figure 1.10: linear compression and unloading-reloading lines in semi-logarithmic compression plane

the relationships between stress and volume change then become somewhat more linear both during
loading and during unloading. Looking at the typical loading and unloading response in an oedometer (Figure 1.10) the division of the volume changes into elastic and plastic parts can be easily determined. The average slope κ of an unload-reload line is used to characterise the elastic volumetric response and κ ·is assumed as a soil constant:

$$v = v_\kappa - \kappa \ln p' \tag{1.38}$$

where $v = e + 1$ is the specific volume and v_κ is a reference value of specific volume on a particular unloading-reloading relationship. This can be converted to an incremental relationship:

$$d\varepsilon_p{}^e = -\frac{dv}{v} = \frac{\kappa}{v}\frac{dp'}{p'} \tag{1.39}$$

which implies that the bulk modulus K is not constant but is dependent on stress level:

$$K = \frac{dp'}{d\varepsilon_p{}^e} = \frac{vp'}{\kappa} \tag{1.40}$$

As regard to the deviatoric elastic part, the response is (see Equation (1.18)):

$$d\varepsilon_p{}^e = \frac{dq}{3G} \tag{1.41}$$

It may be convenient to choose a constant shear modulus G as seen from the initial behaviour in any compression test or an alternative could be to choose a constant value of Poisson's ratio v, thus forcing a constant ratio of shear modulus and bulk modulus:

$$G = K\frac{3(1-2v)}{2(1+v)} \tag{1.42}$$

Clearly if G is constant then the variation of bulk modulus K with stress will lead to a varying v. However, if Poisson's ratio v is assumed to be constant then G changes together with bulk modulus. If both G and K functions are function of p' there are thermodynamic problems as described previously and more in detail in Chapter 5. It becomes possible, in fact, to generate or dissipate energy on supposedly elastic cycles of stress change.

(2) *Yield criterion*

In the triaxial stress plane it is assumed that the yield locus has an elliptical shape passing through the origin of the stress plane (Figure 1.11). This introduces two variables: the aspect ratio of the ellipse M which controls the shape of the ellipse and is the ratio of the vertical axis q to the horizontal p' axis at critical state ($\eta = q/p'$); and the size of the ellipse p'_0 which is the hardening parameter h for the Cam clay model. The equation of the ellipse can be presented in various different ways:

$$F(p', q; p'_0) = \frac{q^2}{M^2} - p'(p'_0 - p') \tag{1.43}$$

so that, as usual $F < 0$ indicates elastic behaviour, $F = 0$ indicates yielding is occurring and $F = 0$ is not permitted.
However, the equation of the ellipse can also be written:

$$\frac{p'}{p'_0} = \frac{M^2}{M^2 + \eta^2} \tag{1.44}$$

or:

$$\frac{q}{M^2} = p'(p'_0 - p') \tag{1.45}$$

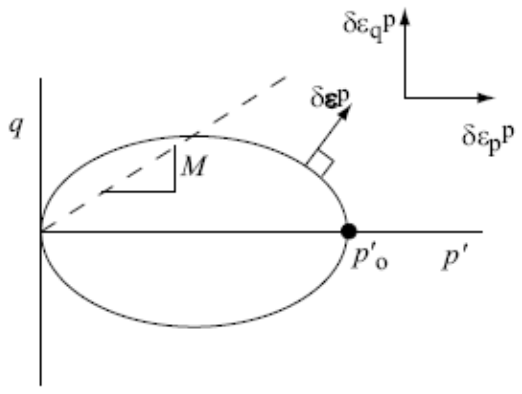

Figure 1.11: Cam Clay yielding surface

Imposing the consistency equation: $dF = 0$, for a given stress change (dp', dq) causing yield, the change size of yield locus can be obtained differentiating the above equations:

$$dp'_0 = (2p' - p'_0)\frac{dp'}{p'} + \frac{2q}{M^2}\frac{dq}{p'} \tag{1.46}$$

or:

$$dp'_0 = \frac{M^2 - \eta^2}{M^2}dp' + \frac{2\eta}{M^2}dq \tag{1.47}$$

or:

$$\frac{dp'_0}{p'_0} = \frac{dp'}{p'} + \frac{2\eta}{M^2 + \eta^2}d\eta \tag{1.48}$$

As the size of the yield locus changes, the shape remains the same and he locus grows from the origin. Along any line at constant stress ratio $\eta = q/p'$ the angle of intersection with any yield locus is always the same.

(3) *Hardening rule*:

The hardening rule describes the dependence of the size of the yield locus p'_0 on the plastic strain. Cam clay is a volumetric hardening model in which it is assumed that the size of the yield locus depends only on the plastic volumetric strain through the expression:

$$\begin{pmatrix} dp'_0 / d\varepsilon_p{}^p \\ dp'_0 / d\varepsilon_q{}^p \end{pmatrix} = \begin{pmatrix} vp'_0/(\lambda - \kappa) \\ 0 \end{pmatrix} \tag{1.49}$$

This hardening rule introduces one additional soil parameter λ. During isotropic normal compression we have change in mean stress p' with distortional stress q kept constant at zero. There will be elastic volumetric strains given by (1.39) and, because the mean stress is always at the tip of the yield surface ($p' = p'_0$), there will be plastic volumetric strains given by a rearrangement of (1.49):

$$d\varepsilon_p{}^p = \frac{\lambda - \kappa}{v}\frac{dp'}{p'} \tag{1.50}$$

The total volumetric strain is then:

$$d\varepsilon_p = d\varepsilon_p{}^e + d\varepsilon_p{}^p = \frac{\kappa}{v}\frac{dp'}{p'} + \frac{\lambda - \kappa}{v}\frac{dp'}{p'} = \frac{\lambda}{v}\frac{dp'}{p'} \tag{1.51}$$

Since the definition of the volumetric strain is:

$$d\varepsilon = \frac{dv}{v} \tag{1.52}$$

expression (1.51) can be integrated to give the form of the normal compression relationship linking specific volume v and mean effective stress p':

$$v = N - \lambda \ln p' \tag{1.53}$$

where N is a reference value of specific volume for unit value of mean effective stress. This is a linear normal compression relationship with slope λ , in the semi-logarithmic plot (Figure 1.10).

(3*) Flow rule*:

It is assumed that Cam Clay obeys the hypothesis of associated flow so that the plastic strain increment vector is assumed to be normal to the yield surface at the current state (Figure 1.11). The plastic potential function then has the same form as the yield criterion:

$$Q(p', q; p'_0) = F(p', q; p'_0) = \frac{q^2}{M^2} - p'(p'_0 - p') \tag{1.54}$$

The plastic strain increments are given by:

$$\begin{pmatrix} d\varepsilon_p{}^p \\ d\varepsilon_q{}^p \end{pmatrix} = d\lambda \begin{pmatrix} \frac{dQ}{dp'} \\ \frac{dQ}{dq} \end{pmatrix} = d\lambda \begin{pmatrix} 2p' - p'_0 \\ \frac{2q}{M^2} \end{pmatrix} \tag{1.55}$$

Alternatively, using form (1.44) of the equation of the elliptical yield locus, the ratio of plastic volumetric strain to plastic distortional strain, which characterizes the plastic deformation mechanism, can be written as:

$$\frac{d\varepsilon_p{}^p}{d\varepsilon_q{}^p} = \frac{M^2 - \eta^2}{2\eta} \tag{1.56}$$

The mechanism of plastic deformation depends only on the stress ratio at which yielding is occurring and changes continuously as the stress ratio changes. Several particular cases are of interest:

- for $\eta = 0 \Rightarrow d\varepsilon_p{}^p \big/ d\varepsilon_q{}^p \to \infty$ which implies compression without distortion and this is appropriate for isotropic consolidation without application of distortional stresses;
- for $\eta = M \Rightarrow d\varepsilon_p{}^p \big/ d\varepsilon_q{}^p = 0$ which implies distortion without compression: this is the critical state condition;
- yielding with low values of stress ratio $\eta < M \Rightarrow d\varepsilon_p{}^p \big/ d\varepsilon_q{}^p > 0$ which implies compression plus distortion;
- yielding with high values of stress ratio $\eta > M \Rightarrow d\varepsilon_p{}^p \big/ d\varepsilon_q{}^p < 0$ which implies expansion plus distortion.

Chapter 2 - Time dependent behaviour

Introduction

In his famous paper for the twenty-fifth Karl Terzaghi Lecture Schmertmann wrote: "everything on this earth has at least one thing in common: everything changes with time, all soils age and change".

Two are the possible interpretations: that intrinsic soils parameters change with time and that time plays a relevant role in soil behaviour, in the sense that when considering a whole phenomenon, time has to be involved as a main independent variable.

The principal evidence of time dependency in soils behaviour is the empirical observations of large settlements developing with time in soils subjected to constant effective stress. This phenomenon is referred to as *creep* behaviour and it is clearly evident mostly in clays but it is observed in sandy soils, as well.

Based on the visual observation of deformations of ancient structures and natural slopes, the existence of a creep in soils is known since long time. However, proper investigation on this phenomenon started in 19th century due to the intensive building activities.
Creep started to be interesting for scientists and specialists after the observation of unacceptably large prolonged deformations, affecting normal exploitation of structures and roads. The first highlighting of the creep's phenomenon in clayey soils can be found in Karlovich (1869).

Today one can find a lot examples of in-situ creep behaviour. A classical one is the uneven settlement of the Tower of Pisa in Italy. The construction of the Tower was started in 1173 and completed in 1370. The height of the tower is 58 m from the foundation and 54.58 m from the ground, weight has been calculated as 14.453 tones (140 MN), the area of the annular foundation is 285 m^2 and the mean pressure on the base is about 500 kPa. Due to the creep deformation of clays deposited in the form of lenses in the sandy base, the Tower settled and tilted towards the South side. The mean settlement of the structure according to one of the many evaluations is 3 meters, and the Tower still continues to settle, although the recent restauration works have brought it back to a safe configuration. The maximum tilt of the tower of 5.5 meters was reached in 1993, for an inclination of about 5.5°. It is important to note that time-dependent behaviour of soils is not related to primary consolidation (dissipation of excess pore pressures generated during loading), but rather to the viscosity of soil skeleton.

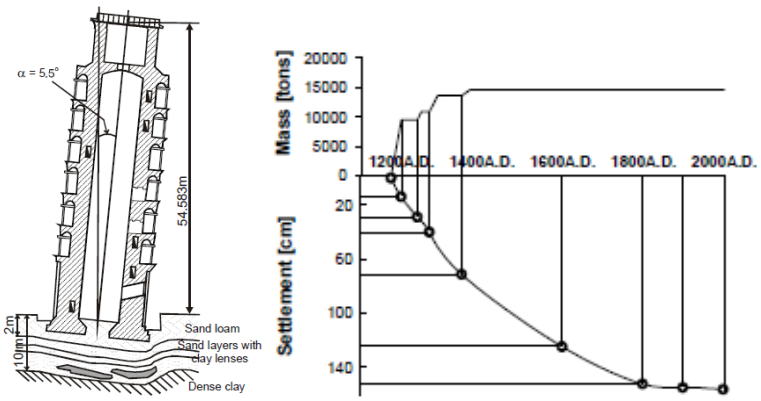

Figure 2.1: the Leaning Tower of Pisa, settlement with time

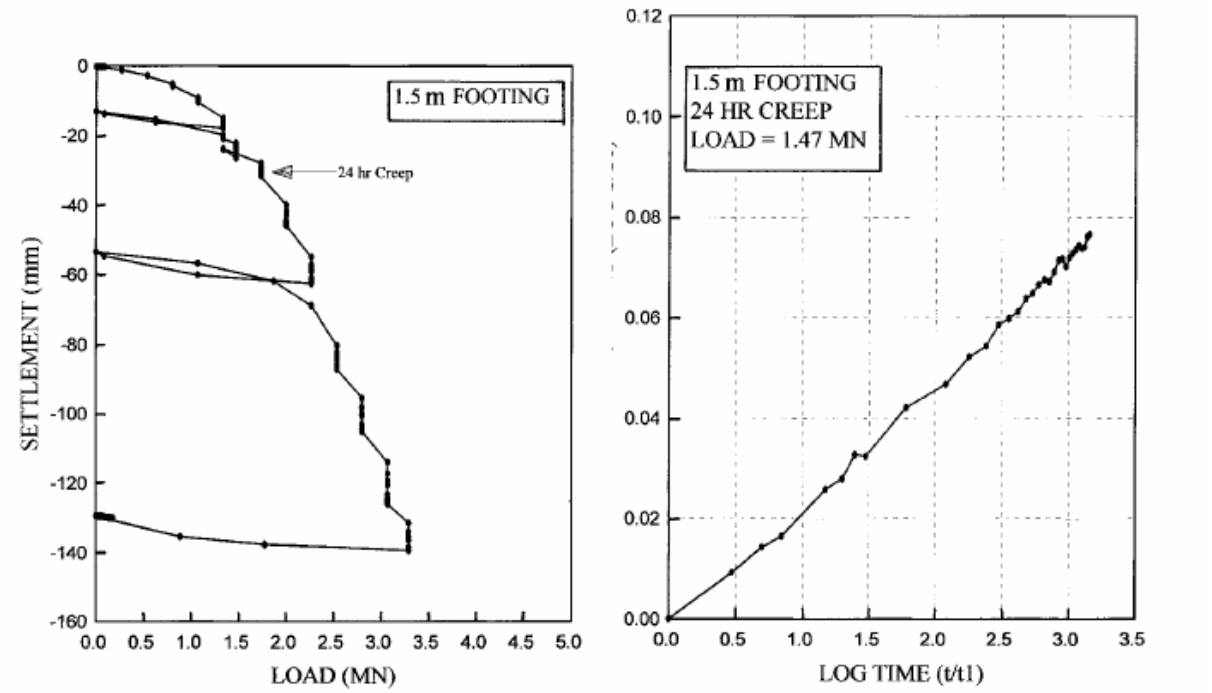

Figure 2.2: loads settlements curves of a dense sand under a shallow squared foundations (Briaud & Gibbens, 1994)

Examples of creep behaviour in sandy soils can also be found. In Figure 2.2 load-settlement curves are reported for the spread footing tests performed at the National Geotechnical Experimentation Site on the Texas A&M University Riverside Campus (Briaud and Gibbens, 1994). The soil at the site is a medium dense, fairly uniform, silty fine silica sand with the following average properties near the footings and within the top 5 meters: mean grain size D_{50} = 0.2 mm, cone penetrometer test point resistance 6 MPa, pressuremeter test limit pressure 800 kPa, dilatometer test modulus 30 MPa, borehole shear test friction angle 32°, estimated total unit weight 15.5 kN/m^{3}and crosshole shear wave velocity 240 m/s.

The testing procedure consisted of applying concentrated load on square footings, in increments equal to 1/10 of the estimated bearing capacity as determined by traditional methods. Each load step lasted 30 min, with settlement readings at 1, 3, 5, 7, 10, 20, and 30 min. As a settlement of about 25 mm, the load was held for 24 h while recording the settlement. From those two graphics it appears clearly that sands which are generally considered non-viscous, exhibit time-dependent behaviour under constant effective stress.

Definition of creep

By definition creep is the phenomenon in which the strain increases at constant effective stress, due to viscous effect involving the soil solid skeleton. A creep test (stress path A-B) is described in Figure 2.3 considering a soil sample at the initial stress-strain state A and letting the stress be constant over time. As time advances, the strain state moves toward B. During this process the strain is gradually increasing with constant effective stress acting on the specimen, in other words the soil exhibits creep behaviour.

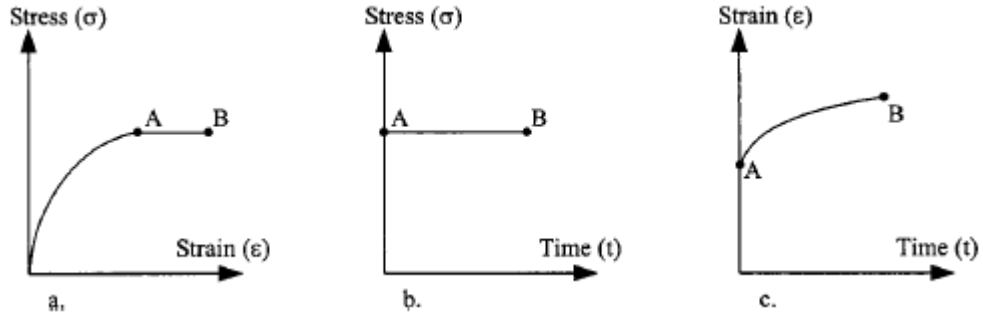

Figure 2.3: definition of creep test

The results of a creep process performed at constant stress in a triaxial apparatus may be plotted in a strain–time diagram with linear axes (Figure 2.4 a). The process can be divided into three parts: primary creep or transient creep, secondary creep or stationary creep, and tertiary creep or acceleration creep. The primary phase, in some literature also called transient or fading, can be defined as a creep deformation during which the strain rate decreases continuously with time. Deformation at a constant rate (material flow) is denoted as the secondary phase, and sometimes also called non-fading. In the case of the tertiary or the accelerated phase the strain rate is continuously increasing and this leads to the creep rupture.

This fact is further demonstrated plotting the logarithm of the strain rate against the logarithm of time as in Figure 2.4 b. It should be noted that tertiary creep is only valid for a creep test performed by means of a triaxial device. According to the acting stress it is possible, in fact, to divide creep behaviour into volumetric and deviatoric (or shear) creep. Here, volumetric creep is caused by the constant volumetric stress and deviatoric creep is caused by the constant deviatoric stress.

Volumetric creep consists only of the primary phase of the creep deformation, i.e. it tends to stabilise. Deviatoric creep may or may not consist all three phases, depending on the shear mobilisation. If the deviatoric stress is low, then only primary creep phase will appear, but after crossing some level of the shear mobilisation primary phase will be followed by the secondary phase which can lead to the tertiary phase and creep rupture. The first case is representative for a step load tests performed in an oedometer apparatus in which volumetric stress increases much more than deviatoric stress (that is equal to $(1-K_0)\sigma'_z$).

For oedometer tests, primary, secondary, and tertiary compression can be defined by plotting strains versus the logarithm of time, as reported in Figure 2.5.

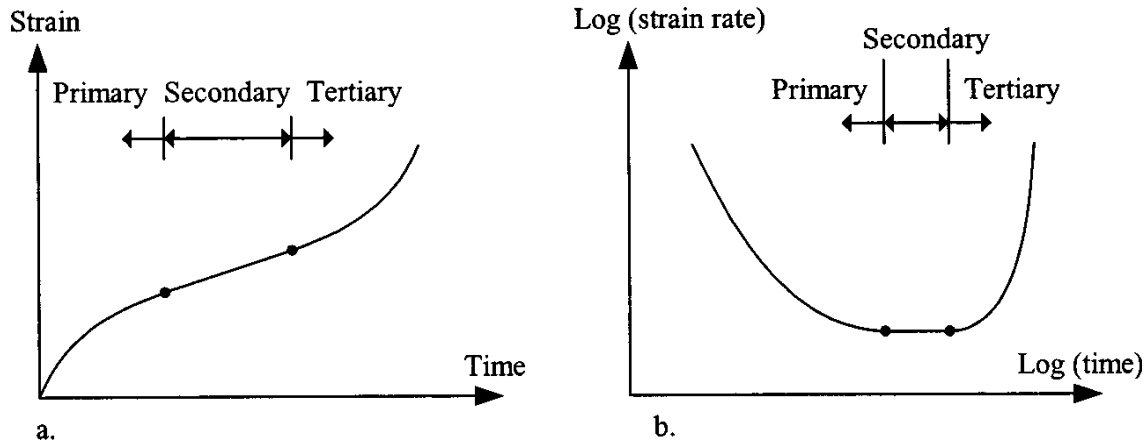

Figure 2.4: three phases of creep in a triaxial apparatus (Augustesen, Liingaard & Lade, 2004).

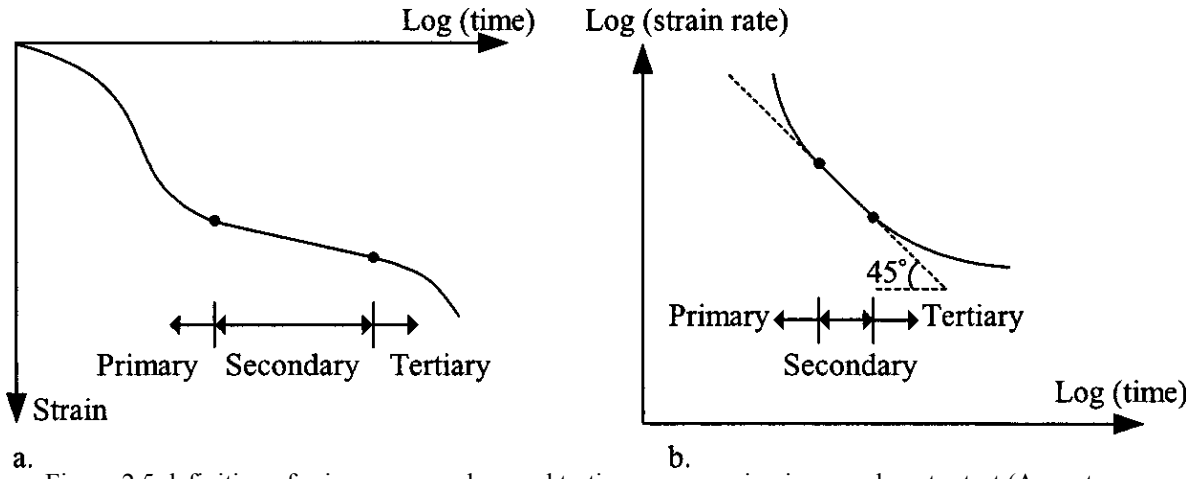

Figure 2.5:definition of primary, secondary and tertiary compression in an oedometer test (Augustesen, Liingaard & Lade, 2004).

The primary phase coincides with the primary consolidation, i.e., the primary phase is the phase where excess pore pressure dissipates. The secondary phase is also denoted as secondary consolidation and, in oedometer tests, this phase corresponds to pure creep, i.e., deformations occur due to deformations in the soil skeleton. Tertiary compression corresponds to pure creep, too. The tertiary compression phase is subsequent to the secondary compression phase and it is characterized by a nonlinear relationship between the logarithm of time and strain. In both the primary, the secondary and the tertiary phases the strain rate decreases with time as shown in Figure 4.5 b thus confirming that in oedometric conditions only primary creep can be expressed.

Hypothesis A and hypothesis B: when does creep start to occur?

When a fully saturated soil sample (typically a clay sample) is suddenly loaded one-dimensionally, its void ratio decreases producing ,at least for normally consolidated samples, the well known S-shaped curve, reported in Figure 2.6.

During primary compression settlement is controlled by dissipation of excess pore pressure and Darcy's law, i.e. it is a consolidation process, on the other hand, during secondary compression, the rate of viscosity is controlled by soil viscosity; however, as settlements requires hydraulic gradient, excess pore pressure also exist during that stage.

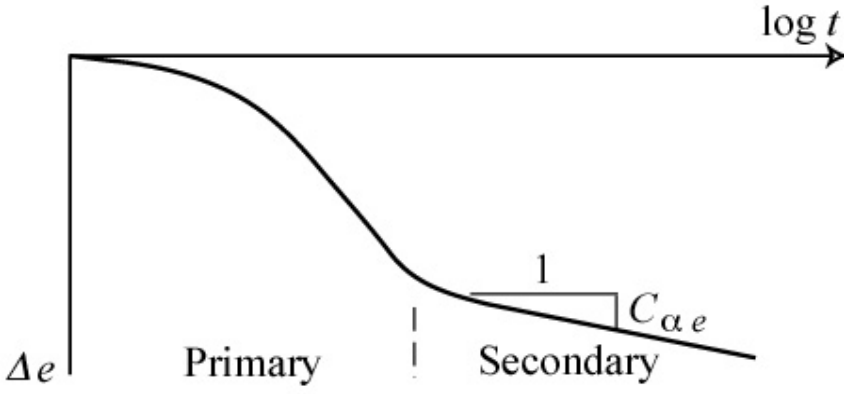

Figure 2.6: -shaped compression curve in semi-logarithmic plot

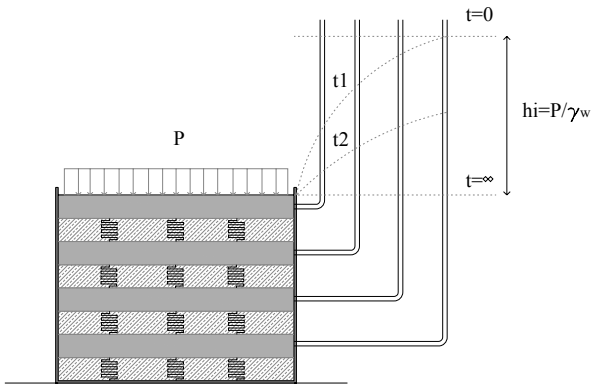

Figure 2.7: Terzaghi one-dimensional consolidation theory scheme

The classical theory of consolidation that was developed by Terzaghi (1923) is still the basis of one-dimensional consolidation theory. The theory is based on the assumption that a unique relationship exists between effective stress and strain independent of time expressed by the following equation:

$$\frac{\partial u}{\partial t} = \frac{m_v}{\gamma_w}\frac{\partial}{\partial z}\left(k_v \frac{\partial u}{\partial z}\right) \tag{2.1}$$

The Terzaghi consolidation theory is formulated with the hypotheses of linear elastic mechanical behaviour of soil, of validity of Darcy's law, of soil grains and water incompressibility and of fully saturated conditions. It is described through the following scheme made of a series of interconnected springs in a box full of water. Once one applies a stress to them this is instantaneously transferred to the water and only after time it passes to springs against dissipation of the so-called *excess pore pressure* being generated during loading.
Time is involved in this diffusion problem just because consolidation takes time to occur and the delay is proportional to the permeability coefficient.

The integrated solution over finite boundaries offers a curve in terms of consolidation degree like the two shown in Figure 2.8. Broken lines represent the real soil behaviour that continues to deform even if the consolidation process has finished.

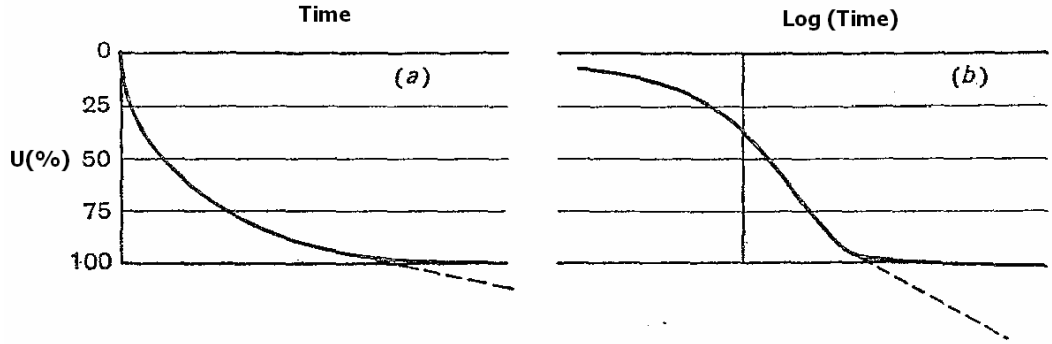

Figure 2.8: consolidation curve in terms of consolidation ratio and time

In 1925 Terzaghi introduced the first oedometer device and suggested a test procedure where a specimen is loaded stepwise, each load step doubling the previous value, until the excess

pore pressure has dissipated. For clays, duration of 24 hours is quite common. This procedure is still widely used, and is commonly referred to as an incremental load oedometer test.

In Figure 2.6 the typical compression curve for a generic loading step is shown, the transition between the consolidation phase and the secondary compression is in correspondence of a time value defined as *end of primary consolidation time* (t_{EOP}) when excess pore pressure has almost completely dissipated. Prior to t_{EOP}, one-dimensional compression takes places with an increase of vertical effective stress. When the effective stress has stabilised (i.e. after complete dissipation of excess pore pressure), deformation occurs without variation of effective stress (creep).

The need to involve time in describing compressibility of soils has been first put forward by Taylor & Merchant :

$$e = f(\sigma'_v, t) \tag{2.2}$$

As the compression curve derives from oedometer tests, the fundamental question has been raised whether or not strain referred to end of primary consolidation time from a thin laboratory soil specimen should be directly used in settlement analysis in the field. The question was first posed explicitly by Leonards (1972) and then highlighted by Ladd (1977) who stated the problem in terms of extreme sample thickness, as shown in Figure 2.9.

The issue was again reformulated by Jamiolkowski (1985), concerning the reference time for the creep occurrence. Hypothesis A (Ladd 1977, Leonards 1977, Mesri & Choi 1985) claim that creep strain rate depends on the stress rate, and consequently that the stress-strain curve followed in situ is the same as that obtained in the laboratory on small specimen at the end of primary consolidation. even though the time of primary consolidation is different for different thickness specimens.

Hypothesis B (Suklje 1957, Wahls 1962, Bjerrum 1967, Barden 1969, Leroueil 1985, Kabbaj 1986 etc.) assumes that some sort of structural viscosity is responsible for creep, that this phenomenon occurs during pore pressure dissipation also and therefore that the strain at the end of primary consolidation increases with sample thickness.
As a consequence even the preconsolidation pressure mobilized in the field will be different from that determined from laboratory oedometer tests.

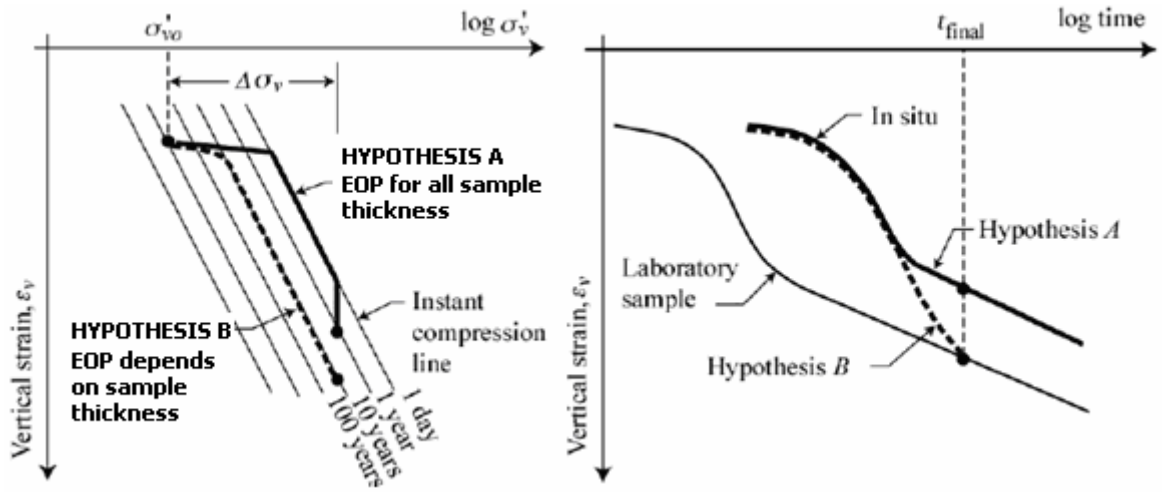

Figure 2.9:predicted strain -stress and strain -time curve for Hypothesis A and B

As for the issue of reference time for the viscous behaviour, the Osaka bay clay clearly shows that soil exhibits creep behaviour also before the end of consolidation (see Figure 2.10 and Figure 2.11).

Kansai International Airport was in fact projected and built 5 km offshore in Osaka Bay. Construction of the island began in 1987 and was completed in 1991; the inauguration of the Airport was in September 1994. Sea depth at this location is about 18m. The subsoil consists of an about 18 m of soft alluvial clay over several hundreds of metres of Pleistocene clay. These latter deposits show alternating clay and relatively thin sand or gravel layers. The overconsolidation ratio of Pleistocene clay increases with depth to reach a value of about 1.4 at a depth of 160 m.

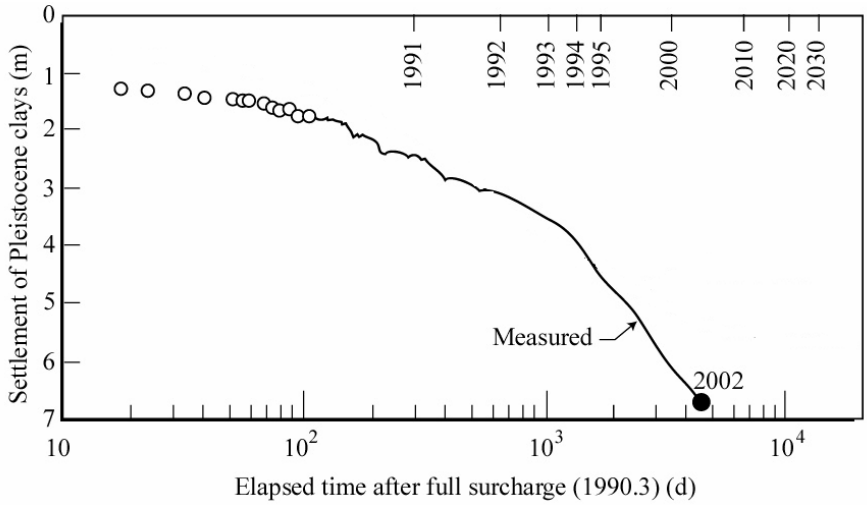

Figure 2.10: settlement of Pleistocene clays at Kansai International Airport Island (Leroueil, 2006)

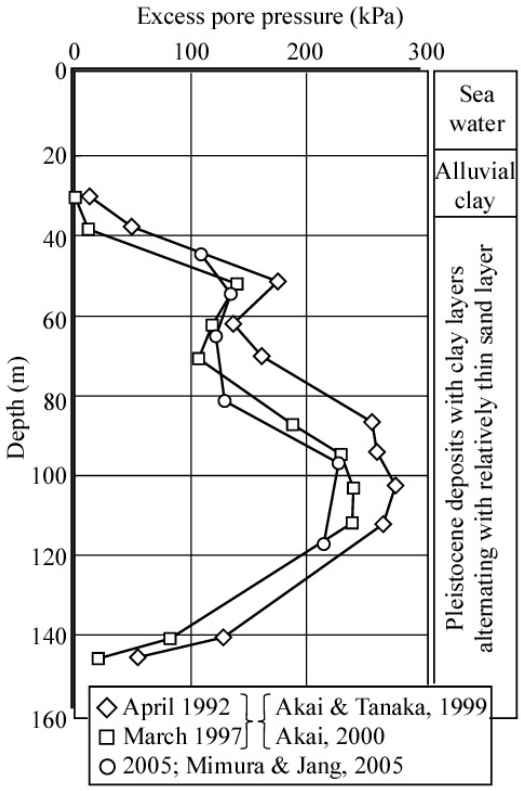

Figure 2.11: excess pore pressure at Kansai International Airport Island (Leroueil, 2006)

The alluvial clay layer was treated with sand drains and rapidly settled in about 6 months. The settlements observed since are due to compression of Pleistocene deposits over a thickness of about 150 m. The excess pore pressures measured in 1992, shortly after the end of construction, and then in 1997 and 2005, decrease only slowly and, in 2005, excess pore pressures larger than 200 kPa still exist at depths between 100 and 120 m.
The Pleistocene clay deposit is thus far from the end-of-primary consolidation but, as one can see from the next figure, a pure creeping behaviour is clearly evident being the total stress and pore pressure constant while settlement continues to increase. This demonstrates that creep deformations occur even before the end of primary consolidation.

Mesri (2003) pointed out that the problem is not when creep begins but what the consolidation and creep combined effects are at the end of primary consolidation. During consolidation soil compression in response to the effective vertical stress increase is characterized by the compressibility parameter $(\partial e/\partial \sigma'_z)_t$ i.e. in the compression stress-strain plane and the continued compression with time is characterized by the compressibility parameter $(\partial e/\partial t)_{\sigma'_z}$.
As soon as primary consolidation begins, both the parameters contribute to compression while only the latter contributes to compression during secondary consolidation. Therefore, the rate of compression in terms of rate of change of void ratio consists of two parts:

$$\frac{de}{dt} = \left(\frac{\partial e}{\partial \sigma'_z}\right)\frac{d\sigma'_z}{dt} + \left(\frac{\partial e}{\partial t}\right)_{\sigma'_z} \tag{2.3}$$

the former is produced by the rate of increase in effective vertical stress $(d\sigma'_v/dt)$ and the latter is controlled by time. In an oedometer test, Equation (2.3) can be integrated to obtain total compression in a period of elapsed time t:

$$\int_0^t de = \int_0^{tEOP}\left[\left(\frac{\partial e}{\partial \sigma'_z}\right)\frac{d\sigma'_z}{dt} + \left(\frac{\partial e}{\partial t}\right)_{\sigma'_z}\right]\cdot dt + \int_{tEOP}^{t}\left(\frac{\partial e}{\partial t}\right)_{\sigma'_z}\cdot dt = \Delta e_{EOP} + \Delta e_{creep} \tag{2.4}$$

The first term represent the period during which effective vertical stress increases and during which both $(\partial e/\partial \sigma'_z)_t$ and $(\partial e/\partial t)_{\sigma'_z}$ are responsible for ; beyond end of primary consolidation effective vertical stress remains constant and, as long as $(\partial e/\partial \sigma'_v)_t$ does not become zero, secondary compression will continue indefinitely.

According to Mesri (2003) $(\partial e/\partial \sigma'_z)_t$ and $(\partial e/\partial t)_{\sigma'_z}$ are not constant soil properties as they do not remain constant during primary and secondary compression stages. The latter parameter in fact represents creep rate and in Mesri interpretation creep does not act as a separate phenomenon. Consequently, incremental compressibilities with respect to effective stress and with respect to time are interrelated. This is the reason why EOP compression curve, following the Hypothesis A, are independent of the sample thickness, or, in other words, of the duration of primary consolidation.

The question is still open even because there is experimental evidence for both the approaches in terms of measured EOP strain, both in field and in laboratory tests. For further details the interested reader is referred to Mesri (2003) and Leroueil (2006).

One-dimensional compression and creep coefficients: stress dependency

As for the approach put forward by Mesri (2003), in order to describe time dependent behaviour it is necessary to account for compression parameters not only with reference to time but also in the stress-strain plane, because the phenomenon described interrelates time, stress and strain. The two compression parameters $(\partial e/\partial \sigma'_z)_t$ and $(\partial e/\partial t)_{\sigma'_z}$ represent the compressibility of soil structure for a fixed time, or generally, for any time, in response to an increase in effective vertical stress and the compressibility of soil structure at any effective vertical stress in response to elapsed time.

The most common way of plotting compression data is in a semi-logarithmic scale, both in the void ratio-stress plane and in the void ratio-time one, thus defining compression parameters as the slope of the curve before and after the preconsolidation pressure for the recompression coefficient C_r and the virgin compression coefficient C_c respectively, and the slope of the final part of the S- shaped curve with respect to time, for the creep index C_α (see Figure 2.12 and Figure 2.13).

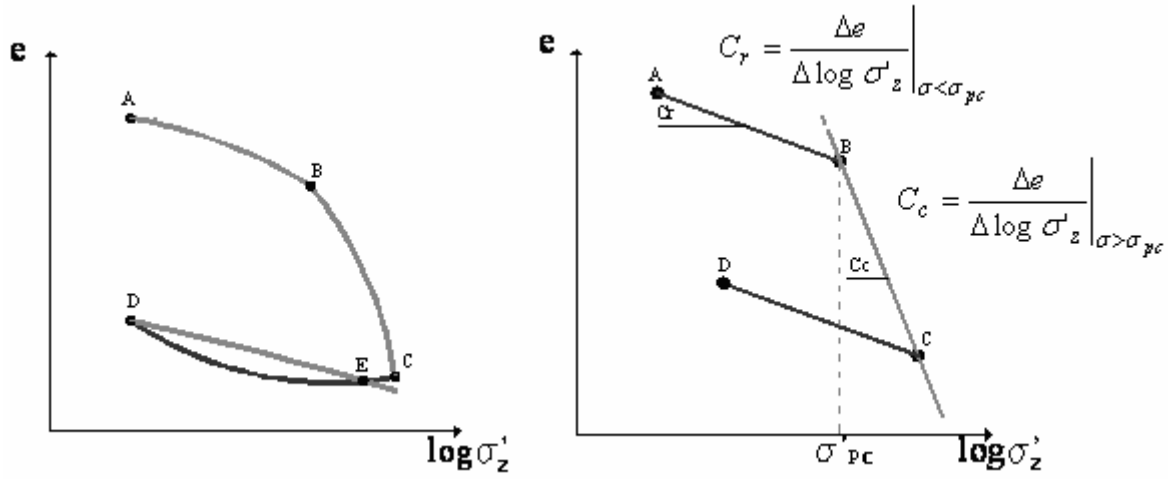

Figure 2.12: Compression coefficients in compression void ratio- stress plane

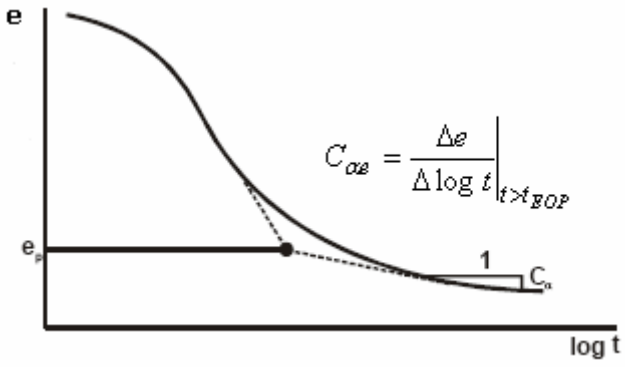

Figure 2.13: Creep index definition

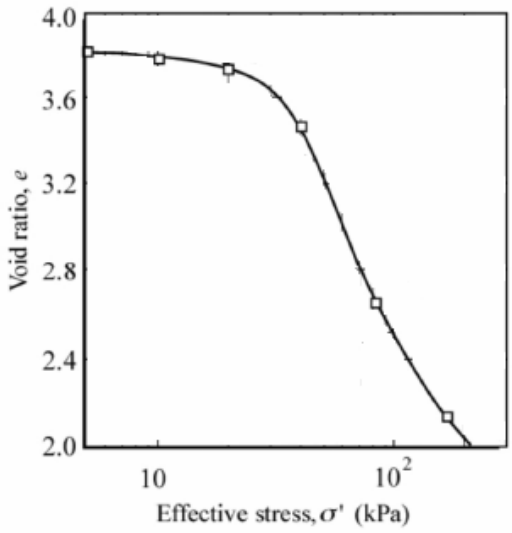

Figure 2.14: the concave shape of the compression curve

It is evident that an elasto-plastic framework can be used to describe the compression curve of a clay: before the preconsolidation pressure the soil strain is fully recoverable and the stiffness is higher than beyond it where the soil shows an elasto-plastic behaviour. The preconsolidation pressure represents in the one-dimensional compression a yielding point.

The most simplistic approach considers all the parameters as constant with $C_r < C_c$, and C_α independent of the stress level and considered time, but this does not reflect the real situation.

As regard to the stress-strain compressibility, it is intuitive to understand that in the compression plane there has to be a theoretical boundary for $e = 0$, so that a soil can not deform indefinitely. The real shape of the compression curve in the semi-logarithmic plot is slightly concave when the strain level becomes large, so that C_c diminishes and eventually reaches an horizontal asymptote for very large strains (see Figure 2.14). That region is usually of little interest for day-to-day engineering purposes.

One the other hand, experimental data show that C_α varies whether the soil is normally consolidated or overconsolidated, not always showing the classical S-shaped form, with a trend summarized in Figure 2.15, where on the x axis the ratio between the actual stress and the soil preconsolidation pressure is reported. Besides, a significant increase in C_α with time can be observed. In Figure 2.16 settlements curves of buildings in Drammen (Bjerrum, 1967) are shown. Both the OCR dependency and the C_α increase with time are evident.

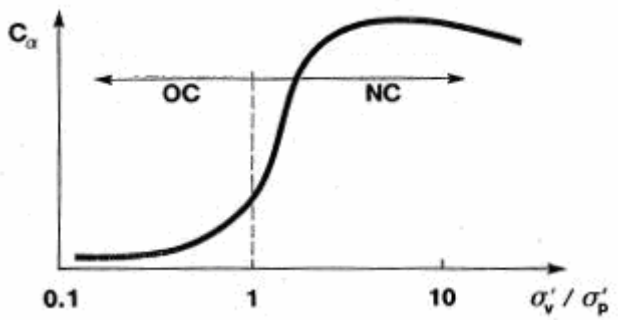

Figure 2.15: C_α variation with OCR

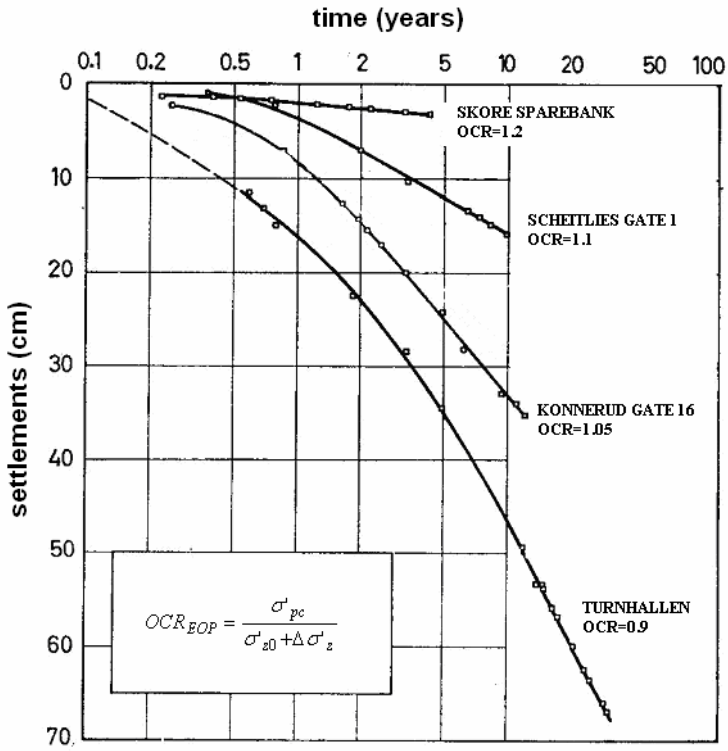

Figure 2.16: settlements curves of buildings in Drammen (Bjerrum, 1967)

The effects of the effective vertical stress on C_α have been subjected to numerous investigations presented in literature.

Walker and Raymond (1968) found that the secondary compression rates in the laboratory tests on sensitive Leda Clay appeared to be linearly related to the compression index C_c over the entire applied stress range with an average ratio of about 0.025.

Mesri (1973) considered the relationship between C_α and C_c and concluded that soils that are highly compressible in the primary phase would show high compressibility in the secondary phase as well.

Mesri and Godlewski (1977) proposed that a unique relationship exists between C_α and C_c throughout the secondary compression stage, and for all compression pressures from the recompression to the compression range (i.e C_c stands both for C_c itself and C_r).
Each corresponding pair of C_α and C_c at any instant (e, σ'_z, t) during secondary compression, represents, respectively slope of the e versus $\log t$ and e versus $\log \sigma'_z$ curve passing through that point. This law of compressibility is illustrated in Figure 2.17.

They directly related the magnitude and behaviour of C_α with time t to magnitude and behaviour of C_c with preconsolidation pressure σ'_{pc}. In general C_α remains constant, decreases or increases with time, in the compression range at which C_c remains constant, decreases or increases with σ'_{pc} respectively.

Examples of secondary settlement versus $\log t$ are shown in Figure 2.18.

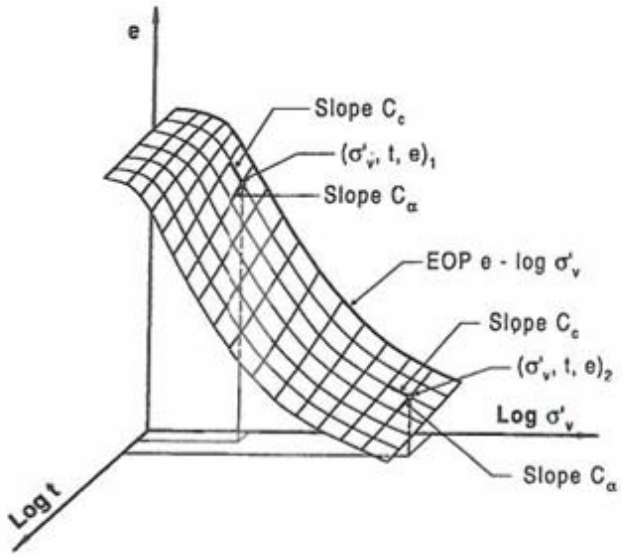

Figure 2.17:compression surface in void ratio-log stress-log time space (Mesri, 2003)

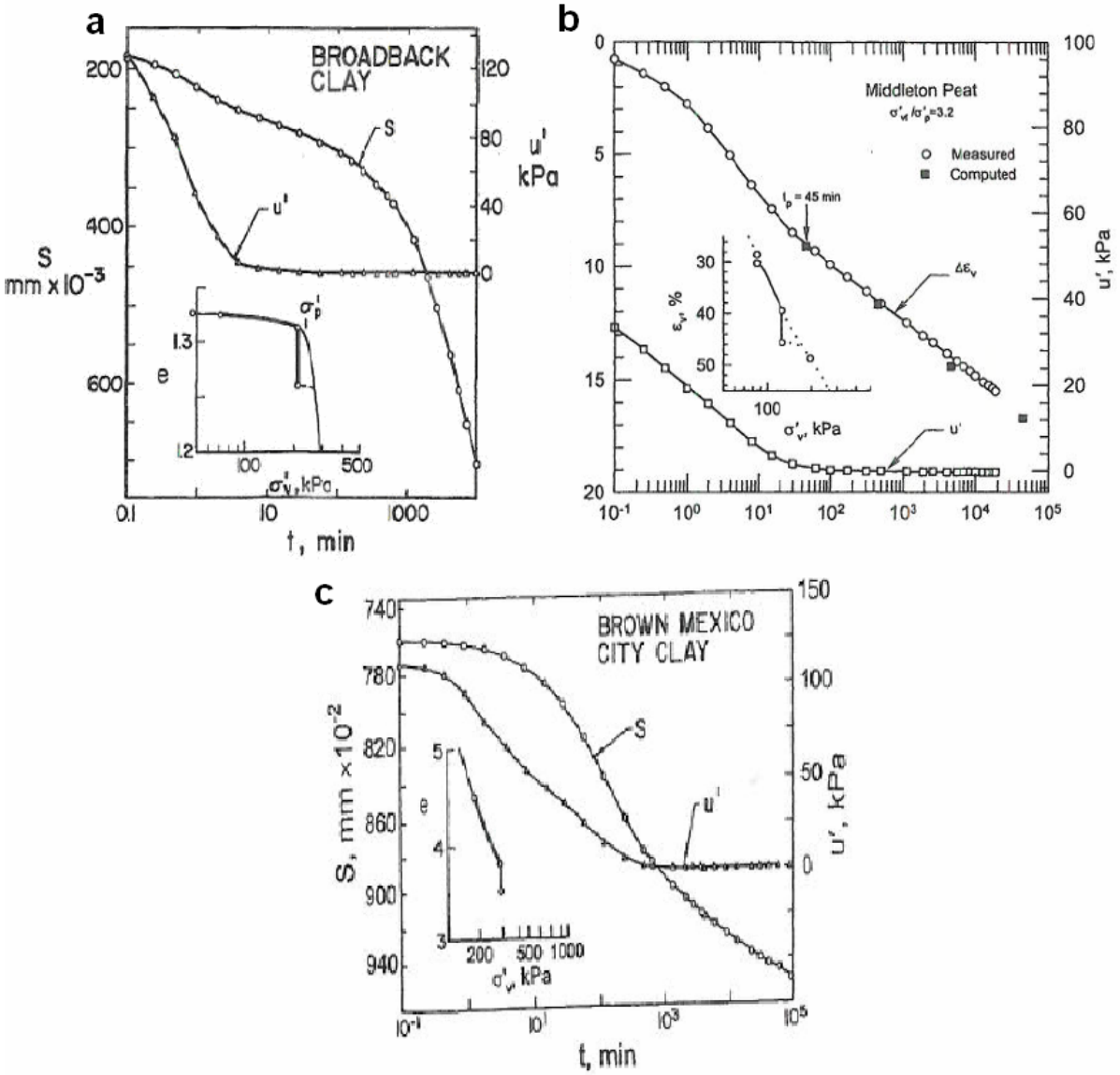

Figure 2.18:examples of C_α from Mesri, 2003

The pressure increment in Figure 2.18a) loads the Broadback clay sample to a pressure near the preconsolidation pressure σ'_{pc} where C_c is dramatically increasing with σ'_{pc}. The pressure increment in Figure 2.18b) is in the compression range beyond σ'_{pc} where C_c is reliably taken constant, so secondary compression shows C_α practically constant with time. Again, the pressure increment on the Mexico city clay in Figure 2.18c) is in the compression range where C_c is gradually decreasing with σ'_z, therefore C_α gradually decreases with time.

Semilogarithmic creep law

Although it has been realized that secondary compression takes effect from the beginning of loading, there has been a tendency to deal with it separately from primary compression. It is suggested by the classical way of plotting secondary compression observed in oedometer tests is against the logarithm of time (Figure 2.19), thus defining the coefficient of secondary compression:

$$C_{\alpha\varepsilon} = \frac{\Delta\varepsilon_z}{\Delta \log t} = \frac{-\Delta e}{(1+e_0)\Delta \log t} = \frac{C_{ae}}{1+e_0} \tag{2.5}$$

that is the slope of the semi-logarithmic plot after the end of primary consolidation ($t > t_{EOP}$). Strain at a certain time is decomposed to a term representing strain at the end of primary consolidation and a pure creep term. If this is evaluated in terms of vertical creep strains, the increase in secondary compression for a given soil can be written as:

$$\varepsilon_z = C_{\alpha\varepsilon} \log(1 + \frac{t}{t_{EOP}}) = C_{\alpha\varepsilon} \log\left(\frac{t_{tot}}{t_{EOP}}\right) = C_{\alpha\varepsilon}(\log t_{tot} - \log t_{EOP}) \tag{2.6}$$

where t is the creep time, t_{EOP} is the end of primary consolidation time, and t_{tot} is the time since the start of the test.

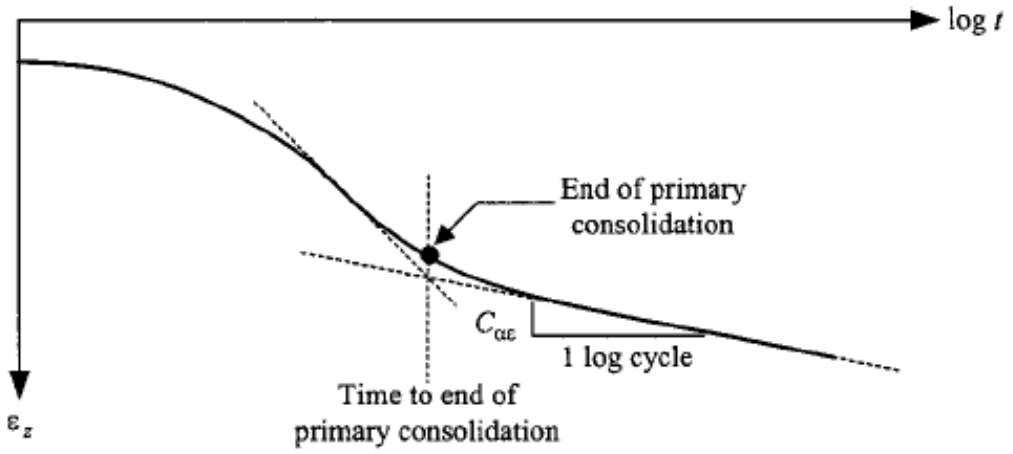

Figure 2.19: semi-logarithmic time- strain plot

The simplest approach in the framework of the logarithmic law is the assumption that C_α is taken constant for a given soil. Usually, in order to avoid misunderstanding, a subscript *e* or ε is added if it is evaluated in the void ratio or vertical strain versus Log_{10} vertical stress plane, To improve the modelling of secondary compression one should account for the stress and the time dependency of the coefficient.
The first modification can be done using the $C_\alpha / C_c = const$ approach along which both C_α and C_c increase as the effective stress approaches the preconsolidation pressure, then reach a maximum at or just beyond the preconsolidation, and then remain reasonably constant, keeping their ratio approximately constant. Combining the semi-logarithmic law with the concept of constant C_α / C_c the semi-logarithmic law becomes:

$$\varepsilon_z = \frac{1}{m'} C_{c\varepsilon} \log(1 + \frac{t}{t_{EOP}}) \tag{2.7}$$

where $m' = \frac{C_{c\varepsilon}}{C_{\alpha\varepsilon}}$ is the aforementioned ratio that is a rate parameter defining the unique relationship between primary and secondary compression.

One-dimensional creep coefficients: time dependency

The observation that creep behaviour is well-captured by a linear relation in stress-log(time) diagram may be valid for several log cycles of time, but it does not hold true in general. Leroueil et al (1985) reported a general nonlinear strain–time behaviour based on long-term creep tests (Figure 2.20). The strain-time curves for overconsolidated specimens, type I, showed a continuously increasing slope with the logarithm of time after end of primary consolidation. On the other hand, specimens in the normally consolidated range, type III, showed a continuously decreasing slope with the logarithm of time. The above states that the semi-logarithmic relation does not hold true, in general.

In an oedometer creep tests performed on samples in the vicinity of the preconsolidation stress, type II at first the specimen reacts as an overconsolidated soil, but after a certain time the strain rate remains momentarily constant. Finally, the sample reacts as a normally consolidated soil.

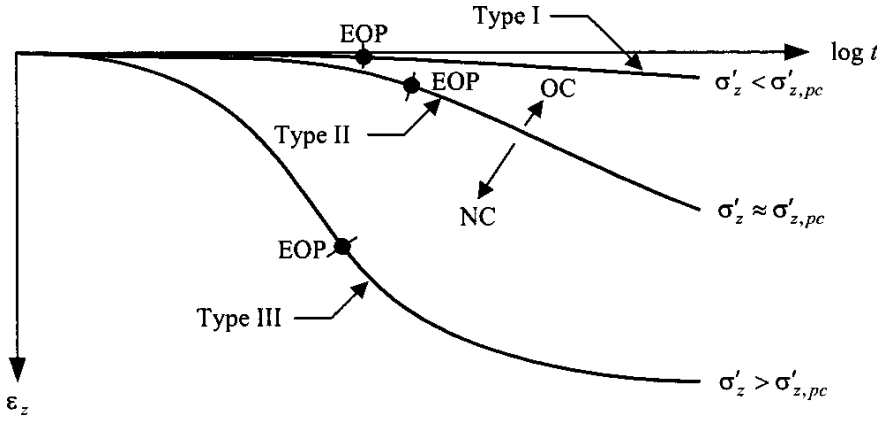

Figure 2.20: types of strain-log(time) curves (Leroueil, 1985)

To visualize this kind of behaviour, the creep test data are plotted in a $\log(d\varepsilon_z/dt) - \log t$ diagram, as shown in Figure 2.21.

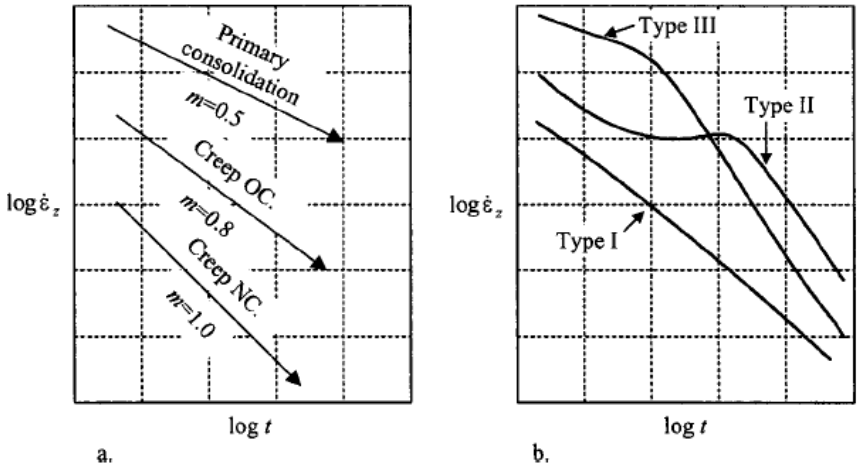

Figure 2.21:characteristic m values in $\log(d\varepsilon_z/dt) - \log t$ diagram

The main feature of this figure is that the slope of the straight line in the $\log(d\varepsilon_z/dt) - \log t$ diagram is characterized by the *m* parameter by Singh and Mitchell (1968):

$$m = -\frac{\Delta \log(d\varepsilon_z/dt)}{\Delta \log t} \tag{2.8}$$

In the $\log(d\varepsilon_z/dt) - \log t$ diagram a straight line with a downward slope m=0.5 corresponds to Terzaghi's solution for primary consolidation. This slope is observed in the beginning of the type III curve that corresponds to a normally consolidated soil. In a further stage, the type III soil shows a slope that corresponds to an *m* value greater than 1.0. The type I soil that is overconsolidated throughout the test shows an *m* value below 1.0 during the test period. The type II soil starts out with an *m* value corresponding to the overconsolidated soil (type I), but then the strain rate stops decreasing for a while. Thereafter, the type II soil shows the behaviour of a normally consolidated soil.

In this approach it appears evident that C_α is dependent both on stresses (vicinity or not to preconsolidation pressure) and time of creep.

Bjerrum approach: evolution of preconsolidation pressure

Even though the semi-logarithmic law uses end primary consolidation time to evaluate creep strain, suggesting the idea that creep follows the consolidation process, this does not imply a theoretical belonging to the Hypothesis A framework. It rather represents a "practical" way of calculating strain and it is in fact used in a lot of Hypothesis B models, like, for example, the Bjerrum's theory of time-dependent compression.

In this model, in particular, just a new definition of compression types are given. The volume change which has occurred in a clay sediment is divided into two components:

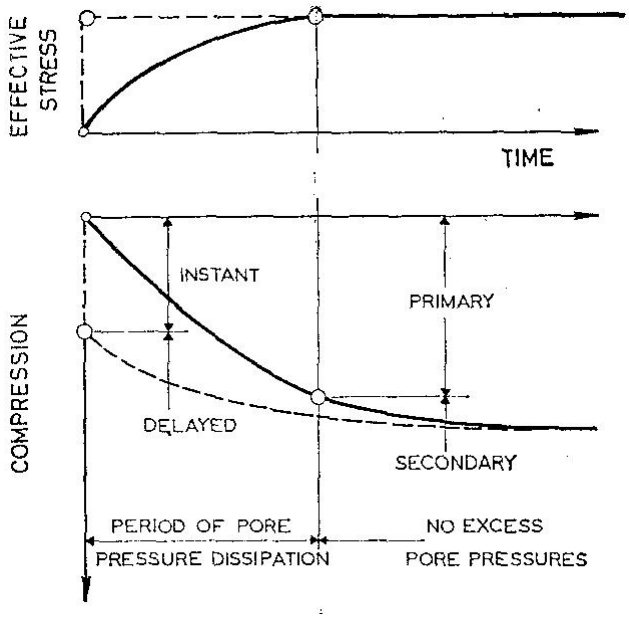

Figure 2.22: definition of instant and delayed compression (Bjerrum, 1967)

- an *instant compression* which would occur instantaneously with the increase in total stress, if the hydrodynamic process would not interfere with the compression process. It is, more precisely, the reduction in void ratio due to the effective stress increase until an equilibrium value at which the structure effectively supports the overburden pressure.

- a *delayed compression* representing the reduction in volume at unchanged effective stress.

The two new terms substitute the well-known expression 'primary' and 'secondary' compression because they do not separate the compression with reference to the end of excess pore pressure dissipation.

Figure 2.22: definition of instant and delayed compression (Bjerrum, 1967) shows how the compression of a clay layer develops with time if loaded with a suddenly applied uniformly-distributed pressure. The dashed curve shows the reaction of the soil structure that would occur if the pore water in the void of the clay were incapable of retarding the compression and the applied pressure were transferred instantaneously to the clay structure as an effective pressure. Due to the viscosity of the water, effective stresses will increase gradually as the pore pressure dissipates and compression will occur along the fully-drawn curve.

As a result of the secondary compression, there is not a single stress-strain curve for one - dimensional compression of clay, but a family of curves called *time lines*, each curve corresponding to a different duration of the applied load in a standard oedometer test. Each of these lines represents the equilibrium void ratio for different values of effective overburden pressure at a specific time of sustained loading. Compression tests have shown that the system of lines is approximately made of parallel straight lines showing that the rate of delayed compression is about the same throughout a homogeneous deposit, or, as the lines are actually slightly curved, it decreases slightly with increasing overburden pressure.

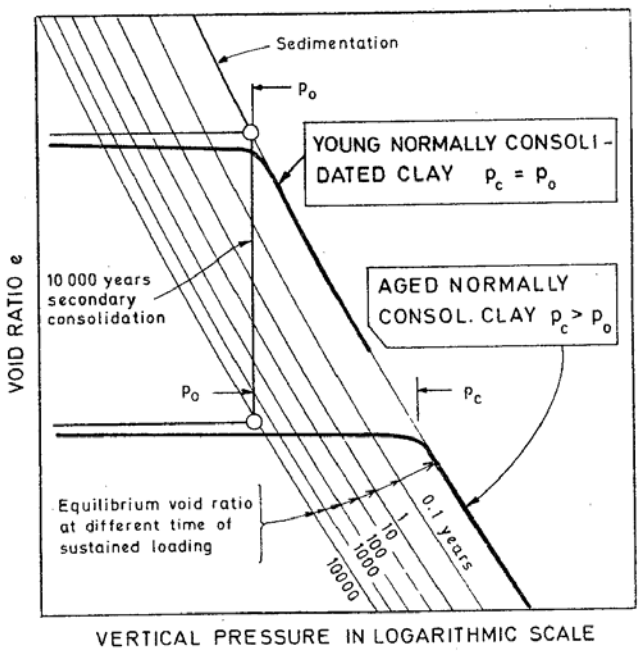

Figure 2.23: preconsolidation pressure evolution due to creep (Bjerrum, 1967)

Volume reduction during delayed compression will clearly lead to a more stable configuration of the structure in fact the number of contact points between clay particles will increase. This means that during delayed compression a cohesive clay will develop increased strength and a reserve resistance against further compression. Such a clay can support an additional load in excess of the overburden pressure without any significant volume change produced by slippage in the contact points. Therefore it is possible to distinguish in "young" and "aged" normally consolidated clays.
Young NC clays are recently deposited and at the equilibrium under their own weight but have not experienced delayed compression, whereas aged NC clays have undergone significant delayed compression at constant effective stress.

As shown in Figure 2.23 the young clay will follow the upper curve and the preconsolidation pressure is equal to the present effective stress p_0. If the young clays is left intact for several years (or thousand years) it will continue to compress with time under constant effective stress and, once it is loaded, it will follow the lower curve and the observed preconsolidation pressure has increased to p_c. Creep, therefore, causes an increase of preconsolidation pressure even without varying the effective stress. The increase of preconsolidation pressure without any variation of effective stresses accounts for the overconsolidation ratio slightly above unity which is found in natural clays that have never experienced geological unloading (erosion of overlying layers, thawing of ice in glaciers, groundwater level changes, weathering etc.).

In Figure 2.24 a), just for seek of completeness, it is shown the double effect on OCR due to unloading and creep.

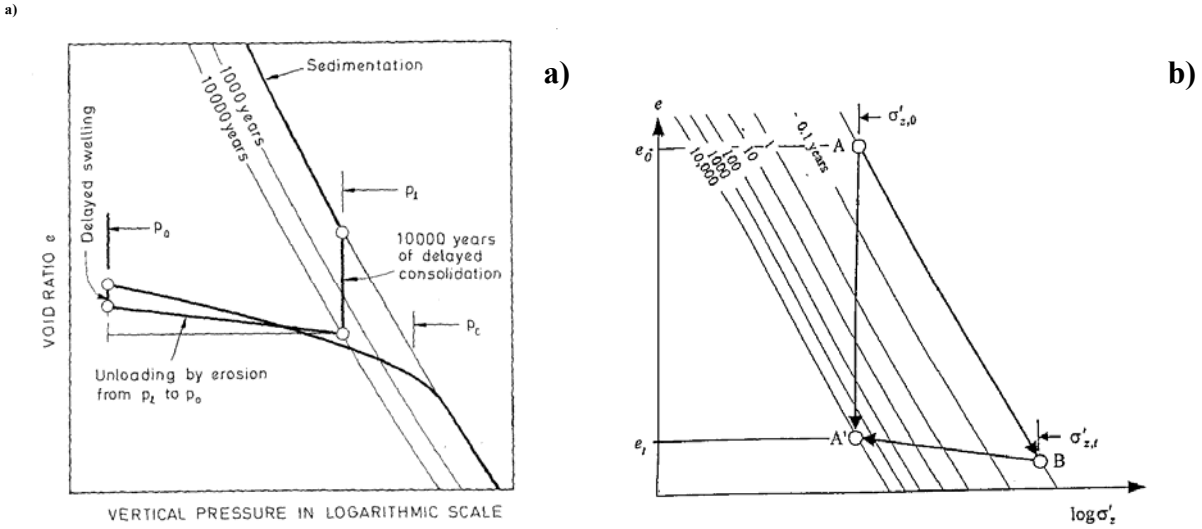

Figure 2.24: two possible stress path to reach the same stress-strain state (Bjerrum, 1967)

Transforming Bjerrum's concepts in terms of the well-known compression coefficients (Garlanger, 1972), using the assumption that the change in void ratio in a soil element is composed by an elastic part, an elasto-plastic irreversible time-independent part and a creep plastic term, it gives:

$$e = e_0 - e^e - e^{ep} - e^c = \\ e_0 - C_{re}\log\frac{\sigma'_{z,pc}}{\sigma'_{z,0}} - C_{ce}\log\frac{\sigma'_z}{\sigma'_{z,pc}} - C_{\alpha e}\log\frac{t_{EOP}+t}{t_{EOP}} \tag{2.9}$$

And then, describing with this expression the final void ratio in A' of Figure 2.24 b), reached through ABA' path or AA' path and then equating them, the evolution of preconsolidation pressure equation is given:

$$C_{ce}\log\frac{\sigma'_{zt}}{\sigma'_{z0}} = C_{re}\log\frac{\sigma'_{zt}}{\sigma'_{z0}} + C_{\alpha e}\log\frac{t_{EOP}+t}{t_{EOP}} \\ \Rightarrow \left(\frac{\sigma'_{zt}}{\sigma'_{z0}}\right) = \left(\frac{t_0+t}{t_0}\right)^{\frac{C\alpha e}{Cce-Cre}} \tag{2.10}$$

As already highlighted the semi-logarithmic creep law is used in the framework of this model, but this does not imply that creep is considered to occur only after end of primary consolidation.

Isotache approach: constant rate of strain

To describe one-dimensional compressibility of soils, Leroueil (2006) schematically defined four families of rheological models:

$$R(\sigma'_z, e) = 0 \tag{2.11}$$
$$R(\sigma'_z, e, t) = 0 \tag{2.12}$$
$$R(\sigma'_z, e, d\sigma'_z/dt, de/dt) = 0 \tag{2.13}$$
$$R(\sigma'_z, e, de/dt) = 0 \tag{2.14}$$

The classical Terzaghi consolidation theory belongs to the first one, as time is not involved, while the Bjerrum approach is represented by the second equation, in which void ratio is a function of the effective stress and time. A major difficulty may be encountered with these models when applied load varies with time and an origin for time has to be defined. Models belonging to the third and fourth families overcome this difficulty since the behaviour of the material then depends only on its present conditions and is not a function of previous history.
The fourth class of rheological models was first proposed by Suklje (1957) and it is based on the existence of a unique relationship between the current state of stress σ'_z and strain (ε'_z or e) for a given constant strain rate ($d\varepsilon'_z/dt$ or de/dt). The curves made of stress-stress point characterized by the same strain rate are called *isotaches*.

The original model proposed by Suklje has been deeply investigated by Leroueil performing multiple stage loading tests, constant rate of strain tests and long-term creep tests, all of them in oedometric condition.

A constant rate of strain test (CRS) (Figure 2.25 a), is a tests in which a constant total strain rate is applied throughout the experiment (i.e. $d\varepsilon_z/dt = const$). The stress response is the measured in order to obtain a stress-strain relationship (Figure 2.25 b).

Typical CRS oedometer tests results are presented in Figure 2.26. It can be seen that a set of CRS curve is made of a set of almost parallel line, moving towards right increasing the strain rate: at a given strain, the higher the strain rate, the higher the effective stress or, under a given effective stress the smaller the strain rate, the larger the strain.

Besides, excess pore pressure abruptly increases after local yielding of clay structure takes place as if small compressibility of soil structure in the recompression range were responsible for very rapid dissipation of excess pore pressure. So excess pore pressure development can be use to detect the preconsolidation pressure value. The higher the strain rate, the higher the pore pressure increase at the base of the specimen and for strain rate lower then $5x10^{-7}$ s^{-1} the excess pore pressure is extremely small.

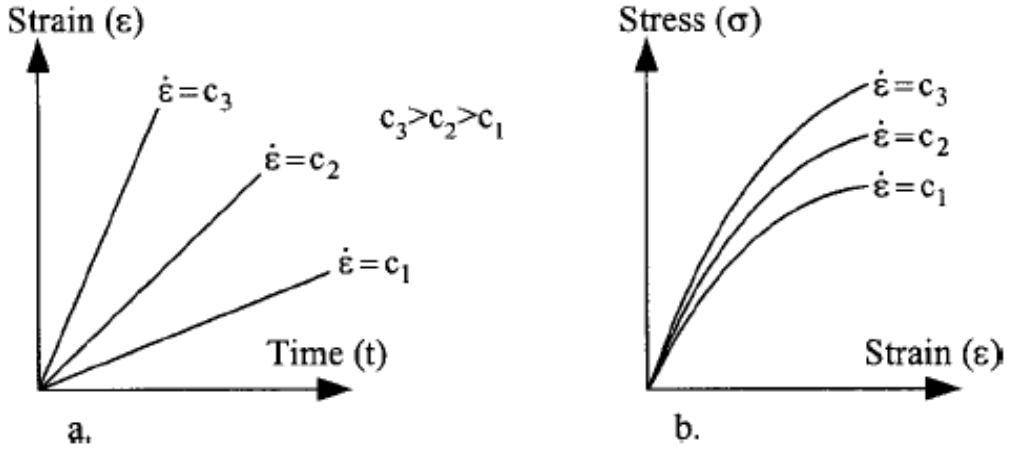

Figure 2.25: definition of constant rate of strain test

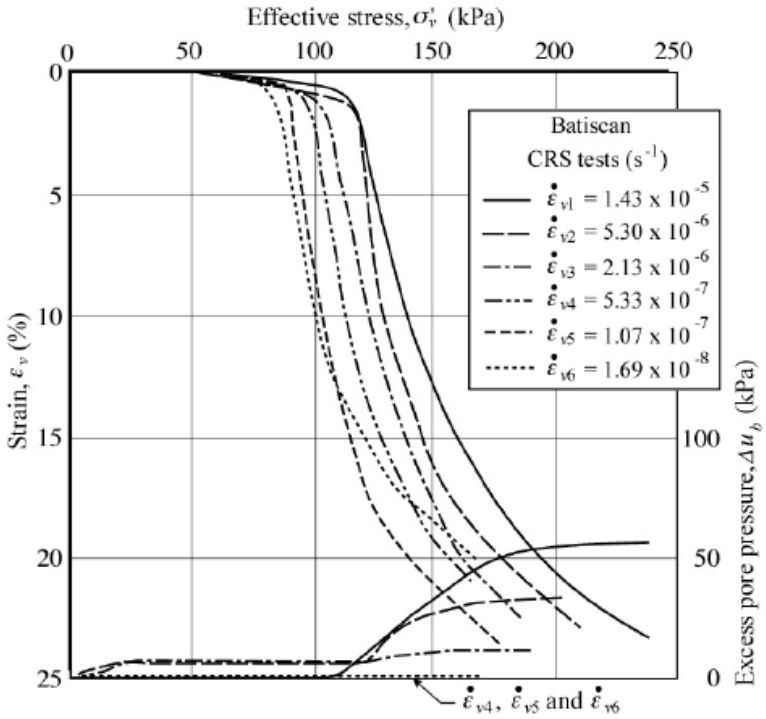

Figure 2.26: CRS oedometer tests on Batiscan clay (Leroueil at al., 2006)

It can be seen that this set of curves is very similar in shape and position to the well-known stress-strain behaviour shown by the soil in a classical oedometer multiple-stage loading tests. This is thus proving that $d\sigma'_z/dt$ has no significant influence on soil behaviour, which is well described by the fourth family: $R(\sigma'_z, e, de/dt) = 0$.

This framework is in agreement with the Bjerrum approach, which becomes a particular case of its more general view. Supposing that creep shows since the beginning of the test, it is possible to identify the *instant compression line* as a reference and then the different time lines shifted towards left each corresponding to a fixed creep time.
Being those lines parallel, moving from every stress-strain point on the instant compression line, soil experiences the same strain in the same time. Therefore, a time line (called also sedimentation line) corresponds to an isotache.

From Figure 2.26 it is evident that preconsolidation pressure varies with strain rate. An interpretation could be that the recompression curve is not affected by the strain rate, in fact on the recompression line isotaches superpose, so since slower isotaches are shifted on the left of the diagram they will cross the recompression line for smaller stress values. A first equation that describes the isotache curve has to account for that, thus setting a point in the stress strain plane:

$$\sigma'_{pc} = f(d\varepsilon_z/dt) \tag{2.15}$$

Plotting preconsolidation pressure values against strain rate in a bi-logarithmic scale it can be observed that the slope is a constant, as shown in Figure 2.27.

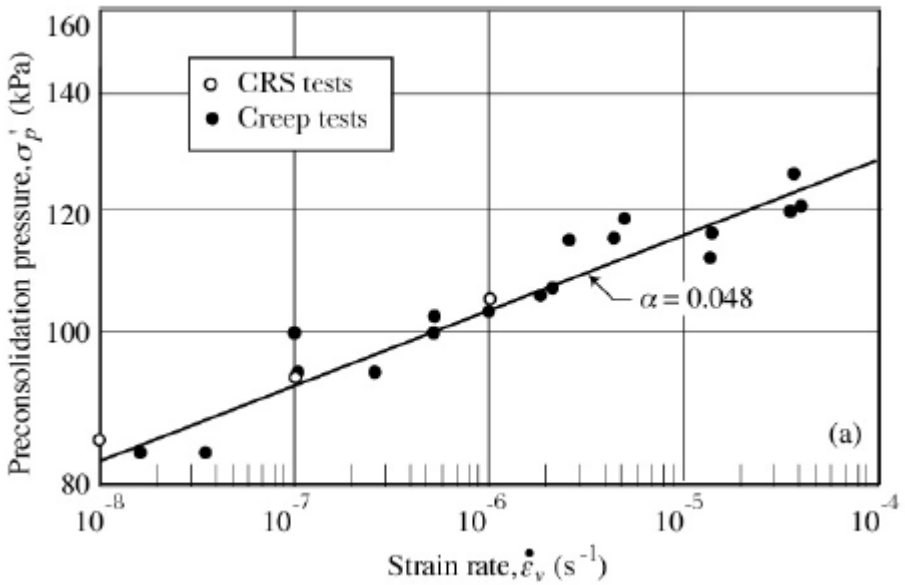

Figure 2.27: variation of preconsolidation pressure with strain rate in Batiscan clay (Leroueil, 2006)

The ratio $\alpha = \Delta \log \sigma'_{pc} \Big/ \Delta \log\left(\frac{d\varepsilon_z}{dt}\right)$ is in fact equal to:

$$\alpha = \frac{\Delta \log \sigma'_{pc}}{\Delta \log\left(\frac{d\varepsilon_z}{dt}\right)} = \frac{\Delta \varepsilon_z / C_c}{\Delta \log \varepsilon_z} = \frac{\Delta \varepsilon_z / C_c}{\Delta \varepsilon_z / C_\alpha} = \frac{C_\alpha}{C_c} \tag{2.16}$$

and, as Mesri demonstrated, C_α / C_c is a constant for a given soil.

The equation to describe the preconsolidation pressure evolution can thus be written as:

$$\log \sigma'_{pc} = A + \alpha \log(d\varepsilon_z / dt) \tag{2.17}$$

This equation gives also some information about the distance among the isotaches. Along the normalconsolidation line in fact $\sigma'_{pc} \equiv \sigma'_z$ so the isotache distance should be spaced by α distance, in a log –log diagram. To describe the compression curve once one stress-strain point is set (preconsolidation pressure), it is sufficient to give the slope of the curve. Compression index (slope of stress-strain curve in semi-logarithmic plane) is not a constant, so it will not be constant even in the natural stress-stress plane but it depends on strain. (For further details see Chapter 3).
Conversely, it does not depend on strain rate, since the set of isotaches is constituted by parallel lines.
Hence, the second equation that describes the isotache model is:

$$\sigma'_z / \sigma'_{pc} \, (d\varepsilon_z / dt) = g(\varepsilon_z) \tag{2.18}$$

This shows that if stress is normalized with preconsolidation pressure it becomes strain rate independent.

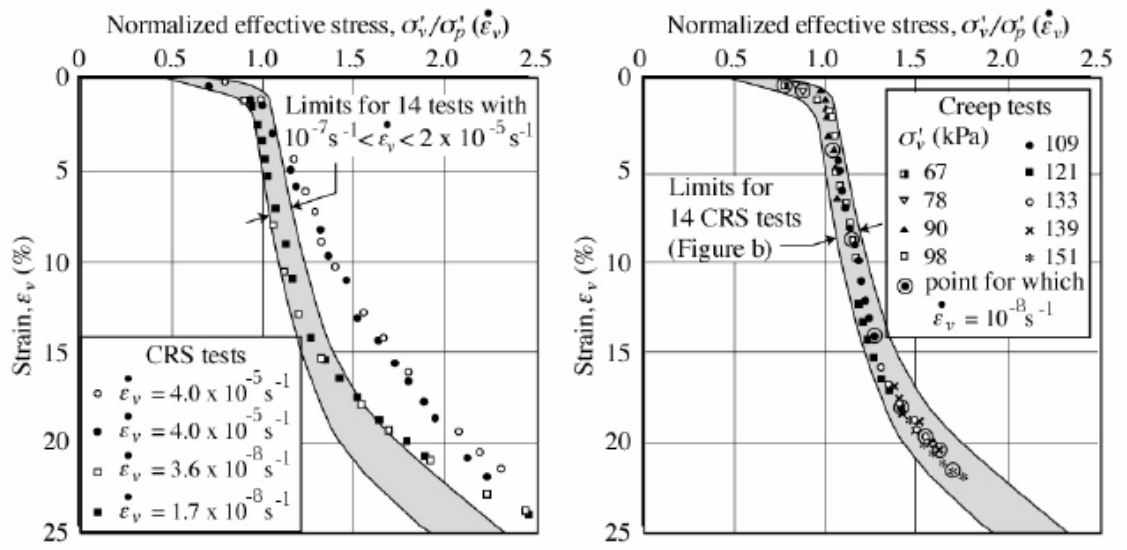

Figure 2.28: normalized effective stress-strain curves from CRS and creep tests (Leroueil, 2006)

In fact if the curves of Figure 2.26 are normalized with respect to the preconsolidation pressure, as in Figure 2.27, fourteen tests over eighteen (strain rates between $1.4x10^{-5}$ s^{-1} and $1.07x10^{-7}$ s^{-1}) fall in a narrow range, while the two more rapid tests ($4x10^{-5}$ s^{-1}) and the two slowest test (3.6 and $1.7x10^{-8}$ s^{-1}) are out of this range, both shifted towards right.

Even considering the creep tests performed by Leroueil on the same clay, all the normalized data fall within the range obtained from the CRS tests (corresponding to a strain rate of approximately 1 $x10^{-7}$ s^{-1}). This confirms that there is a unique effective stress-strain-strain rate relationship that can be described by Equations (2.15) and (2.18).

As for the four tests out of the range, the unexpected behaviour of the two rapid tests is probably due to the high excess pore pressure developed. The two slow tests, on the other hand, show at a stress higher than expected compared to those in the range because of the development of microstructure (i.e. the slope is not the same because the soil behaviour is much more rigid).

In general, due to their viscous behaviour, soils have a tendency to rearrange their particles and decrease their void ratio with time under constant effective stress. But they may also be subjected to structuring phenomena that have a tendency to fix particles in their position.

The rate of strain determines which one of the two opposing mechanisms dominates. At relatively high strain rates, the former mechanism will dominate whereas at relatively low strain rates, structuring effects may become important and modify the stress-strain- strain rate relationship.
The influence of structuration can be seen also in evaluation of α (Equation (2.16)) that is higher at higher strain rates and smaller strain rates, as shown in Figure 2.29.

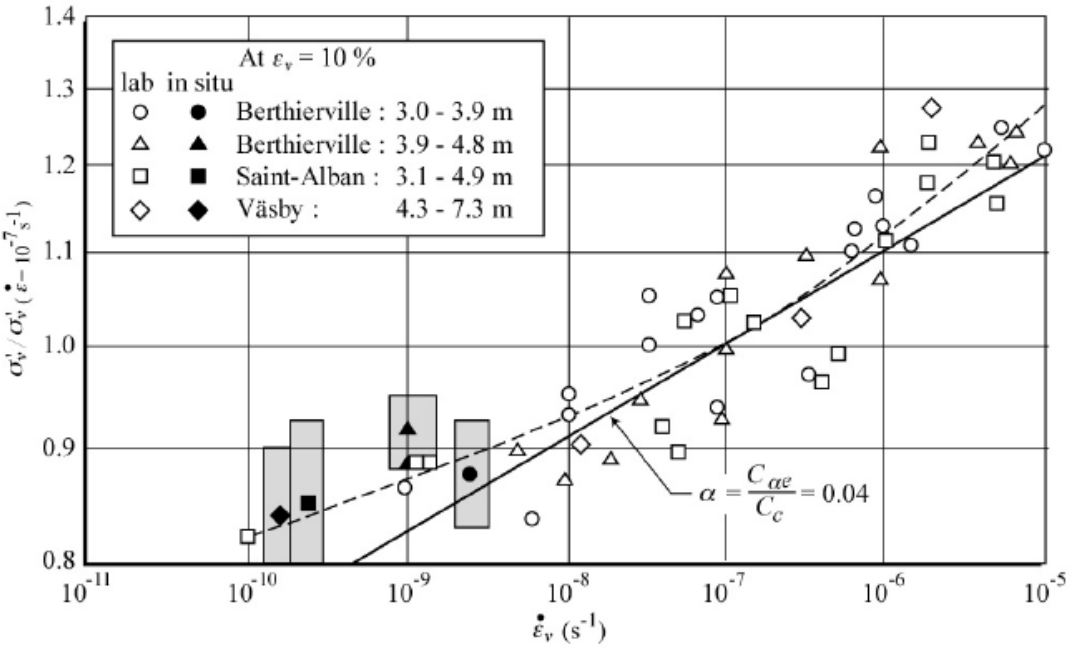

Figure 2.29: normalized stress-strain rate relations at a strain of 10% (Leroueil, 2006)

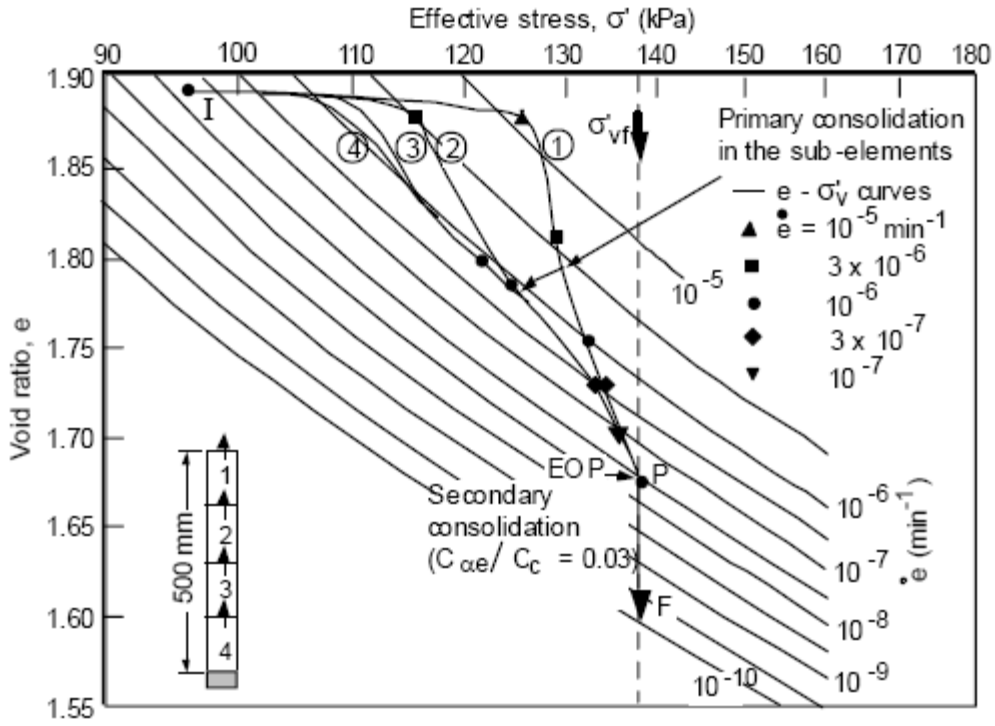

Figure 2.30: special four sub-elements oedometer test (Mesri, 1986; Leroueil 2006)

This observation is further supported by the observation that isotaches traced from a special oedometer test performed by Mesri (1986) and interpreted by Leroueil (1986,1996, 2006) are not equally spaced (Figure 2.30), and, in particular, the distance is higher for higher strain rates.

Apart from phenomena such as structuration, the slope of the compression curve (depending on strain level or not, the latter case if the curve is plotted in bi-logarithmic scale as described in the next Chapter) is a sort of "finger print" of the considered soil, being independent of

strain rate. This fact is evident in Figure 2.31 in which normalized compression curves of two different clays are plotted.

Consequently, whenever soils are very heterogeneous, the only way of detecting the validity of isotache approach is to change strain rate while performing the same CRS tests. The result will be that whenever the strain rate changes, soil conditions move from an isotache to another, as shown Figure 2.32. By comparing two or more different tests at different strain rates, different slopes will be obtained due to differences in the specimens.

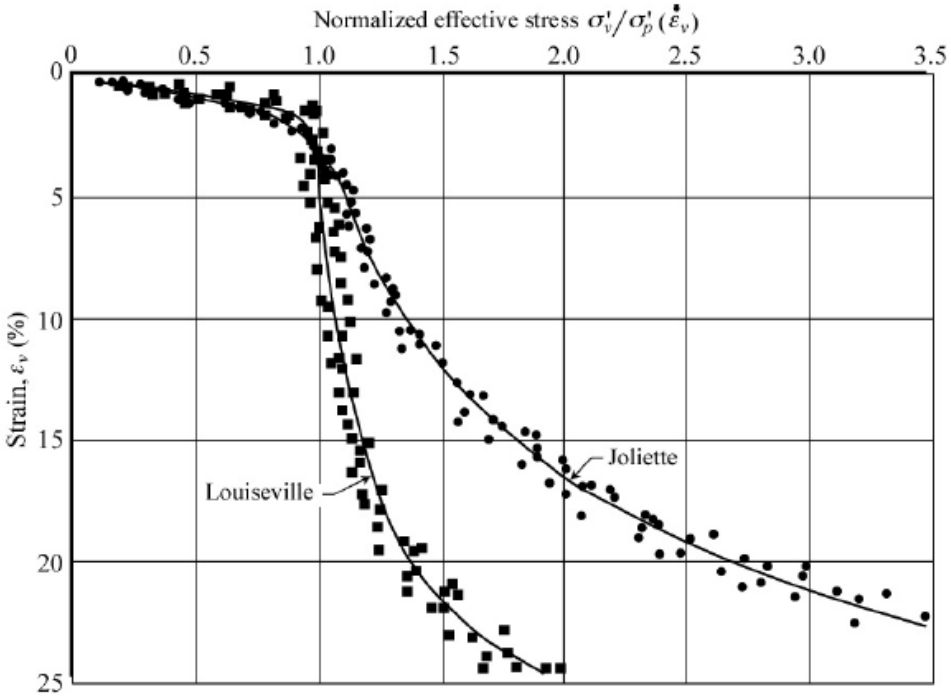

Figure 2.31: Joliette and Louiseville clays compression curves (Leroueil, 2006)

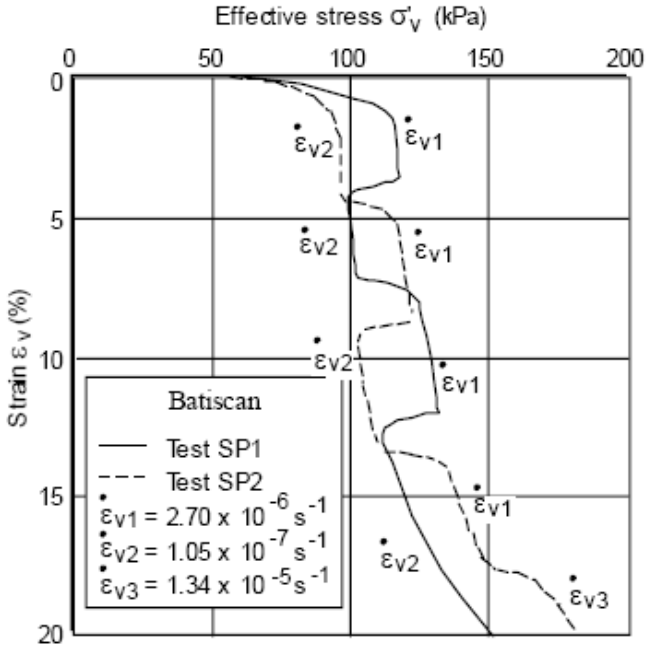

Figure 2.32: oedometer CRS tests on Batiscan clay with strain rate changes (Leroueil, 2006)

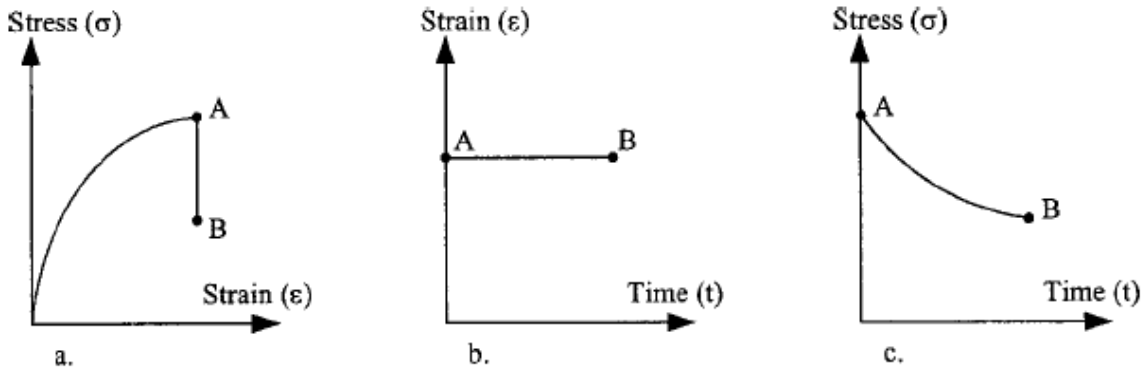

Figure 2.33. definition of relaxation test

The isotache approach is, in the end, a very powerful interpretation of time-dependent behaviour. It has been established on the basis of tests in which the strains were always increasing, and it has proven valid only under such conditions.

In relaxation tests, the strain is constant, the strain rate is thus equal to zero and, for such conditions, the uniqueness of an effective stress-strain-strain rate relationship would imply a constant effective stress. However it is well-known that the effective stress decreases during relaxation as reported in Figure 2.33.

One possible explanation is that the strain-rate model should apply only to the plastic component of strain, so that in relaxation tests where the total strain is kept constant, the increase in plastic strain associated with creep is compensated by a decrease in elastic strain and thus a decrease in effective stress, so the Equation (1.23) becomes:

$$d\varepsilon = d\varepsilon^e + d\varepsilon^p = 0 \tag{2.19}$$

so then:

$$\frac{d\varepsilon^e}{dt} = -\frac{d\varepsilon^p}{dt} \tag{2.20}$$

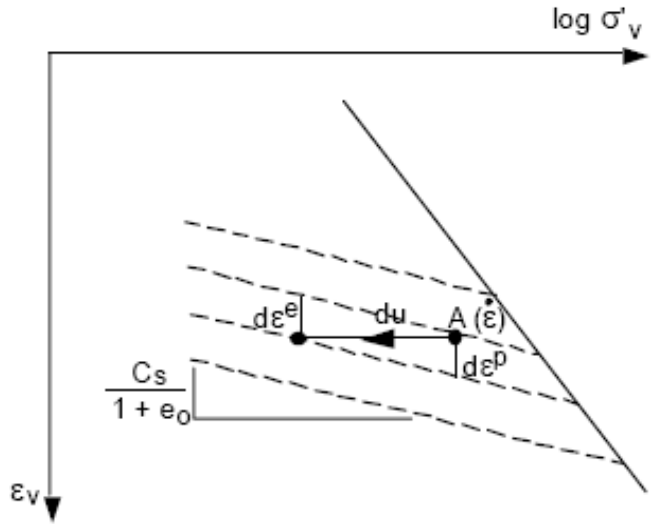

Figure 2.34. strain component in a relaxation test (Leroueil, 2006)

Creep in triaxial tests: sand behaviour

Two definitions of triaxial creep are found in literature. In drained creep, the effective stresses are kept constant and the creep process corresponds to a single stress point. In undrained conditions, mean effective stress p' decreases due to build-up of excess pore pressures during testing.and the deviatoric stress q, which is independent of pore pressure, remains constant. Strictly speaking, it can be concluded that undrained creep does not represent a pure creep process, whereas drained creep does.

As the principal results are given for cohesive soil, mentioning creep behaviour in triaxial tests allows to depict some aspects of creep in sands. There are only a few reported laboratory studies of one-dimensional creep tests performed on sand. In sands, in fact, oedometer test is not so representative since the initial stress-strain state (and also OCR value, whether a OCR definition can be considered meaningful for sands) may be easily modified by means of just a small vibration or any sort of compaction.

From isotropic triaxial tests it is possible to investigate the stress confining role in creep behaviour.
In the low stress regime, the strain–time relation seems to be linear when plotted as strain versus logarithm of time. Colliat-Dangus et al.(1988). And Mejia et al. (1988) reported that the strain–time behaviour for sand under K_0 conditions far from failure converged toward a logarithmic relation after some high initial strain rates in the first few seconds of the creep tests. In the high stress regime, the evolution of creep strains over time is approximately linear when plotted in $\varepsilon_z - \log t$ diagram as well (see Figure 2.35 and Figure 2.36).

On the other hand, in real triaxial condition (not just in a triaxial apparatus performing isotropic or K_0 tests) attention can be focused on the stress level dependency, i.e. proximity to failure. In order to visualize the observed creep behaviour in triaxial conditions, the creep test data are again plotted in $\log \dot{\varepsilon}_z - \log t$ diagrams. When the data are presented in such diagrams, the creep behaviour can be analyzed by the parameter *m*, which is the slope of a straight line in the $\log \dot{\varepsilon}_z - \log t$ diagram.
The reported values of *m* in triaxial creep tests show that the strain–time relation, in general, differs from the classical logarithmic relation.

Several writers report that *m* is not always independent of deviator stress level as assumed by Singh and Mitchell (1968) shown in Figure 2.21. In some cases, *m* decreases with increasing deviator stress; other cases show the opposite. It is a general observation that the strain rate increases with increasing deviator stress or stress level. The general opinion is that the creep behaviour in sand for various stress levels is similar to that of clay.

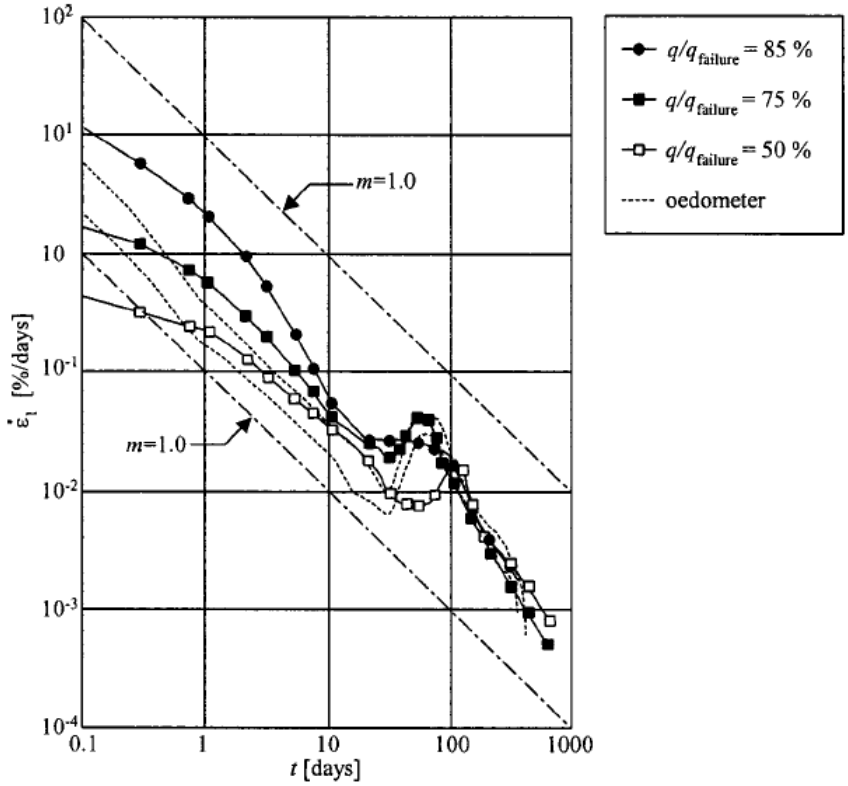

Figure 2.35: Axial strain rate as a function of time for various stress levels given as a percentage of deviator stress at failure on NC Pancone clay. (Bishop and Lovenbury,1969)

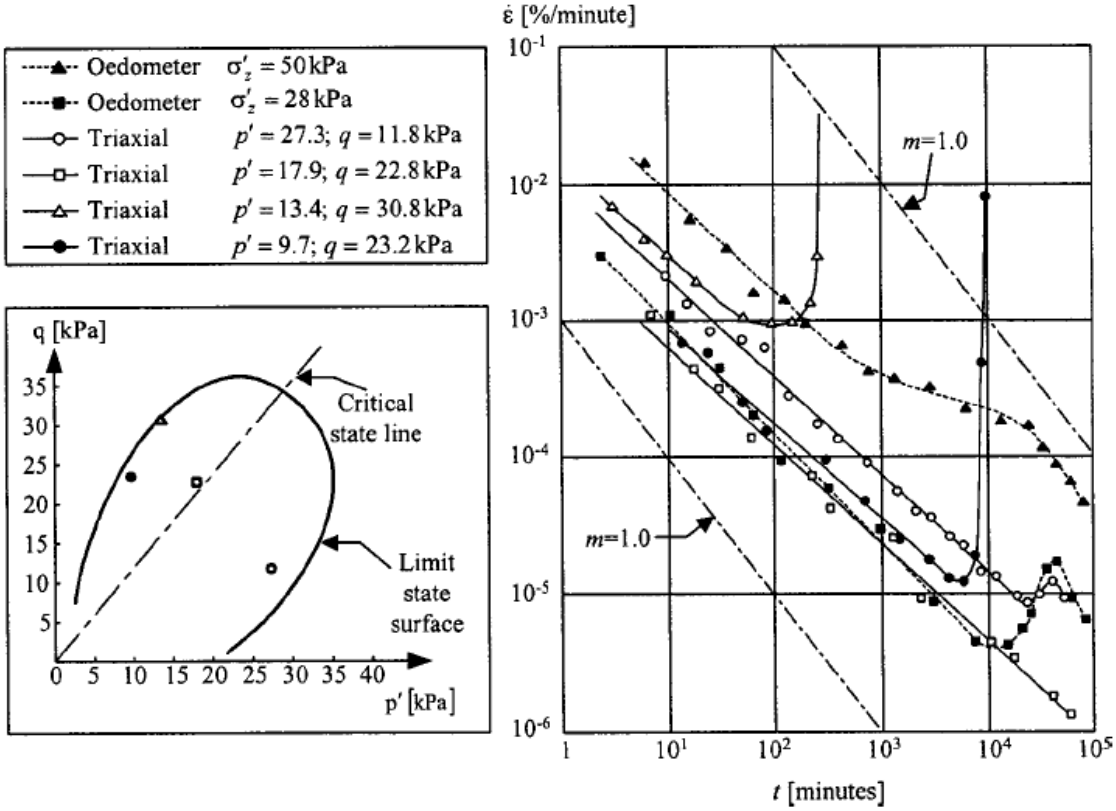

Figure 2.36: Axial strain rate as a function of time for various stress levels on St. Alban clay, plotted also in relation to the limit state surface and critical state line (Tavenas, 1978)

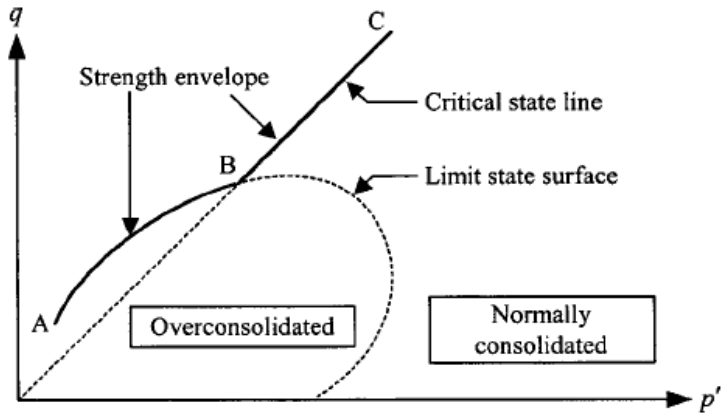

Figure 2.37: strength envelope scheme for a clay

Strain rate dependency (isotache approach) can also be examined in triaxial condition: the effect of strain rate on the peak strength (from A to B in Figure 2.37) and the strength in the normally consolidated range (from B to C in Figure 2.37) will be evaluated.

Tavenas and Leroueil (1977) indicated that the effects of time and strain rate on the preconsolidation pressure can be generalized to the entire limit state surface of the soil: in other words: stress-strain relations are similar in nature. For example, in undrained triaxial CRS tests, the greater the strain rates, the greater the peak strength. In general, the higher the strain rate, the more rigid the material behaviour.

In Figure 2.38 this behaviour is illustrated and it is also shown a stress–strain curve obtained by a hypothetical test performed at a strain rate approximating zero. The peak strength is denoted q_0 . The corresponding limit state surface in the next figure is denoted *static yield surface.* The existence of this surface has been debated in literature because several constitutive models based on Perzyna's overstress theory rely on the existence of it. The part of the strength envelope denoted 'critical state line' in Figure 2.38 seems to be independent of rate effects.

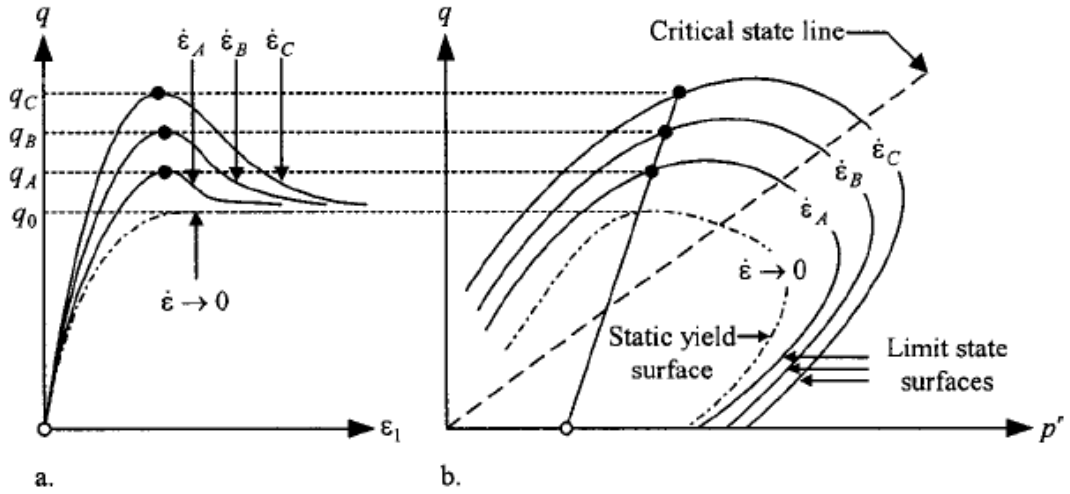

Figure 2.38:schematic strain rate effects on limit surface (Augustesen, 2004)

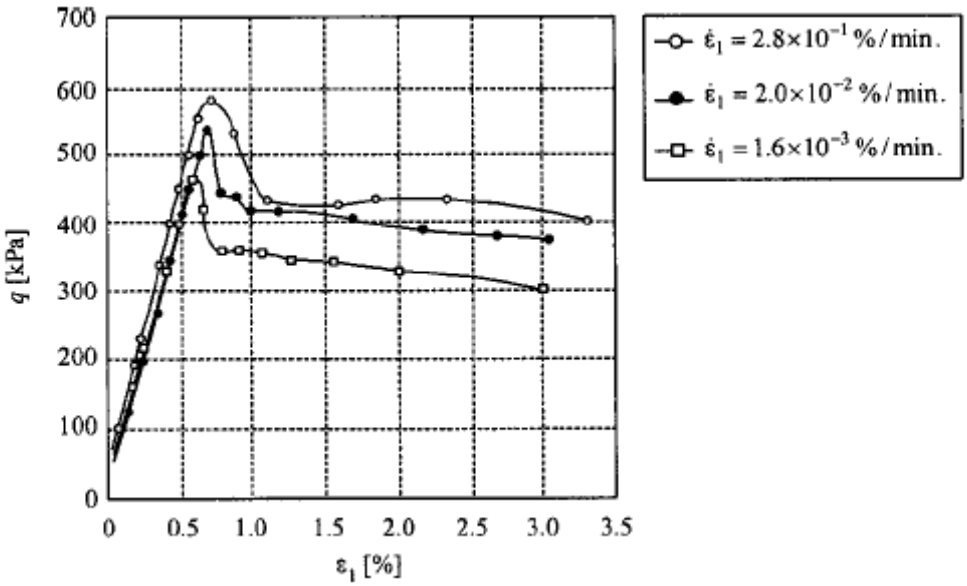

Figure 2.39:isotache behaviour of St. Jean Vianny clay in undrained CRS triaxial tests (Vaid et al.,1979)

Hypothetical theories are validated through experimental observation (Figure 2.39). Performing such tests in sands, both undrained and drained, do not show any significant rate of strain effect while the strain rate is kept constant for each test, whereas results are different if the strain rate is changed stepwise. In fact in the latter case (Matsushita et al., 1999), the stress-strain relationship temporarily overestimates the unique relationship for the constant rate of strain curve when the strain rate is increased stepwise. After having exhibited clear yielding, the stress-strain relationship gradually rejoins the unique relationship for the constant rate of strain curve (Figure 2.40 d).

This behaviour is labelled as *non-isotache*, and it is a case in which creep relaxation and rate dependency can not be considered due to the same mechanism (the 'correspondence principle' is not valid).

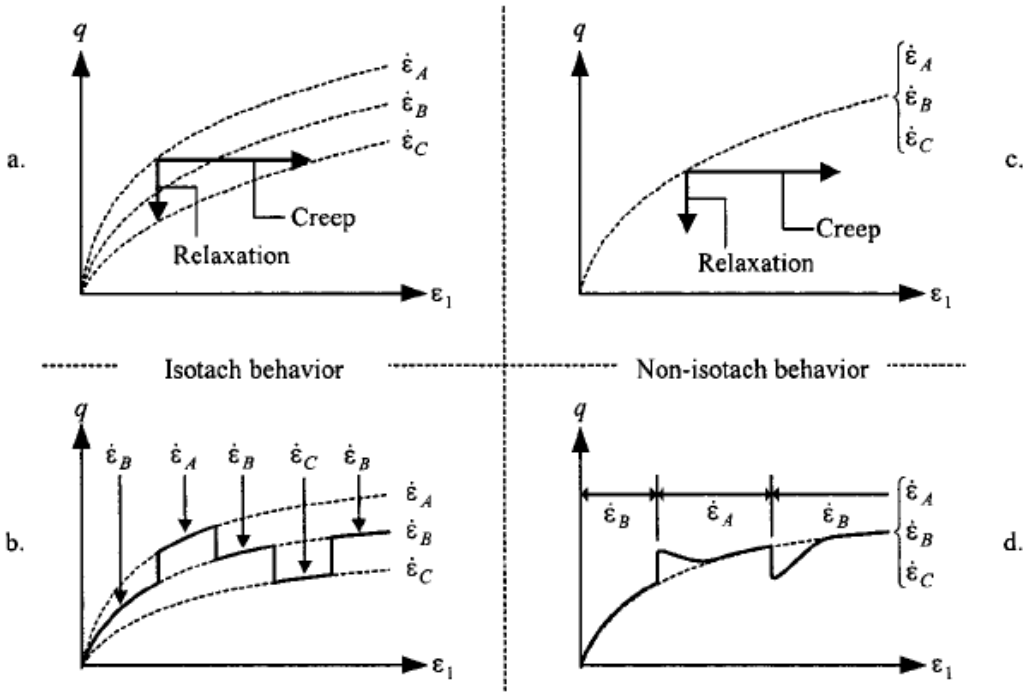

Figure 2.40: isotach behaviour (clay) versus non isotach behaviour (sand) in triaxial tests. (Augustesen, 2004)

Ageing effects and mechanisms: friction and cohesion

When a soil is subjected to constant effective stress for a long period of time, the void ratio and strain rate progressively decrease; if the soil is loaded again, there would be an increase in strain rate and the compression curve would move to the constant strain rate corresponding to the new strain rate, showing a new preconsolidation value, as described by Bjerrum and Garlanger.

Oedometer tests performed by Leonards and Altshaeffl (1964) showed otherwise. They reported that the tested soil exhibited a preconsolidation pressure much higher than that due to its new void ratio only (after 90 days of secondary compression). Such a behaviour is associated with the development of bonds between particles and aggregates and is referred to as 'structuration.' The phenomenon of structuration was postulated by Leroueil et al. (1996) for oedometer tests on artificially sedimented clay. In one of the tests, the soil was consolidated for 120 days under an applied vertical effective stress of 10 kPa. If the increase in the apparent preconsolidation pressure were to be determined from the concept of Bjerrum, as shown in Figure 2.41 the preconsolidation pressure would have increased from 10 kPa to 11.5 kPa. However, due to the structuration effects, the preconsolidation pressure increased to 18.5 kPa during reloading. The compression curve for the oedometer test reported by Leroueil et al. (1996) is reproduced in the following Figure 2.41.

Schmertmann showed that the same aging- preconsolidation effect can also occur in sand (Figure 2.42).

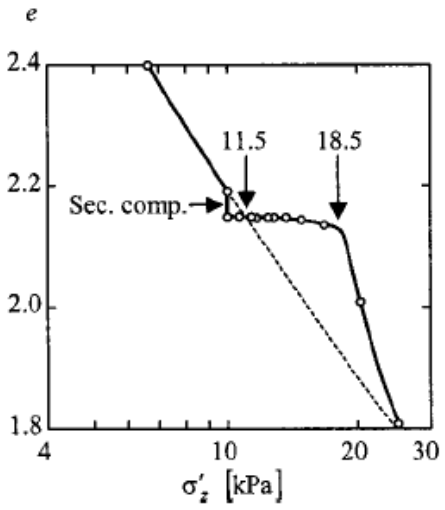

Figure 2.41: compression curve with structuration (Leroueil, 1996)

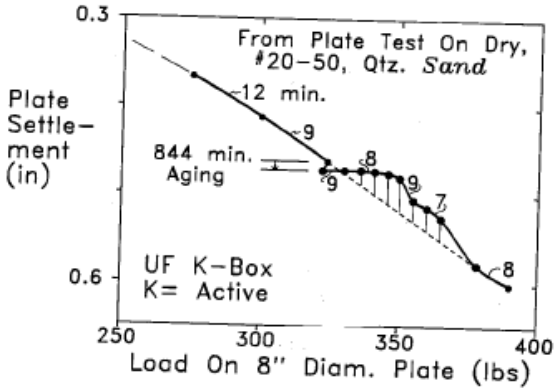

Figure 2.42:aging preconsolidation effect in sand for plate load test (Schmertmann, 1991)

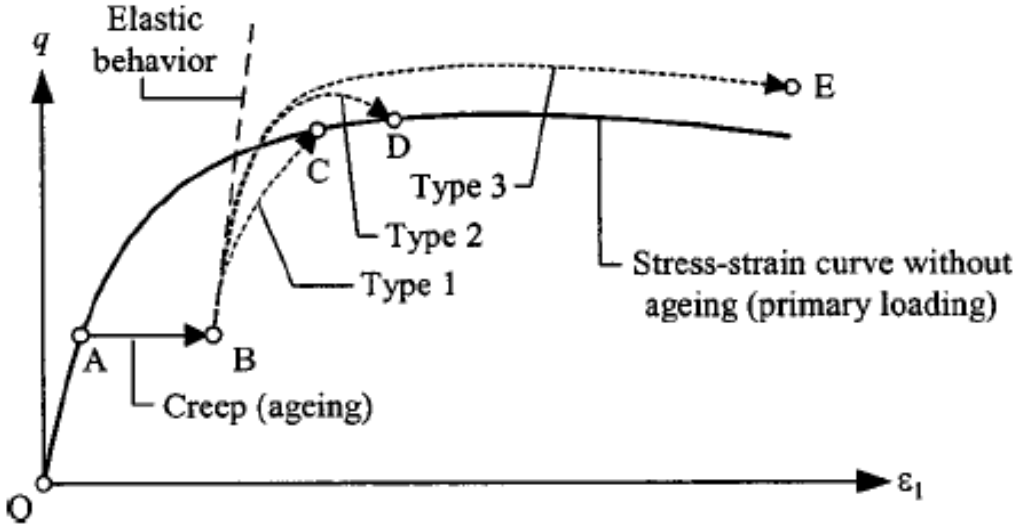

Figure 2.43: the three types of post- ageing stress-strain relationships (Tatsuoka, 2000)

Tatsuoka et al. (2000) distinguished three types of post-aging stress-strain relationship, as shown in Figure 2.43:
-soils that age without structuration: the stress-strain relationship after aging rejoins the original primary loading curve without overshooting (B to C);
-temporary structuration effects: the stress-strain relationship after ageing rejoins the original primary loading curve after having exhibited a temporary overshooting (B to D);
-persistent structuration effects: the stress- strain relationship after ageing overshoots but never rejoined the original primary loading curve (B to E).

A further effect of ageing is testimonied by the evolution of stiffness moduli (M, E, G_0) or shear stress developed after different ageing times. In the next figures a few examples of these effects are shown (Schmertmann, 1991)

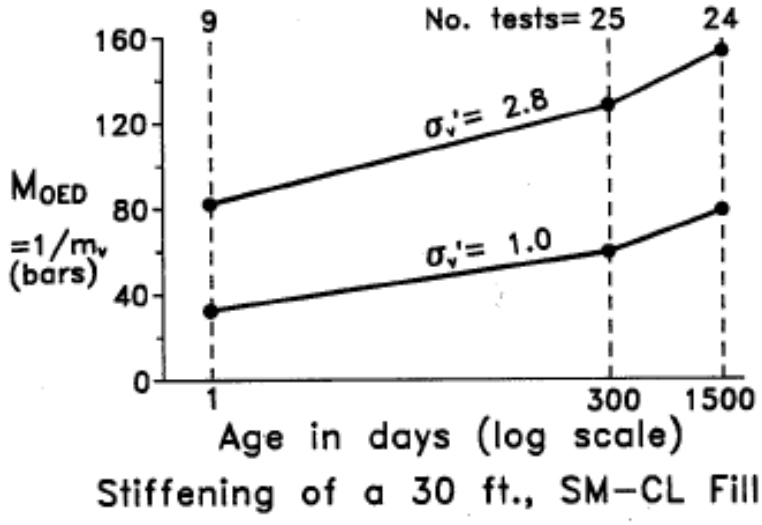

Figure 2.44: increasing oedometer modulus in compacted, cohesive fill (Schmertmann, 1991)

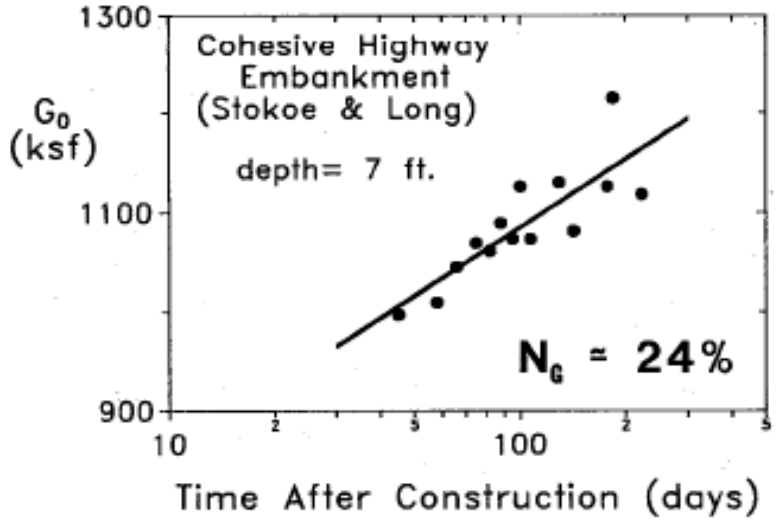

Figure 2.45:icreasing small strain shear modulus in field (Schmertmann, 1991)

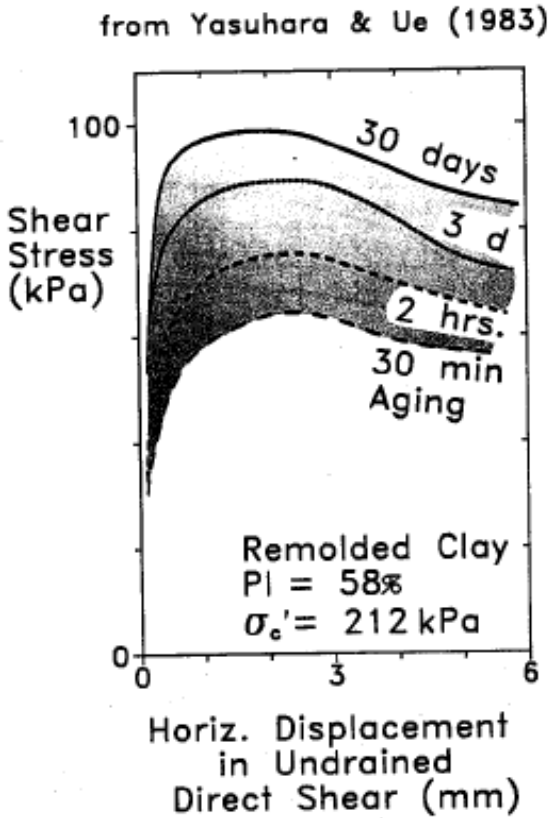

Figure 2.46:laboratory increased undrained strength of clay due to ageing (Schmertmann, 1991)

The question is what kind of micromechanical mechanism causes these ageing effects. Schmertmann (1964) proposed a technique to take out the effect of variable soil structure: in particular he retraced a friction parameter Φ'' that accounts for the soil structure and also a sort of cohesion parameter c'' that denotes the part of the mobilized shear strength not assigned to $\sigma' \tan \Phi''$.The procedure is described in Schmertmann (1991) and sketched in Figure 2.47. Basically, it consists in choosing two samples similar in structure from the unloading part of an oedometer curve, and then perform a triaxial test on them keeping constant the vertical effective stress reached in oedometric condition.

At this point the difference in mobilized shear strength comes from the frictional component, because the two sample have essentially the same initial void ratio and structure at the start of compression and they are brought to the same axial strain state: it is therefore possible to infer that they have the same cohesion. Plotting results, for each axial strain level, in Mohr plane it is possible to deduce Φ'' and c'' values. This procedure can be repeated for soils with different aging levels and then compare the results in order to understand what happens "inside" the soil, i.e. which the principal mechanism that drives ageing changes is.

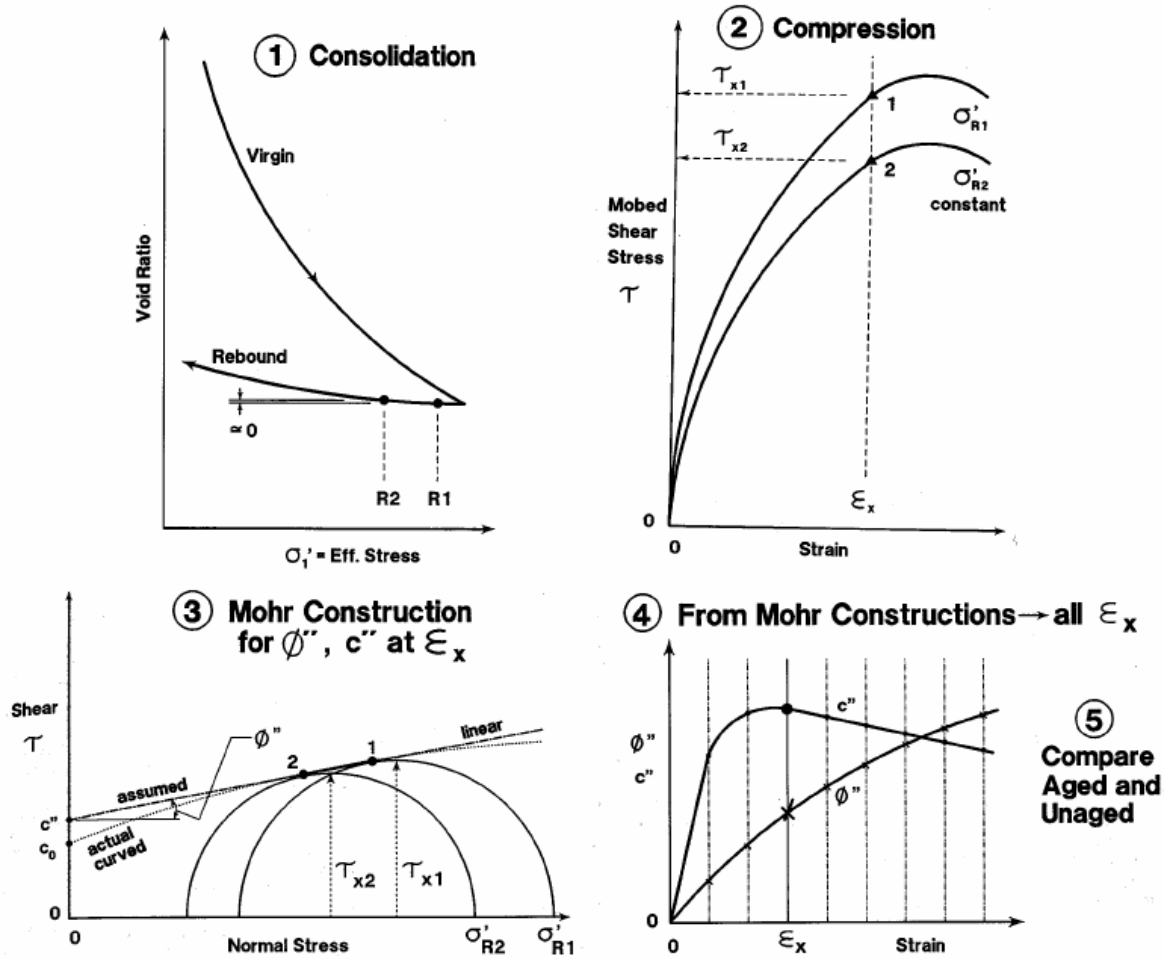

Figure 2.47: Schmertmann procedure to isolate cohesion and friction component in soil behaviour (Schmertmann, 1991)

Results clearly showed that while the cohesion remains almost constant ore decreases with time, friction increases dramatically (see Figure 2.48)

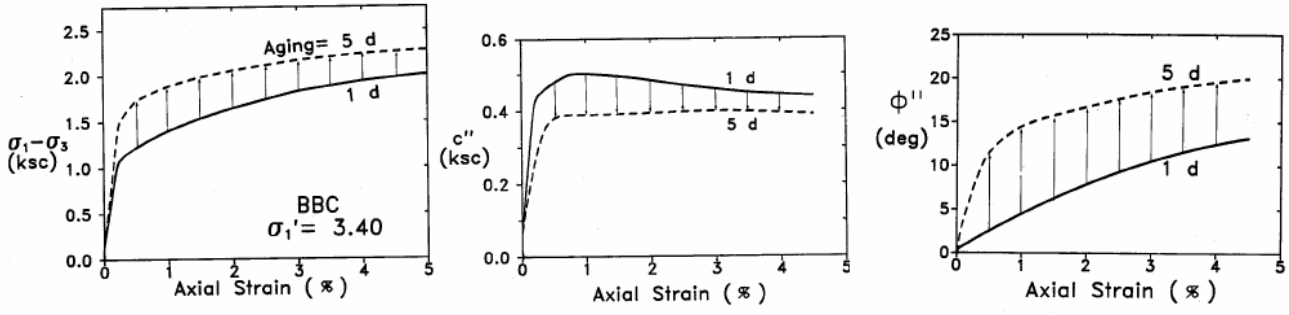

Figure 2.48: laboratory compression after 1 day and five days ageing: comparative cohesion and friction components (Schmertmann, 1991)

From this experimental evidence creep turns out to be a mainly frictional mechanism. It is in fact intuitive to think that, being creep a viscous behaviour linked with the soil solid skeleton, it is caused by slippage and rolling of particles. This produces a significant increase in particle to particle interlocking (besides the well-known decrease in void ratio) and then higher friction. As pointed out by Schmertmann (1991), the density change is not sufficient to explain alone the evolution in preconsolidation pressure when it overshoots the compression curve.

Leroueil (2006) proposed to take into account, in ageing phenomena, also a competing mechanism of structuration that tends to fix particles into positions. The rate of strain determines which one of the two opposing mechanisms (frictional slippage or fixing mechanism) dominates.
This could be the reason why some soil after creep show greater preconsolidation pressure than expected considering the decrease in void ratio.

Chapter 3 - Soft Soil Creep model

Introduction: oedometric condition

Creep behaviour of soft soils substantially refers to the oedometer test, that is a particular case of axysimmetric test in which deformations occur only in the vertical direction while radial strain are constrained ($\varepsilon_r = 0$). Therefore, by definition, vertical strain coincides with volumetric strain ($\varepsilon_z = \varepsilon_a$) and this is the reason why the void ratio $e = V_v / V_s = -d\varepsilon_v \cdot (1 + e_0) + e_0$ is commonly used to described the compression process. So creep behaviour herein described is actually volumetric creep behaviour.

In oedometer one-dimensional compression is applied, but the presence of a metal ring which prevents horizontal displacements plays a significant role in defining the mechanical behaviour of soils. The different mechanical behaviour of an oedometer and an unconfined test is depicted in Figure 3.1. Soil stiffness, defined as the ratio between axial stress and axial strain increment (denoted respectively as E and M) has an opposite trend: it reduces in unconfined tests, while it increases in an oedometer test. Furthermore, the former test reaches the critical state, while in oedometer critical state is never reached due to lateral confinement. The oedometric soil stiffness is therefore referred to as *constrained modulus*.

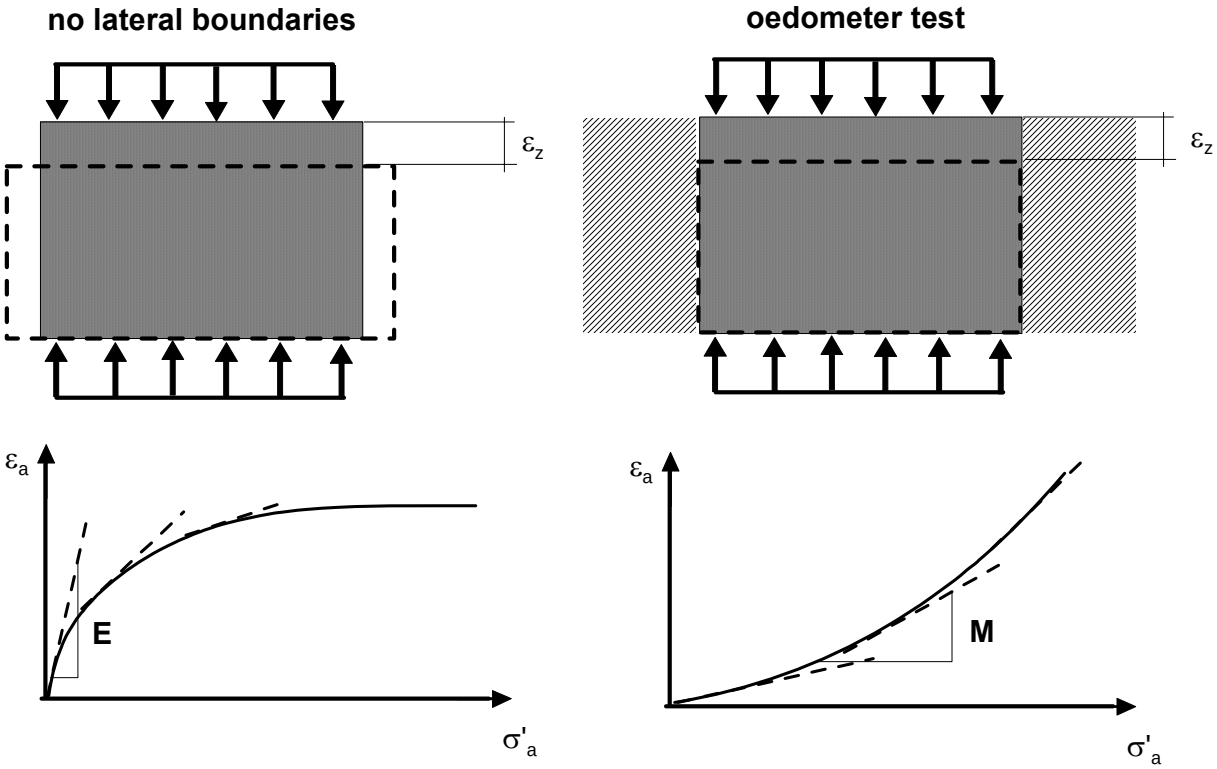

Figure 3.1:oedometer compression curve versus one-dimensional compression without lateral boundaries

In the theory of elasticity radial strain is related to axial strain through the Poisson's ratio ν so that $d\varepsilon_r = \nu \cdot d\varepsilon_z$ and in an oedometric compression Poisson's ratio to be constant, because at the end soil is no more compressible and Poisson's ratio needs to reach the undrained value (i.e. zero volumetric strains) that is 0.5. Besides, it is well-known that for an isotropic elastic material only two over four elastic constant are independent, so, defining two of them (for example ν and E) a third can be directly known.

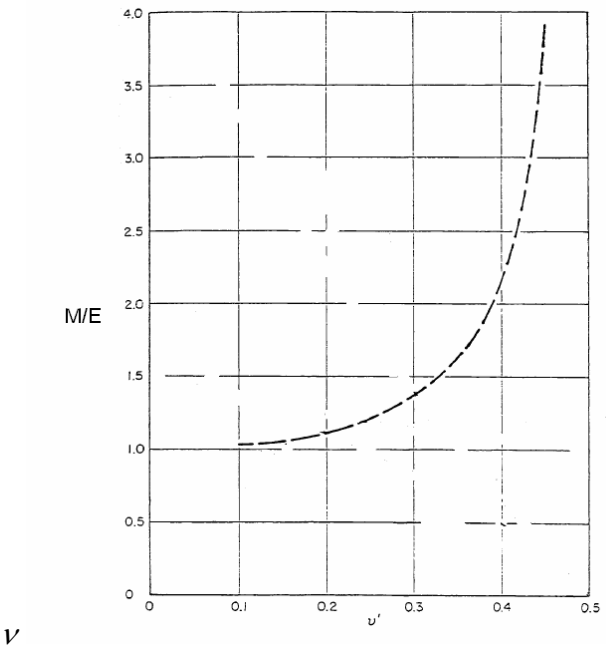

Figure 3.2: constrained modulus versus Young modulus for different Poisson's ratio values

In Figure 3.2 the relationship between M and E, varying , is traced, for elastic conditions. Once again it has been evident that M increases. As previously mentioned, the whole compression process is not elastic, and it is also known that plasticity tends to reduce stiffness. Observing from experimental oedometer curves that stiffness is always increasing it is evident how powerful is the boundary condition influence in resulting behaviour.

Stress resistance concept: Janbu modulus

The resistance concept is widely used in almost all engineering disciplines. Essentials to this concept can be found in the Newton's laws of motion. In 1822 Fourier's relation was introduced which expresses as the conduction of heat in two-dimensional objects. Modification of this relation is known as the thermal resistance concept, or just the resistance concept, described as in Equation (3.1):

$$Q = A \cdot \Delta T / R_t \tag{3.1}$$

where Q is the rate of flow of heat, A is the area through which heat flows, ΔT is the difference between the temperature of the warm and cold faces of the material and R_t is the thermal resistance.

In 1827 Ohm introduced a relation between the potential difference V, or voltage, and the rate of flow of charge I, or current, today known as Ohm's law, in the form of Equation (3.2):

$$R_e = V / I \tag{3.2}$$

where R_e is electric resistance, defined as the opposition offered to the passage of a steady electric current through a body, circuit, or substance. Besides this example one can find many forms of resistance, e.g. dynamic resistance, hydraulic resistance, and elastic resistance.

By virtue of these relations, it is possible to generalize by stating that media possess resistance against a forced change of existing equilibrium conditions. The resistance of a medium, or of an isolated part of it, can therefore be determined by measuring the incremental response to a given incremental action. The general definition of the resistance can be therefore defined as:

$$R = \frac{Incremental \cdot cause}{Incremental \cdot effect} = \frac{dX}{dY} \tag{3.3}$$

As for soils, which are proven to show non-linear (and incrementally non linear) response, the resistance is defined as the tangent to the action-effect curve. The definition of the resistance concept in graphical form is shown in Figure 3.3:

Soils respond to forced changes in existing equilibrium conditions. As already said in the previous chapter, the strain ε_z which develops over an elapsed time t after the application of a stress change $d\sigma'_z$ is a function of stress and time. The overall stress-strain result can be studied when all load increments have acted over a specified length of time, say $\bar{t}$ constant.

The soil sample resistance against deformation (*stress resistance*) in oedometric loading, according to Janbu definition, is defined as:

$$M = \frac{d\sigma'_z}{d\varepsilon_z} \tag{3.4}$$

which matches the definition of constrained modulus.

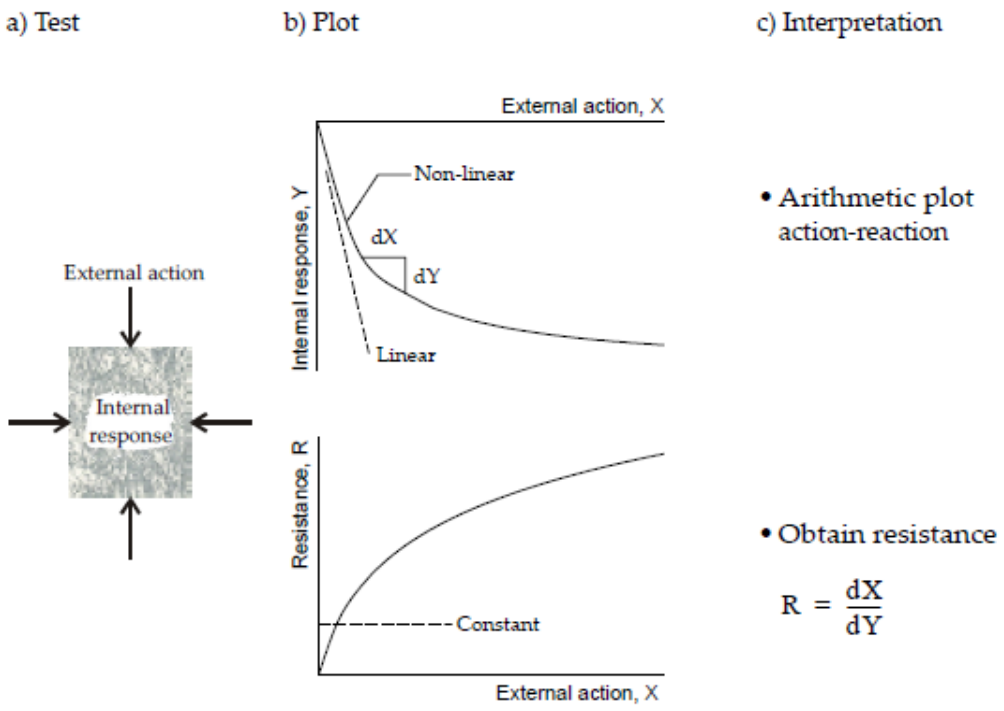

Figure 3.3: resistance concept (Janbu, 1969)

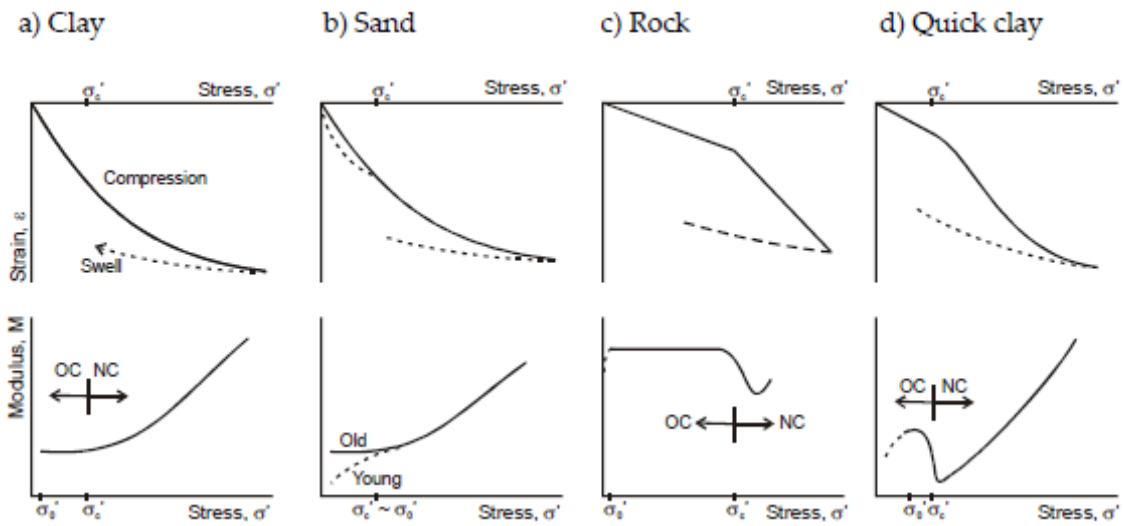

Figure 3.4:Typical stress-strain and M-stress curves from oedometer tests (Janbu, 1969)

In a saturated clay sample, if $\bar{t} < t_{EOP}$, i.e. just after a load application, the strain- time behaviour is governed by primary consolidation. In this case the coefficient of consolidation c_v is the main parameters in defining the early phase of the strain -time relationship $c_v = M/S$ where M is the stress resistance herein defined, and S represent the seepage resistance $S = \gamma_w / k$. In general, in order to discuss the stress resistance, time is assumed to be far above the end of primary consolidation: $\bar{t} > t_{EOP}$.

Four sets of diagrams are shown in Figure 3.4: a) an over-consolidated clay, b) a silty sand at in-situ porosity, c) an intact sample of a cemented moraine, a shale or sedimentary rock and d) a sample of the intact, fairly undisturbed quick clay, or an extra-sensitive soil in general, with loose, porous structure, easily collapsible for increasing stress about preconsolidation pressure

The great advantage of the M-σ'_z curves is that one can clearly distinguish the overconsolidated (OC) and normally consolidated (NC) range, i.e. the preconsolidation stress σ'_{pc} causes a significant change in the M-σ'_z curve's shape. The most dramatic change between these two areas is typical for the extra-sensitive soil material due to the grain structure collapse caused by the breakage of contact points between mineral particles.

In general M is a function of the effective stress. For the ideal normally consolidated clay the constrained modulus increases linearly with mean stress:

$$M = m\sigma_z' \tag{3.5}$$

thus giving the following strain equation:

$$d\varepsilon_z = \frac{1}{M} d\sigma'_z = \frac{1}{m} \cdot \frac{d\sigma'_z}{\sigma'_z} = \lambda^* \cdot \frac{d\sigma'_z}{\sigma'_z} \tag{3.6}$$

that is a differential expression for a semi-logarithmic expression; in fact integrating between two effective vertical stress values $(\sigma'_{z,0} \div \sigma'_z)$ it becomes:

$$\varepsilon_z = \frac{1}{m} \cdot \ln \frac{\sigma'_z}{\sigma'_{z,0}} = \lambda^* \cdot \ln \frac{\sigma'_z}{\sigma'_{z,0}} \tag{3.7}$$

Equation (3.7) demonstrates that a semi-logarithmic stress-strain relationship is simply explained by a linear stress resistance, i.e. a stress linearly dependent constrained modulus. The semi-logarithmic stress -strain plane in this framework has the natural logarithm as abscissa, and the axial strain (or indifferently the volumetric strain, as they coincide in oedometric conditions) as vertical axis. This is qualitatively the same when making use of base 10 logarithm for stress and the void ratio instead of vertical strain. In particular, the modified compression index λ^* is defined as:

$$\lambda^* = \frac{1}{m} = \frac{\Delta \varepsilon_z}{\Delta \ln \sigma'_z} = \frac{C_c}{\ln 10 \cdot (1 + e_0)} \tag{3.8}$$

where C_c is the compression coefficient.

As for overconsolidated clays, the constrained modulus M can be taken as constant and in a sense this case is equivalent to linear elasticity. The oedometric modulus varies with the type of soils, as can be seen in Figure 3.5:

The most general expression for the oedometric modulus put forward by Janbu (1963) is given in Equation (3.9):

$$M = m \cdot \sigma_{ref} \left(\frac{\sigma'_z}{\sigma_{ref}} \right)^{1-n} \tag{3.9}$$

where σ_{ref} a is reference stress, σ'_z is effective stress (kPa), m is the modulus number (dimension-less) and α is the stress exponent (dimensionless).

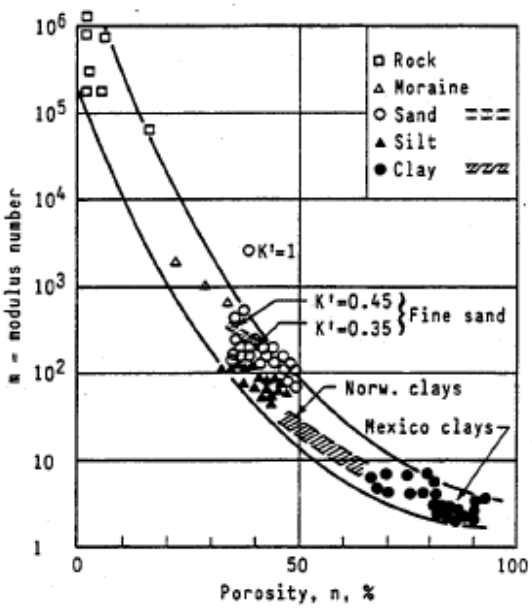

Figure 3.5: soil compressibility as determined by oedometer and triaxial tests (Janbu, 1963)

The integral expression of vertical strain is thus:

$$\varepsilon = \int_{\sigma'_{z0}}^{\sigma'_{z0}+\Delta\sigma'_z} \frac{d\sigma'_z}{M} \tag{3.10}$$

Different types of the M-σ'_z behaviour can be described by this equation using various values of the stress exponent α. According to Janbu (1963) there are four main categories of the M-σ'_z variations, as summarized in Figure 3.6 :

1. Overconsolidated soils ($\sigma'_z < \sigma'_{pc}$) denoted OCS equivalent elastic, where the stress exponent $n = 1$. In this case:

$$M = m\sigma_{ref} = const \tag{3.11}$$

$$\varepsilon_z = \frac{\Delta\sigma'_z}{M} \tag{3.12}$$

2. Normally consolidated sand (NCS) with $n = 0.5$. In silty sandy soils (NC) the α-value may range typically between 0.4 to 0.65, so 0.5 should be considered as an average choice for practical purposes only. The forms for the tangent modulus M and strain ε then are:

$$M = m\sqrt{\sigma'_z \cdot \sigma_{ref}} \tag{3.13}$$

$$\varepsilon_z = \frac{2}{m}\left[\sqrt{\frac{\sigma'_{z0}+\Delta\sigma'_z}{\sigma_{ref}}} - \sqrt{\frac{\sigma'_z}{\sigma_{ref}}}\right] \tag{3.14}$$

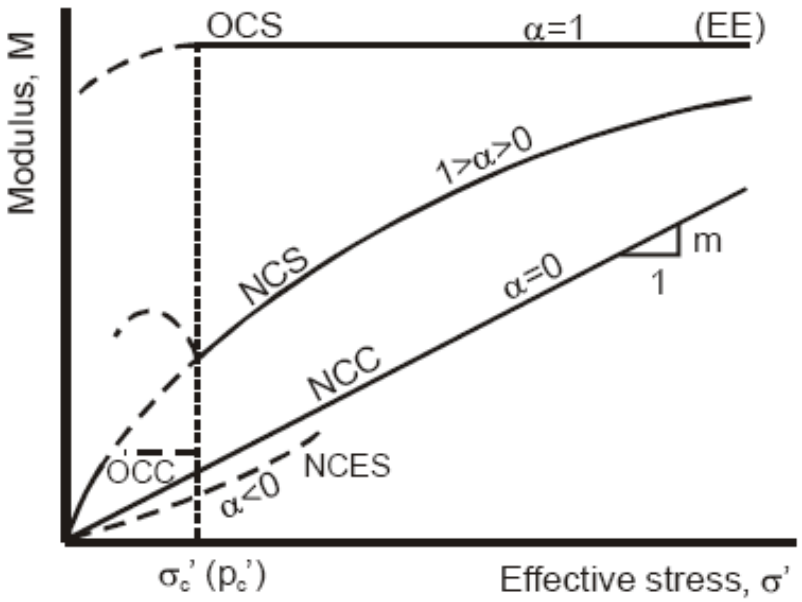

Figure 3.6: idealized M- stress curves for four soils categories

3. The normally consolidated clays (NCC), as above, have $n = 0$, so:

$$M = m\sigma'_z \tag{3.15}$$

$$\varepsilon_z = \frac{1}{m}\ln\frac{\sigma'_z}{\sigma'_{z0}} \tag{3.16}$$

4. The normally consolidated quick clays (NCQC) or extra sensitive soils (NCES), which can described by $n = -0.5$

$$M = m\sigma'_z\sqrt{\frac{\sigma'_z}{\sigma_{ref}}} \tag{3.17}$$

$$\varepsilon_z = \frac{2}{m}\left[\sqrt{\frac{\sigma'_z}{\sigma_{ref}}} - \sqrt{\frac{\sigma'_{z0}+\Delta\sigma'_z}{\sigma_{ref}}}\right] \tag{3.18}$$

Janbu's modulus as a work conservative modulus in elastic region

The relationship between stress and strain in an elastic framework is a bijection. The main consequence is that the work spent during the deformation process is returned once you remove the cause of deformation, so the process is completely reversible. Consequently it is possible to define a state function *U* depending on the process extremes and not on the path that is a potential function and it is called strain energy function or *elastic potential* (Green, 1839).

Since the work done in a deformation is: $\partial W = \sigma_{ij}\partial\varepsilon_{ij}$ by definition it is: $\partial U = \sigma_{ij}\partial\varepsilon_{ij}$ thus giving:

$$\sigma_{ij} = \frac{\partial U}{\partial\varepsilon_{ij}} \tag{3.19}$$

If we require that a strain energy function U does exist we postulate that the elastic potential energy should be a unique function of the state of strain, and it can be proven that this requires that the elastic matrix has to be symmetric. In fact $D_{ij} = \frac{\partial^2 U}{\partial\varepsilon_i\partial\varepsilon_j}$, and since U has to be independent on the sequence of deformations, the symmetry is proven. There is a parallel between stiffness and compliance formulations, interchanging stresses and strains.

An equivalent alternative formulation of hyper-elasticity involves a complementary strain energy function U_c, such that: $\partial U_c = \varepsilon_{ij}\partial\sigma_{ij}$ thus giving:

$$\varepsilon_{ij} = \frac{\partial U_c}{\partial\sigma_{ij}} \tag{3.20}$$

consequently one gets the symmetric compliance Cij matrix as:

$$C_{ij} = \frac{\partial^2 U_c}{\partial\sigma_i\partial\sigma_j} \tag{3.21}$$

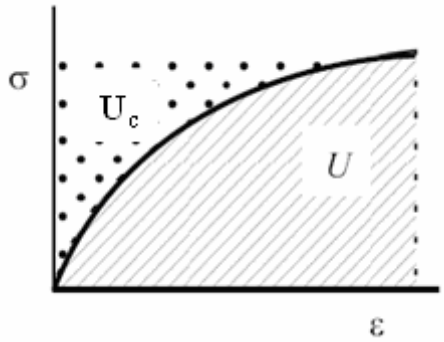

Figure 3.7: strain energy functions U and complementary energy function U_c

The simplest case of elastic law is the linear elastic one. For the one-dimensional formulation the strain energy function and the complementary energy function are given in the Figure 3.8.

Obviously, Janbu's modulus is not elastic when used to describe virgin compression, but in an elastic framework it represents a conservative modulus suitable to describe non-linear elastic response. In fact it is derived moving from a complementary energy function, and it results, as known, depending on stress state (see Figure 3.9).

When a strain energy function does exist, energy generation in a closed circle is prevented and the formulation is more consistent, thus not violating thermodynamics. However, in most cases stress dependent moduli from curve fitting of laboratory tests results are proposed, and there is no guarantee that a strain energy function exists, and use of such moduli may cause thermodynamical inconsistencies, as reported in Chapter 1.

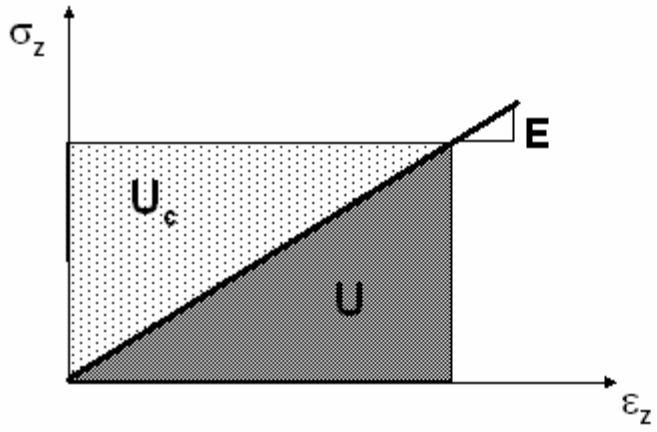

$$U = \frac{1}{2}E\varepsilon^2$$

$$\sigma = \frac{\partial U}{\partial \varepsilon} = \frac{1}{2}(2E)\cdot\varepsilon = E\cdot\varepsilon$$

$$U_c = \frac{1}{2E}\sigma^2$$

$$\varepsilon = \frac{\partial U_c}{\partial \sigma} = \frac{1}{2E}2\sigma = \frac{\sigma}{E}$$

Figure 3.8: strain energy function and complementary energy function for linear elasticity

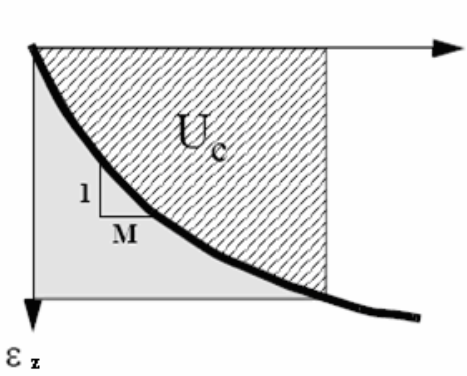

$$U_c = \frac{\sigma_a}{n(n+1)m}\left(\frac{\sigma'}{\sigma_a}\right)^{n+1}$$

$$\varepsilon = \frac{\partial U_c}{\partial \sigma'} = \frac{1}{nm}\left(\frac{\sigma'}{\sigma_a}\right)^{n}$$

$$\frac{d\varepsilon}{d\sigma'} = \frac{1}{m\sigma_a\left(\frac{\sigma'}{\sigma_a}\right)^{1-n}}$$

$$M = \frac{d\sigma'}{d\varepsilon} = m\sigma_a\left(\frac{\sigma'}{\sigma_a}\right)^{1-n}$$

Figure 3.9: complementary energy function for Janbu modulus

Compression parameters in bi-logarithmic stress plane: natural strain

Janbu's approach can be extended to describe the compression in terms of mean stress. In the special case of oedometer test, in fact, axial strain coincides with volumetric strain and mean stress is proportional to axial stress: $p = (1+2K_0)\sigma'_z/3$ where K_0 is the ratio of horizontal to vertical effective (at-rest coefficient). Hence:

$$\varepsilon_v \equiv \varepsilon_z = \frac{1}{m}\cdot \ln\frac{\sigma'_z}{\sigma'_{z,0}} = \lambda^*\cdot \ln\frac{\sigma'_z}{\sigma'_{z,0}} = \lambda^*\cdot \ln\frac{p_z}{p_{z,0}} \tag{3.22}$$

It has been highlighted that the slope λ^* of the compression curve is not costant being the soil not indefinitely incompressible. Another way of describing soil compression is to use the bi-logarithmic frame, by means of the definition of the natural strain (or Hencky strain) instead of the Cauchy strain used so far. In this case it is possible to find a constant slope that describes the soils' compression.

Den Haan (1992), in fact, has shown that the virgin compression of a wide range of soils is adequately formulated by:

$$v = v_1(p' - p'_s)^{-b} \tag{3.23}$$

which relates the specific volume (the ratio of total soil volume to solid volume, $v = 1+e$) to effective mean stress p'. The power curve has a vertical asymptote at $p' = p'_s$ and v_1 is a reference value of specific volume at stress $p' = p'_s + 1$, and b is a dimensionless positive number.
The value of p'_s is usually near to zero for remoulded clay, or more in general for normally consolidated clay, but also for granular soils and peats. The equation then simplifies to:

$$v = v_1 \cdot p'^{-b} \tag{3.24}$$

which can be linearized by writing:

$$\ln v = \ln v_1 - b \ln p' \tag{3.25}$$

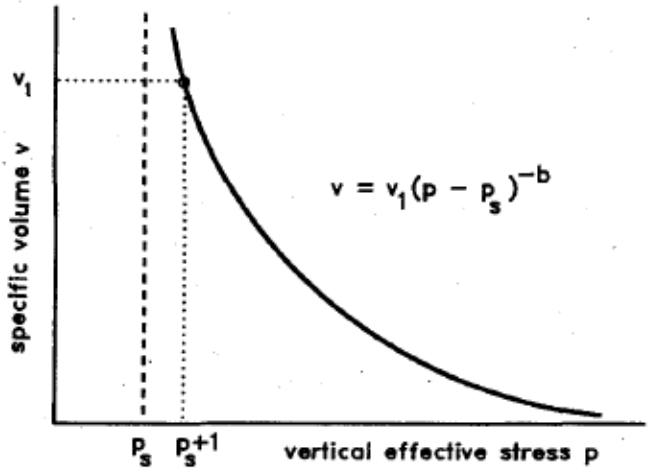

Figure 3.10: generalized power formulation of virgin compression (Den Haan, 1994)

or in an equivalent way:

$$\ln \frac{v}{v_0} = \ln \frac{v_0}{v_1} - b \ln p' \tag{3.26}$$

Natural strain is defined as the strain measured incrementally with respect to the momentary dimension rather than with respect to the initial dimension, case that represent the Cauchy strain:

$$\varepsilon_v{}^C = \int_{V_0}^{V} \frac{dV}{V_0} = \frac{V}{V_0} - 1 \tag{3.27}$$

The natural strain results to be:

$$\varepsilon_v{}^H = \int_{V_0}^{V} \frac{dV}{V} = \ln\left(\frac{V}{V_0}\right) = \ln\left(\varepsilon_v{}^C + 1\right) \tag{3.28}$$

For small strain ($\varepsilon_v{}^C \to 0$) the Mc Laurin formula shows that the two definition coincides:

$$\lim_{\varepsilon^C \to 0} \varepsilon_v{}^H = \lim_{\varepsilon^C \to 0} \ln\left(\varepsilon_v{}^C + 1\right) = \varepsilon_v{}^C + o(\varepsilon_v{}^C) \tag{3.29}$$

Introducing the natural strain in the previous compression equation (reminding that specific volume is proportional to volume by means of solids volume so that a ratio between specific volume coincides with a ratio between volumes), it results:

$$\ln\left(\varepsilon_v{}^H\right) = \ln\left(\varepsilon_v{}^C + 1\right) = c - b \ln p' \tag{3.30}$$

where b is a constant.

In this bi-logarithmic approach, indeed, the compression curve is effectively a line and the parameter b introduced by Den Haan (1992), called the natural compression index, is the slope of the virgin compression curve:

$$b = \frac{\Delta \varepsilon_v{}^H}{\Delta \ln p} \tag{3.31}$$

On the other hand, again, it is demonstrable that the slope in the semi-logarithmic plane is not a line.

In fact:

$$\Delta \varepsilon_v{}^H = \frac{\Delta V}{V} = \frac{\Delta e}{1+e} = \frac{1}{1+e} \cdot \frac{\Delta \varepsilon_v{}^C}{1+e_0} \tag{3.32}$$

and so

$$\lambda^* = \frac{\Delta\varepsilon_v{}^C}{\Delta \ln p} = \frac{\Delta\varepsilon_v{}^H \cdot (1+e_0)}{(1+e)} \cdot \frac{1}{\Delta \ln p} = b\frac{(1+e_0)}{(1+e)} \tag{3.33}$$

for small strains ($e \approx e_0$): $\lambda^* \cong b$ and can be taken as a constant, for large strains $\lambda^* \propto e$.

Time resistance concept: the time resistance number

Similarly to stresses, one can apply the resistance concept to the strain-time behaviour of soils. As matter of fact, time can be considered as an action and strain as a response. Hence, the time resistance of the soil R can be defined as:

$$R = \frac{dt}{d\varepsilon_z} = \frac{dt}{d\varepsilon_v} = \frac{1}{(d\varepsilon_v/dt)} \tag{3.34}$$

keeping in mind that axial strain coincides with volumetric strain in oedometric conditions.

For most granular media the time resistance generally increases with time for one-dimensional compression under a certain stress, as shown in Figure 3.11.

The R- t curve can be divided in three zones: in zone A $(t < t_\ell)$ the R-t curve is represented by a second degree parabola, corresponding to the early stage of the primary consolidation. In zone B $(t_\ell < t < t_{EOP})$ a transition takes place from the parabolic shape of R in zone A to the linear R variation of zone C. In zone C $(t > t_{EOP})$ excess pore pressure is zero, corresponding to secondary compression.

In zone B primary and secondary compression usually overlap. The idea of Janbu is to interprete this phase B considering gradients and seepage forces so small that time-delayed compression for all practical purpose is governed by intergranular shear stress and shear strains only. The creep phenomenon can in this way be described by the straight line starting from the time t_r and with slope $r_s = \frac{dR}{dt}$ that is called *time resistance number*. Irrespective of the magnitude of the load increment, the R-t relationship will eventually become a straight line, at least for clays.
Hence, for $t > t_{EOP}$ one can write:

$$R = r(t - t_r) \tag{3.35}$$

On introducing the time resistance definition: $R = dt/d\varepsilon_z$, the differential expression of strain becomes

$$\partial\varepsilon_v = \frac{dt}{r_s(t-t_r)} = \frac{1}{r_s} \cdot \frac{d(t-t_r)}{(t-t_r)} \tag{3.36}$$

where r_s and t_r constant for a given effective stress.

Integrating over the time range from t_{EOP} to any generic time $t = t_{EOP} + t'$ one obtains the following formula for secondary strains $(t > t_{EOP})$:

$$\begin{aligned} \varepsilon_v &= \frac{1}{r_s} \cdot \ln \frac{t - t_r}{(t_{EOP} - t_r)} = \\ &= \frac{1}{r_s} \cdot \ln \frac{t - t_r}{(t_{EOP} - t_r)} = \mu^* \ln \frac{t - t_r}{(t_{EOP} - t_r)} = \mu^* \ln \frac{t^*}{\tau_c} = \mu^* \ln \frac{\tau_c + t'}{\tau_c} \end{aligned} \tag{3.37}$$

where $t' = t - t_{EOP}$ is the pure creep time.

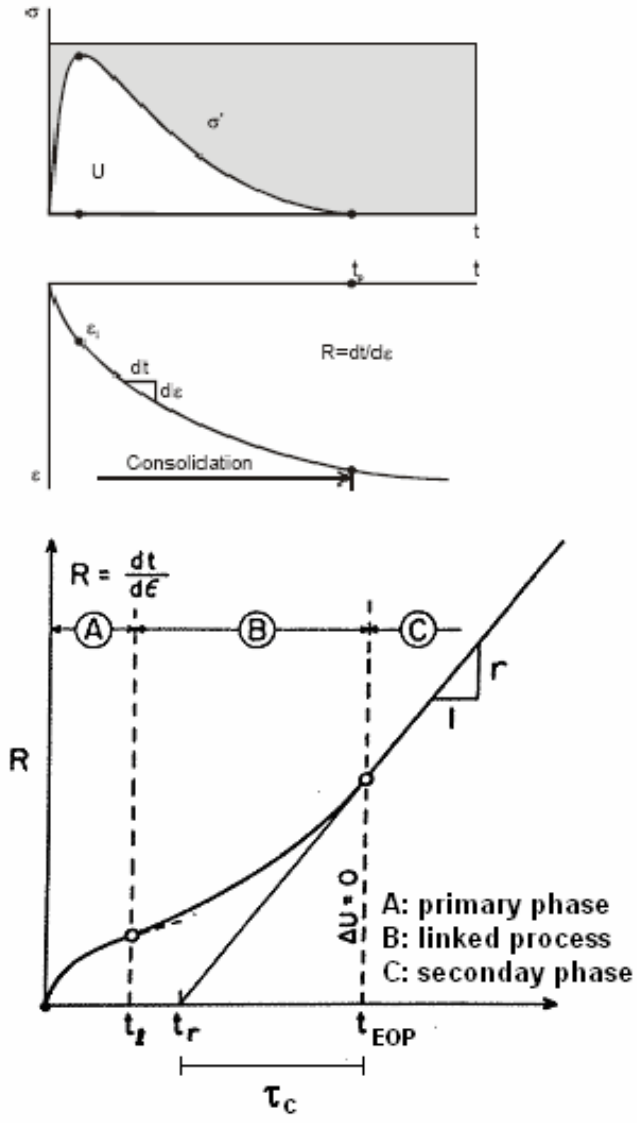

Figure 3.11:strain and time resistance as function of time (Janbu, 1969)

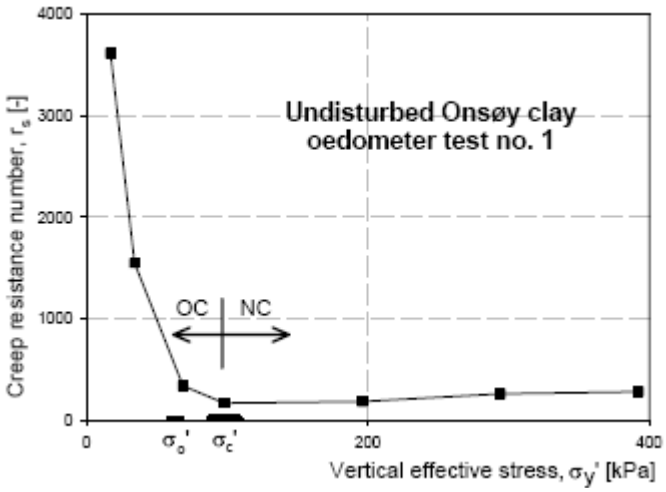

Figure 3.12:resistance number variation dependency on effective stress (Havel, 2004)

Both in the differential and the integral equations time scale needs to be altered by the quantity t_r which is called (De Rijk, 1978) *reference time shift*. The difference between "test time" t (measured from the beginning of the loading) and reference time shift is given the name *intrinsic time* t^* (Den Haan, 1994).

It has been proven also, by a large amount of oedometer tests, that the creep resistance number r_s depends on the level of the effective stress.

Figure 3.12 shows the typical relation between the creep resistance number r_s and effective stress for the undisturbed Norwegian soft clay. Generally, the creep resistance is very large in the OC range and drops radically when the effective stress approaches the preconsolidation pressure. The minimum value of the creep resistance r_s is at $\sigma' = \sigma'_{pc}$ and thereafter increases slightly.

The stress dependency of the creep parameter has been already mentioned with reference to secondary compression coefficient C_α. Time resistance number is strictly linked with it (apart from the use of intrinsic time instead of time and the use of natural logarithm instead of 10 base logarithm) so the stress dependency of time resistance number is consistent with previous approaches.

As compression coefficient is not properly a constant unless the stress-strain curve is plotted in bi-logarithmic plane (or equivalently using Henky strain), the same has to be done for creep coefficient. The previous relationship between intrinsic time and strain can be rewritten in the as in Equation (3.38) (Den Haan, 1994):

$$\varepsilon_v{}^H = c \ln \frac{t - t_r}{(t_{EOP} - t_r)} \tag{3.38}$$

where $c = \Delta \varepsilon_v{}^H \big/ \Delta \ln t$.

Only in this way c can be taken as a constant and, analogously to the compression coefficient, the creep coefficient in semi-logarithmic plane varies with strain, having a theoretical boundary for $e = 0$:

$$\mu^* = \frac{\Delta \varepsilon_v{}^C}{\Delta \ln t} = c \frac{(1 + e_0)}{(1 + e)} \tag{3.39}$$

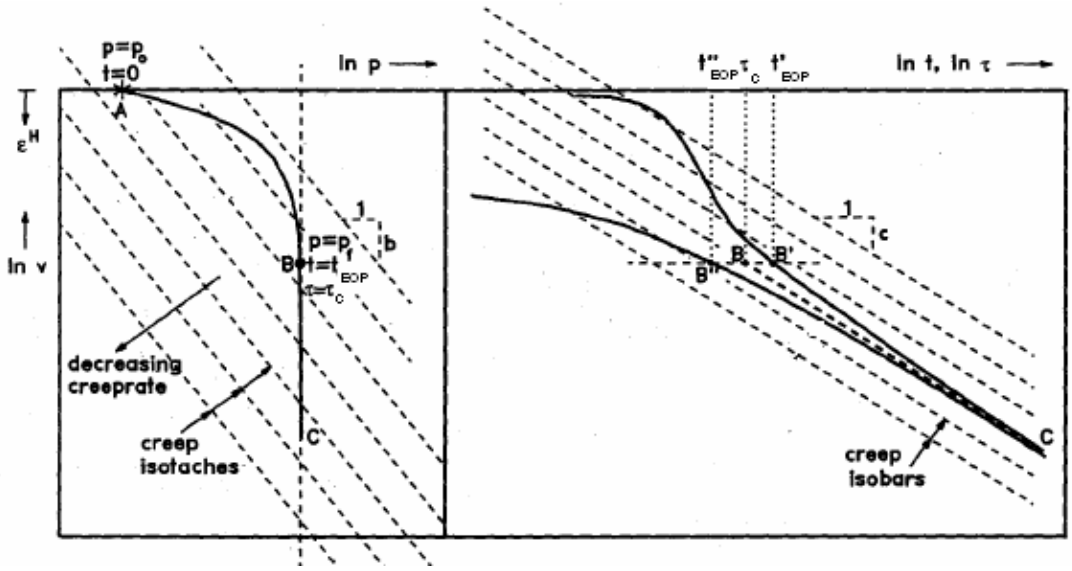

Figure 3.13: intrinsic time and reference time shift in the definition of secondary compression slope (Denn Haan, 1994)

It is worth highlighting that, even in bi-logarithmic plane, the slope would not be straight if one chose the 'test time' as a variable, and not the intrinsic time.

With reference to Figure 3.13, the secondary compression curve could be either B'C or B''C depending on whether the primary period t_{EOP} is longer or shorter than the intrinsic time τ_c.Eventually, at large time, the importance of the time shift diminishes and the slope tends to c in both cases.

Soft Soil creep model: rheological behaviour

The foundation of the science of rheology was laid by Newton in 1687, in his laws of motion of an ideal viscous fluid, commonly known as Newtonian fluid. Newton found a linear relation that existed between the flow rate and flow resistance of an ideal viscous fluid. The viscosity of the Newtonian ideal viscous fluid can be determined by a relation between stress and the rate of flow:

$$\sigma = \eta \frac{d\varepsilon^{viscous}}{dt} \tag{3.40}$$

Where η is the coefficient of viscosity and $\varepsilon^{viscous}$ is the viscous strain. In rheological models the Newtonian fluid is simulated as a viscous element, consisting of a cylinder with a perforated piston filled with a viscous fluid, called viscous dashpot.

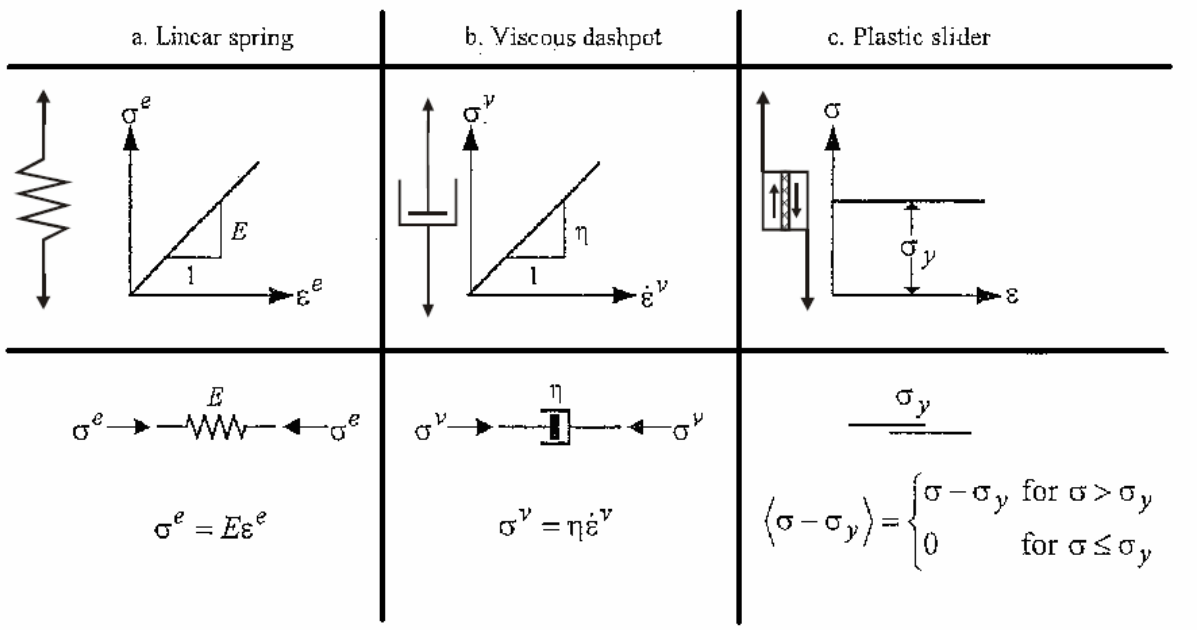

Figure 3.14:rheological mechanical elements

In rheological models the properties of elasticity are described through the ideal elastic Hooke medium simulated as an elastic spring. The characteristic feature of the ideal elastic Hooke medium is a linear relation between stress and strain:

$$\sigma = E\varepsilon^e \tag{3.41}$$

where E is Young's modulus or modulus of elasticity and ε^e is the elastic strain. However, in rheological models this relation can be non-linear as well.
The ideal rigid plastic Saint Venant body (plastic slider) is used for the description of plastic behaviour. The body is simulated by the dry Coulomb friction that appears on a rough surface when a load is moved on it under the action of a horizontal force producing a stress equal to the plastic flow limit σ_y.When $\sigma < \sigma_y$ the deformation of rigid plastic body is zero while at $\sigma > \sigma_y$ it experiences unlimited plastic strain.
The meaning of the mechanical elements is summarized in Figure 3.14.

The Soft Soil Creep model (SSC) was proposed by Vermeer and Neher (1999). The constitutive law is visco-elastic: the basic idea is that all inelastic strain are time-dependent. In Figure 3.15 the rheological model of SSC is presented. It is constituted by a linear spring and a viscous dashpot connected in series. (i.e. it belongs to the Maxwell model families), whose meaning will be clarified later on in this Section.

The Maxwell visco-elastic rheological model (Maxwell body) was first presented in 1868 by James C. Maxwell

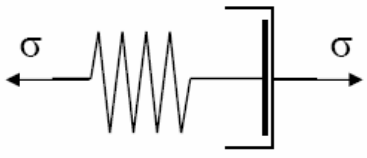

Figure 3.15: The Soft Soil Creep constitutive law rheological behaviour:Maxwell model

After the application of a certain stress, the elastic spring produces instant strain, whereas in the viscous element the instant strain is zero. As the stress continues to act, viscous flow due to the movement of the performed piston in the viscous fluid will occur and so-called delayed strain will be produced. The total strain will be the sum of immediate and delayed strains, and the stress will be equal on both the basic elements.

$$\varepsilon = \varepsilon^{e} + \varepsilon^{viscous} \tag{3.42}$$

$$\sigma = \sigma^{e} = \sigma^{viscous} \tag{3.43}$$

The first equation can be expressed in terms of strain rates:

$$\frac{d\varepsilon}{dt} = \frac{d\varepsilon^{e}}{dt} + \frac{d\varepsilon^{viscous}}{dt} = \frac{\dot{\sigma}}{E} + \frac{\sigma}{\eta} \tag{3.44}$$

and integrating for a constant stress σ_0 (pure creep condition) acting for a certain time t:

$$\varepsilon(t) = \frac{\sigma_0}{E} + \frac{\sigma_0}{\eta} \cdot t = \varepsilon_0 + \frac{d\varepsilon^{viscous}}{dt} \cdot t \tag{3.45}$$

In general, not depending the elastic strain on time it is:

$$\frac{d\varepsilon(t)}{dt} = \frac{d\varepsilon^{viscous}}{dt} \tag{3.46}$$

The creep behaviour of the Maxwell rheological model during loading and subsequent unloading with linear viscosity is shown in Figure 3.16.

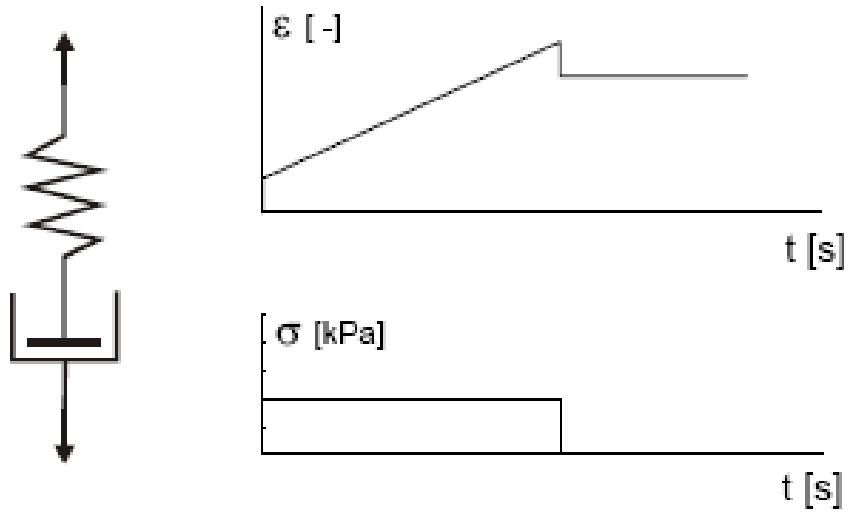

Figure 3.16: Maxwell model creep behaviour

The whole three- dimensional Soft Soil Creep model is indeed described by a Bingham model, because besides the constitutive law, a failure criterion is introduced (Figure 3.17).

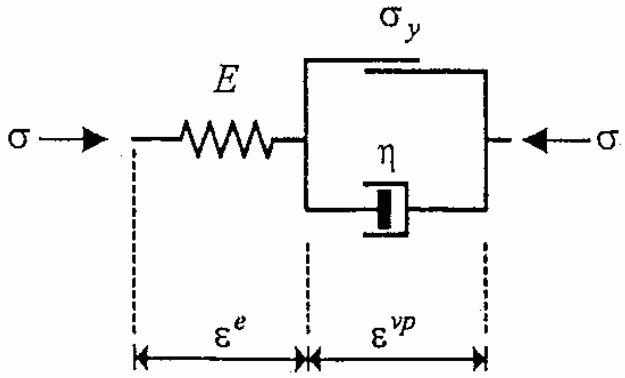

Figure 3.17: Soft Soil Creep model as a Bingham model

Soft Soil creep model: compression parameters

Soft Soil Creep model takes into account the evolution of preconsolidation pressure and results in a isotache approach model, making use of Modified Cam Clay constitutive ellipses (see Chapter 1).

In order to derive the genesis of the model, since it moves from the Cam Clay model given in terms of mean stress and on the other hand it describes a typically one-dimensional oedometric behaviour, a clarification about compression indexes is needed.

To describe the oedometric virgin compression behaviour of a soft soil the Janbu equation for the constrained modulus has been chosen with n exponent equal to 1 (in which, due to the oedometric condition: $\varepsilon_z = \varepsilon_v$), thus giving a stress-dependent soil stiffness:

$$M = \frac{d\sigma'_z}{d\varepsilon_v} = m\sigma_{ref}\left(\frac{\sigma'_z}{\sigma_{ref}}\right)^{1-n} = M_{ref}\left(\frac{\sigma'_z}{\sigma_{ref}}\right) = \frac{\sigma'_z}{\lambda^*} = M(\sigma'_z) \qquad (3.47)$$

$$\lambda^* = \frac{\sigma_{ref}}{M_{ref}} = const \qquad (3.48)$$

In order to have a constant value of λ^* that realistically describes soils' behaviour, strain have to be expressed by the Henky definition (i.e. with respect to the momentary dimension). Since in soil mechanics one usually deals with small strain, Cauchy strain and Henky strain can be alternatively used. As previously mentioned, this form of constrained modulus, offers the well-known logarithmic expression of strain in virgin compression:

$$d\varepsilon_v = \frac{1}{M}d\sigma'_z = \lambda^* \cdot \frac{d\sigma'_z}{\sigma'_z} \qquad (3.49)$$

$$\varepsilon_v = \lambda^* \cdot \ln\frac{\sigma'_z}{\sigma'_{z,0}} \qquad (3.50)$$

It can be easily proven that the oedometric NC line and the isotropic NC line have the same slope.

The mean stress is in fact proportional to axial stress throughout the at-rest coefficient K_0:

$$p = \frac{(1+2K_0)\sigma'_z}{3} \tag{3.51}$$

The compression index thus results equivalent in terms of vertical stress and mean stress:

$$\lambda^* = \frac{\Delta\varepsilon_v}{\Delta \ln \sigma'_z} = \frac{\Delta\varepsilon_v}{\ln \frac{\sigma'_{z,2}}{\sigma'_{z,1}}} = \frac{\Delta\varepsilon_v}{\ln \frac{p'(3/(1+2K_0))}{p'_0(3/(1+2K_0))}} = \frac{\Delta\varepsilon_v}{\Delta \ln p'} \tag{3.52}$$

$$\varepsilon_v = \lambda^* \cdot \ln \frac{p'}{p'_0} \tag{3.53}$$

The same can not be inferred for the slope of the compression curve in the elastic region (unloading-reloading line), because K_0 is not a constant for overconsolidated soils. K_0 value can be retraced, using the elastic constitutive law in oedometric condition:

$$\varepsilon_r = \frac{1}{E}(-\nu\sigma'_a + (1-\nu)\sigma'_r) = 0 \Rightarrow \sigma'_r = \frac{\nu}{1-\nu}\sigma'_a \Rightarrow K_0 = \frac{\nu}{1-\nu} \tag{3.54}$$

where ν is the Poisson's ratio in the unloading-reloading phase.
The mean stress can be expressed in the following way with respect to the vertical stress:

$$dp' = \frac{\left(1+2\frac{\nu}{1-\nu}\right)d\sigma'_z}{3} = \frac{\nu+1}{3(1-\nu)} \cdot d\sigma'_z \tag{3.55}$$

On the other hand modified Cam Clay model uses for elastic strain an expression similar to that resulting for elasto-plastic one, that gives, in the integrated form, a logarithmic expression:

$$\varepsilon^e{}_v = \kappa^* \cdot \ln \frac{p'}{p'_0} \tag{3.56}$$

with κ^* taken as a constant. With reference to equation (1.39), $\kappa^* = \kappa/\nu$, since the expression here is given in terms of volumetric strain, instead of specific volume.
The differential one is:

$$\varepsilon^e{}_v = \kappa^* \cdot \frac{dp'}{p'} = \frac{dp'}{K} \tag{3.57}$$

and imply the stress-dependency of the elastic bulk modulus:

$$K = \frac{p'}{\kappa^*} = \frac{p_{ref}}{\kappa^*} \cdot \frac{p'}{p_{ref}} = K_{ref} \cdot \frac{p'}{p_{ref}} = K(p') \tag{3.58}$$

Re-writing the constitutive law in terms of vertical stress, one obtains:

$$\varepsilon^{e}{}_{v} = \kappa^{*} \cdot \frac{dp'}{p'} = \kappa^{*} \frac{\frac{(v+1)\, d\sigma'_z}{3(1-v)}}{\frac{(1+2K_0)\sigma'_z}{3}} = \frac{1+v}{1-v} \cdot \frac{\kappa^{*}}{(1+2K_0)} \cdot \frac{d\sigma'_z}{\sigma'_z} \tag{3.59}$$

The slope in unloading-reloading path has a different value in oedometric conditions (C_c)and in isotropic compression (κ^{*}).
So then the value of compression index in unloading reloading phase, derived from a classical one-dimensional oedometer test, in terms of void ratio and 10 base logarithm has to be transformed to κ^{*} as put forward in Neher & Vermeer (1999):

$$\kappa^{*} = \frac{C_r}{\ln 10(1+e_0)} \frac{1-v}{1+v}\left(1+2K_0\right) \tag{3.60}$$

The creep index definition does not involve stresses, so that it can be defined in terms of natural logarithm of time and volumetric stress μ^{*}, once one knows the creep coefficient in terms of void ratio and 10 base logarithm (C_α):

$$\mu^{*} = \frac{C_\alpha}{\ln 10(1+e_0)}.$$

It is worthy of noting that, from a theoretical point of view, all the strains used in the model are Henky strains, so that, to be precise in the previous expressions the void ratio should be the current void ratio and not the initial value. In the following the superscript H will be omitted, for seek of simplicity. Once that the slope parameters are defined in terms of mean stress, it is possible to formulate the model in one-dimensional formulation, as it describes an isotropic compression.

Soft Soil creep model: genesis of one dimensional formulation

At the end of primary consolidation, the total elasto-plastic strain increment can be decomposed in an elastic part and a plastic part (Equation (1.23)), so that:

$$d\varepsilon_{v,eop} = d\varepsilon_v{}^{e}{}_{,eop} + d\varepsilon_v{}^{p}{}_{,eop} \tag{3.61}$$

As in the Cam Clay framework, elastic and plastic strain can respectively be expressed in differential terms as (see Equation (1.40) and Equation (1.49)):

$$d\varepsilon_v{}^{e}{}_{,eop} = \kappa^{*} \frac{dp'}{p'} = \frac{dp'}{K} \tag{3.62}$$

$$d\varepsilon_v{}^{p}{}_{,eop} = (\lambda^{*} - \kappa^{*}) \frac{dp'_{pc}}{p'_{pc}} \tag{3.63}$$

being the second the hardening rule.
In integral form the total strain due to an increase in effective stress from p'_0 to p' is:

$$\varepsilon_v = \varepsilon_v{}^{e}{}_{,eop} + \varepsilon_v{}^{p}{}_{,eop} = \kappa^* \ln \frac{p'}{p'_0} + (\lambda^* - \kappa^*) \ln \frac{p'_{pc,eop}}{p'_{pc0}} \tag{3.64}$$

Where p'_{pc0} and $p'_{pc,eop}$ represent the preconsolidation pressure corresponding to before-loading and end-of- consolidation states respectively.
After a time $t = t_{eop} + t'$ where t' is the pure creep time, the total strain will be:

$$\begin{aligned} \varepsilon_v &= \varepsilon_v{}^{e}{}_{,eop} + \varepsilon_v{}^{p}{}_{,eop} + \varepsilon_v{}^{creep} = \\ &= \kappa^* \ln \frac{p'}{p'_0} + (\lambda^* - \kappa^*) \ln \frac{p'_{pc,eop}}{p'_{pc0}} + \mu^* \ln \frac{\tau_c + t'}{\tau_c} \end{aligned} \tag{3.65}$$

where τ_c is the intrinsic time at the end of primary consolidation and it is called here *reference time* and t' is pure creep time.

The Soft Soil Creep model uses, as already mentioned, the intrinsic time concept, whose physical meaning is still under debate since there are no precise information a part from Janbu's method of experimental determination. In order to find an analytical expression for the quantity τ_c, the basic idea that all inelastic strains are time dependent is assumed: for non failure situations as met in oedometer loading conditions, an instantaneous plastic strain component is not postulated, as used, on the contrary, in traditional elasto-plastic modelling.

$$\varepsilon_v = \varepsilon_v{}^{e} + \varepsilon_v{}^{creep} = \varepsilon_v{}^{e} + \varepsilon_{v,eop}{}^{creep} + \varepsilon_v{}^{purecreep} \tag{3.66}$$

The three component are schematically illustrated in Figure 3.18.

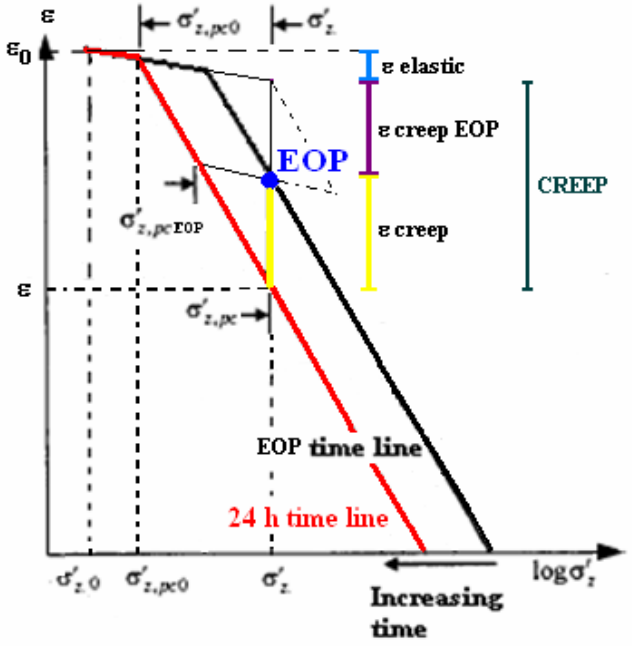

Figure 3.18: strain components in the stress- strain plane

At the same time the Bjerrum's idea that the preconsolidation stress depends entirely on the time dependent strain accumulated is adopted. The longer a soil sample is left to creep the larger the preconsolidation pressure grows.

The integrated form of the hardening rule thus becomes:

$$p'_{pc} = p'_{pc0} \exp\left(\frac{\varepsilon_v^{creep}}{\lambda^* - \kappa^*} \right) \tag{3.67}$$

where p'_{pc} is the preconsolidation pressure at the end of the elapsed time $t = t_{EOP} + t'$, and the differential expression is:

$$d\varepsilon_v^{creep} = (\lambda^* - \kappa^*) \frac{dp'_{pc}}{p'_{pc}} \tag{3.68}$$

Hence:

$$\varepsilon_v = \varepsilon_v^{e} + \varepsilon_v^{creep} = \kappa^* \ln \frac{p'}{p'_0} + (\lambda^* - \kappa^*) \ln \frac{p'_{pc}}{p'_{pc0}} \tag{3.69}$$

Equating equations (3.65) and (3.69), it results:

$$\varepsilon_v = \kappa^* \ln \frac{p'}{p'_0} + (\lambda^* - \kappa^*) \ln \frac{p'_{pc,eop}}{p'_{pc0}} + \mu^* \ln \frac{\tau_c + t'}{\tau_c} = \kappa^* \ln \frac{p'}{p'_0} + (\lambda^* - \kappa^*) \ln \frac{p'_{pc}}{p'_{pc0}} \tag{3.70}$$

thus obtaining:

$$\mu^* \ln \frac{\tau_c + t'}{\tau_c} = (\lambda^* - \kappa^*) \ln \frac{p'_{pc}}{p'_{pc,eop}} \tag{3.71}$$

In conventional oedometer testing the load is stepwise increased and each load steps is maintained for a constant period of time: $\tau = t_{EOP} + t' = 24h$ obtaining the so-called normal consolidation line (in this case isotropic consolidation line) with $p'_{pc} = p'$ by definition.

On assuming $p'_{pc} = p'$ and $t' = \tau - t_{EOP}$ in the previous equation, one obtains for OCR=1:

$$\mu^* \ln \frac{\tau_c + \tau - t_{EOP}}{\tau_c} = (\lambda^* - \kappa^*) \ln \frac{p'}{p'_{pc,eop}} \tag{3.72}$$

It is now assumed that $|\tau_c - t_{EOP}| << \tau$ so that this quantity can be neglected with respect to τ and it follows that:

$$\frac{\tau}{\tau_c} = \left(\frac{p'}{p'_{pc,eop}} \right)^{\frac{(\lambda^* - \kappa^*)}{\mu^*}} \tag{3.73}$$

so:

$$\tau_c = \tau \cdot \left(\frac{p'_{pc,eop}}{p'} \right)^{\frac{(\lambda^* - \kappa^*)}{\mu^*}} = \tau \cdot \left(OCR_{eop} \right)^{\beta} \tag{3.74}$$

with

$$\beta = \frac{\lambda^* - \kappa^*}{\mu^*} \tag{3.75}$$

Hence τ_c depends both on the effective stress p' and the end-of-primary preconsolidation pressure. In order to verify the assumption $\left|\tau_c - t_{eop}\right| << \tau$ it should be realized that usual oedometer samples consolidate for relatively short periods of less than one hour ($t_{eop} << \tau$). Considering loading steps on the normal consolidation line, OCR=1 both at the beginning and at the end of the load step.
During such a load step p'_{pc} increases from p'_{pc0} up to $p'_{pc,eop}$ during the short period of primary consolidation. Hereafter p'_{pc} increases further from $p'_{pc,eop}$ to p' during a relatively long creep period. Hence, a the end of the day the sample is again in a state of normal consolidation, but directly after the short consolidation period the sample is under-consolidated with $p'_{pc} < p'$.
The whole procedure is summarized in Figure 3.18.

For the usually very high ratios of $\beta = (\lambda^* - \kappa^*)/\mu^*$, τ_c results very small with respect to τ. It thus follows that the assumption $\left|\tau_c - t_{eop}\right| << \tau$ is certainly correct.

The differential creep equation can be formulated deriving the strain formulation with respect to time:

$$\dot{\varepsilon}_v = \dot{\varepsilon}_v^{\,e} + \dot{\varepsilon}_v^{\,creep} = \kappa^* \frac{dp'}{p'} + \frac{\mu^*}{\tau_c + t'} \tag{3.76}$$

in which $\tau_c + t'$ can be eliminated trough Equation (3.72) to obtain:

$$d\varepsilon_v = d\varepsilon_v^{\,e}{}_{,eop} + d\varepsilon_v^{\,creep} = \kappa^* \frac{dp'}{p'} + \frac{\mu^*}{\tau_c} \left(\frac{p'_{pc,eop}}{p'_{pc}} \right)^{\frac{(\lambda^* - \kappa^*)}{\mu^*}} \tag{3.77}$$

and remembering the expression of τ_c, one obtains:

$$\begin{aligned} & d\varepsilon_v = d\varepsilon_v^{\,e}{}_{,eop} + d\varepsilon_v^{\,creep} = \\ & = \kappa^* \frac{dp'}{p'} + \frac{\mu^*}{\tau} \left(\frac{p'}{p'_{pc}} \right)^{\frac{(\lambda^* - \kappa^*)}{\mu^*}} = \kappa^* \frac{dp'}{p'} + \frac{\mu^*}{\tau} \left(\frac{1}{OCR} \right)^{\frac{(\lambda^* - \kappa^*)}{\mu^*}} \end{aligned} \tag{3.78}$$

in which the viscous strain rate is governed by the inversed of OCR, here expressed in terms of effective mean stress.

Soft Soil Creep model: about OCR, strain rate and reference time

The Soft Soil Creep model accounts for the main creep characteristics pointed out in the last 50 years. The integrated expression for pure creep strain (constant effective stress) is given in Equation (3.79):

$$\varepsilon_v^{creep} = \mu^* \ln \frac{\tau_c + t'}{\tau_c} = \mu^* \ln\left(1 + \frac{t'}{\tau_c}\right) \tag{3.79}$$

Similarly to Modified Cam Clay (Schofield and Wroth, 1958, Roscoe and Burland, 1968), evolution of preconsolidation pressure against creep strain is assumed as:

$$p'_{pc} = p'_0 \exp\left(\frac{\varepsilon_v^{creep}}{\lambda^* - \kappa^*}\right) \tag{3.80}$$

The result is a model belonging to the isotaches' family in which the preconsolidation ratio plays a very important role.

$$\dot{\varepsilon}_v^{creep} = \frac{\mu^*}{\tau}\left(\frac{p'}{p'_{pc}}\right)^{\frac{(\lambda^* - \kappa^*)}{\mu^*}} = \frac{\mu^*}{\tau}\left(\frac{1}{OCR}\right)^{\beta} = \frac{\mu^*}{\tau_c + t'} \tag{3.81}$$

For typical soil values, the exponent β ranges between 20 and 30. The high influence of OCR on the creep rate is shown in Figure 3.19.It is clear that creep rate becomes negligible for OCR above unity.

OCR	$\dot{\varepsilon}^c$
1.0	$\dot{\varepsilon}_{nc}$
1.3	$\dot{\varepsilon}_{nc} \cdot 10^{-3}$
1.7	$\dot{\varepsilon}_{nc} \cdot 10^{-6}$

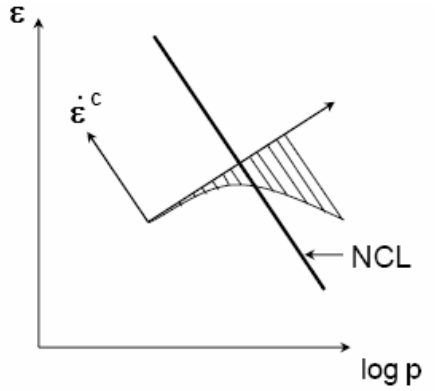

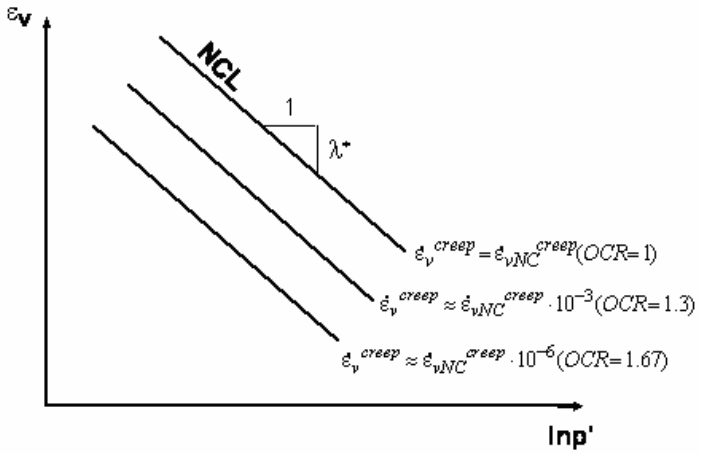

Figure 3.19: variation of the creep rate with OCR (after Vermeer et al., 2006)

As regard to the creep rate during the primary consolidation, he previous expression will become:

$$\dot{\varepsilon}_v^{creep}\Big|_{primary} = \frac{\mu^*}{\tau}\left(\frac{p'}{p'_{pc,eop}}\right)^{\frac{(\lambda^*-\kappa^*)}{\mu^*}} = \frac{\mu^*}{\tau}\left(\frac{1}{OCR_{eop}}\right)^{\beta} \tag{3.82}$$

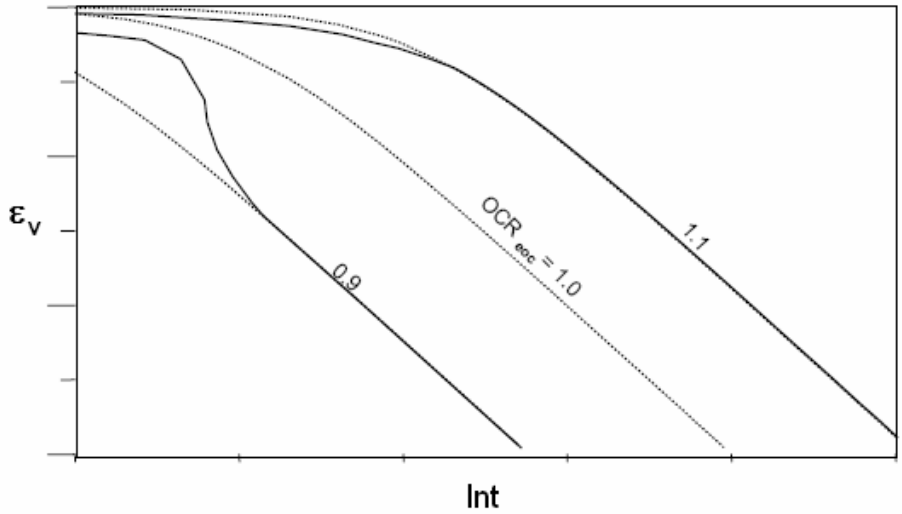

Figure 3.20: creep rate during consolidation (Vermeer, 2006)

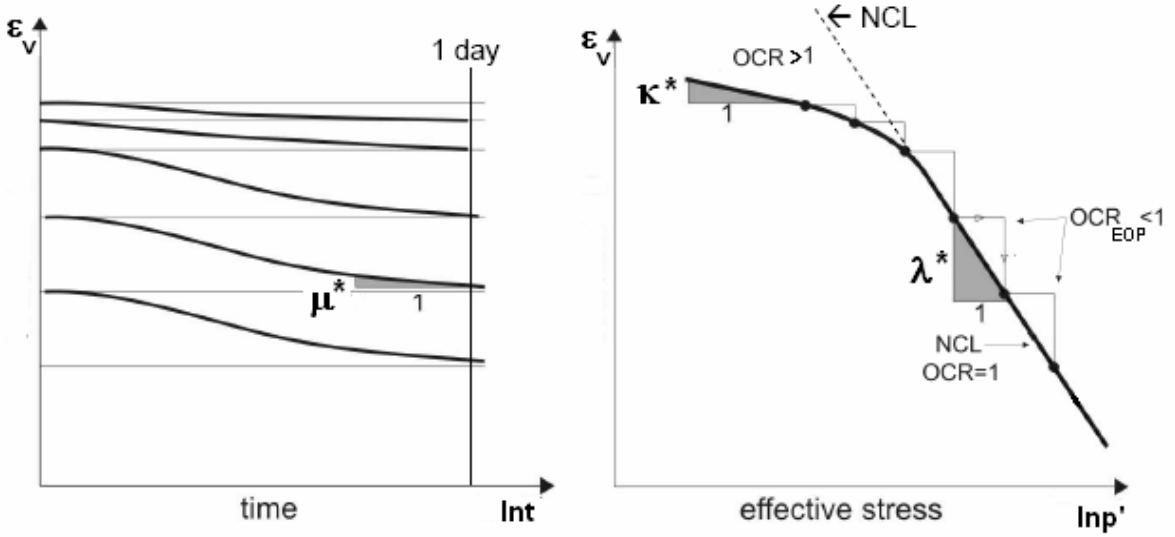

Figure 3.21: standard oedometer test: different final slopes for different OCR values (after Vermeer et al., 2006)

The reference time τ_c depends completely on the initial state of overconsolidation, in particular on the end-of-primary-consolidation OCR_{eop} :

$$\tau_c = \tau \cdot \left(\frac{p'_{pc,eop}}{p'}\right)^{\frac{(\lambda^*-\kappa^*)}{\mu^*}} = \tau \cdot \left(OCR_{eop}\right)^{\beta} \tag{3.83}$$

Since it is involved in the creep expression, it is responsible for the different behaviour of OC samples and NC sample. τ_c

The slope of the final part of the strain-time curve in semi-logarithmic plane (i.e. C_α, here μ^*) depends on stress state, i.e. it depends on OCR (see Figure2.16 and Figure 2.17).

In Soft Soil Creep model only one is the value to be chosen for μ^*, but, thanks to the OCR_{eop} dependency of τ_c the slope of the final part of $\varepsilon_v - \ln t$ curves varies with OCR in the overconsolidated range, as shown in Figure 3.21.

Considering an overconsolidated soil sample being stepwise recompressed: during recompression the sample is in a state of overconsolidation with $OCR_{EOP}>1$ (and also, by definition, $OCR>1$).
As a consequence the reference time $\tau_c = \tau \cdot \left(OCR_{EOP}\right)^{\beta}$ has a very high value, so that in general for OC sample $t' << \tau_c$. In this case the strain rate becomes:

$$\frac{\varepsilon_v^{creep}}{dt} = \frac{\mu^*}{\tau_c + t'} \approx \frac{\mu^*}{\tau_c} \tag{3.84}$$

In OC states, on a usual time scale with $t' << \tau_c$, as relevant in laboratory testing, soils show a very small nearly constant creep rate.

Since:

$$\frac{d\varepsilon_v^{creep}}{dt} = \frac{d\varepsilon_v^{creep}}{d\ln t} \cdot \frac{d\ln t}{dt} = \frac{d\varepsilon_v^{creep}}{d\ln t} \cdot \frac{1}{t} \tag{3.85}$$

it results that the slope of the strain time curve in semi-logarithmic scale is very small for overconsolidated soil for $t' << \tau_c$:

$$\frac{\varepsilon_v^{creep}}{d\ln t} = \mu^* \frac{t'}{\tau_c + t'} \approx 0 \tag{3.86}$$

In soil mechanics it has been often suggested that even overconsolidated clays show logarithmic creep, but this is only true in a very large time scale. In fact, whenever $t' >> \tau_c$ Equation (3.86) reads:

$$\frac{\varepsilon_v^{creep}}{d\ln t} = \mu^* \frac{t'}{\tau_c + t'} \approx \mu^* \tag{3.87}$$

In other words, if the creep time is enough long to overcome the time reference τ_c, even overconsolidated sample has a slope equal to μ^* in semi-logarithmic scale.

As for NC condition, in standard oedometer tests, samples are recompressed until the normalconsolidation line is reached. The load is then increased beyond the NC-line and the sample is left to consolidate and creep back to the NC-line, as indicated in Figure 3.21.

The NC-line is by definition traced linking all the stress-strain states at the end of an incremental testing load. As oedometer samples are relatively thin, consolidation is generally fast and most of the deformation occurs at a constant effective stress. During such a creep period, the overconsolidation ratio increases from the low initial value of $OCR_{eop} < 1$ at the end of consolidation up to $OCR = 1$. In a standard 24-hour incremental test the load is daily doubled so that $OCR_{eop} = 0.5$.

In such a situation $\tau_c = \tau \cdot \left(OCR_{eop}\right)^{\beta}$ is extremely small and the testing is done on a time scale with $t' >> \tau_c$ .In this case (as for OC states but with very high creep time) :

$$\frac{\varepsilon_v^{\,creep}}{d\ln t} = \mu^* \frac{t'}{\tau_c + t'} \approx \mu^* \tag{3.88}$$

the volumetric strain increases linearly with $\ln t$ with slope μ^*, so that the creep index can directly measured from load steps in the normally consolidated range.

In conclusion, the Soft Soil Creep model takes into account the different slopes that soil shows at different OCR values for the same creep time. though being a model with constant value of the creep index.

This is due to the definition of time reference τ_c that involves OCR_{eop} . The higher OCR_{eop} , the larger is τ_c , thus giving a smaller slope for a fixed creep time, as presented in Figure 3.22.

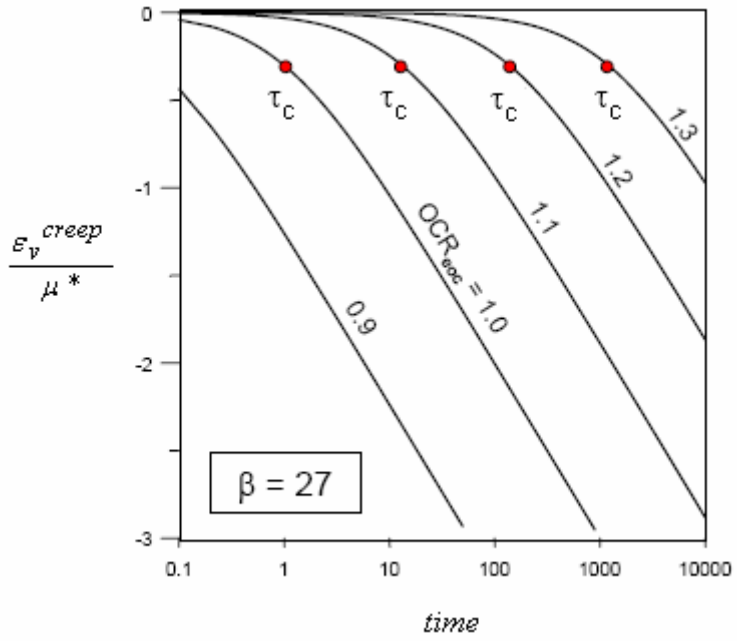

Figure 3.22: time reference connection with OCR at the end of primary consolidation (Vermeer, 2006)

The Soft Soil Creep model is, indeed, a model based on the isotache approach. The creep strain rate is given by Equation (3.81) where τ is another reference time parameter, strictly linked with $\tau_c = \tau \cdot \left(OCR_{eop}\right)^{\beta}$ (Equation (3.83)),that relates to the definition of the NC

surface. The usual definition of this surface implies $\tau = 1$.Substituting Equation (3.83) in OCR definition:

$$OCR^{\beta} = \left(\frac{p'_{pc}}{p'}\right)^{\beta} = \left(\frac{p'_{pc}}{p'_{pcEOP}}\right)^{\beta} \cdot \left(\frac{p'_{pcEOP}}{p'}\right)^{\beta} = \\ = \frac{\tau_c + t'}{\tau_c} \cdot OCR_{EOP}{}^{\beta} = \frac{\tau_c + t'}{\frac{\tau_c}{OCR_{EOP}{}^{\beta}}} = \frac{\tau_c + t'}{\tau} \tag{3.89}$$

it results:

$$OCR = \left(\frac{\tau_c + t'}{\tau}\right)^{1/\beta} \tag{3.90}$$

For normally consolidated states, τ_c is very small and the expression simplifies in:

$$OCR \approx \left(\frac{t'}{\tau}\right)^{1/\beta} \tag{3.91}$$

Load is increased every 24 hours and consolidation takes typically so little time that the creep time t' can be taken as $t' = 1day$. Substituting $OCR = 1$, $t' = 1$ one obtains $\tau = 1$.

With reference to a standard oedometer test, the creep strain rate once the stress-strain state is back on the NC- line will be:

$$\dot{\varepsilon}_v{}^{creep} = \frac{\mu^*}{\tau}\left(\frac{1}{OCR}\right)^{\beta} = \mu^* \tag{3.92}$$

Final states of an oedometer tests (reported on the compression plane) can be interpreted as an isotache with rate μ^*. Oedometer tests may also be carried out with 12 or 48 hours load steps, for example, to find somewhat shifted NC-lines with $\tau = 12h$ or $\tau = 48h$.

Consider an extreme case in which $\tau = 1s$ and compare to the standard oedometer test with $\tau = 1day$. They will have different final creep strain rates thinking of them as two different odeometer test ending both on the NC-line (i.e. $OCR = 1$ for both of them):

$$\dot{\varepsilon}_v{}^{creep}\Big|_{1s} = \frac{\mu^*}{1s} > \dot{\varepsilon}_v{}^{creep}\Big|_{1day} = \frac{\mu^*}{1day} \tag{3.93}$$

It is well-known from the isotaches theory that lower strain rate (more time testing for each step) corresponds to lower preconsolidation pressure because the isotache line is shifted towards left in the stress-strain plane, and consequently the NC line corresponds to an higher OCR value.

To compare OCR values in this framework it is necessary to equate strain rates thus getting the relationship between the two OCR values. It a sort of tricky thing because it is necessary to overcome the strain dependency of τ, described in the following.
On will get:

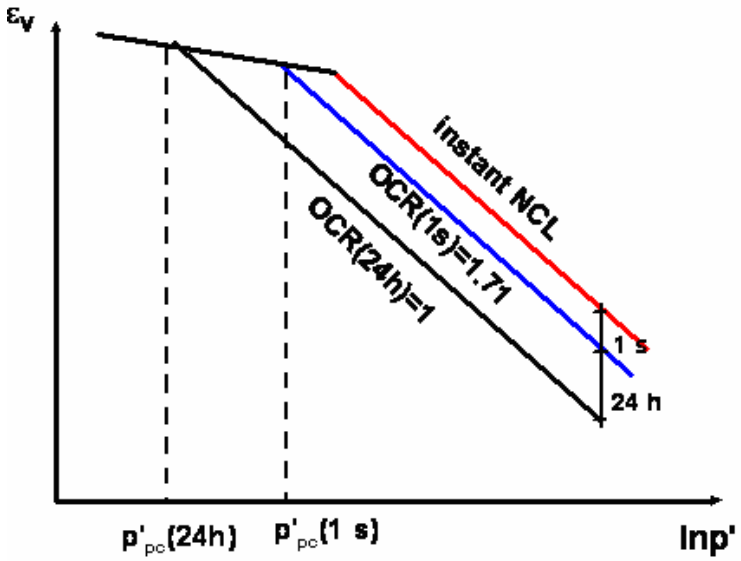

Figure 3.23: OCR referred to different reference time values

$$\frac{\mu^*}{\tau_{1s}}\left(\frac{1}{OCR_{1s}}\right)^{\beta}=\frac{\mu^*}{\tau_{1day}}\left(\frac{1}{OCR_{1day}}\right)^{\beta}\Rightarrow\left(\frac{1}{OCR_{1s}}\right)^{\beta}=\frac{\tau_{1s}}{\tau_{1day}}\left(\frac{1}{OCR_{1day}}\right)^{\beta} \tag{3.94}$$

In this special case (with $\beta=21$) one gets: $OCR_{1\,\mathrm{sec}}=1.718\cdot OCR_{1day}$.

The faster oedometer test shows and higher OCR, i.e. an higher preconsolidation pressure value, as reported in Figure 3.21.

Parameters' values to be used, have to be referred to a creep test in which each stage lasts τ. So, implicitly, if $\tau=1s$, μ^*,λ^*,κ^* have to be deduced from an oedometer test with loading steps lasting 1 s.

Instead of defining the normal-consolidation line of a particular soil on the basis of a multi-stage loading test, one may use a constant rate of strain test, in fact the result is a curve that resembles the multi-stage test one. many cases CRS are done relatively fast and the results overshoot the NC-line from a 24 hour test, as can be seen in Figure 3.24. However, any CRS test line can be adopted as NC-line, provided that an appropriate reference time τ is assigned to this line.

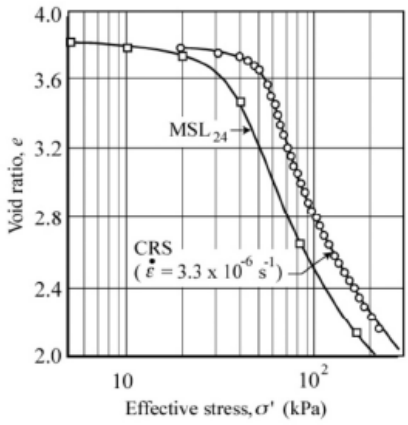

Figure 3.24: comparison between stress-strain curves obtained in conventional 24h test and CRS oedometer test (Hanzawa, 1989)

Remembering Equation (3.69) and that on the NC-line: $dp'/p' = dp'_{pc}/p'_{pc}$ it follows that:

$$\dot{\varepsilon}_v^e = \frac{\kappa^*}{(\lambda^* - \kappa^*)} \dot{\varepsilon}_v^{creep} \Rightarrow \dot{\varepsilon}_v = \frac{\lambda^*}{(\lambda^* - \kappa^*)} \dot{\varepsilon}_v^{creep} = \frac{\lambda^*}{(\lambda^* - \kappa^*)} \cdot \frac{\mu^*}{\tau} \left(\frac{1}{OCR} \right)^{\beta} \quad (3.95)$$

On the NC-line $OCR = 1$ so that:

$$\dot{\varepsilon}_{v,NC} = \frac{\lambda^*}{(\lambda^* - \kappa^*)} \cdot \frac{\mu^*}{\tau} = \frac{\lambda^*}{\beta} \cdot \frac{1}{\tau} \quad (3.96)$$

so, knowing the creep rate (i.e. the total strain rate, because elastic strain are time independent), one may compute the corresponding reference time:

$$\tau = \frac{\lambda^*}{\beta} \cdot \frac{1}{\dot{\varepsilon}_{vNC}} \quad (3.97)$$

Soft Soil Creep model: three-dimensional formulation

To extend the one-dimensional formulation to a three dimensional one, modified Cam Clay ellipses are considered as creep potentials.

$$p' - p' p_{pc} + \frac{q^2}{M^2} = 0 \quad (1.43)$$

What in the one-dimensional formulation is represented by the preconsolidation pressure, here is represented by the whole ellipse (see Figure 3.25).

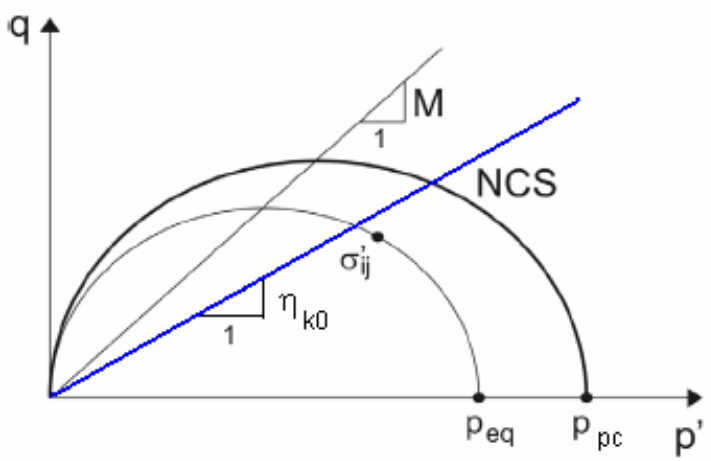

Figure 3.25: modified Cam Clay ellipse

The model, indeed, deviates from the modified Cam Clay one in the sense that there is not truly elastic domain inside the ellipse, as in the one-dimensional formulation creep can occur even for overconsolidated states.
Well below the NC- surface the creep rate is negligible, as previously pointed out, but just below this surface the creep rate is significant.
Moreover, unlike modified Cam Clay model, stresses may exceed the NC surface, so that it is not a yield locus in the sense of plasticity. The same happens in one-dimensional formulation whenever load is increased and the stress-strain states overshoots the NC-line since it reaches again, creeping.
Overall, considering that strain rates are very high around the NC surface and negligible well below, this surface creates the effect of a yield surface even if it is not.

The one-dimensional constitutive law, given for isotropic compression, is still valid in the three-dimensional domain, but it has to be applied to a scalar quantity that represents the vertex of the ellipse:

$$p_{eq} = p' + \frac{q^2}{M^2 p'} \tag{3.98}$$

where $M = 6\sin\varphi / 3 - \sin\varphi$ is the slope of the critical state line in the invariant plane.

Using p_{eq} stress measure it is a way to project a general stress state (p', q) to the isotropic axis, and in this way it is possible to bring a bi-dimensional problem back to a one-dimensional one. This projecting procedure allows also to say if a soil element is overconsolidated whether $p_{eq} < p_{pc}$ if it is "underconsolidated" whether $p_{eq} > p_{pc}$ or if it is normally consolidated whether $p_{eq} = p_{pc}$ (see Figure 3.25).

The volumetric component of the creep strain is thus defined using the one-dimensional formulation referred to the equivalent stress. The deviatoric part of the problem has to be taken into consideration apart.

In the special case of oedometric conditions the relation between the mean stress and the deviatoric stress is constant (see Figure 3.25):

$$\eta_{k0} = \left.\frac{q}{p}\right|_{\varepsilon_r = 0} = \frac{(1-K_0)}{(1+2K_0)} \tag{3.99}$$

so that the equivalent stress assumes the following expression:

$$p_{eq} = p' + \frac{(\eta_{k0} p')^2}{M^2 p'} = p'\left(1 + \left(\frac{\eta_{k0}}{M}\right)^2\right) \tag{3.100}$$

As in classical elasto-plasticity the three-dimensional model has a flow rule giving the 'direction' of the creep strain rate. Similarly to the modified Cam Clay model associated plasticity is assumed and ellipses are thus taken as plastic potential surfaces:

$$d\varepsilon_v{}^c = d\lambda \frac{\partial p_{eq}}{\partial p'} = 1 - \frac{q^2}{M^2 p'^2} \tag{3.101}$$

$$d\varepsilon_q{}^c = d\lambda \frac{\partial p_{eq}}{\partial q} = \frac{2q}{M^2 p'} \tag{3.102}$$

so that the deviatoric creep strain is equal to:

$$d\varepsilon_q{}^c = d\varepsilon_v{}^c \frac{\partial p_{eq}/\partial q}{\partial p_{eq}/\partial p'} = d\varepsilon_v{}^c \frac{2(q/p')}{M^2 - (q/p')^2} \tag{3.103}$$

For the case of oedometric condition it gives:

$$d\varepsilon_q{}^c = d\varepsilon_v{}^c \frac{\partial p_{eq}/\partial q}{\partial p_{eq}/\partial p'} = d\varepsilon_v{}^c \frac{2\eta_{k0}}{M^2 - \eta_{k0}{}^2} \tag{3.104}$$

Just like the modified Cam Clay model, the creep model involves dilation and associated softening for stress states on the dry side (left of the intercept of the critical state line).
In numerical analysis softening cannot easily be simulated, so in order to avoid such difficulties the dry side of critical state is modelled by a Mohr Coulomb failure surface, introducing two extra constant so far (c', φ).
This solution for modelling the shear strength also allows to have two different M values: one referred to the failure criterion $M_{MC} = 6\sin\varphi/3 - \sin\varphi$ and another M_{NCS} used to define the yield surface in order to best represent one-dimensional compression.
The phenomenon that for normally consolidated soils the at rest coefficient K_0 decreases with increasing internal friction is well-known and clearly expressed in Jaky's formula: $K_0 = 1 - \sin\varphi$. The increase of K_0 is incorporated in the Cam Clay model, throughout the expression: $K_0 \approx \frac{1.6 - 0.2M}{1+M}$, but the predicted values are generally too large compared to Jaky's formula. In order to get better K_0 values, larger values of M should be used, but this would imply too large shearing strength. Having two M values is therefore possible to use one

of them to model the shear strength (M_{MC}) and the other can be chosen such that the model predicts proper values for the coefficient of lateral earth pressure (M_{NCS}).
As a consequence $M_{NCS} > M_{MC}$ so the normal consolidation ellipse is relatively steep (see Figure 3.26).

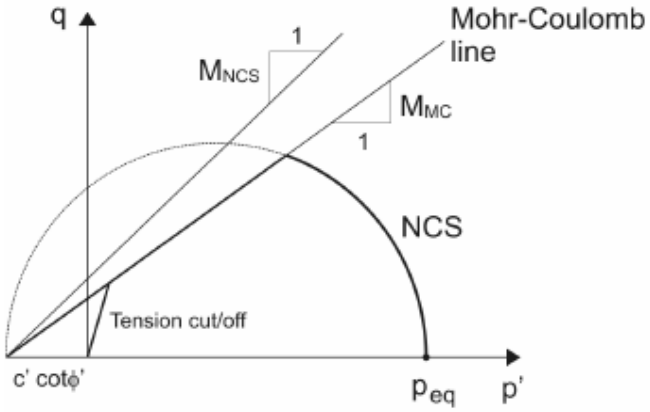

Figure 3.26:NC ellipses with M_{NCS}, Mohr Coulomb failure with M_{MC} (Vermeer et al., 2006)

Similarities and differences with Overstress Model

The Soft Soil Creep model has the characteristic to admit stress states beyond the yield surface, because, as above mentioned, the normal-consolidation surface is not properly a yielding surface, in fact creep plastic strains occur also inside.

The invalidity of the consistency rule is a key assumption also for time-dependent models belonging to the overstress theory, among which the most known is the Perzyna's Overstress model.
In this framework viscous effects are negligible in the elastic region, i.e. no viscous strains occur within the static yield surface f_s, which corresponds to the traditional yield surface associated with time-independent plasticity.
This is the first difference with respect to the Soft Soil Creep model, on the other hand there is also a similarity: in overstress theory while elastic strains are time-independent, all inelastic strain are time dependent and represent combined viscous and plastic effects:

$$\dot{\varepsilon}_{ij} = \dot{\varepsilon}_{ij}^{\,e} + \dot{\varepsilon}_{ij}^{\,vp} \tag{3.105}$$

A huge difference between Soft Soil Creep model and Overstress approach is the presence in the latter of a second dynamic yield function f_d where the current stress state is located on.
In fact while the elastic strain is assumed to obey the generalized Hooke's law, the visco-plastic strain rate is assumed to obey a non-associated flow rule that is a function of the overstress function F:

$$\dot{\varepsilon}_{ij}^{\,vp} = \gamma \cdot \Phi(F) \cdot \frac{\partial g}{\partial \sigma'_{ij}} \tag{3.106}$$

where γ is a viscosity parameter, g the potential function, Φ the viscous nucleus and F is the overstress function.
This latter function F gives the 'distance' between the static yield surface f_s and the current stress state located on the dynamic loading surface f_d :

$$F = F(\sigma'_{ij}, W^{vp}) = \frac{f_d(\sigma'_{ij}, W^{vp})}{\kappa_s(W^{vp})} - 1 \tag{3.107}$$

where κ_s is the hardening parameter. Whenever $F = 0$ the current stress point is on the static yield surface and since in this case $\kappa_s = f_d$, κ_s has to be an expression for the static yield surface f_s.
Since inside the static yield surface there are no visco-plastic strains, the viscous nucleus has to follow the loading criterion:

$$\Phi(F) = 0 \; for F \le 0 \tag{3.108}$$

$$\Phi(F) = \Phi(F) \; for F > 0 \tag{3.109}$$

The direction of $\dot{\varepsilon}_{ij}^{vp}$ is normal to the potential surface g at the current stress point P, as shown in Figure 3.27, in which are summarized the main characteristics of the overstress approach.

The aim of this brief description of the Overstress model is to point out the huge differences between it and the Soft Soil Creep model, even though both do not respect the consistency rule and allow stress state beyond the yielding surface.
In the Overstress approach this is possible thanks to a second surface that describes visco-plastic behaviour with non- associative flow rule.
In Soft Soil Creep model indeed the yielding surface is not properly a yielding surface as theoretically viscous strains are allowed also inside, even though they are small. It is however use as it were a yielding surface, with an associative flow rule.

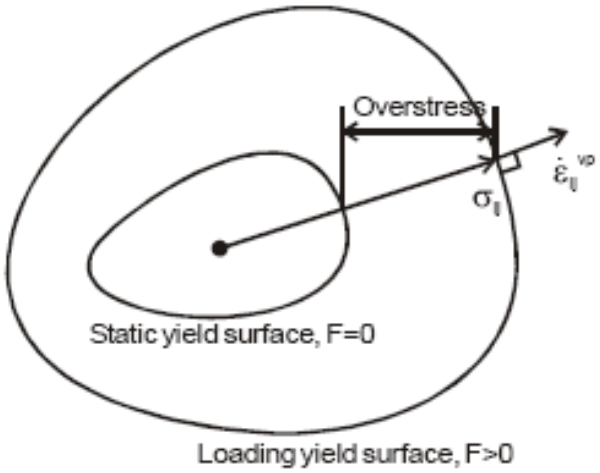

Figure 3.27:Perzyna's overstress concepts

Chapter 4 - Small Strain Stiffness

"Small is beautiful"

This is the fascinating title of the Ninth Bjerrum Memorial Lecture, held by Burland in 1989.

Since the 1970's or even earlier in fact, one of the major problems in ground engineering was the apparent difference between the stiffness of soils measured in laboratory tests and those back-calculated from observations of grounds movements. As reported for the creep theories as well, the most important thing is always to understand how to use information got from laboratory test when dealing with field situations, which scale one need to use.

Now it has been largely acknowledged that the stress-strain behaviour of soil is highly non-linear and soil stiffness may decay with strain by orders of magnitude. This means that for geotechnical structures such as foundations or a retaining walls etc. soil stiffness varies both with position and with loading.

The following figure illustrates a typical stiffness-strain curve for a soil; at small strains the stiffness is relatively large, while at strains close to failure the stiffness is small: this is soil behaviour being not linear. Figure 4.1 includes typical ranges of strain for laboratory testing and for structures.

Generally strains in the ground vary from zero, far away from the structure, to relatively large values near the structure, being a typical characteristic strain in the ground around 0.1 % (Atkinson, 2000). This represents also the smallest strain that can be measured reliably in conventional soil tests. This value is thus considered as a limit beyond which one deals with *large strains*, while strains smaller than 0.1% are defined *small strains*.

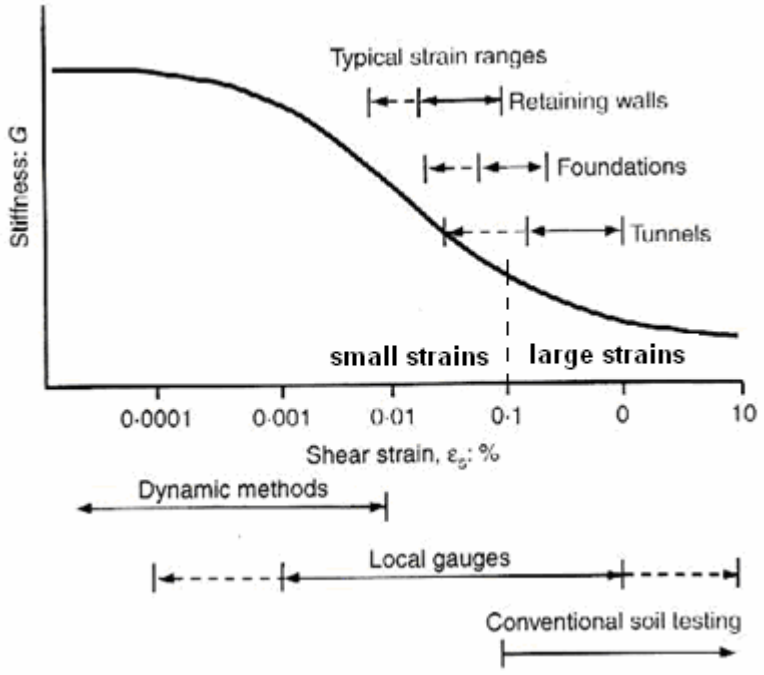

Figure 4.1:characteristic stiffness-strain curve for a soil (Atkinson, 2000)

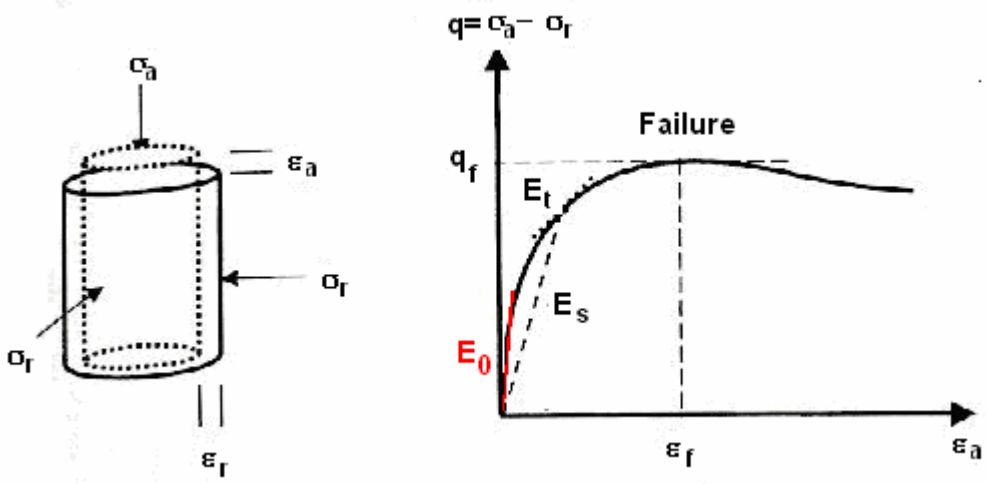

Figure 4.2: triaxial test-definition of secant and tangent stiffness (Atkinson, 2000)

Considering a triaxial test performed on a cylindrical sample as reported in Figure 4.2: on loading the stress-strain curve shows a non-linear behaviour.

The relationship between axial strain and deviatoric strain, is expressed through Young's modulus E:

$$\frac{\partial \sigma_a}{\partial \varepsilon_a} = E = \frac{\partial q}{\partial \varepsilon_a} \tag{4.1}$$

The sample fails at peak deviator stress q_f and at an axial strain ε_f. The stiffness can be defined as a secant stiffness E_s, always considering strain and stress increments from the origin, or a s a tangent stiffness E_t.The stiffness at very small strains, just near the start of loading it is indicated as E_0.Tangent and secant Young's moduli vary with strain as illustrated in Figure 4.3.

In the very small strain region the stiffness is approximately constant and it holds: $E_s = E_t = E_0$. This value is called *initial* or *maximum small strain stiffness*, or again, *very small strain stiffness*.

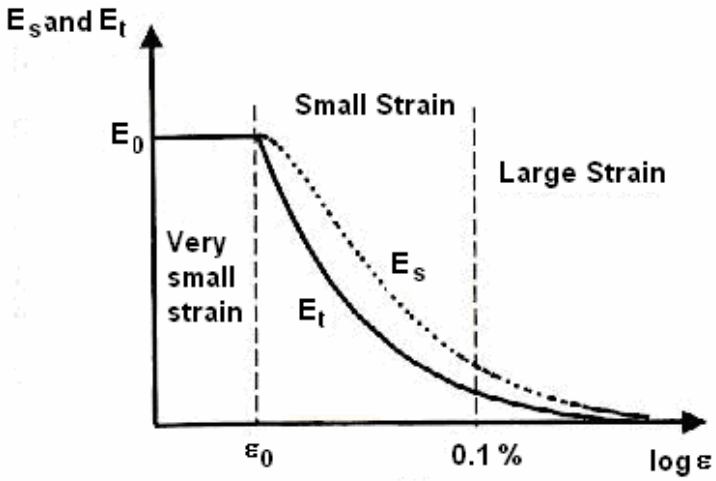

Figure 4.3: evolution with strain of secant and tangent stiffness (Atkinson, 2000)

This region is bounded by a strain ε_0. In this region, soil behaviour is often considered truly linear elastic.

For reconstituted soils the strains at which the stiffness start to decrease (ε_0) varies with plasticity from about 0.001% for low plasticity soils to about 0.01% for plastic clays (Viggiani et Atkinson, 1995). There is then a large strain region beyond 0.1% within which the stiffness is relatively small. At strains exceeding about 1% the stiffness in typically an order of magnitude less than the maximum, and it continues to decrease as the state approaches failure. In the intermediate small strain range the stiffness decreases smoothly with increasing strain. Strains in the ground near structures in stiff soils are generally in the small strain and very small strain regions. (Burland, 1989).

As regard to stiffness moduli, the secant modulus E_s continues to decrease gradually but remains positive even beyond the peak deviator stress while the tangent modulus E_t is zero at failure and then becomes negative as soil softens. In Figure 4.4 an example of secant and tangent stiffness reduction on London clay is given (after Jardine et al., 1991)

In general the degradation curve, as in Figure 4.4, is given in terms of shear modulus and shear strain: $G-\gamma_s$ where $\gamma_s = \varepsilon_a - \varepsilon_r = \frac{3}{2}\varepsilon_q$.If one plotted triaxial data in ε_q and q strain-stress space, tangent stiffness modulus thus is $dq/d\varepsilon_q = 3G$.

It is possible to observe a reduction in soil stiffness, also in unloading-reloading cycles: at the very beginning of loading direction change soil exhibits very stiff behaviour, and then stiffness reduces until the loading direction is changed again. In cyclic loading conditions, the stress-strain relation becomes thus an almost closed, long, narrow loop called *hysteresis loop* (see Figure 4.5).

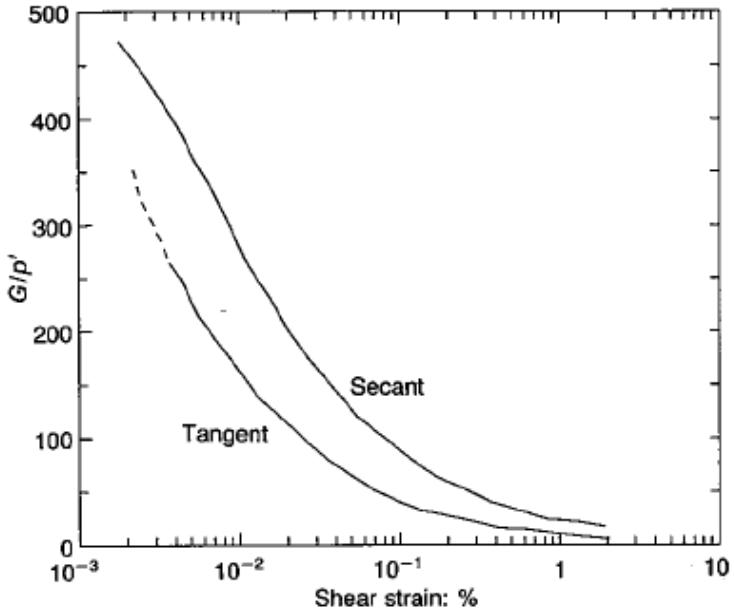

Figure 4.4: stiffness reduction curve from triaxial tests on London clay (after Jardine et al., 1991)

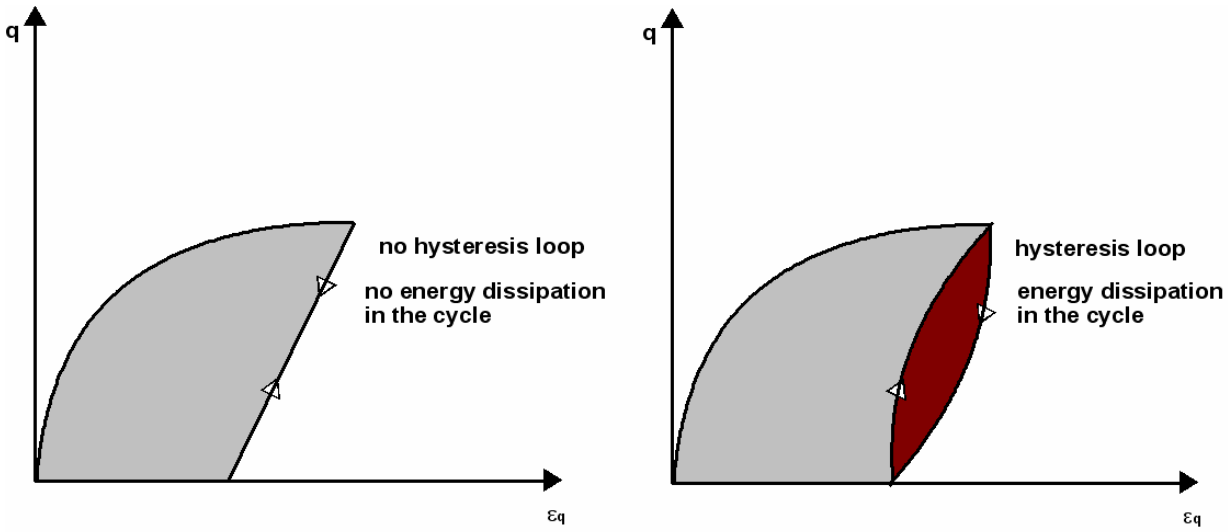

Figure 4.5: energy dissipation in closed cycles

While in case of no hysteresis, there is no energy dissipation in closed load cycles, in case of hysteresis there is irrecoverable energy dissipation, so the behaviour in unloading-reloading path cannot be considered as hyper-elastic.
In soil dynamics, the decay of small strain stiffness with applied strain is usually quantified as *damping*. Damping is in fact a measure for energy dissipation in closed load cycles.

In Figure 4.6 a triaxial test with several unloading-reloading cycles is reported (Benz, 2008). It can be noticed that hysteresis vanishes when reducing the amplitude of the unloading-reloading cycles, i.e. when dealing with very small strain stiffness. Hence an almost truly elastic response is only obtained for very small loops. The truly elastic stiffness is called *very small strain stiffness*. Just at the very beginning of the reduction curve the stiffness modulus can be realistically considered as an elastic stiffness. This confirms the high non-linearity of soil behaviour.

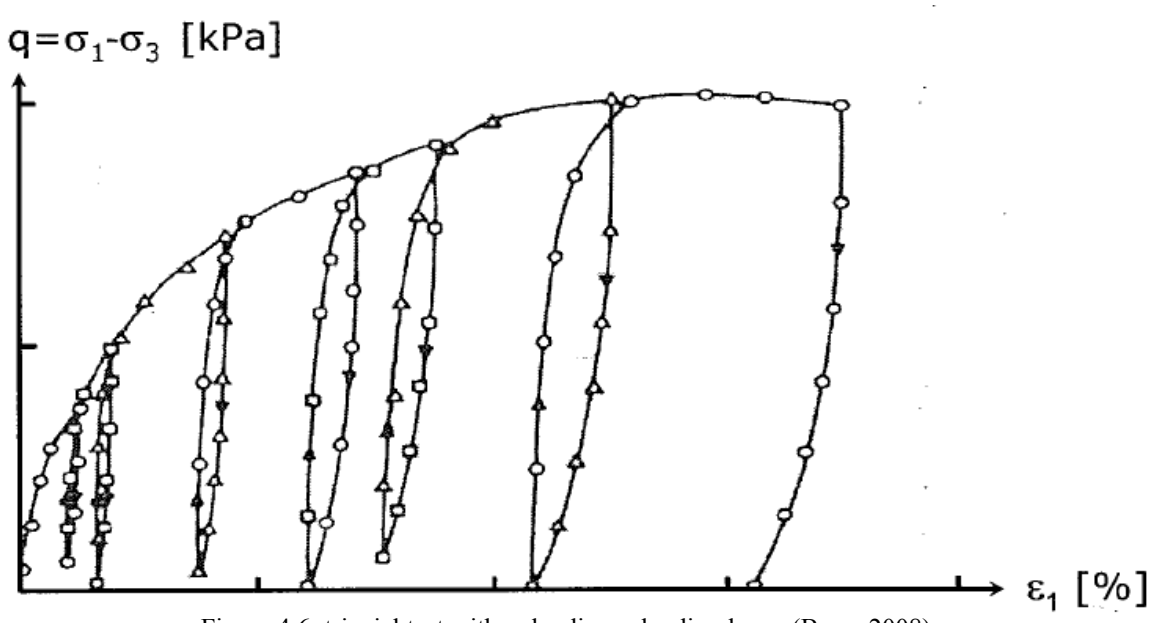

Figure 4.6: triaxial test with unloading-reloading loops (Benz, 2008)

Measurements of stiffness at very small strain

Figure 4.7 shows a characteristic stiffness strain curve for soil with the three regions defined by Atkinson and Sallfors (1991) depending on strains' order of magnitude and at the same time shows the different laboratory equipment and test procedures best able to measure stiffness in each region.
At strain in excess of about 0.1% secant stiffness can be measured with reasonable accuracy in triaxial tests using displacement gauges mounted in the conventional manner outside the cell. Axial strain is then calculated from the relative movement between the apparatus' top cap and its fixed base.

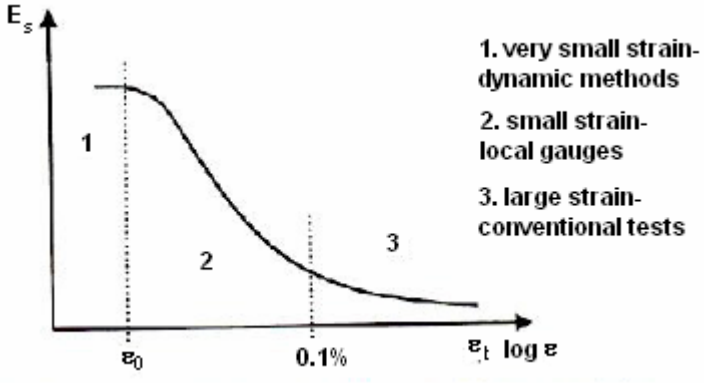

Figure 4.7: measurement of soil stiffness depending on the strain's order of magnitude

The accuracy of measurement can be improved by reducing the bedding, seating and misalignment errors. Reliable measurement of soil stiffness throughout the small strain region from strains of about 0.001% up to about 0.1 % can really only be made using local gauges attached directly to the sample or resonant column tests, etc. If measurements of strain are made outside the cell, the corrections to account for the errors are often greater than the strain being measured, local gauges operating in water or oil are, on the contrary, quite stable and accurate. They cannot completely eliminate the effect of bedding restraint though (Jardine, 1984). Local displacement transducers can resolve strains up to 0.0001% which, for many soils, can be considered very small strains .

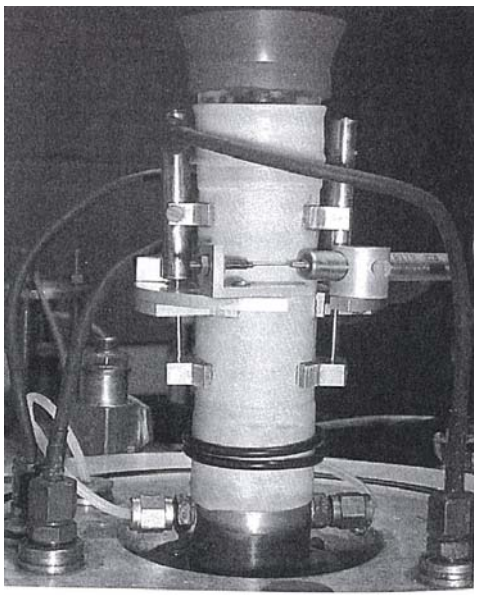

Figure 4.8: example of local gauges (Atkinson, 2000)

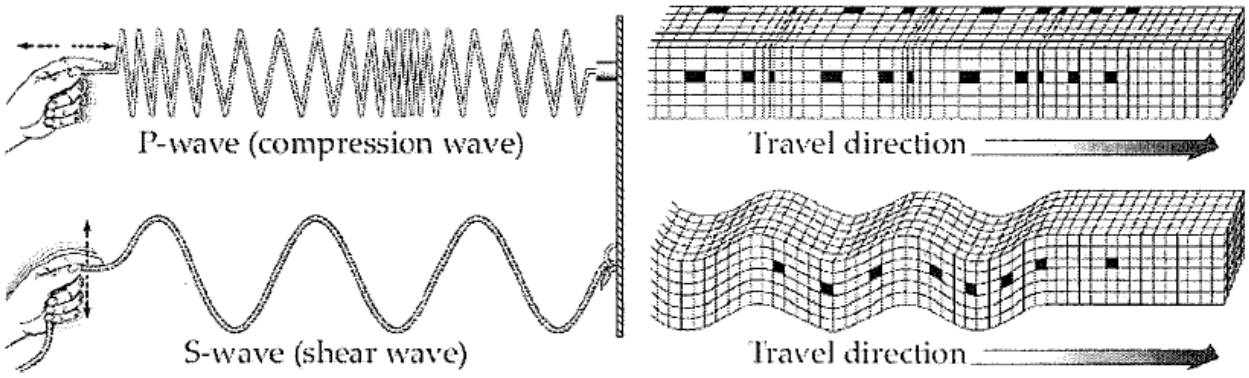

Figure 4.9: S-waves and P- waves (Benz, 2006)

An alternative to the use of local transducers in small-strain measurements is the use of dynamic methods. Dynamic soil tests are typically indirect tests in which one measures other quantities than those desired. Afterwards, measured results are elated to the desired ones through mathematical relationships.

Seismic techniques, for example, are indirect testing methods. Here very small strain stiffness is related to wave propagation velocity .Classically, velocities of elastic body waves in form of P- and S- waves are analyzed. P waves and S waves have different particles motions: P waves are in fact not polarized, particle motion is in the direction of propagation S waves can be polarized as they have transverse particle motion. (See Figure 4.9).

The shear modulus G of a material relates to the velocity V_s of an elastic shear wave through the theory of elasticity:

$$G = \rho V_s^{\,2} = \frac{\gamma}{g} V_s^{\,2} \tag{4.2}$$

where ρ is density, γ is unit weight and g is the acceleration gravity. The strains generated by the passage of a shear wave will be very small, generally less than 0.001%, so that the shear modulus calculated by means of this equation will be the initial shear modulus G_0. Being G_0 a truly elastic parameter, for an isotropic soil it holds: $E_0 = G_0(1+2\nu)$.

Directly measured in this test is the wave propagation velocity. This can be done both in laboratory tests and in field tests. In laboratory tests shear waves are commonly generated and recorded by bender elements; in situ, shear waves can be generated at the ground surface or below ground by impact or explosives. In situ recording is accomplished by geophones mounted on the surface, in boreholes, or in probes.

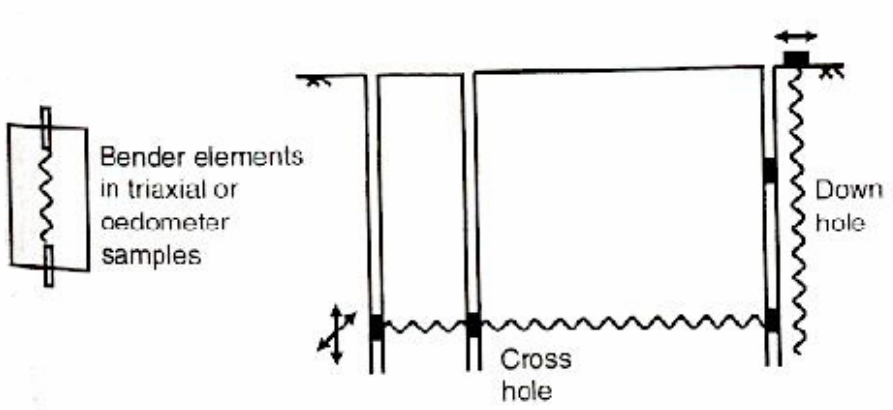

Figure 4.10: measurement of stiffness from wave velocity (a) laboratory test (b) in situ test (Atkinson, 2000)

In common applications the source generates both shear waves and compression waves It is the faster travelling P waves which arrive first and mask the arrival of S waves. For stiffness measurements through S wave velocities, it is therefore strived for a source that generates high energy S-wave signals so that their arrivals can be distinguished from other signals such as P waves or surface waves.

In situ measurements of shears wave velocity, are often accomplished in down hole tests or cross hole tests, as illustrated in Figure 4.10. Alternatively a seismic cone or a seismic flat dilatometer can be used. The commercially available seismic cone and seismic flat dilatometer are hybrid tests that combine down hole seismic surveying with penetration and dilatometer testing respectively. Instead of placing seismic receivers in a predrilled hole, they are, in this case, pushed in, while the energy source is locate at the surface like in a conventional down hole survey.

As for laboratory tests, it has been mentioned that bender elements are commonly used. A bender element is a piezo-ceramic device that bends if a voltage across it is changed or, if bent by an external force, the voltage across it changes. Bender elements are usually set into the top and bottom platens of a triaxial or oedometer cell (Figure 4.11) and penetrate about 3 mm into the sample. One element is vibrated by changing the voltage across it, shear waves propagate through the sample and vibrate the other element. The voltage input and output voltages are continuously recorded and the travel time determined.

There are also other indirect laboratory methods for measuring shear modulus in dynamic tests such as in laboratory resonant column tests. Resonant column tests are cyclic tests in which an axially confined cylindrical soil specimen is set in a fundamental mode of vibration by means of torsional or longitudinal excitation of one of its ends. Once the fundamental mode of resonance frequency is established, the measured resonant frequency can be related to the column stiffness using the theoretical elastic solution. This test is the dynamic version of the torsional shear test that is indeed a quasi-static cyclic test that can be used to measured small strain stiffness as well but with the limitations of a direct test like it is.

Alpan in 1970 proposed a chart in which static and dynamic soil stiffnesses are related (respectively named E_s and E_d). Actually this chart relates stiffness from conventional laboratory tests to very small stiffness: the dynamic modulus is the initial, or very small strain modulus E_0 and the static modulus is the apparent elastic Young's modulus in conventional soil testing, i.e. at axial strains of about 0.1% in triaxial testing.

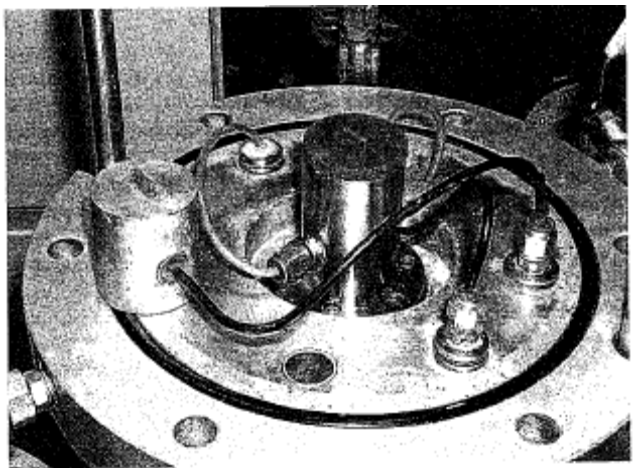

Figure 4.11:bender elements in the platens of a triaxial cell (Atkinson, 2000)

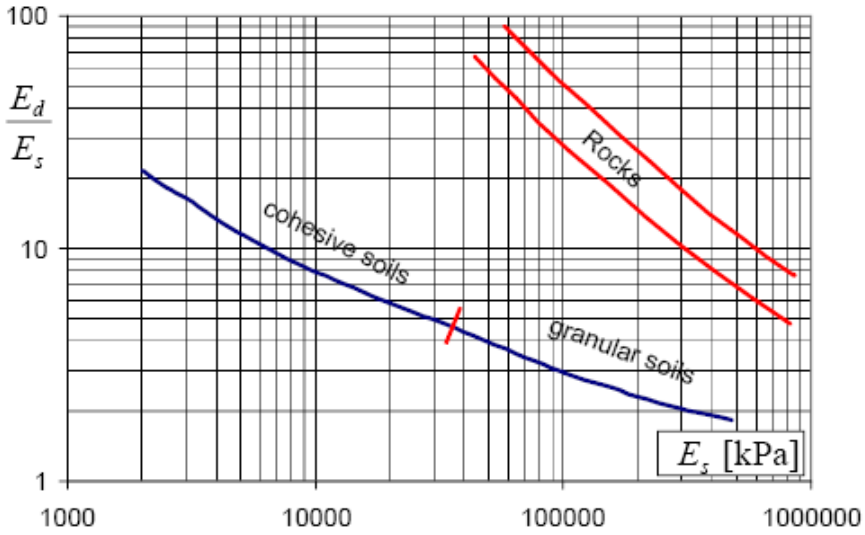

Figure 4.12: correlation between dynamic modulus and static modulus (Alpan, 1970)

Reduction of stiffness with shear strain

It has been already acknowledged that soils conserve their initial stiffness G_0 only at very small strain, with increasing strain soil stiffness decreases. On the other hand, soils instantaneously recover their initial stiffness upon load reversal and then stiffness decreases again with strain. Hence the accumulated strain since the last load reversal is the main variable in small strain stiffness reduction. It is called *strain amplitude*.

From a micromechanical point of view, assuming that a simple Coulomb-type frictional law exists in-between the particles of a soil skeleton, the influence of strain amplitude on small strain stiffness can be explained as a change or rearrangement of intermolecular and surface forces.

Initially all inter-particle contacts are in a sticking mode, then, due to a certain normal and tangential contact-elasticity, most contacts remain in the sticking mode for a finite strain amplitude, that can be considered to be equivalent to the truly elastic very small region. Further increase of the shear strain will cause an increasing number of particles to slip. Strain

reversals switch back the model's inter-particle contacts to sticking mode so that the maximum small-strain stiffness is recovered.

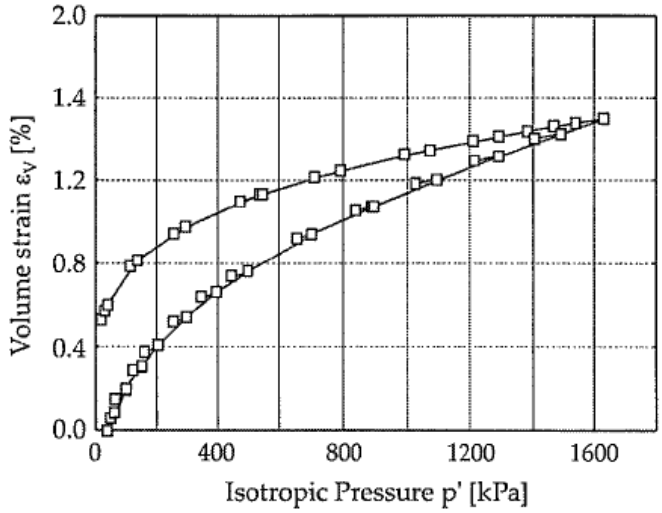

Figure 4.13:isotropic compression test interrupted by small strain-cycles (after Lade and Abelev, 2005)

Whether only deviatoric strains are responsible for that behaviour, as extensively showed in literature, or also volumetric strains can produce stiffness decrease is discussed next.

In literature most of the tests performed to detect the very small strain behaviour involve exclusively shear strains. Lade and Abelev, on the other hand, carried out a series of isotropic compression tests in which small cycles of isotropic stress were performed at each load increment during loading of the specimen to the maximum pressure and during unloading back to the original state. Isotropic compression without small pressure cycles were also performed in comparison with those with small pressure cycles. In Figure 4.13 the stress-strain results are plotted (Lade and Abelev, 2005).

Looking at the plot it is possible to observe that in small unloading –reloading cycles there are almost no recover in stiffness when loading direction is changed, on the other hand, looking at the continue swelling curve, when changing direction of loading, at the very beginning there is a stiffness recover, and the same thing can be observed in Figure 4.14 by Viggiani et Atkinson representing an isotropic compression test on London clay. It is possible to notice small hysteresis loops, indeed, so that damping in unloading-reloading is very small too.

“In deviatoric loading damping in small strain range is less during unloading-reloading than in primary loading, but still of the same magnitude. In isotropic loading, damping in small strain unloading reloading is much less than in primary loading" (Benz, 2006). This is also in agreement with the findings of Zdravkovic & Jardine: "The secant and tangent bulk moduli curves developed during swelling fall relatively gently with strain remaining far above the tangent compression value”. The interpretation one could give to this phenomenon is that deviatoric loading distorts inter-particle forces more than isotropic loading. The latter in fact causes only an upscale and no rearrangement of existing inter-particle forces.

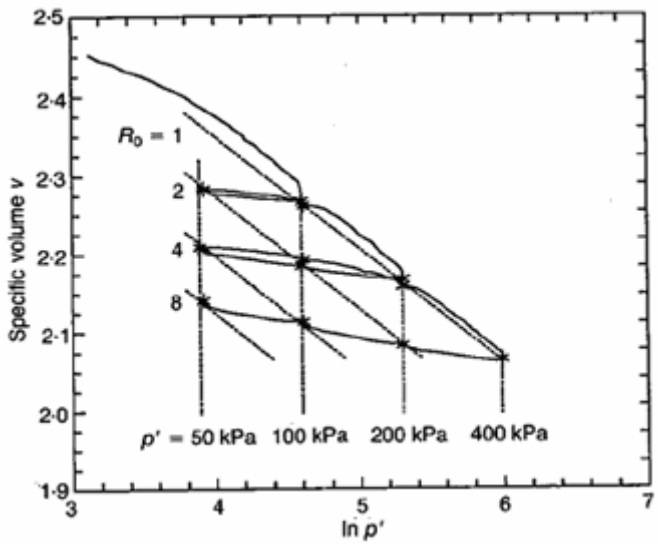

Figure 4.14: isotropic compression tests with unloading-reloading cycles (Viggiani and Atkinson, 1995)

Soil state dependency of very small strain stiffness

It has just mentioned that the stiffness modulus decreases rapidly with strain amplitude: there is apparently no strain level below which the modulus is constant. An example is shown in Figure 4.15 (Hardin and Drnevich ,1972). In the same figure one can see also the influence of mean effective stress and number of loading cycles in dynamic tests. The influence of mean pressure on stiffness, for example, is already well known, even referred to a general strain level, not only to the small-strain range. It is therefore evident that also the initial strain stiffness has to be stress-dependent.

However, there are several parameters that affect soil stiffness at very small strains. In particular, beside strain amplitude, void ratio, confining stress and the amount of in-situ inter-particle bonding turn out to be the most important parameters influencing very small strain stiffness (Benz, 2006). This results was basically published by Seed and Idris as early as 1970, particle bonding excluded (see Figure 4.16).

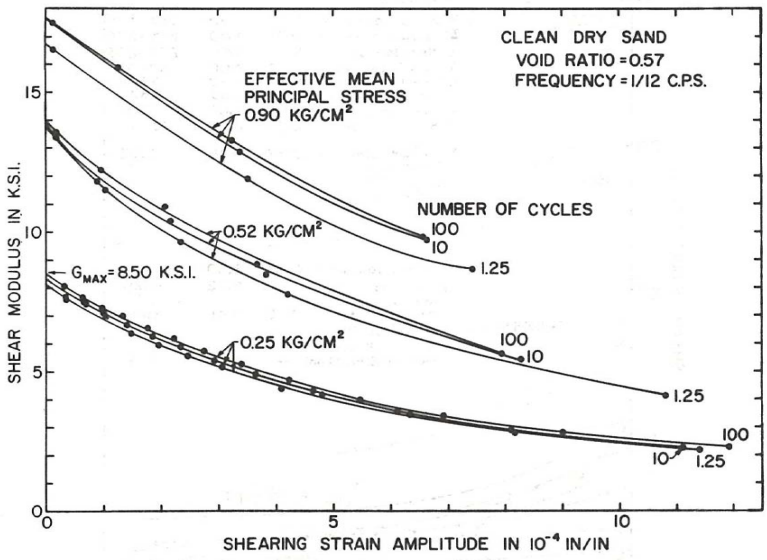

Figure 4.15: effects of strain amplitude (effective mean principal stress and number of cycles of loading) on shear modulus (Hardin and Drnevich, 1972)

In this chapter a few parameters affecting very small strain stiffness will be briefly discussed, while the interested reader is suggested to refer to the complete review made by Benz (2006). In particular in Table 4.1 a list of the main parameters is reported. The list is based on Hardin and Drnevich research as modified by Benz, and gives to each of them an importance value.

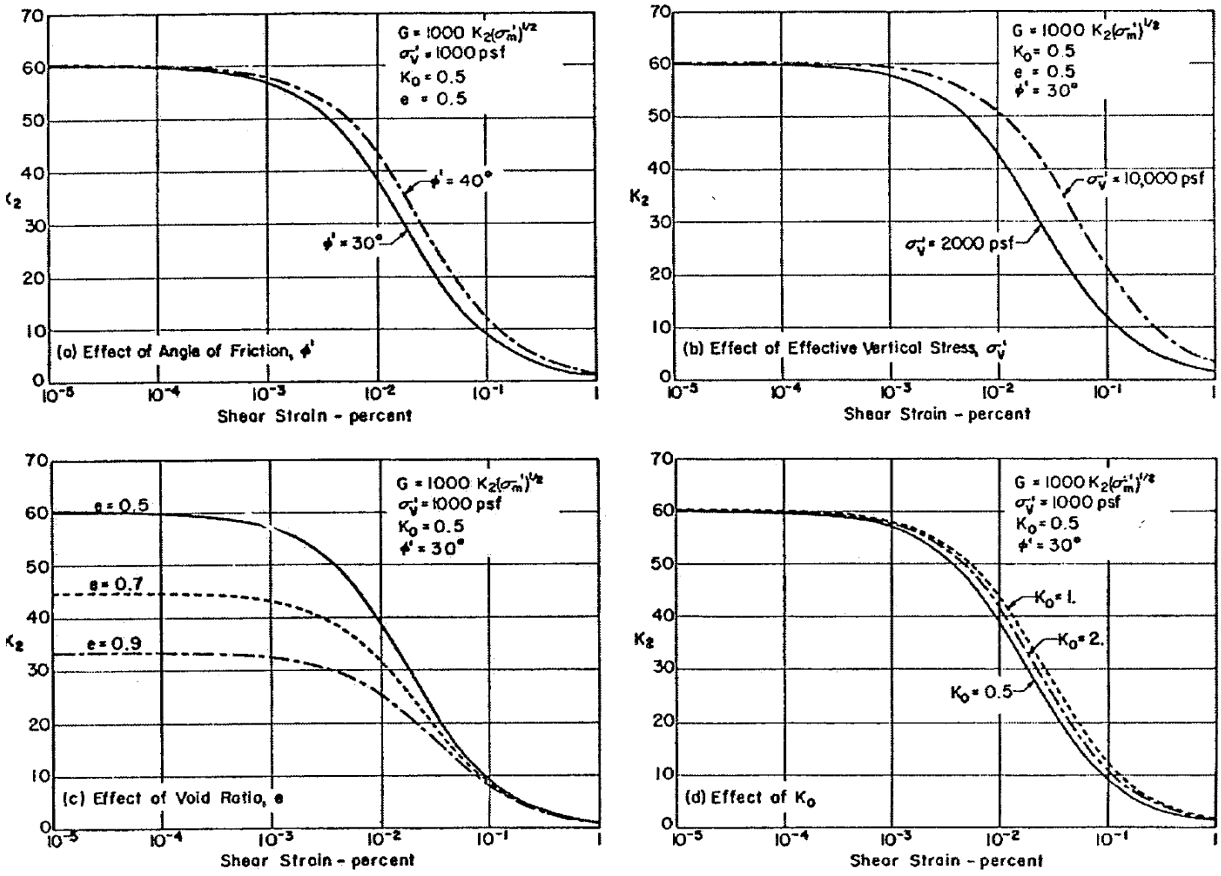

Figure 4.16: small strain stiffness decay as a function of several parameters (Seed and Idris, 1970)

Parameter	Importance to [a]			
	G_0		$\gamma_{0.7}$	
	Clean sands	Cohesive soils	Clean sands	Cohesive soils
Strain amplitude	V	V	V	V
Confining stress	V	V	V	V
Void ratio	V	V	R*	V
Plasticity index (PI)*	-	V	-	V
Overconsolidation ratio	R	L	R	L
Diagenesis*	V*	V*	R*	R*
Strain history*	R	R	V	V
Strain rate	R	R	R	R*
Effective material strength	L	L	L	L
Grain Characteristics (size,shape,gradation)	L*	L*	R	R
Degree of saturation	R	V	L	L*
Dilatancy	R	R	R	R

[a] V means Very Important, L means Less Important, and R means Relatively Unimportant

* Modified from the original table presented in Hardin & Drnevich

Table 4.1: parameters that affect small strain stiffness (Benz, 2006)

The variation of very small strain stiffness with stress, specific volume and overconsolidation has been investigated extensively in the past. A number of relationships have been proposed and most take the general form:

$$\frac{G_0}{p_{ref}} = A \cdot f(e) \cdot \left(\frac{p'}{p_{ref}} \right)^m \cdot OCR^k \tag{4.3}$$

where G_0 is the maximum small-strain shear modulus in MPa, p' is the mean effective stress in kPa, p_{ref} is a reference pressure to make equation dimensionally consistent and is usually takes as 100 kPa, OCR is the overconsolidation ratio, $f(e)$ is some function of void ratio and A, m, k are the material parameters.

Benz summarized parameter values for some soils in two tables (Table 4.2,Table 4.3) herein reported, where D_{50} is the mean grain diameter, U_c is the uniformity coefficient and PI the plasticity index.

Soil tested	PI [%]	A [-]	$f(e)$ [-]	k [-]	m [-]
Avezzano clay (Holocene-Pleistocene)	10-30	74	$e^{-1.27}$	NA	0.46
Garigliano clay (Holocene)	10-40	44	$e^{-1.11}$	NA	0.58
Montaldo di Castro clay (Pleistocene)	15-34	50	$e^{-1.33}$	NA	0.40
Speswhite caolin clay (recon.)	24	40	1	0.20_2	0.65
Recon. Vallericca clay (Pleistocene)	27	44	1	...	0.85
Kaolin clay	35	45	$\frac{(2.97-e)^2}{1+e}$	NA	0.50
Pisa clay (Pleistocene)	23-46	50	$e^{-1.43}$	NA	0.44
London clay (reconstituted)	41	13	1	0.25_2	0.76
Panigaglia clay (Holocene)	44	52	$e^{-1.30}$	NA	0.50
Fucino clay (Holocene-Pleistocene)	45-75	64	$e^{-1.52}$	NA	0.40
Bentonite	60	4.5	$\frac{(4.40-e)^2}{1+e}$	NA	0.50

Table 4.2:parameters' value for the initial shear modulus of clays (Benz, 2006)

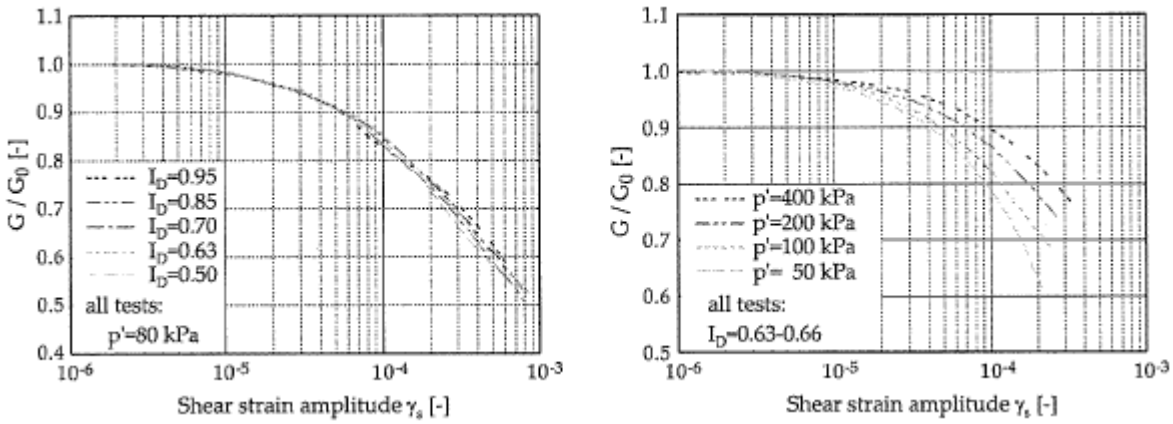

Figure 4.17: influence of void ratio and confining stress on the decay of small strain stiffness (Benz, 2006)

Soil tested	D_{50} [mm]	U_C [-]	A [-]	$f(e)$ [-]	k [-]	m [-]
Kenya carbonate sand	0.13	1.86	101-129	$e^{-0.8}$	0	0.45-0.52
Toyoura sand (subangular)	0.16	1.46	71-87	$\frac{(2.17-e)^2}{1+e}$	0	0.41-0.51
Toyoura sand (subangular)	0.19	1.56	84-104	$\frac{(2.17-e)^2}{1+e}$	0	0.50-0.57
Silica sand (subangular)	0.20	1.10	80	$\frac{(2.17-e)^2}{1+e}$	0	0.50
Silica sand (subangular)	0.20	1.70	62	$\frac{(2.17-e)^2}{1+e}$	0	0.50
Silica sand (subangular)	0.20	1.10	62	$\frac{(2.17-e)^2}{1+e}$	0	0.50
Toyoura sand (subangular)	0.22	1.35	72	$e^{-1.3}$	0	0.45
H.River sand (subangular)	0.27	1.67	72-81	$\frac{(2.17-e)^2}{1+e}$	0	0.50-0.52
Glass ballotini (spheres)	0.27	1.28	64-69	$\frac{(2.17-e)^2}{1+e}$	0	0.55-0.56
Hostun sand (angular)	0.31	1.94	80	$\frac{(2.17-e)^2}{1+e}$	0	0.47
Silica sand (angular)	0.32	2.80	48	$\frac{(2.17-e)^2}{1+e}$	0	0.50
Ticino sand (subangular)	0.50	1.33	61-64	$\frac{(2.17-e)^2}{1+e}$	0	0.44-0.53
Ticino sand (subangular)	0.54	1.50	71	$\frac{(2.27-e)^2}{1+e}$	0	0.43
Silica sand	0.55	1.80	275	$\frac{(1.46-e)^2}{1+e}$	0	0.42
Ticino sand (subangular)	0.55	1.66	79-90	$e^{-0.8}$	0	0.43-0.48
SLB sand (subround)	0.62	1.11	82-130	$\frac{(2.17-e)^2}{1+e}$	0	0.44-0.53
Ottawa sand No. 20-30	0.72	1.20	69	$\frac{(2.17-e)^2}{1+e}$	0	0.50
Quiou carbonate sand	0.75	4.40	71	$e^{-1.3}$	0	0.62
Decomposed granite	1.30	≈75	45	1	0	0.88
Hime gravel (subround)	1.73	1.33	53-94	$\frac{(2.17-e)^2}{1+e}$	0	0.45-0.51
Chiba gravel	7.90	≈10	76	$\frac{(2.17-e)^2}{1+e}$	0	0.50

Table 4.3: parameters' value for the initial shear modulus of clean sands and gravels (Benz, 2006)

In Figure 4.17 damping dependency on confining stress for a given void ratio and void ratio dependency for a given mean stress are given where $I_D = (e - e_{\min}) / (e_{\max} - e_{\min})$.

As evident, the mean stress dependency is very clear : historically a great deal of data have been published to show that G_0 varies with the square root of p', however, especially at large strain amplitudes the modulus depends mainly on the strength of the soil, which is more nearly a function of p' to the first power. Hardin and Richard used the power law exponent $m = 0.5$ for both cohesive and non-cohesive soils. Today their exponent is widely confirmed (or it varies in a narrow range) for non-cohesive soils (see Table 4.3), but for cohesive soil there are researchers that propose higher m values (up to $m = 0.8$)

As regard to the very small strain stiffness dependency on void ratio, the most frequently applied relationship dates back to Hardin and Richart. They proposed:

$$G_0 \propto \frac{(2.17 - e)^2}{1 + e} \tag{4.4}$$

for round-grained sands ($e < 0.80$)

$$G_0 \propto \frac{(2.97-e)^2}{1+e} \tag{4.5}$$

for angular grained sands ($e > 0.60$).

Hardin and Black later indicated that the second expression also correlates reasonably well for clays with low surface activity. For clays with higher surface activity other researchers proposed to keep the basic structure of the relationship, replacing the coefficient 2.97 with something higher as reported in Table 4.2.

The soil state is described by the current effective stress and a specific volume with respect to a reference line (i.e. OCR is given). Considering Figure 4.18, at a state A the behaviour will be different to that at B at the same effective stress and different to C at the same void ratio (or specific volume, or water content). If the reference line is the normal compression line, the point A can be defined throughout its OCR.

A fine grained soil can reach an overconsolidated state by virgin compression down to the normal compression line followed by unloading and swelling (and also by creeping, but in this framework it is negligible). The state of a coarse grained soil can move directly from B to A by vibration or compaction at constant effective stress.

Therefore Viggiani and Atkinson proposed to define the soil state by means of only two of e, p', OCR . The general equation can thus be simplified in:

$$\frac{G_0}{p_{ref}} = A \cdot \left(\frac{p'}{p_{ref}} \right)^m \cdot OCR^k \tag{4.6}$$

In fact , from the previous tables by Benz, it can be noticed that while an expression for $f(e)$ was given, not the same was for OCR. In this latter approach by Viggiani et Atkinson the opposite way is chosen. They also showed the variation of the parameters A, m, k with plasticity, as reported in Figure 4.19.

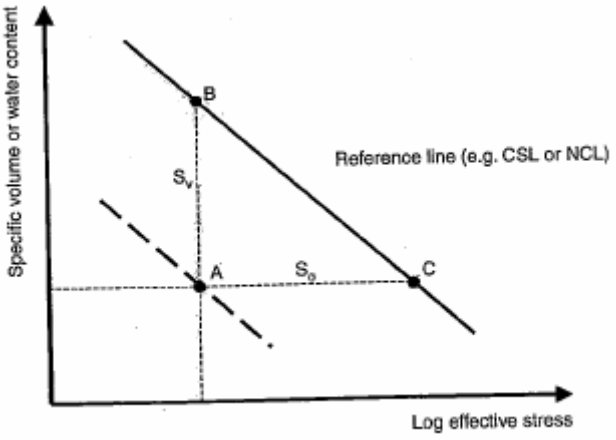

Figure 4.18: soil current state (Atkinson, 2000)

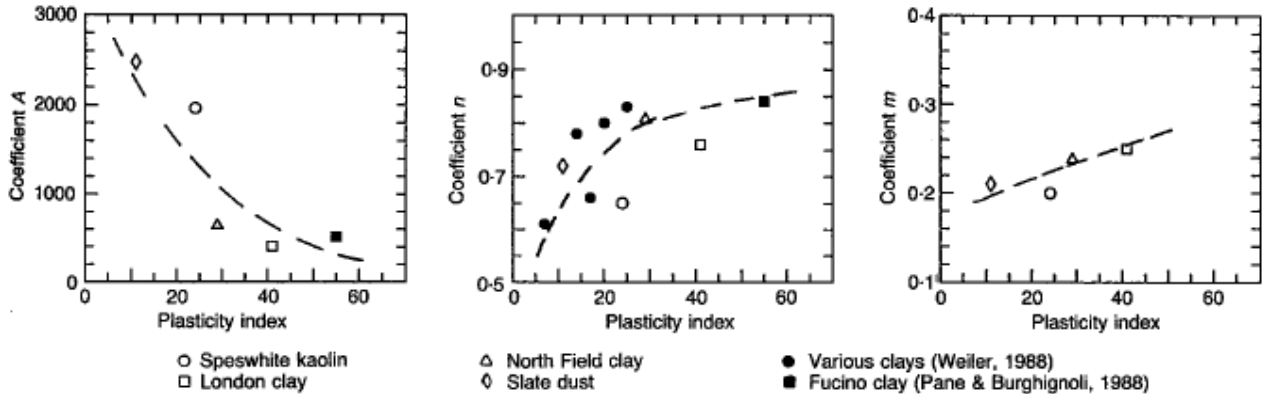

Figure 4.19:variation of initial stiffness parameters with plasticity index

As the main topic of this thesis is time dependent behaviour of soils, next it is looked more closely at time dependency of very small strain stiffness G_0. Schmertmann reported (see Chapter 2) stiffness moduli increase with time. Ageing can be in fact considered as a diagenetic processes and diagenetic processes, altering the existing inter-particle soil structure, alter as a consequence also soil stiffness.

As proposed by Leroueil and already mentioned before in this thesis, time is responsible for structuration phenomena of soils, that tends to fix particles into positions thus increasing stiffness (sticking way), both in clays and sands. The time - dependent increase in G_0 due to ageing may be linked to the secondary compression index C_α with empirical expressions of the type:

$$\frac{G_0(t)}{G_0(t_{EOP})} \propto \left(\frac{t}{t_{EOP}}\right)^{N_G} \tag{4.7}$$

where t_{EOP} is the end-of- primary- consolidation time, $t > t_{EOP}$ is any time greater than the time required to reach the end of primary consolidation, $G_0(t_{EOP})$ is the maximum stiffness at time t_{EOP} and $G_0(t)$ the maximum stiffness at any time.
N_G can be related to the secondary compression coefficient; for example Lo Presti proposed the following relationship:

$$N_G = C_\alpha{}^{0.5} \tag{4.8}$$

Another diagenetic process that affect very much small strain stiffness is the cementation, especially in sandy soils, but this phenomenon is not necessarily linked to secondary compression.

As a measure of the strain rate effect the *strain rate shear modulus parameter* is defined as:

$$\alpha_G = \frac{\Delta G}{\Delta \log \dot{\gamma}} \tag{4.9}$$

as the slope of the plot in semi-logarithmic plane reported in Figure 4.20.

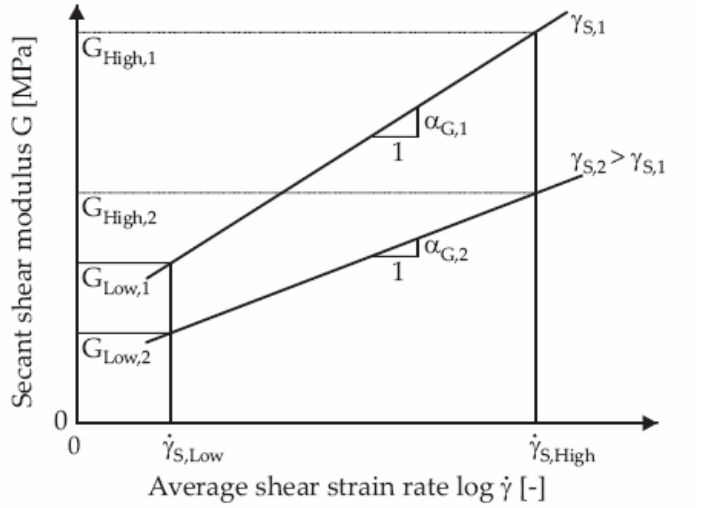

Figure 4.20: strain rate shear modulus parameter (Benz, 2006)

From Figure 4.20 it can be noticed that the strain rate effect increases with strain rate (i.e. the shear stiffness decreases) The strain rate effect in soil damping increases with plasticity index, but in general it has been shown that, compared to those already mentioned (mean stress, void ratio etc. dependency), it can be often neglected.

Stiffness' degradation: Hardin- Drnevich reduction curve

Hardin and Drnevich in 1972 proposed a relationship that extrapolates the whole degradation curve based on initial strain stiffness (G_0) and a reference strain amplitude parameter γ_r. They in fact introduced the neediness of normalizing strain with a reference value, since they observed that a given strain does not have the same effect on all soils nor on the same soil under different pressure.

The *damping ratio* is defined as $D = A_L / 4\pi A_T$ where A_L is the area inside a closed stress-strain loop and A_T is the triangular area shown in Figure 4.21.

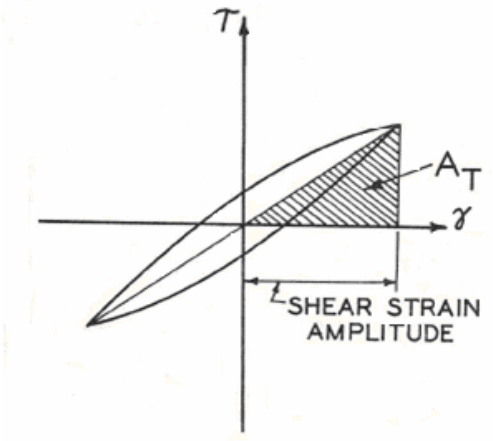

Figure 4.21: load loop with definition of triangular area used in damping ratio definition (Hardin and Drnevich, 1972)

In general as shear stiffness decreases with strain amplitude, the damping ratio increases being the hysteresis loop bigger. Hardin and Drnevich found damping ratio to be higher for

lower confining pressure. They showed that even if the relationship between damping ratio and strain amplitude is clearly not the same for different confining pressure, when the same data are plotted against normalized strain γ / γ_r a single curve describes that behaviour, as shown in Figure 4.22.

The reference strain amplitude parameter is defined as:

$$\gamma_r = \frac{\tau_{\max}}{G_{\max}} = \frac{\tau_{\max}}{G_0} \tag{4.10}$$

where $\tau_{\max}$ is the shear stress at failure and $G_{\max} = G_0$ is the very small strain stiffness value.
In other words the initial slope of the stress strain curve (G_0) is extended to intersect the line $\tau = \tau_{\max}$. The abscissa of that point is the reference value γ_r, as reported in Figure 4.23.

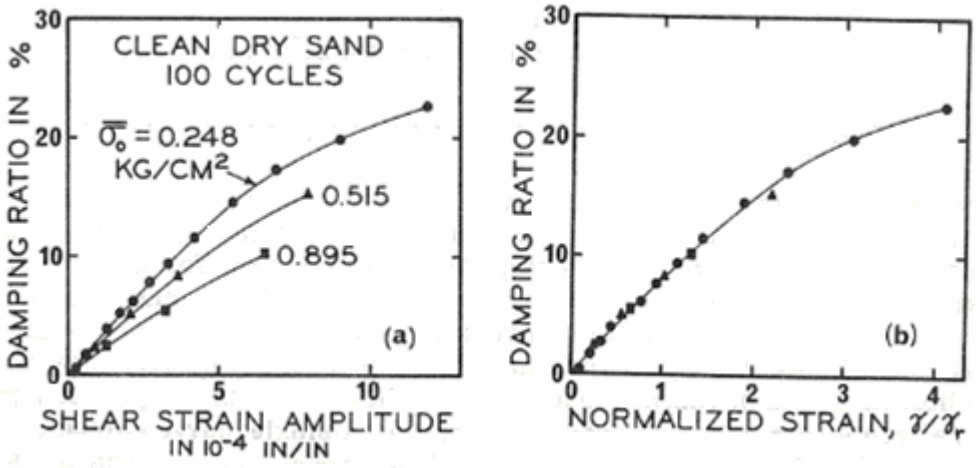

Figure 4.22: reference strain to normalize damping data (Hardin and Drnevich, 1972)

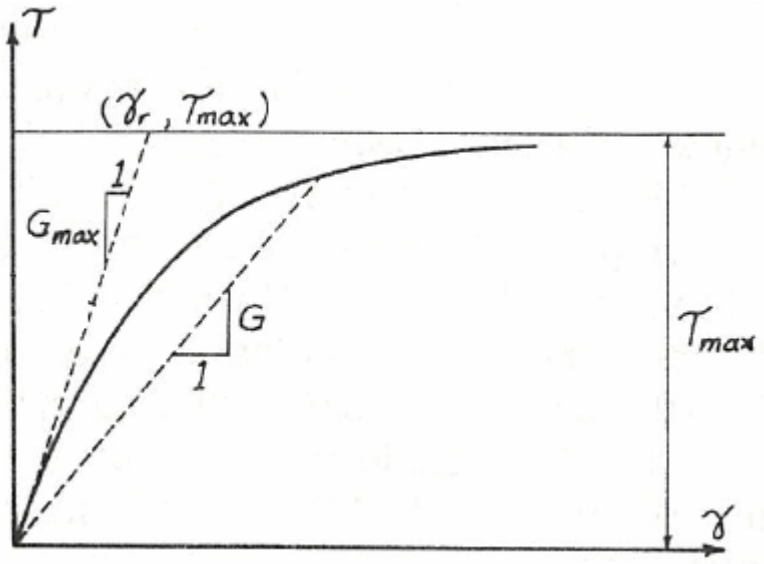

Figure 4.23: reference strain amplitude definition (Hardin and Drnevich, 1972)

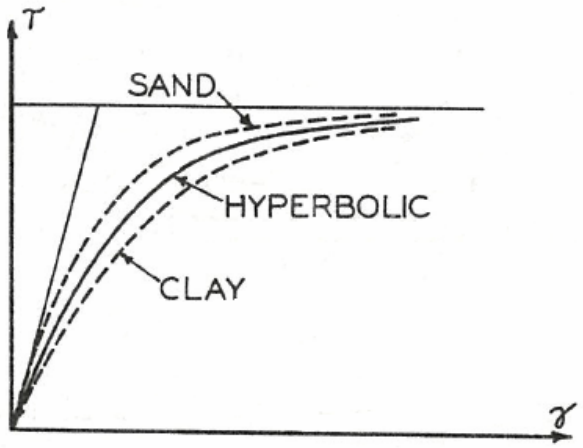

Figure 4.24: hyperbolic stress-strain relationship for soils (Hardin and Drnevich, 1972)

The definition of reference strain amplitude as a parameter that relates a very small strain property (initial stiffness) and a large strain one (failure shear stress) is used also by Atkinson (2000) to describe the rigidity of a material. The rigidity is defined as the inverse of the reference strain amplitude parameter:

$$\frac{1}{\gamma_r} = \frac{G_{\max}}{\tau_{\max}} \tag{4.11}$$

Non-linear materials fail at strains γ_f grater than γ_r and the ratio $n = \gamma_f / \gamma_r$ is a measure of the degree of non-linearity of the material. "Rigidity and the degree of non-linearity together serve to characterize the non-linear stress –strain behaviour" (Atkinson, 2000). The reference strain parameter thus seems even 30 years later to be a good parameter in describing such problems.

Hardin and Drnevich proposed the following hyperbolic shape of the stress strain curve (see Figure 4.24):

$$\tau = \frac{\gamma}{\frac{1}{G_{\max}} + \frac{\gamma}{\tau_{\max}}} \tag{4.12}$$

Dividing both terms of (4.12) by the actual shear strain the secant modulus $G = \tau/\gamma$ is obtained and then subsequentially dividing by $G_{\max} = G_0$ the result is:

$$\frac{G}{G_{\max}} = \frac{1}{\frac{\tau_{\max} + \gamma \cdot G_{\max}}{\tau_{\max}}} = \frac{1}{1 + \gamma \cdot \frac{G_{\max}}{\tau_{\max}}} = \frac{1}{1 + \frac{\gamma}{\gamma_r}} \tag{4.13}$$

Once one knows the initial stiffness and the reference shear amplitude parameter the stiffness value for any strain amplitude can be extrapolated based on the expression above. $G_{\max} = G_0$ can be deducted from laboratory or in situ tests as described previously, $\tau_{\max}$ can be calculated, with reference to the following figure as:

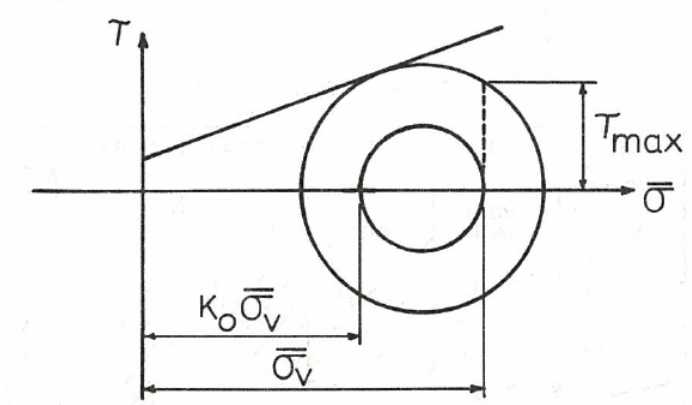

Figure 4.25: maximum shear stress (Hardin and Drnevich, 1972)

$$\tau_{max} = \left\{ \left[\left(\frac{1+K_0}{2} \sigma'_v + \frac{c}{\tan\varphi} \right) \sin\varphi \right]^2 - \left[\frac{1+K_0}{2} \sigma'_v \right]^2 \right\}^{1/2} \qquad (4.14)$$

K_0 being the at rest coefficient.

Hardin and Drnevich also showed that, analogously, once one know the maximum value of damping ratio and the reference strain amplitude parameter, the damping ratio at any shear strain can be determined (supposing to perform a complete stress reversal). The basic assumptions they made were that when the direction of loading is reversed, the slope of stress-strain relation immediately after reversal is approximately equal to $G_{max} = G_0$, independent of the strain amplitude of the loop, and that the cross hatched area in Figure 4.26 is a constant percentage of the area of the triangle a-b-c. The triangle a-b-c is formed by the loop modulus line ac with slope secant G, the line ab which according with the first assumption has slope $G_{max} = G_0$ and the horizontal line bc. The cross hatched area is, by symmetry, half the area of the loop, therefore: $A_L / 2 = K_1 \cdot A_{abc}$ with $K_1 = const$.

It results:

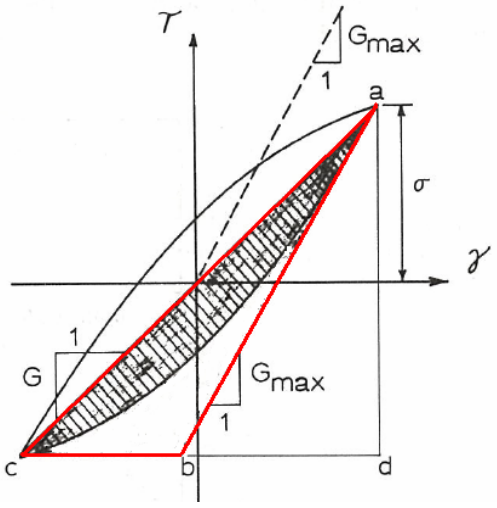

Figure 4.26:geometrical relationship between shear modulus and damping ratio (Hardin and Drnevich,1972)

$$D = \frac{A_L}{4\pi A_T} = \frac{2K_1}{\pi}\left(1 - \frac{G}{G_{\max}}\right) \tag{4.15}$$

and, since it has to be: $D = D_{\max}$ for $G = 0$ it turns out:

$$D = D_{\max}\left(1 - \frac{G}{G_{\max}}\right) \tag{4.16}$$

As previously mentioned, damping and shear stiffness show the opposite trend: when the first increases the second decreases and vice versa.

If one plots in a log-log graph D and $\left(1 - G/G_{\max}\right)$ versus normalized strain one should notice that there is a constant distance between the two curves equal to $D_{\max}$ being from the previous equation: $\log D = \log D_{\max} + \log\left(1 - G/G_{\max}\right)$. In Figure 4.27 experimental data from a clean dry sand are shown.

Substituting the stiffness reduction curve (4.13) in the expression for the damping ratio (4.16), the relation in terms of reference strain amplitude parameter is given:

$$\frac{D}{D_{\max}} = 1 - \frac{1}{1 + \dfrac{\gamma}{\gamma_r}} = \frac{\dfrac{\gamma}{\gamma_r}}{1 + \dfrac{\gamma}{\gamma_r}} \tag{4.17}$$

It can be noticed that the larger is γ_r the less is the damping.

Since the use of γ_r involves in the same parameter very small strain properties and failure properties, it has considered more straightforward to use a smaller threshold shear strain.

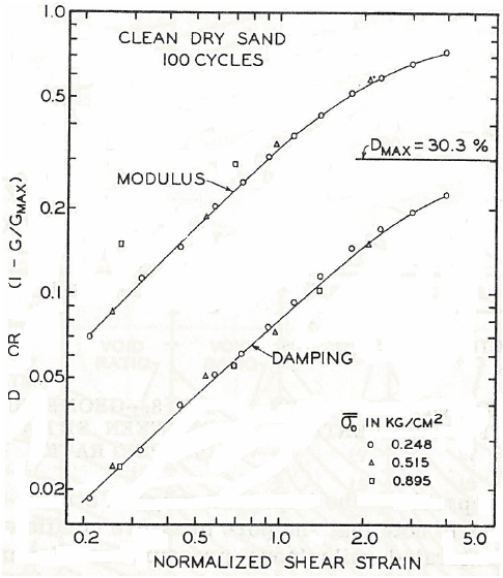

Figure 4.27: relationship between modulus and damping (Hardin and Drnevich, 1972)

In particular Santos and Correia (2001) proposed to use in the Hardin and Drnevich equation (4.13) a reference value corresponding to that strain amplitude at which the initial strain stiffness decays to
$G = 0.7 \cdot G_0$. In this case it is indicated as $\gamma_{0.7}$. It is necessary, as a consequence, to add a multiplier constant in order to get $G = 0.7 \cdot G_0$ for $\gamma = \gamma_{0.7}$. The modified Hardin-Drnevich relationship becomes:

$$\frac{G}{G_{\max}} = \frac{1}{1 + a\dfrac{\gamma}{\gamma_{0.7}}} \tag{4.18}$$

so than $\gamma_{0.7} = \gamma_r \cdot a$

If $a = 3/7$ the equation perfectly coincides with the Hardin Drnevich one, since at $\gamma = \gamma_{0.7}$ it holds: $G = 0.7G_0$, but Santos and Correia using many test results found as a best fit $a = 0.385$ for which at $\gamma = \gamma_{0.7}$ it is $G = 0.722G_0$. This latter value will be used also in this thesis, being the difference however so small to be considered negligible (see Figure 4.28).

The Hardin-Drnevich approach is probably the most frequently used model in soil dynamics. As a matter of completeness, the expression of other typical models are herein reported in the shear strain –shear stress space, together with the Hardin-Drnevich:

$$\text{Hardin-Drnevich: } \tau = \frac{G_0\gamma}{1 + \dfrac{\gamma}{\gamma_r}} \tag{4.19}$$

$$\text{Ramberg-Osgood: } \gamma = \frac{\tau}{G_0}\left(1 + \alpha\left(\frac{\tau}{\tau_y}\right)^k\right) \tag{4.20}$$

$$\text{Bilinear: } \tau = G_0\gamma \text{ for } \gamma < \gamma_y$$
$$\tau = \tau_y + G_0(\gamma - \gamma_y) \text{ for } \gamma > \gamma_y \tag{4.21}$$

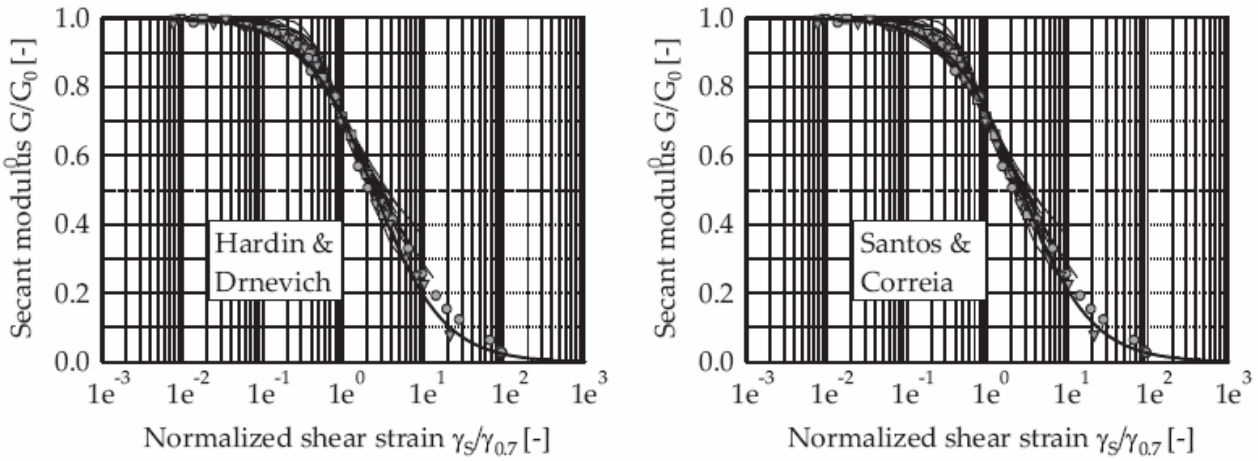

Figure 4.28: original Hardin-Drnevich curve and modified by Santos and Correia (Benz, 2006)

In terms of normalized secant stiffness G/G_0 the Ramberg-Osgood model has the same structure of the Hardin-Drnevich:

$$\frac{G}{G_0} = \frac{1}{1+\left(\frac{\tau}{\tau_y}\right)^k} \tag{4.22}$$

with the basic difference that the stiffness decay is a function of stress instead of strain amplitude.

The influence of loading history: Masing's rules

Masing's (1927) original work is concerned with the behaviour of brass under cyclic loading but his results describe soil behaviour quite well, too (Pyke, 1979).

Given a functional form to describe the initial loading curve, hysteresis loops that appear to model the actual behaviour in unloading –reloading can be readily constructed by adopting a set of rules.

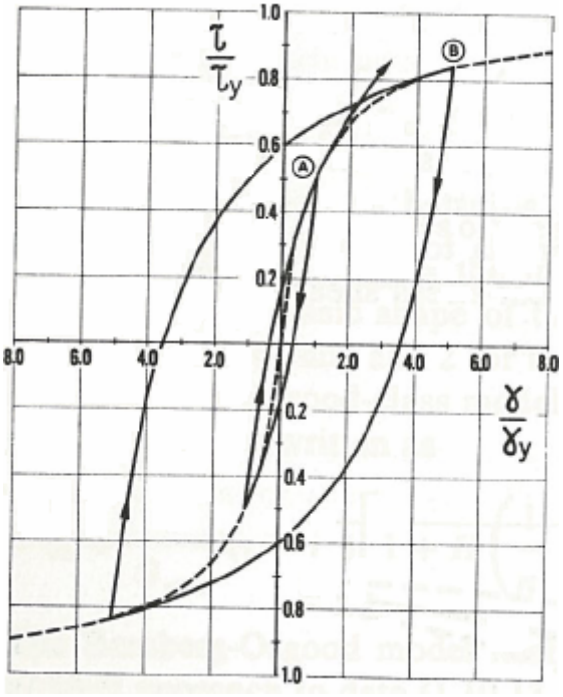

Figure 4.29: hysteresis loop according with Masing's rules (Pyke, 1979),τ_y is the failure strength

The two Masing's rules state that:

1. The shear modulus on each loading reversal assumes a value equal to the initial tangent stiffness for the initial loading curve;
2. The shape of the unloading or reloading curves is the same as that of the initial loading curve, except that the scale is enlarged by a factor of two.

The first rule is fulfilled assuming G_0 as a constant, the second by assuming a shape factor of two in terms of threshold shear strain amplitude: $(\gamma_{0.7})_{unloading-reloading} = 2 \cdot \gamma_{0.7}$.
However, if the loading is irregular (not symmetrical or periodic) two additional rules are commonly added to the original two, and the four together are referred to as the *extended Masing rules*.

The initial loading curve (called skeleton or backbone curve) is shown in Figure 4.29 by a dashed line. If a reloading curve, such as that for the smaller loop in figure, is carried beyond the previous limit of symmetrical cyclic loading, (labelled A), it diverges from the initial loading curve. A third rule suggested by Pyke is therefore:

3. Unloading and reloading curves should follow the initial curve in case the previous maximum shear strain is exceeded.

Figure 4.30 represents another point that has be to considered: if small amplitude cycles are superimposed on the reloading segment of larger amplitude cycles, in the absence of additional restrictions it may be seen that the result is that the larger amplitude loops are shifted along the stress axis, and the shear strength of the material may be exceeded. This problem in fact arises whenever strain amplitude increases again after one or more cycles of decreasing amplitude.

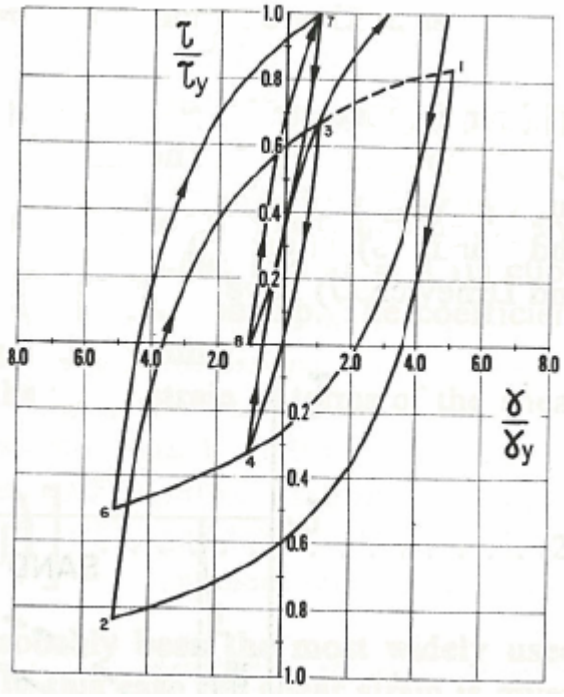

Figure 4.30: Cundall's Problem (Pyke, 1979), τ_y is the failure strength

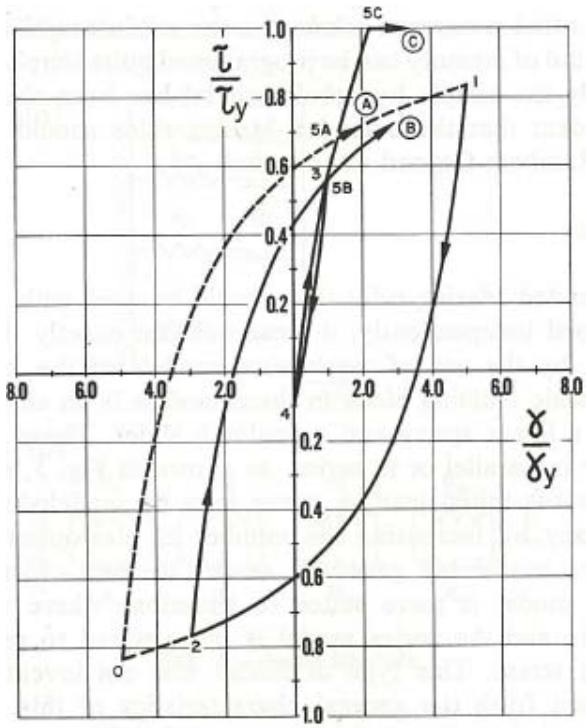

Figure 4.31: fourth rule (Pyke, 1979)

A fourth rule was thus proposed by Rosenblueth and Herrera (1964):

4. If the current loading curve intersects a previous one, it should follow the previous curve.

In Figure 4.31 an example is given: following this formulation of the fourth rule, reloading from point 4, the stress-strain relationship follows the previous curve: i.e. follows the B curve.

Another approach suggested by Jennings (1965) proposes that upper and lower bounds on the stress-strain relationship could be given by the reloading and unloading curves corresponding to the previous minimum and maximum strain amplitudes.
Thus, if the dotted curve 0-1 is the greatest previous reloading curve, on reloading from point 4 the stress-strain relationship would follow path A; if, however, point 2 is the previous minimum strain amplitude and the curve 2-3 is the greatest previous reloading curve, on reloading from point 4, the stress-strain relationship would follow path B.

There is a third solution for the fourth rule, given by Richart that consists simply of limiting the shear stress that can be developed at any time to a value no grater than the shear strength, as shown by path C.

The third and fourth rules would require an internal memory of previous change in the stress-strain path. This is to be considered in the model formulation presented in the next Chapter.

Chapter 5 - A proposal: a creep model that accounts for small strain behaviour

Introduction

In order to improve numerical analysis involving creep behaviour – especially in unloading-reloading situations - it is necessary to introduce the aforementioned non-linear stiffness relationship into a constitutive creep model.
The Soft Soil Creep model was chosen here as the basic creep model to enhance with small strain stiffness behaviour . Here a one-dimensional formulation is proposed.

The structure of the creep model and its equations have been all deduced in Chapter 3. The reader is therefore referred to this chapter for the model's framework, its structure and the main features.
The historical background of several aspects summarized in the Soft Soil Creep model and therefore also in the modified version herein presented, is explained in Chapter 3 as well.
As regard to the small strain behaviour that is the focal point of the proposed modification, Chapter 4 describes the phenomenon and especially the equations that will be introduced in the creep model.

The basic idea

To model stiffness decay over strain evolution, it was chosen to operate on the elastic stiffness applying to it the Hardin-Drnevich degradation law. The damping curve, indeed, describes the decay of stiffness, being the stiffness the secant or tangent line to the stress-strain curve, without distinguishing between elastic components or plastic ones. Since the truly elastic behaviour is shown over a very small range of strains, theoretically the damping curve does not describe the evolution of the elastic modulus.

In general models that are used in engineering practice rarely have more that one elastic domain, and their elastic stiffness is generally taken as secant stiffness of larger strain unloading-reloading cycles ($G = G_{ur}$) and small strain stiffness is neglected. Therefore soil behaviour is modelled as too soft both in very first step of loading and at the beginning of unloading or reloading. Whenever one uses the small strain stiffness value $G = G_0$ in the entire elastic domain, the model will end up responding too stiff in larger unloading-reloading cycles, as a consequence. Hence it is necessary to model the stiffness degradation from its highest value G_0 corresponding to very small strain stiffness and truly elastic behaviour until the mean value used in general in soil modelling G_{ur}, this value being the secant between the start and end points of large unloading-reloading cycles. Theoretically this lower value already overshoots the truly elastic limit, but this approximation for the lowest elastic stiffness value is exactly the same used in models without small strain behaviour, as for example the Soft Soil Creep model.

A one-dimensional formulation of the soft soil creep model including small strain stiffness is next proposed for oedometric conditions.
The one-dimensional formulation could be established either for isotropic loading or for oedometric loading. The latter is preferred because it includes deviatoric loading: in particular $\gamma_s\big|_{oedom} = \varepsilon_a - \varepsilon_r = \varepsilon_a$.

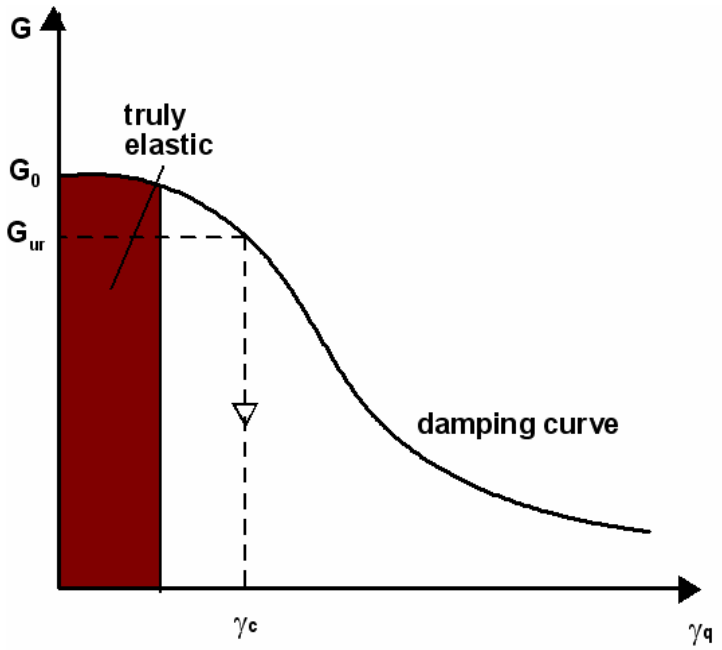

Figure 5.1: truly elastic modulus in the stiffness reduction curve and G_{ur} value usually taken in modelling

The basic equation is (see Equation (3.62) and Equation (3.67)):

$$d\varepsilon_v = d\varepsilon_v^{\,e} + d\varepsilon_v^{\,c} = \frac{dp'}{K} + \mu^* \ln\left(1 + \frac{dt}{\tau_c}\right) \tag{5.1}$$

where K is the bulk modulus, dt is the creep time (or equivalently the total time involved in the process, since the consolidation process has taken as very fast, μ^* the modified creep index and $\tau_c = \tau \cdot \left(OCR_{eop}\right)^{\beta}$ (Equation (3.74)) a reference time parameter that accounts for the overconsolidation ratio at the end of primary consolidation.

What is modified with respect to this formulation is the elastic bulk modulus, that in the creep formulation is stress dependent being $K = \frac{p'}{\kappa^*} = \frac{p_{ref}}{\kappa^*} \cdot \frac{p'}{p_{ref}} = K_{ref} \cdot \frac{p'}{p_{ref}} = K(p')$ (Equation (3.58)), while the new formulation takes into account also the strain dependency, moving from an initial value corresponding to the very small strain stiffness down to the unloading-reloading value for larger strains.

The main input parameters in the proposed formulation are the total strain increment and the time to develop it: the model herein proposed, therefore, substantially describes a CRS test. What is obtained as output is the stress increment.

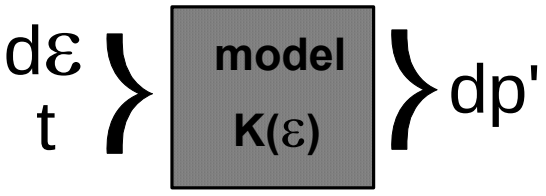

Figure 5.2: scheme of input and output of the model

The basic equation above is integrated using the Newton-Raphson procedure. Supposing $F(x)=0$ is the equation to be solved, and let x the variable to be solved for. Newton Raphson is an iterative scheme that approximates the variable as $x = x_{previous} + dx$. The Taylor expansion is:

$$F(x_{previous} + dx) = 0 = F(x_{previous}) + F'(x_{previous})dx + o(dx) \tag{5.2}$$

where $o(dx)$ is the higher order term that can be neglected since the assumption is to be in the proximity of the solution. It results: $dx = -F(x_{previous}) / F'(x_{previous})$ and then:

$$x = x_{previous} + dx = x_{previous} - \frac{F(x_{previous})}{F'(x_{previous})} \tag{5.3}$$

In this framework the equation to solve is:

$$\varepsilon_v{}^e + \varepsilon_v{}^c - \varepsilon_v = \frac{dp'}{K} + \mu * \ln\left(1 + \frac{t}{\tau_c}\right) - \varepsilon_v = 0 \tag{5.4}$$

Small strain stiffness evaluation: Hardin Drnevich relation and its application to the basic creep model

Before solving the equation for each total strain increment and time, it is necessary to identify which is the actual elastic stiffness value that depends on the strain amplitude level: if the model detects small or very small strain amplitudes, it increases the stiffness accordingly.

To evaluate the stiffness as a function of strain amplitude, the Hardin-Drnevich damping curve is used. It represents, as pointed out in Chapter 3 , the secant stiffness decay over the strain amplitude. To define the whole curve two input parameters have to be given: the maximum stiffness value G_0 and the strain amplitude value $\gamma_{0.7}$ corresponding to the stiffness decay to the 70% of its initial value:

$$G = G_0 \frac{1}{1 + a\dfrac{\gamma}{\gamma_{0.7}}} \tag{4.18}$$

where $\gamma_{0.7} = \gamma_r \cdot a = \dfrac{\tau_{\max}}{G_0} \cdot a$ with $a = 0.385$.

These two are the only two extra parameters that the model needs to account for elastic stiffness decay. Since $\tau_{\max}$ is given by the Mohr Coulomb law, once one knows the friction angle φ the reference strain amplitude parameter $\gamma_{0.7}$ could be given. Also the initial stiffness could be calculated as a function of soil state at initial condition, as described in Chapter 3, as it is, in general:

$$\frac{G_0}{p_{ref}} = A \cdot f(e) \cdot \left(\frac{p'}{p_{ref}}\right)^m \cdot OCR^k \tag{4.3}$$

In the formulation herein proposed the two parameters G_0 and $\gamma_{0.7}$ are given as independent input parameters.

Since the formulation is incremental and involves the secant stiffness, it is necessary to reformulate it in terms of tangent stiffness between two strain amplitude values: the previous value and the actual one that is the previous incremented by the actual strain increment. The actual elastic tangent shear modulus is thus best calculated integrating the stiffness modulus reduction over the actual shear strain increment in an explicit numerical way:

$$G_{i+1} = \frac{\Delta\tau}{\Delta\gamma} = \frac{\gamma_{i+1}G_{i+1} - \gamma_i G_i}{\gamma_{i+1} - \gamma_i} = \frac{G_0}{\gamma_{i+1} - \gamma_i}\left(\frac{\gamma_{i+1}}{1 + a\frac{\gamma_{i+1}}{\gamma_{0.7}}} - \frac{\gamma_i}{1 + a\frac{\gamma_i}{\gamma_{0.7}}}\right) \tag{5.5}$$

where i and $i+1$ denote quantities of the previous and the actual calculation step respectively.
In Figure 5.3 the procedure is graphically explained.

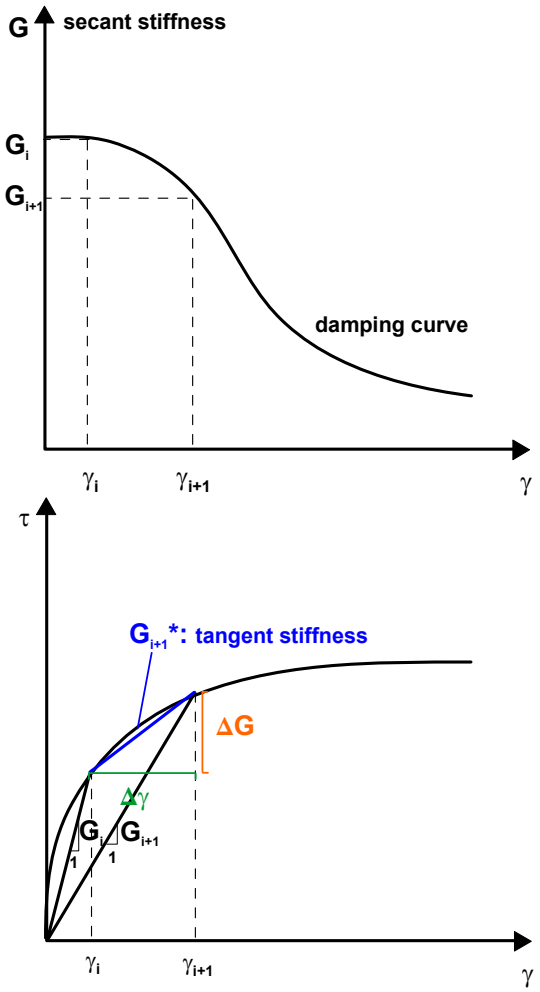

Figure 5.3: numerical tangent stiffness for a strain increment

As previously mentioned, a cut-off in the hyperbolic small strain reduction curve is introduced at the shear strain γ_c where tangent stiffness is reduced to the unloading-reloading stiffness G_{ur} in larger strain cycles.

The degradation curve, in fact, is an empirical relationship that describes the modulus reduction with strains that is deduced from laboratory and in situ tests, so the stiffness represented is a material parameter, that is neither completely elastic nor completely plastic. The use of an elasto-plastic model constrains, on the other hand, to divide the elastic component from the plastic one and the hardening plasticity itself causes a decrease in stiffness, that reflects into the decreasing steepness of the strain-stress curve describing, for example, a triaxial test. The cut off has to be activated with hardening plasticity formulation, as the case of Soft Soil Creep model, otherwise material stiffness for larger strains would become too small.

The shear strain γ_c is then obtained form the modified Hardin-Drnevich relationship for the tangent stiffness. In this case it is not possible to use the incremental expression for the tangent stiffness as calculated before, because here it has to be compared with a single value corresponding to the shear strain γ_c. The tangent stiffness expression has to be derived analytically, considering that

$$G_{\tan} = \frac{\partial \tau(\gamma)}{d\gamma} \tag{5.6}$$

and

$$\tau(\gamma) = G_{\sec}\gamma \tag{5.7}$$

thus obtaining, equating the tangent stiffness value to the unloading-reloading stiffness:

$$G_{\tan} = G_0\left(\frac{a\gamma_c}{\gamma_{0.7}\left(1-a\frac{\gamma_c}{\gamma_{0.7}}\right)^2}+\frac{1}{1-a\frac{\gamma_c}{\gamma_{0.7}}}\right) = G_0\left(\frac{\gamma_{0.7}}{\gamma_{0.7}+a\gamma_c}\right)^2 = G_{ur} \tag{5.8}$$

and hence:

$$\gamma_c = \frac{\gamma_{0.7}}{a}\left(\sqrt{\frac{G_0}{G_{ur}}}-1\right) \tag{5.9}$$

In Figure 5.4 the shear strain cut-off is defined graphically. Three are the possible cases then: that a generic couple of strain amplitudes falls well before the cut-off value ($\gamma_i < \gamma_{i+1} < \gamma_c$), the case in which the first value is before the cut-off value and the second is beyond ($\gamma_i < \gamma_c < \gamma_{i+1}$), and in the third case both are beyond the threshold value ($\gamma_c < \gamma_i < \gamma_{i+1}$). In the first case the formula to find the actual stiffness value is the generic one:

$$G_{i+1} = \frac{G_0}{\gamma_{i+1}-\gamma_i}\left(\frac{\gamma_{i+1}}{1+a\frac{\gamma_{i+1}}{\gamma_{0.7}}}-\frac{\gamma_i}{1+a\frac{\gamma_i}{\gamma_{0.7}}}\right) \tag{5.5}$$

where G_{i+1} is the actual tangent stiffness value.

In the second case the strain amplitude that overcomes the threshold shear strain so it has to be equate to the cut-off shear strain ($\gamma_{i+1} \equiv \gamma_c$) thus giving:

$$G_{i+1} = \frac{G_0}{\gamma_c - \gamma_i}\left(\frac{\gamma_c}{1+a\frac{\gamma_c}{\gamma_{0.7}}} - \frac{\gamma_i}{1+a\frac{\gamma_i}{\gamma_{0.7}}}\right) \tag{5.10}$$

otherwise in the third case both the strain amplitudes overcome the cut-off value so the unloading reloading stiffness for large strains has to be chosen:

$$G_{i+1} = G_{ur} \tag{5.11}$$

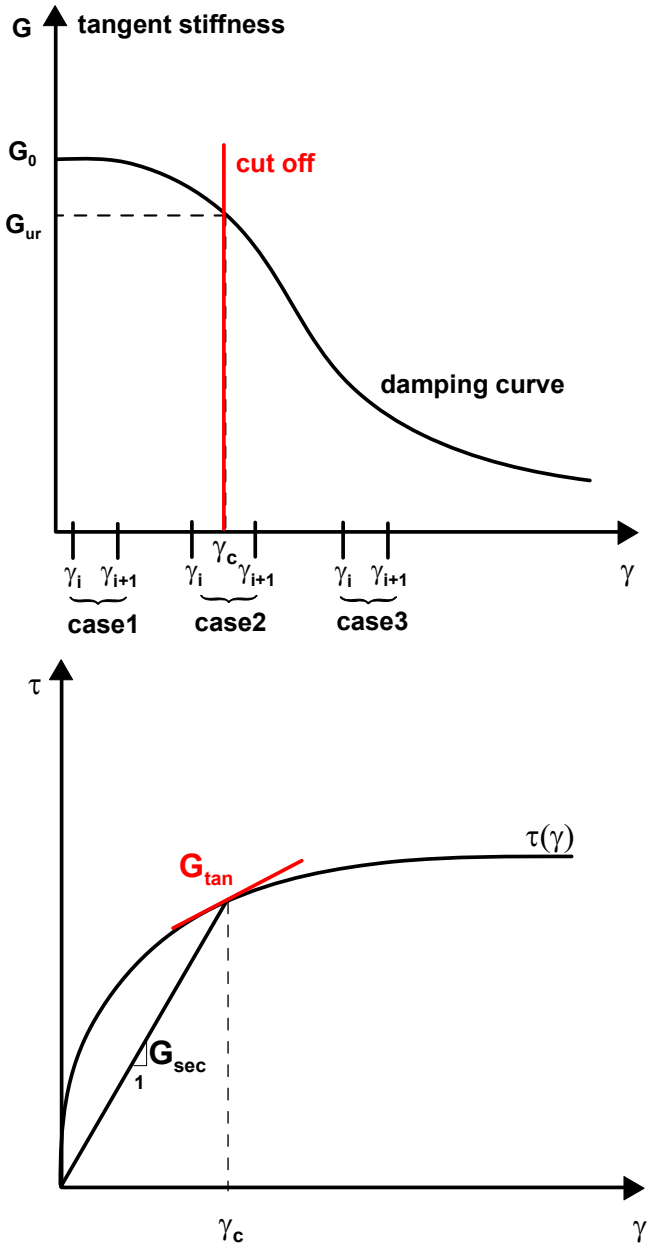

Figure 5.4: cut-off shear strain definition and three possible cases

Small strain stiffness evaluation: stress dependency

Once that the elastic shear stiffness G is evaluated, throughout the Poisson's ratio v, the Young modulus E and the bulk modulus K are interrelated as in Equation (1.42):

$$K = \frac{E}{3(1-2v)} = G\frac{2(1+v)}{3(1-2v)} \tag{1.42}$$

The formulation herein proposed uses a constant Poisson's ratio $v = const$.

In the Soft Soil creep model K is taken stress dependent, analogously to Janbu' s modulus formulation for the constrained modulus M :

$$M = \frac{d\sigma'_z}{d\varepsilon_v} = M_{ref}\left(\frac{\sigma'_z}{\sigma_{ref}}\right) = \frac{\sigma'_z}{\lambda^*} = M(\sigma'_z) \tag{3.47}$$

This formulation in fact gives a constant value of the compression index $\lambda^* = \frac{\sigma_{ref}}{M_{ref}} = const$

that is the slope of the stress-strain relation semi-logarithmic scale:

$$\varepsilon^{ep}{}_v = \lambda^* \cdot \ln\frac{\sigma'_z}{\sigma'_{z,0}} = \lambda^* \cdot \ln\frac{p'}{p'_{z,0}} \qquad \text{(3.50) and (3.53)}$$

For further details the reader is send back to Chapter 3.

As regard to the elastic part, analogously to the elasto-plastic slope above described, it holds:

$$\varepsilon^{e}{}_v = \kappa^* \cdot \frac{dp'}{p'} = \frac{dp'}{K} \tag{3.57}$$

$$\Rightarrow K = \frac{p'}{\kappa^*} = \frac{p_{ref}}{\kappa^*} \cdot \frac{p'}{p_{ref}} = K_{ref} \cdot \frac{p'}{p_{ref}} = K(p') \tag{3.58}$$

where the unloading reloading index $\kappa^* = p'/K$ is taken as a constant.

Since the bulk modulus K and the shear modulus G are interrelated by means of the Poisson's ratio, the stress dependency of the first reflects to the latter as well:

$$G = G_{ref} \cdot \frac{p'}{p_{ref}} = K(p') \tag{5.12}$$

being the reference pressure $p'_{ref} = 100kPa$ in this formulation.

In the proposed model the shear modulus is stress-dependent along the whole reduction curve including the initial shear stiffness G_0. The previously discussed void ratio and OCR dependency of G_0 is neglected in the current model.

In other words one fixed value for the reference initial shear stiffness G_0 is given, together with the threshold strain amplitude parameter $\gamma_{0.7}$. By means of these two parameters, depending on the strain amplitude level, the actual reference stiffness value is deduced. This is then modified on the basis of the stress level resulting in the actual shear stiffness G_{ref}. Through Poisson's ratio the corresponding bulk modulus K is found. From the latter $\kappa^* = p'/K$ is deduced. In contrast to the simple Soft Soil Creep model the unloading reloading index $\kappa^* = p'/K$ is now formulated as strain-dependent.

The cut-off value of unloading-reloading stiffness G_{ur} is therefore linked with the unloading-reloading index κ^* one would have used in the creep model without taking into account small strain behaviour. In other words once $\kappa^* = const$ is given as an input, the bulk modulus in unloading reloading large cycles is deduced as $K_{ur} = p_{ref}/\kappa^*$ and then $G_{ur} = K_{ur}\frac{3(1-2\nu)}{2(1+\nu)}$.
All these values are referred to the reference stress, being the stiffness linearly stress dependent in the Soft Soil Creep model framework.

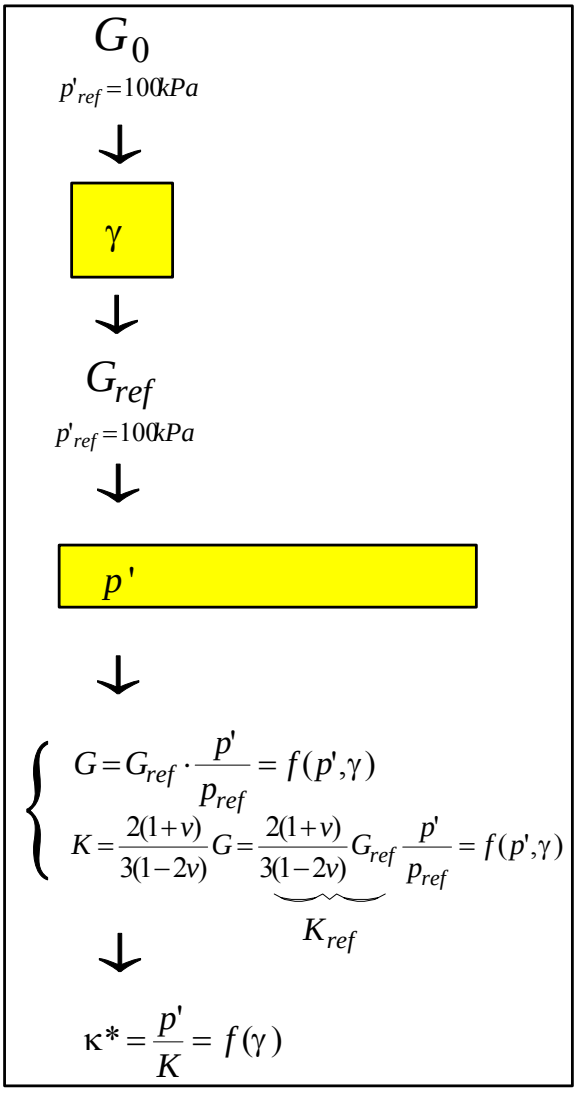

Figure 5.5:strain and stress dependency of stiffness in modified creep model

Small strain stiffness evaluation: Masing's rules

As pointed out in Chapter 4, once the direction of loading is reversed, the stiffness regains a maximum recoverable value. This behaviour is expressed in the first Masing's rule that predicts an unloading initial modulus equal to the initial tangent modulus for the loading curve. While loading in reversed direction is continued, the stiffness decreases again.

From a modelling point of view it is therefore essential to keep track of the material's strain history. In a one-dimensional formulation this is straight forward: Load is not reversed if $d\gamma_i \cdot d\gamma_{i+1} > 0$. Otherwise, strain direction has changed and so the tangent stiffness has to be calculated imposing $\gamma_i = 0$ thus obtaining:

$$G_{i+1} = \frac{G_0}{1 + a\dfrac{\gamma_{i+1}}{\gamma_{0.7}}} \tag{5.13}$$

The second Masing's rule states that the shape of the unloading and reloading curve is equal to the initial loading curve except for the scale that is enlarged by a factor of two. This rule is obeyed in the model by checking whether the actual strain level is lower the maximum strain amplitude ever reached ($\gamma_{i+1} < \gamma_{\max}$). If so, the whole damping curve it scaled by setting:: $\gamma_{0.7_{ur}} = \gamma_{0.7} \cdot 2$.

In a three-dimensional formulation the implementation of both Masing rules is more complex since the model deals with tensors and matrices and not with scalar values. Benz, 2006, for example, suggested a scalar valued strain history variable, that is calculated from a strain history tensor. On the other side in a three-dimensional formulation the material memory required to enforce the second Masing rule can be defined in strain space by memorizing the minimum stiffness in loading history $G_{\min}$: for a given strain increment, it is always assumed first that the material is unloaded or reloaded. If:

$$G_{i+1} = \frac{G_0}{1 + a\dfrac{\gamma_{i+1}}{\gamma_{0.7_{ur}}}} \geq G_{\min} \tag{5.14}$$

holds, the assumption is verified, otherwise primary loading is indicated. This solution leads to a slightly different result with reference to the one-dimensional simpler formulation.

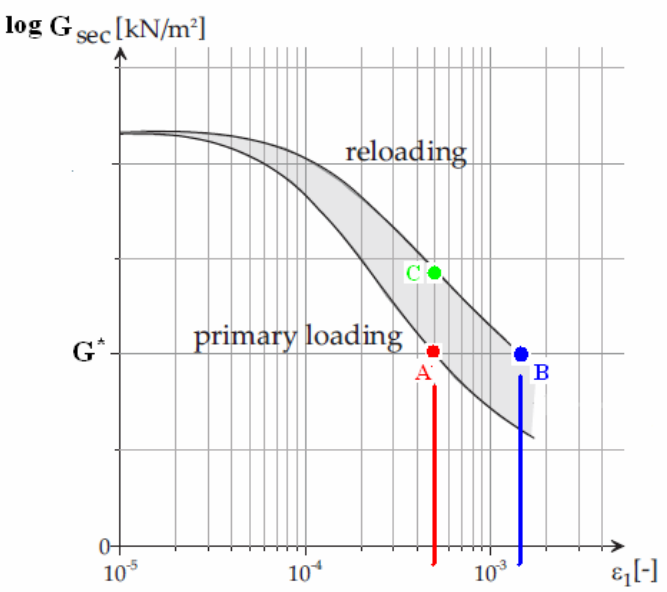

Figure 5.6: primary loading and unloading-reloading stiffness reduction curve

Let suppose in fact that a $G*$ value is reached moving on the first loading stiffness reduction curve until point A in Figure 5.6. Then the sample is unloaded and reloaded . In the three-dimensional formulation, the stiffness will move on the less steep curve characterizing the unloading-reloading behaviour until it reaches the minimum stiffness value ever reached (point B in Figure 5.6) and then it will pass on the primary loading curve again. In this case the strain amplitude value at which this happens is higher than the maximum ever reached.

In the one-dimensional formulation, since the control is on the strain amplitude and not on the modulus, the stiffness will pass from the unloading-reloading curve to the primary loading one once the previous maximum shear strain amplitude is reached (point C in Figure 5.6):this will happens at a higher stiffness value level. In this latter case the third Masing's rule is fulfilled: unloading and reloading curves should follow the initial curve in case the previous maximum shear strain is exceeded. In the three-dimensional formulation, using the control on G they do not.

The fourth Masing rule("if the current loading curve in stress-strain space intersects a previous one, it should follow the previous curve") is neglected in both the formulations.

Creep formulation: oedometric conditions

In oedometric conditions, the strain amplitude coincides with the axial strain: $\gamma_s|_{oedom} = \varepsilon_a - \varepsilon_r = \varepsilon_a$. The stress path is described by a straight line in p', q stress space with slope equal to:

$$\eta_{k0} = \left.\frac{q}{p}\right|_{\varepsilon_r = 0} = \frac{(1-K_0)}{(1+2K_0)} \tag{3.99}$$

since: $\sigma'_r = K_0 \cdot \sigma'_z$ where K_0 is the earth pressure at rest coefficient.

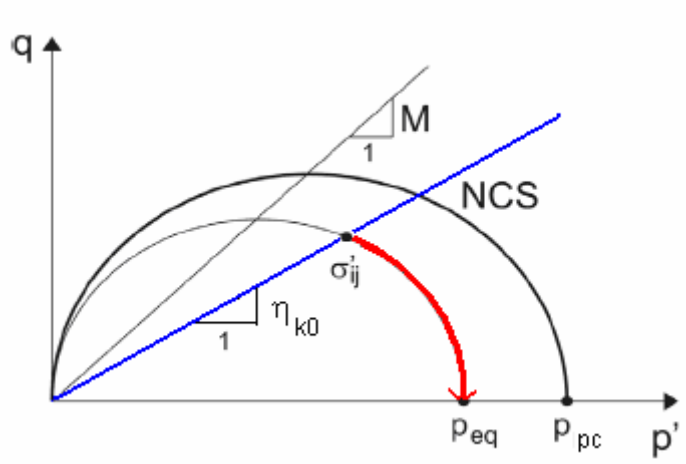

Figure 5.7: the oedometric stress path in stress plane, in the framework of Modified Cam Clay ellipses representing the creep rate contour

K_0 is evaluated using the well known formula by Jacky: $K_0 = 1 - \sin\varphi$. K_0 is used in calculating the mean stress and the deviator stress from the vertical stress. Vertical or axial stress is directly measured in an oedometer test.

Since the Modified Cam Clay ellipses are taken in the model as contours of volumetric creep rate and the creep rate is strictly OCR dependent:

$$\dot{\varepsilon}_v^{creep} = \frac{\mu^*}{\tau}\left(\frac{p'}{p'_{pc}}\right)^{\frac{(\lambda^*-\kappa^*)}{\mu^*}} = \frac{\mu^*}{\tau}\left(\frac{1}{OCR}\right)^{\beta} \tag{3.81}$$

the best way to define the OCR is to refer the stress state to a scalar quantity that represents the vertex of the ellipse:

$$p'_{eq} = p' + \frac{q^2}{M^2 p'} \tag{3.98}$$

As already highlighted in Chapter 5, p_{eq} projects the general stress state (p', q) to the isotropic axis. In this way the bi-dimensional problem is simplified to a one-dimensional one. In an oedometric stress condition the projection gives:

$$p'_{eq} = p'\left(1 + \left(\frac{\eta_{k0}}{M}\right)^2\right) \tag{3.99}$$

The overconsolidation ratio is be defined with reference to Figure 5.7 as:

$$OCR = \frac{p'_{pc}}{p'_{eq}} \tag{5.15}$$

Hence the equation to be integrated is :

$$d\varepsilon_v = d\varepsilon_v^{\,e} + d\varepsilon_v^{\,c} = \frac{dp'}{K} + \mu^* \ln\left(1 + \frac{dt}{\tau \cdot \left(\frac{p'_{pc}}{(p'+dp')\left(1+\left(\frac{\eta_{k0}}{M}\right)^2\right)}\right)^{\beta}}\right) \quad (5.16)$$

where: $\tau = \frac{\lambda^*}{\beta} \cdot \frac{1}{\dot{\varepsilon}_{v\,NC}}$ (Equation (3.96)). For the simulation of a CRS test (see Chapter 3), the total strain increment and the elapsed time are given as input variables same as in the formulation proposed above.

The OCR is given with reference to the final stress state, at the end of primary consolidation. The final OCR value, after creep, takes into account the increase in preconsolidation pressure due to secondary compression (hardening rule):

$$p'_{pcnew} = p'_{pc} \exp\left(\frac{d\varepsilon_v^{\,creep}}{\lambda^* - \kappa^*}\right) \quad (3.80)$$

Theoretically three are three OCR values for each stress: an initial one, with the non-updated stress state, the value with the updated stress state (end of primary consolidation stage) and the final value with the incremented preconsolidation pressure:

1) $OCR_0 = \frac{p'_{pc}}{p'_{eq}}$

2) $OCR_{EOP} = \frac{p'_{pc}}{(p'+dp')_{eq}}$

3) $OCR_f = \frac{p'_{pcnew}}{(p'+dp')_{eq}}$

OCR_f coincides with OCR_0 of the following load step (see Figure 5.8).

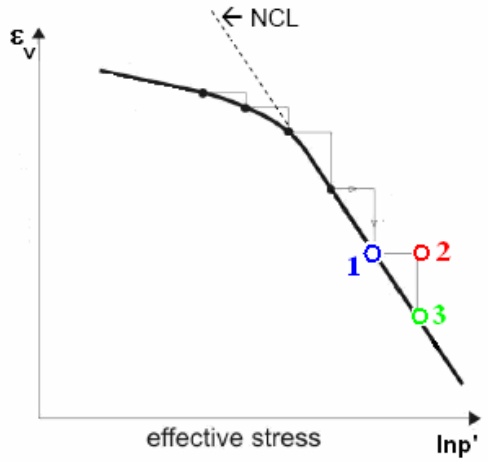

Figure 5.8:OCR values in an oedometer step

This subdivision has more relevance in the framework of a multiple stage loading test in which the three OCR value correspond to three specific moment in the compression process (see Figure 5.8), while in a CRS test they are not so well-defined.

Solving the volumetric strain equation for the mean effective stress increment dp' leads to the new stress state $p' = p' + dp'$ and $q = q + dq = \eta_{k0} p'$ in oedometric condition. From the latter, dq is calculated.

Elastic strain increment components (volumetric and deviatoric) are thus deducted from Equation (1.18):

$$d\varepsilon^e{}_v = \frac{dp'}{K} \text{ and } d\varepsilon^e{}_q = \frac{dq}{3G} \tag{1.18}$$

The creep volumetric component is, from Equation (5.16):

$$d\varepsilon_v{}^c = \mu^* \ln\left(1 + \frac{dt}{\tau \cdot \left(\frac{p'_{pc}}{(p' + dp')\left(1 + \left(\frac{\eta_{k0}}{M}\right)^2\right)}\right)^{\beta}}\right) \tag{5.16}$$

while the deviatoric creep component is given by the associated flow rule that links the deviatoric component to the volumetric component as follows:

$$d\varepsilon_q{}^c = d\varepsilon_v{}^c \frac{\partial p_{eq} / \partial q}{\partial p_{eq} / \partial p'} = d\varepsilon_v{}^c \frac{2\eta_{k0}}{M^2 - \eta_{k0}{}^2} \tag{3.104}$$

the second term being in oedometric conditions.

Parameter review and algorithmic setting

As already mentioned, the model modification introduces two new parameters, that are G_0 and γ_c. The first can be correlated to the initial soil state and the second to the friction angle, so, in the end, there is no need to introduce anything new if one trusts those correlations.
In the formulation herein presented, however, the newly introduced parameters are kept as independent input parameters.

Indeed, the input parameters can be divided into five classes, reported in Table 5.1, being the first the second and the third columns report model parameters properly, while the fourth and the fifth columns report the initial soil state and the strain rate one would choose.

	material	elastic	creep	initial state	strain rate
input					
	φ friction angle	ν Poisson's ratio	λ^* compression index	$\sigma'_{z0}, \sigma'_{r0} = K_0 \sigma'_{z0}$ initial stress state	$d\varepsilon_z$ vertical strain increment
		κ^* unloading-reloading index	μ^* creep index	$OCR = \sigma'_{z,pc} / \sigma'_z$ overconsolidation ratio	dt creep time increment
		G_0 initial stiffness		$\varepsilon_{z0}, \varepsilon_{r0}$ initial strain state	
		γ_{07} reference strain amplitude			
derived					
	M critical state slope	G_{ur} larger strains shear stiffness	$\beta = \frac{(\lambda^* - \kappa^*)}{\mu^*}$	$p'_0, q_0, p'_{eq,0}$ stress state in terms of invariants	$d\varepsilon_v, d\varepsilon_q$ volumetric and deviatoric strain increments
	K_0 at rest coefficient	K_{ur} larger strains bulk modulus		$p'_{pc}, p'_{pc,eq}$ preconsolidation pressure in terms of invariants	$\dot{\varepsilon}_v$ volumetric strain rate
	$\eta_{k0} = \frac{(1-K_0)}{(1+2K_0)}$ oedometric slope	γ_c cut-off strain amplitude		$\varepsilon_{v0}, \varepsilon_{q0}$ initial volumetric and deviatoric strains	$\tau = \frac{\lambda^*}{\beta} \cdot \frac{1}{\dot{\varepsilon}_v}$ reference time

Table 5.1: small strain creep model input

As a material parameter the friction angle φ is given. From this the critical state constant and the at rest coefficient are derived and finally the slope of the oedometric stress path set.

Then there are the elastic parameters besides the small strain stiffness and the threshold strain amplitude: basically they are the Poisson's ratio and the unloading reloading index κ^*, the latter allowing to define the stiffness for larger strain and consequently the corresponding cut off strain values G_{ur} and K_{ur}.

The third group includes the other two compression indexes: the compression index λ^* and the creep indexes μ^*. The relationship between the three compression indexes κ^*, λ^* and μ^* are well-examined and correlated by Kulhawy and Mayne (1990) as:

$$\kappa^* \approx \frac{\lambda^*}{5} \tag{5.17}$$

and

$$\mu^* \approx \frac{\lambda^*}{30} \tag{5.18}$$

The input phase is then followed by the stiffness evaluation and solving for the stress increment dp' corresponding to the strain increment $d\varepsilon_v$ developed in an elapsed time t. Once dp' is known the creep component of the total strain increment is given as well and thus the new preconsolidation pressure can be updated, and a new strain increment can be imposed. The whole process is summarized in the following flow chart:

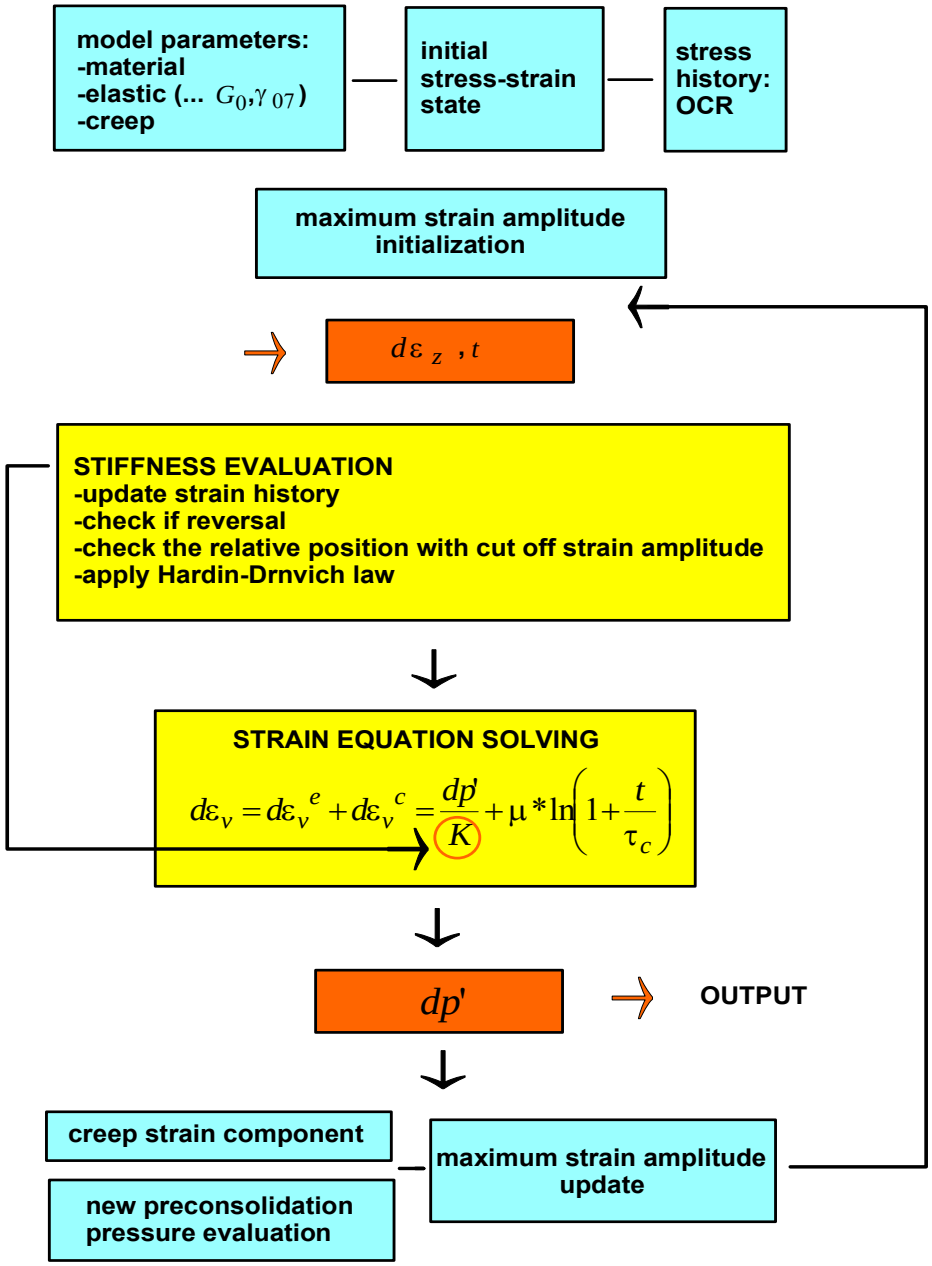

Figure 5.9: model's flow chart

The one-dimensional code written with Mathematica6 language is reported at the end of the Chapter.

Two choices for beta parameter

As pointed out before, the main improvement of the modified creep model herein presented is the strain dependency of the unloading reloading index $\kappa^* = \frac{p'}{K}$ where $K = K_{ref}\frac{p'}{p'_{ref}}$ with $K_{ref} = G_{ref}\frac{2(1+\nu)}{3(1-2\nu)}$.

In fact, since the bulk modulus is taken linearly stress dependent, the unloading-reloading index does not depend on the stress state:

$$\kappa^* = \frac{p'_{ref}}{K_{ref}} \tag{5.19}$$

but with the new formulation K_{ref} is strain amplitude dependent and so does κ^*.

In Figure 5.10 the evolution with strain of tangent G_{ref} in logarithmic scale is shown for: $G_0 = 100.000kPa$, $\gamma_{0.7} = 0.0001, \kappa^*_{ur} = 0.004$ which corresponds to $G_{ur} = 10.000kPa$. In Figure 5.11, besides the G_{ref} reduction, two curves are given for κ^*: one for the primary loading condition and the second for the unloading –reloading path in which the second Masing's rule is applied and κ^* is scaled.

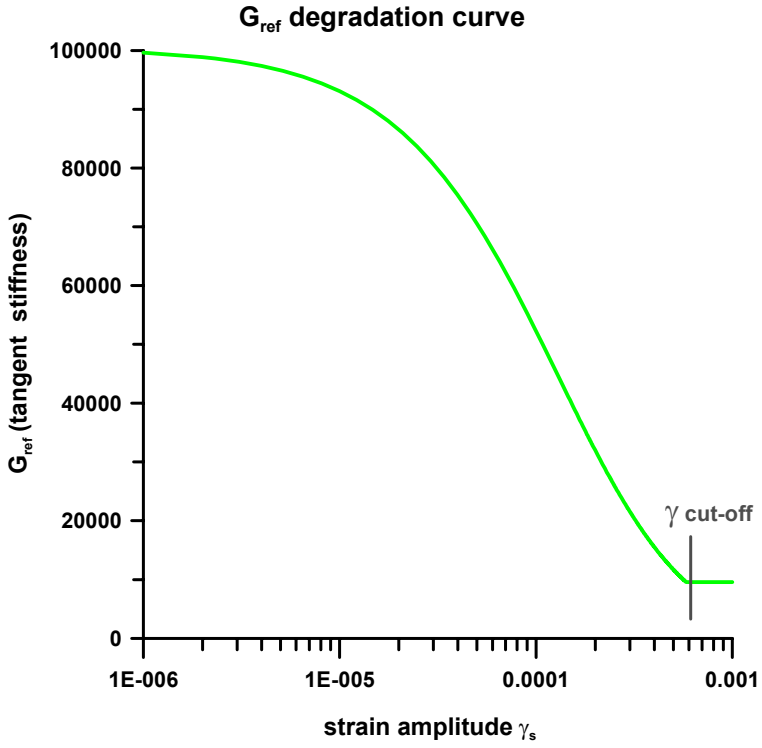

Figure 5.10:stiffness degradation curve in semi-logarithmic space

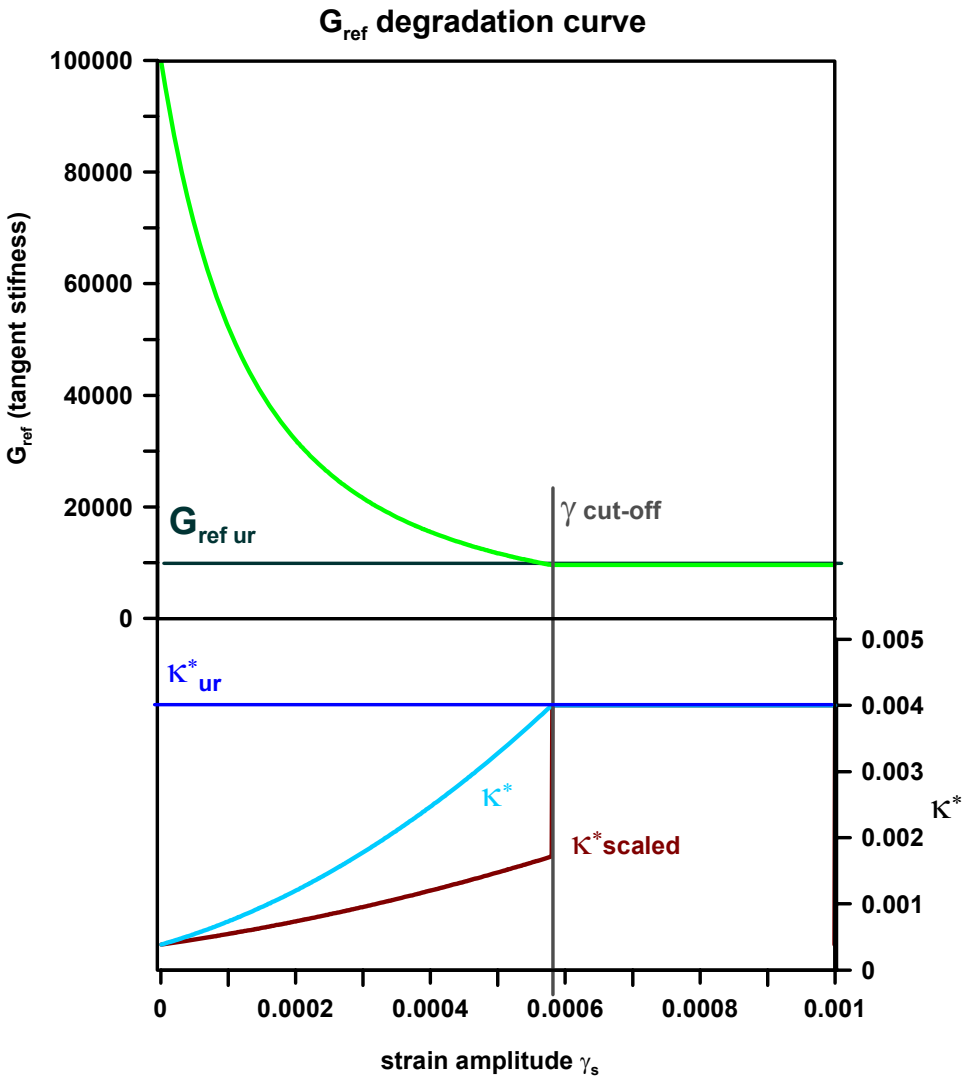

Figure 5.11: stiffness degradation and consequently κ^* evolution with strains, both in primary loading and in unloading-reloading

As a consequence of having a strain dependent κ^*, there are now at least two choices in defining the β parameter:

$$\beta = \frac{\lambda^* - \kappa^*}{\mu^*} \tag{3.75}$$

which in the classical creep formulation is constant, as all the three compression indices are constant.

In the modified formulation for small strain, β can still be assumed to be constant thus giving a strain dependent $\lambda^* = \beta \cdot \mu^* + \kappa^*(\gamma)$. or λ^* can be taken as a constant, and β varies correspondently. In the first case the distance between the two parameters values is $\beta \cdot \mu^* = const$ as shown in Figure 5.12. In the second case β diminishes as κ^* increases as the sum $\beta \cdot \mu^* + \kappa^* = const$ (Figure 5.14). Both assumptions affect the slope of the normally consolidated line. The normal consolidation line differs slightly from λ^* as shown in Figure 5.14. In both cases after the strain cut-off value, the slope tends to λ^* value.

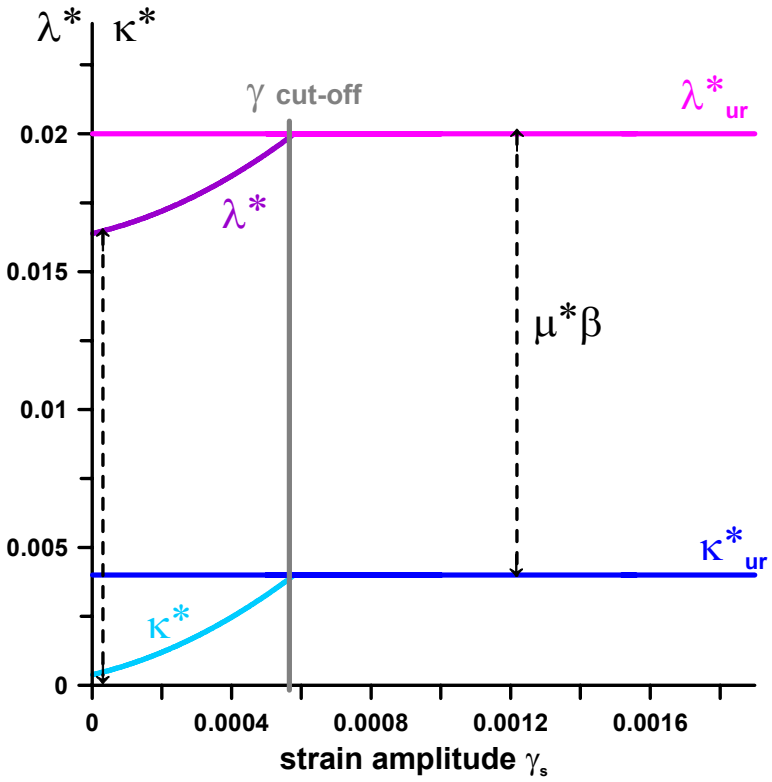

Figure 5.12: parameters' evolution keeping β constant

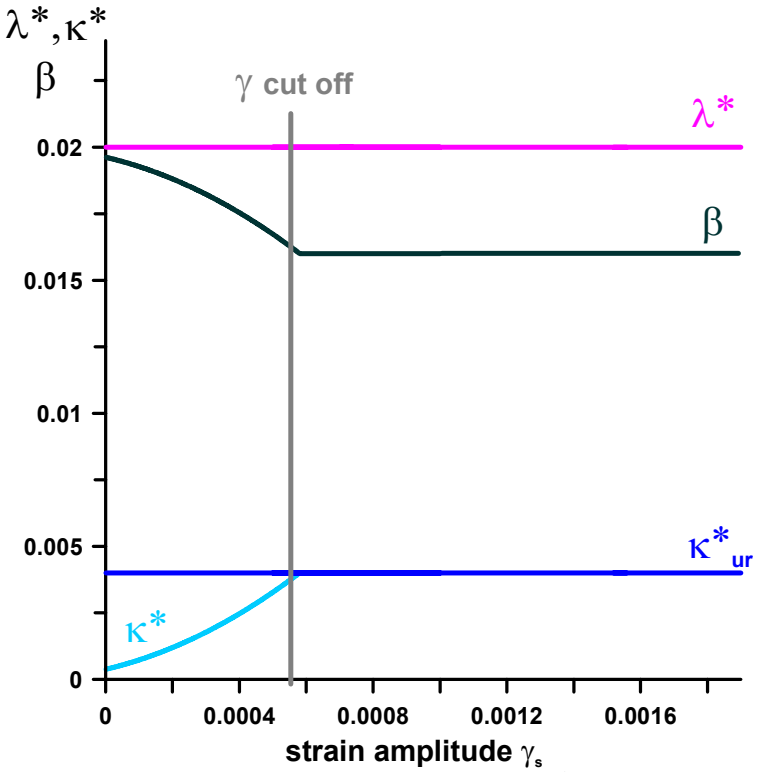

Figure 5.13:parameters evolution keeping λ^* constant

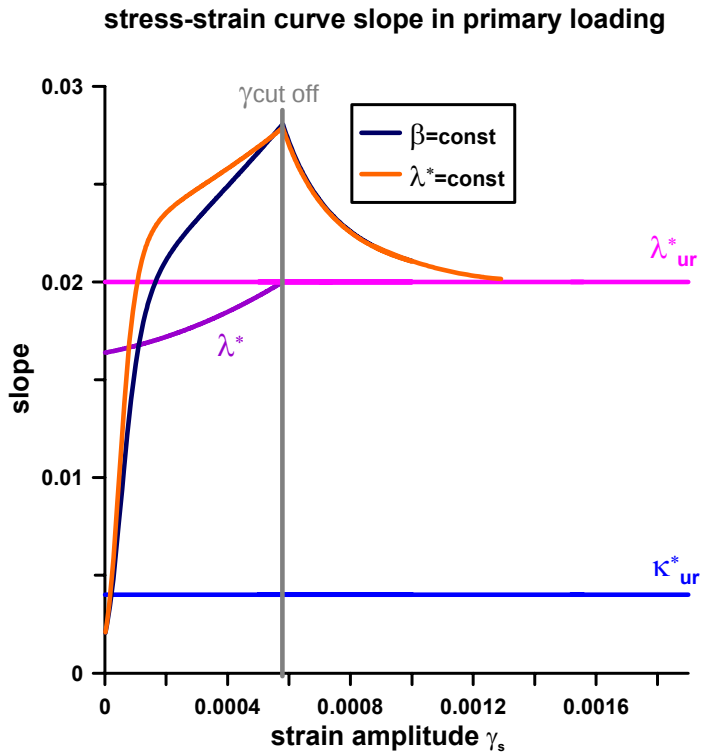

Figure 5.14: slope of the compression curve with the modified creep model

The differences between the two choices, indeed, $\beta = const$ or $\lambda^* = const$ are so small that can be considered negligible, and $\beta = const$ case has been chosen in order to model stress strain behaviour. In both cases, as expected, the very initial slope is lower because the soil is stiffer. Then there is a transitional phase before the slope finally equals to $\lambda^*(ur)$ for larger strains. In Figure 5.15 a simulation with the soft soil creep without small strain stiffness modification and with both the cases ($\beta = const$ and $\lambda^* = const$) are presented.

G_0	100.000 kPa
γ_{07}	0.0001
λ^*	0.02
κ^*	0.004
μ^*	0.001
$\dot{\varepsilon}_v$	0.001
OCR	1

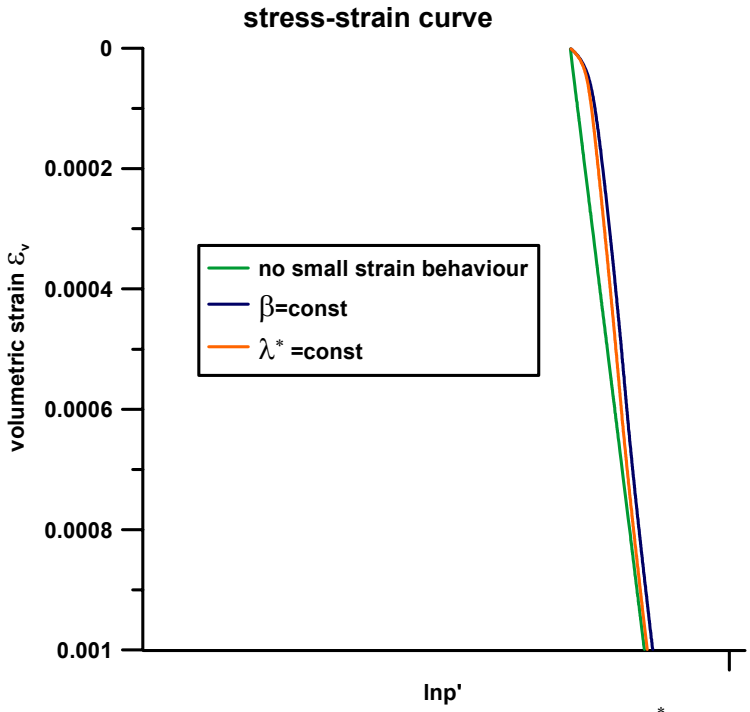

Figure 5.15: compression curve at early stages with the creep model and the modified ones ,keeping λ^* or β constant

Unloading reloading cycles

The difference between the creep model with the small strain formulation and without it, becomes significant in unloading and reloading cycles.

In Figure 5.16 a compression curve with one unloading-reloading cycle is presented. Figure 5.17 shows the same simulation with a larger unloading reloading cycle. The main parameter values are the same used in the previous simulation (Figure 5.15).

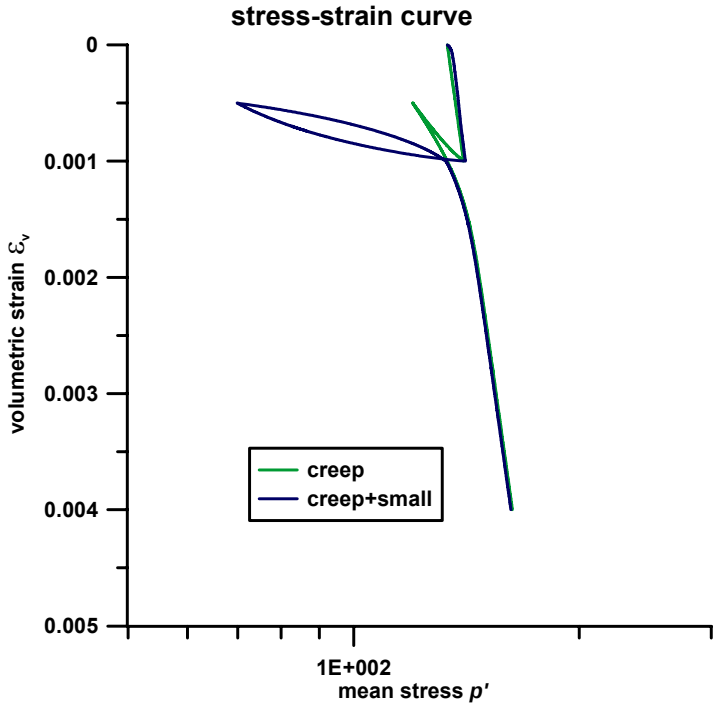

Figure 5.16: stress-strain curve with and without small strain stiffness with unloading-reloading cycle

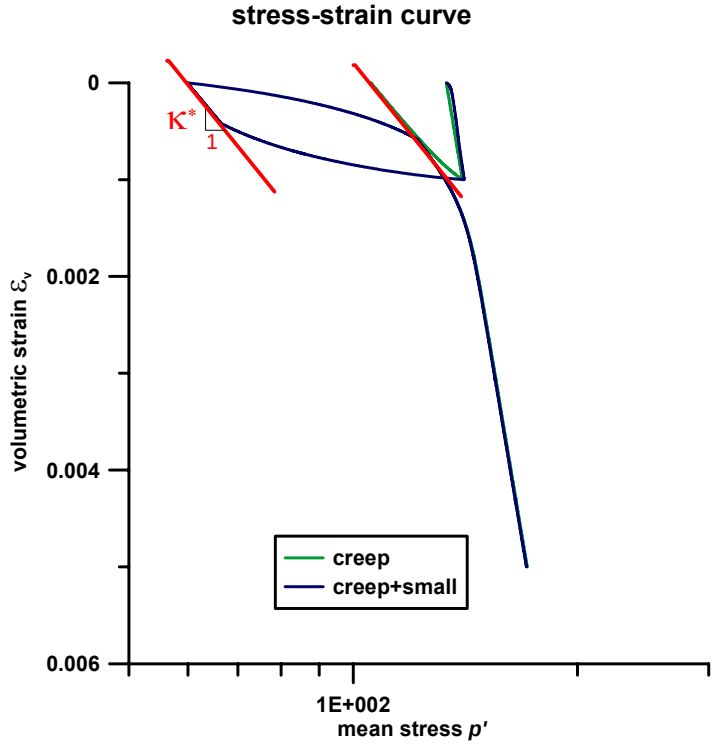

Figure 5.17:stress strain curve with and without small strain stiffness with larger unloading-reloading cycle

It is evident that there is a significant difference in unloading-reloading path between the formulation without the small strain stiffness and the one with small strain stiffness, the latter showing a stiffer behaviour. Initial stiffness is very high, then it decreases with strain. Once there is a reversal the stiffness recovers its high initial value and then decreases again.

For larger unloading reloading cycles, i.e. when the strain amplitude goes beyond the cut-off limit, the stiffness reaches the lower value G_{ur} used in the formulation without small strain stiffness, and so does the slope that reaches the higher value κ^*_{ur} (Figure 5.17).

While in very left part of the cycle (high OCR) the slope value is effectively κ^*_{ur}, on the right part, in the proximity of the normally consolidated line it is not. The unloading-reloading cycle does not close perfectly on the normally consolidated line. This is also a feature of the creep model, not depending on the small strain behaviour. As already mentioned before in fact, the normally consolidated line does not represent a real yield surface since creep can occur even in over-consolidated states. The total strain increment is thus always given by the elastic term and the creep term.

$$d\varepsilon_v = d\varepsilon_v^{\,e} + d\varepsilon_v^{\,c} = \kappa^* \frac{dp'}{p'} + \frac{\mu^*}{\tau}\left(\frac{1}{OCR}\right)^{\beta} \tag{3.78}$$

In the proximity of the normally consolidated line OCR is almost equal to one and gives a considerable contribution to the total strain, while for higher value its contribution is negligible. In the case of unloading this implies that nearby the NCL the slope is lower than κ^* since the creep strain has opposite direction than the elastic strain; in reloading, on the contrary, the two contribution add each other so the slope is higher than κ^*. This holds in the vicinity of the normally consolidated line, while where OCR is high the slope is approximately κ^*. When reloading, thus, the slope moves from κ^* far from the NCL, then it approaches values a bit higher than κ^* near the NCL, and then increases again until it reaches λ^* because the stress-strain state moves on the normally consolidation line.

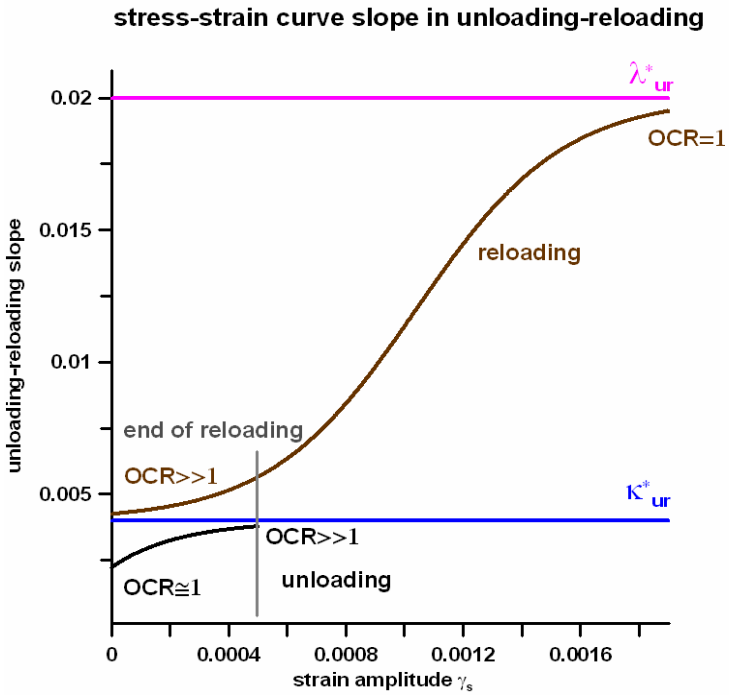

Figure 5.18: slope of unloading reloading curve for the formulation without small strain stiffness

Exactly the same happens in the formulation that accounts for the small strain stiffness behaviour. This aspect, however, does not influence the overall behaviour, the deviation being very small.

If one performed more than one unloading-reloading cycle, slopes for the cycles are the same, the result depending on the distance from the normally consolidation line only, since κ^* is strain dependent only, being the slope in semi-logarithmic plane. An example of two unloading –reloading cycles is given in Figure 5.19.

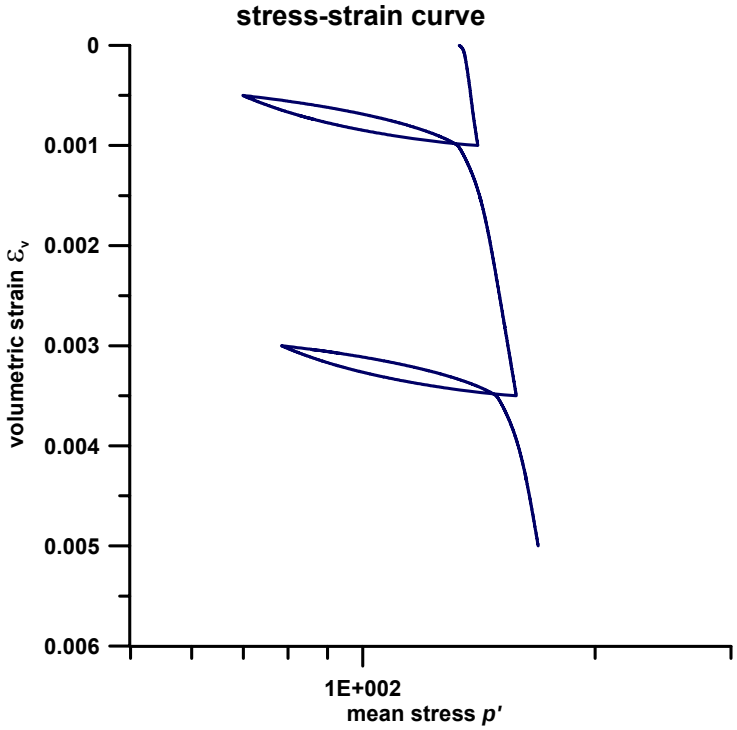

Figure 5.19: two unloading-reloading cycles

Stress dependent moduli: thermodynamic considerations

It has long been recognized that in a consolidation test on soil sample, the volumetric strain varies approximately linearly with the logarithm of the mean effective stress and this leads to the adoption of an elastic bulk modulus which varies linearly with pressure (Equation (3.58)). Of the four elastic constants, E, ν, G, K, only two are independent for an isotropic elastic material. If a constant value of Poisson's ratio ν is chosen and the shear modulus G is deduced from the Hookean relations (Equation (1.42)), the shear modulus is proportional to the mean stress as well (Equation (5.12)).

Such a formulation is not conservative since energy may be continuously extracted from the soil sample by subjecting it to a simple stress cycle (Zytynski et al., 1977). The proposed model is therefore not thermodynamically sound.

Indeed, it has constitutive ingredients that reflect real soil behaviour and performs reasonably well in the cases it has been tested in, as later discussed in Chapter 9.

Appendix: one-dimensional Creep Small code

```
(*FUNCTION TO BE INTEGRATED*)
F=dp/Ks+mistar*Log[1+t/tau*(ppiso/((p+dp)*(1+(eta/M)^2)))^(-beta)]-depsv;
Der=D[F,dp];
(*tolerance*)
tol=0.0001;
nmax=50;


(*INPUT parameters and derived parameters*)

(*elastic parameters*)
v=0.31;
kappastar=0.0062;(*input*)
Kurref=100/kappastar;
Gurref=3*(1-2*v)*Kurref/(2*(1+v));
G0=100000;
gamma07=0.0001;
a=0.385;
gammac=(gamma07/a)*((G0/Gurref)^1/2 -1);


(*material parameters*)
ψ=33;(*deg*)
φ=(ψ*Pi)/180; (*rad*)
M=1.3353;
K0=1-Sin[φ];
eta=3*(1-K0)/(1+2*K0);


(*material parameters creep part*)
mistar=0.001;(*input*)
lambdastar=0.032;(*input*)
beta=(lambdastar-kappastar)/mistar;


(*initial stress state*)
sigmaa0=50;(*input*)
sigmar0=K0*sigmaa0;
p0=(sigmaa0+2*sigmar0)/3;
q0=sigmaa0-sigmar0;
peq0=p0*(1+(eta/M)^2);


(*history*)
ocierre=6.6;(*from vertical stress in oedometric conditions*)
sigmaapc=ocierre*sigmaa0;
sigmarpc=K0*sigmaapc;
ppc=(sigmaapc+2*sigmarpc)/3;
pp0iso=ppc*(1+(eta/M)^2);(*initial isotropic preconsolidation pressure value*)


(*initial strain state*)
epsa0=0.001495;
epsr0=0;
epsv0=epsa0+2*epsr0;
epsq0=epsa0-epsr0;(*in reality it is gamma=3/2 depsq*)

(*strain increments*)
```

```
depsa=0.0001;(*input*)
depsr=0;
depsvb=depsa+2*depsr;
depsqb=depsa-depsr; (*dgamma in reality*)
b=Abs[depsqb];
lmax=270;(*input*)
umax=357;(*input*)
rmax=868;(*input*)


(*strain rate*)
t=0.1;
totrate=depsvb/t;
tau=lambdastar/(beta*totrate);(*input?*)


(*initialization*)
ppiso=pp0iso;
p=p0;
q=q0;
epsa=epsa0;
epsr=epsr0;
epsv=epsv0;
epsq=epsq0;
epsqmax=epsq;
depsqprec=1;
gamma2=epsq;
z=0;

(*LOADING*)
 (*for each step*)
For[i=1,i≤lmax,i++,
  depsv=depsvb;
  depsq=depsqb;

(*G evaluation*)

  (*gamma07 evaluation: if loading or unloading-reloading checking the maximum strain amplitude*)
  epsqnew=epsq+depsq;
  If[epsqnew<=epsqmax,
   gamma07new=2*gamma07,
   gamma07new=gamma07 ];

(*if reversed direction*)
  If[ ((depsq*depsqprec<0)) *(then*)
   gamma1=0;
   gamma2=gamma1+b;
   Gref=G0/(1+((gamma2*a)/gamma07new));
   ,(*else*)

(* not reversed direction*)
   gamma1=gamma2;
   gamma2=gamma2+b;

(*both strain amplitudes before cut-off value*)
 If[(gamma1<gammac && gamma2<gammac),(*then*)
    Gref=G0/(gamma2-gamma1)*((gamma2/(1+((gamma2*a)/gamma07new)))-
(gamma1/(1+((gamma1*a)/gamma07new))))
    ,(*else*)
```

```
(*lower strain amplitude before cutoff value, higher strain amplitude beyond the cutoff value*)
If[(gamma1<gammac&&gamma2>gammac),(*then*)
Gref=G0/(gammac-gamma1)*((gammac/(1+((gammac*a)/gamma07new)))-
(gamma1/(1+((gamma1*a)/gamma07new))))
    ,(*else*)

(*both strain amplitudes beyond cut-off value*)
    Gref=Gurref;
    ]]];

(*only creep:Gref=Gurref*)

(* parameters from Gref*)
 G=Gref*(p/100);
 Ks=G*2*(1+v)/(3*(1-2*v));
 kappastar=p/Ks;
 lambdastar=beta*mistar+kappastar;

(*from strain to stress: basic equation solution→dp'*)
 diff=1;
 n=0;
 dp=0;
 While[(diff>tol && n< nmax),
  dpprec=dp;
  dp =dp -(F/Der);
  diff=Abs[dp-dpprec];
  ];
 dq=(p+dp)*eta-q;(*imposing etaK0 path*)
 rd=dq/dp;

(*initial OCR*)
 OCR0=ppiso/(p*(1+(eta/M)^2));

(*elastic strains*)
 depsvel=dp/Ks;
 depsqel=dq/(3*G);

(*creep strains*)
 depsvcreep=mistar*Log[1+t/tau*(ppiso/(p*(1+(eta/M)^2)+dp*(1+(eta/M)^2)))^(-beta)];
 alpha=(2*(q/p))/(M^2-(q/p)^2);(*associated flow rule*)
 depsqcreep=alpha*depsvcreep;

(*plastic volumetric strain rate*)
 vcrate=depsvcreep/t;

(*new stresses*)
 p=p+dp;
 q=q+dq;
 sigmar=(3*p-q)/3;
 sigmaa=q+sigmar;

(*OCR at the beginning of the creep*)
 OCRel=ppiso/(p*(1+(eta/M)^2)); (*used in the equation to be solved in the creep part*)

(*new preconsolidation pressure*)
 ppiso=ppiso*Exp[(depsvcreep/(lambdastar-kappastar))];
 ppcnew=ppiso/(1+(eta/M)^2); (*on the etak0 line*)
 sigmarpc=(3*ppcnew-eta*ppcnew)/3;
 sigmaapc=eta*ppcnew+sigmarpc; (* vertical new preconsolidation pressure*)

(*OCR at the end of the creep*)
```

```
  OCR=ppiso/(p*(1+(eta/M)^2));

(*theoric plastic volumetric strain rate*)
 teorvcrate=(mistar/tau)*((1/OCR)^beta);

(*new strains*)
  epsv=epsv+depsv;
  epsq=epsq+depsq;(*gamma*)
  epsa=epsa+depsa;

(*maximum strain amplitude update*)
 If[epsq>epsqmax,epsqmax=epsq];
  depsqprec=depsq
  ];


(*UNLOADING*)
(*for each step*)
For[i=(lmax+1),i≤umax,i++,
  depsv=-1*depsvb;
  depsq=-1*depsqb;
……

(*RELOADING*)
(*for each step*)
For[i=(umax+1),i≤rmax,i++,
  depsv=depsvb;
  depsq=depsqb;
……
```

Chapter 6 - The Venice Lagoon soils

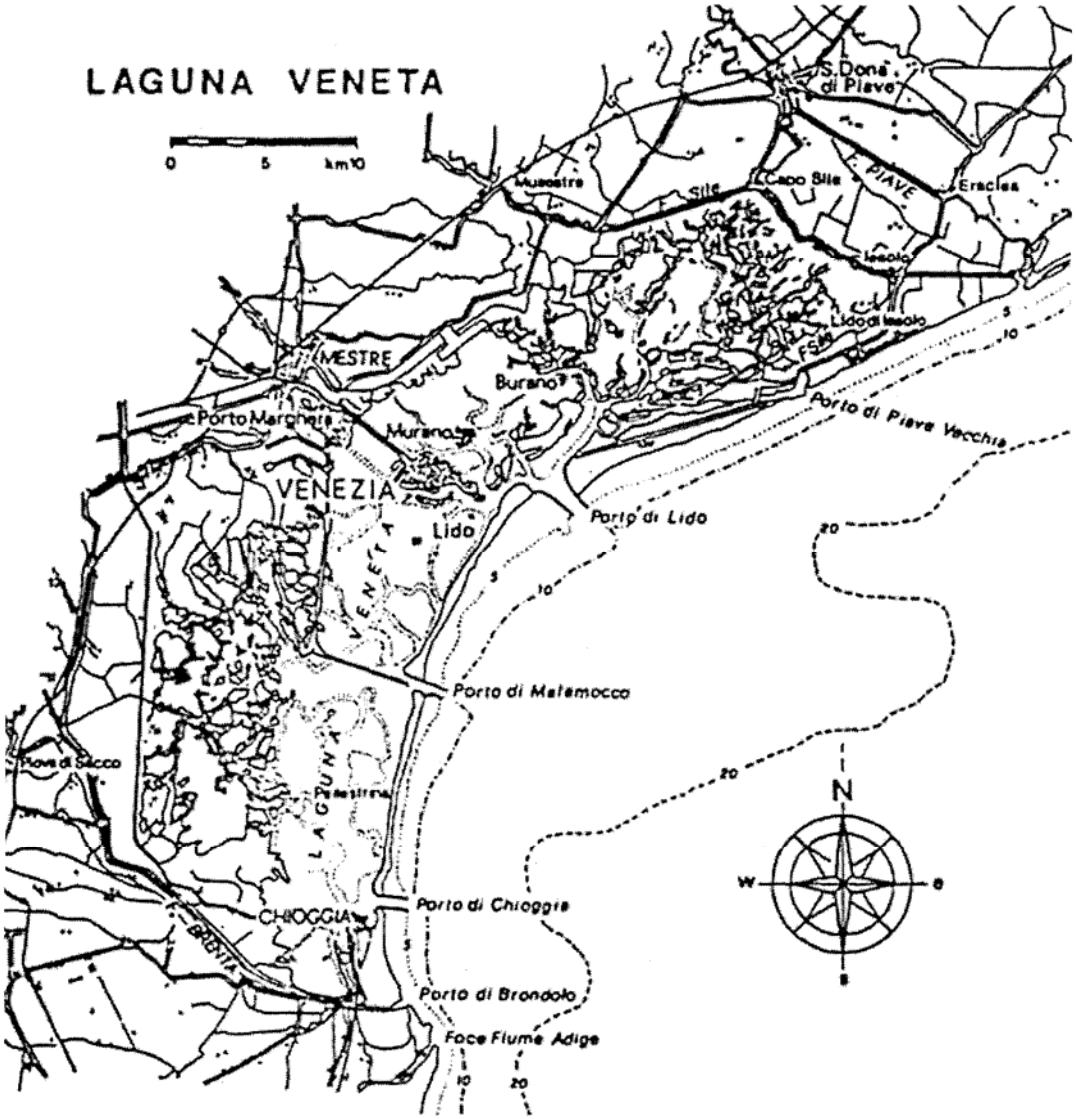

Introduction

The Venetian Lagoon is the enclosed bay of the Adriatic Sea in which the city of Venice is situated. It stretches from the River Sile in the north to the River Brenta in the south, with a surface area of around 550 km². It is around 8% land, including Venice itself and many smaller islands. About 11% is permanently covered by open water, or canal, as the network of dredged channels are called, while around 80% consists of mud flats, tidal shallows and salt marshes.

The lagoon is the largest wetland in the Mediterranean Basin. It is connected to the Adriatic Sea by three inlets: the Lido, Malamocco and Chioggia inlets. Sited at the end of a largely enclosed sea, the lagoon is subject to high variations in water level, that sometimes cause the phenomenon known as the *acqua alta* (literally "high waters"),consisting in the flooding of the city of Venice and its sourroundings.

The worldwide-known historic city, therefore, continues to preserve a rather precarious equilibrium with the surrounding lagoon, although the margin of security is being eroded at an ever increasing rate. The rate of environmental deterioration is being accelerated by the increasing frequency of the flooding of the city caused by the natural eustatic rise of the sea level, by natural subsidence and by a regional man-induced subsidence, the latter particularly important between 1946 and 1970 (Butterfield et al. 2003). Figure 6.1 shows the Venice lagoon in the present configuration: through the inlets of Malamocco, Lido and Chioggia flows the tide, becoming, under particular atmospheric conditions, *acqua alta*, that means flooding of the historic city. Figure 6.2 illustrates eustasy and subsidence evolution during the last century.

Figure 6.1: Venice lagoon with its three inlets

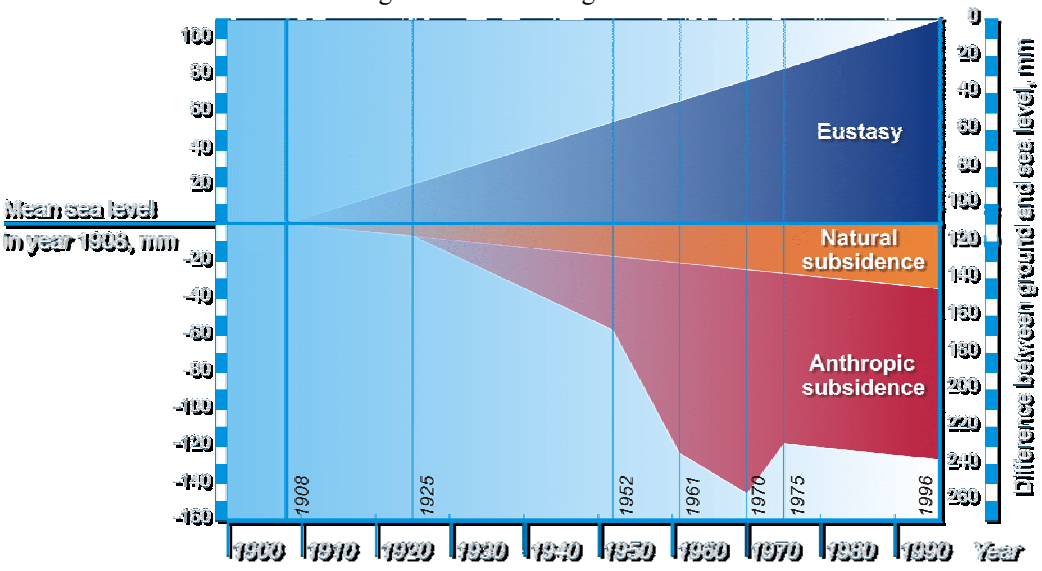

Figure 6.2: eustasy and subsidence in the Venice lagoon (Simonini, 2006)

Geological evolution

The Northern Italian lowlands, namely the Padana and Veneta plains, were formed through the fluvial transport of sediments coming from the erosion of the surrounding Alps and Apennines. At the end of the Pliocene epoch, the sea level was much higher than today and the Padana and Veneta plains were submerged. The Pleistocene epoch was characterized by several glaciation and interglaciation periods with alternating regression and transgression of the shoreline. At the apex of last Würmian (Wiscontsinian) glaciation, the shoreline was located around two hundred kilometres from the present position and, therefore, the Padana and Veneta plains together with a part of the Northern Adriatic Sea were emerged. Then, a warmer period set in about 15,000 years ago and the sea level rose during the de-glaciation period, reaching, between 7000 and 5000 years ago, a value slightly higher than the present one. The origin of the Venice lagoon is traced around 6000 year ago, during the flandrian transgression, with the sea water diffusing into a pre-existing lacustrine basin.

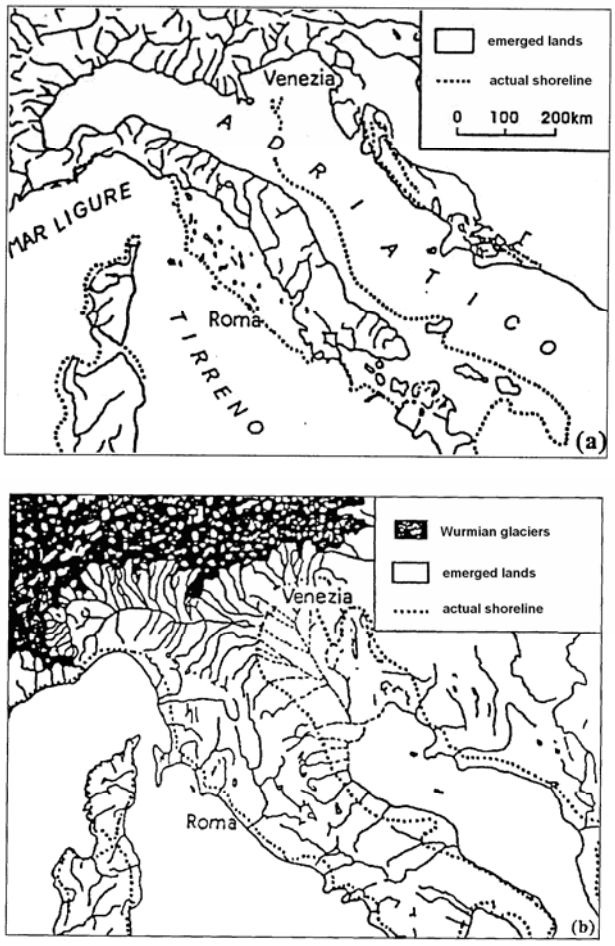

Figure 6.3: shoreline at the end of Pliocene(a), at the end of Pleistocene (b)

In the Venetian lagoon, the upper hundred metres below mean sea level are characterized by a complex system of sands, silts and silty clays chaotically accumulated during the Würmian glaciations. The Holocene epoch is responsible only for the shallowest lagoon deposits, up to 10-15 m below ground level. The top layer of Würmian deposits is composed of a crust of highly overconsolidated very silty clay, commonly referred as to *caranto,* on which many historical Venetian buildings are founded through driven wooden piles. It was subject to a process of overconsolidation as a result of exsiccation during the 10,000 year emergence of

the last Pleistocenic glaciation. Moving from the mainland towards the shoreline, the *caranto* layer lies at depths increasing from less then 5 m to about 16 m below mean sea level.

The present lagoon morphology is the consequence of the intensive human action and of the recent environmental damages. In fact, since the first Venetian citizens settled on the islands (around XII century), the main engineering activities concerned with the conservation of efficient communications between lagoon and sea and the preservation of the city insularity. More particularly, to avoid lagoon filling the Venetians diverted the rivers Brenta, Sile, Piave into extensive canals around the lagoon periphery and constructed robust stone-walls to protect the channel and island banks against erosion. The shape of the three lagoon inlets has been also continuously modified: after the second world war, the sea bottom at the Malamocco inlet was very deeply dredged to allow the large oil tankers to reach the Venice / Marghera port through the so called "*oil canal*". All these modifications caused a continuous decrease of sediment balance, with a significant reduction of the area covered by marshes and wetlands. Figure 6.4 show a comparison between the lagoon morphology in the XII century with that of the XX century.

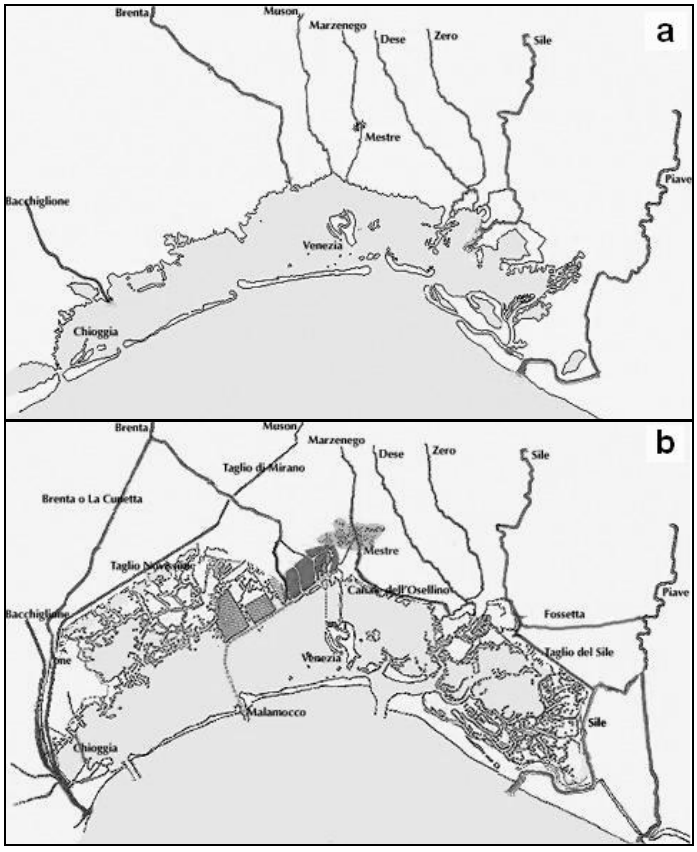

Figure 6.4: . Morphology of the Venice lagoon: 700 years ago (*a*) and at present (*b*).

As regard to the soils that constitute the lagoon, five depositional unit are detected in a high level of interbedding and interdigitation characterizing the youngest soils up to 50-60 m of depth. The shallowest Holocene unit is mainly composed by marine sands with significant shell content along with the shoreline and by finer sediments with significant organic matter in the inner part of the lagoon. The underlying units are mainly formed by fluviatile sediments organized in fining-upward structures, sometimes eroded or lightly desiccated at the top, due to a temporary regression of the shoreline or to brief emersion periods.

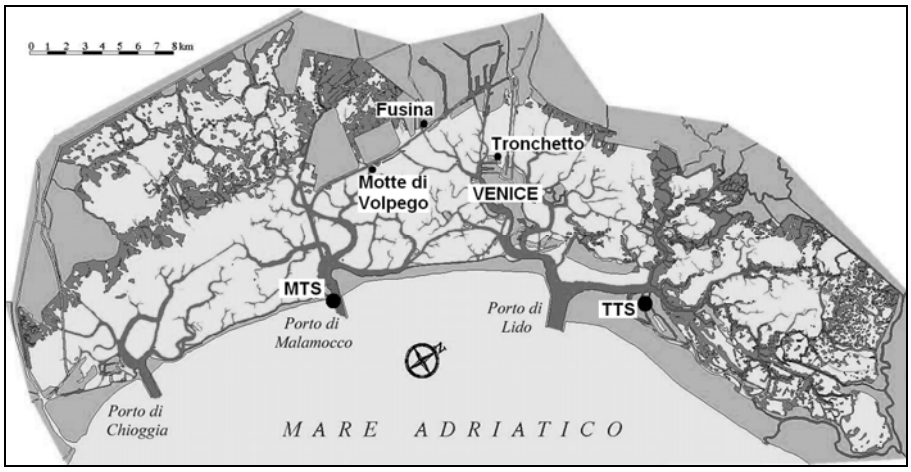

Figure 6.5: in situ campaigns in the Venice lagoon

The thin peaty layers should be related to the occasional presence of lacustrine environment. The rate of accumulation is relatively high, about 3 mm/year in average. In each profile the *caranto* is easily recognizable for the typical grey-yellow colour and the presence of numerous fissures with oxidation traces. The *caranto* layer, slightly sloping toward the shoreline, has thickness varying from a few of centimetres up to some metres.

In situ campaigns

The first comprehensive geotechnical and geological studies on Venice lagoon soils were carried out between 1965 and 1975. Mineralogical and paleontological studies on sediments from the site Motte di Volpego were performed by Bonatti (1968). In 1970 the Italian Government through the Consiglio Nazionale delle Ricerche (CNR) commissioned a 1000 m deep borehole, located at Tronchetto to estimate the aquifer and aquitard system and the geotechnical properties relevant to an evaluation of the subsidence problem (Favero et al., 1973; Rowe, 1973; Ricceri & Butterfield, 1974).

Between 1970s and 1980s, the shallowest ground of the lagoon has been extensively studied, but only through standard geotechnical investigations necessary for the design of the foundations of new large industrial settlements on the mainland. Relevant information on the mechanical behaviour of lagoon clayey/silty materials sampled at Fusina, a small village facing to the inner lagoon where a thermoelectric power plant is located, was also provided by Cola (1994). In Figure 6.5 locations of the in situ campaigns are reported.

To protect the city of Venice and the surrounding lagoon against the recurrent flooding, a huge project was undertaken at the beginning of the ‘80s under the directive of Italian Government, involving the design and construction of movable gates located at the three lagoon inlets (Gentilomo, 1997). These gates, controlling the tidal flow, temporarily separate the lagoon from the sea at the occurrence of particularly high tides, whose annual frequency is continuously increasing (Harleman et al., 2000).

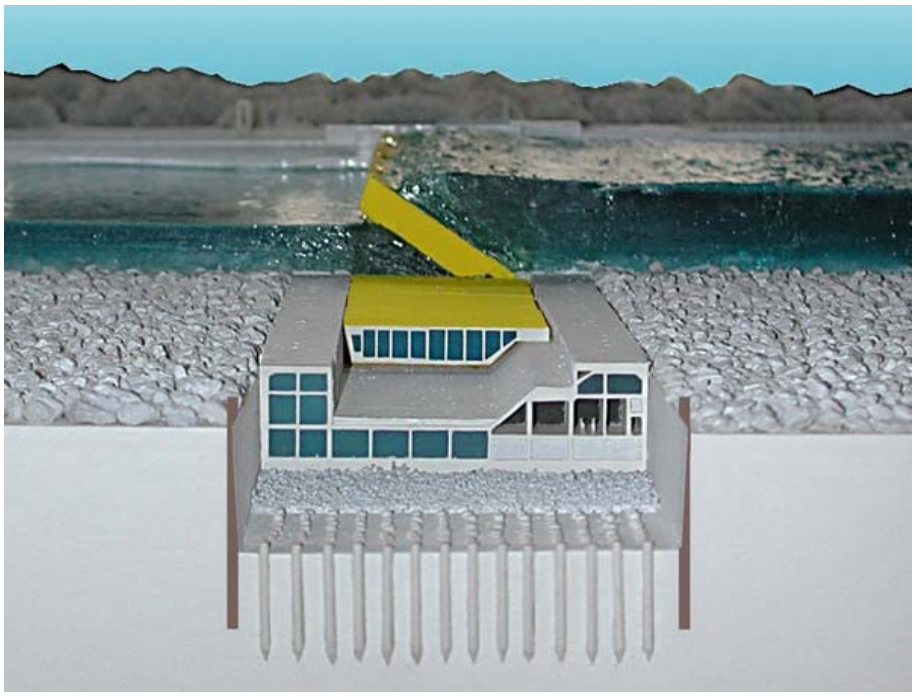

Figure 6.6:scheme of the movable gate in construction at the Lagoon inlets (www.salve.it)

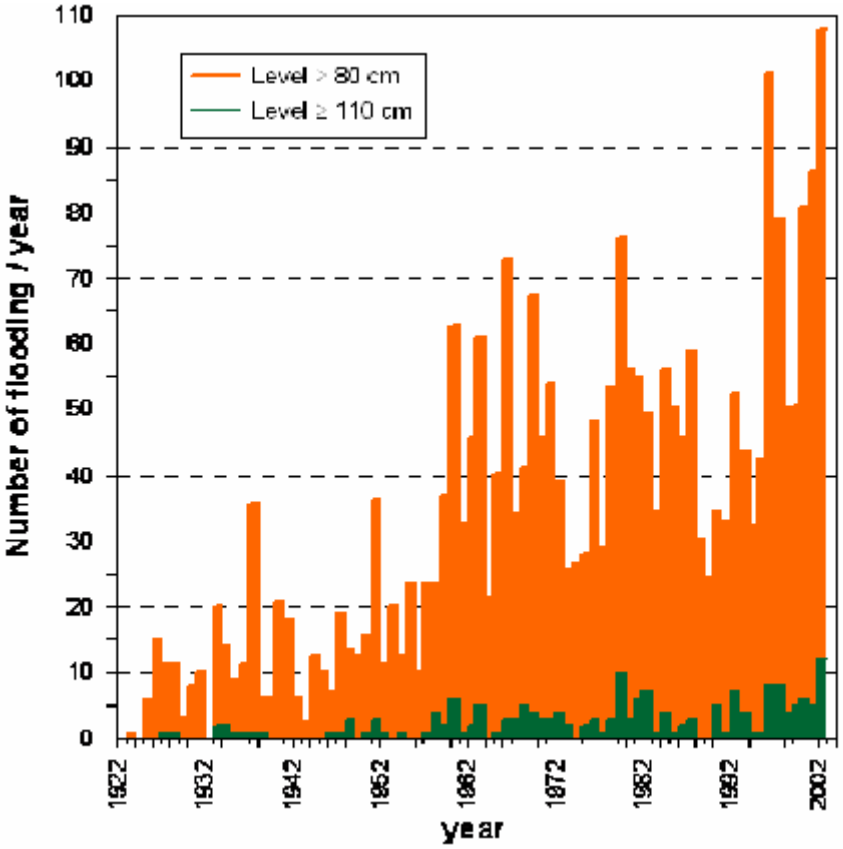

Figure 6.7: high tides occurance in last century (Simonini, 2007)

Therefore, comprehensive geotechnical studies were necessarily carried out to characterize the Venetian soils at the inlets to achieve a suitable design of the movable gates foundations. Preliminary standard geotechnical investigations were therefore performed in the late 1980s,

to draw relevant soil profiles along with cross sections of the three lagoon inlets and to estimate significant geotechnical properties for a preliminary selection of gate foundations.

From the geological and geotechnical investigations carried out so far, it turned out that the main characteristic of the lagoon soils is the presence of a predominant silt fraction, combined with clay and/or sand. These form a chaotic interbedding of different sediments, whose basic mineralogical characteristics vary narrowly, as a result of similar geological origins and common depositional environment. This latter feature, together with the relevant heterogeneity of soil layering, suggested to concentrate the researches on some selected test sites, considered as representative of typical soil profiles, where relevant in-situ and laboratory investigations could be carried out for a careful characterization of the Venetian lagoon soils.

The first test site, namely the *Malamocco Testing Site* (Cola & Simonini 1999, 2002) was located at the Malamocco inlet (Figure 6.5). Within a limited area, a series of investigations that included boreholes, piezocone (CPTU), dilatometer (DMT), self-boring pressuremeter (SBPM) and cross hole tests (CHT) were performed on contiguous verticals. In addition a continuous borehole was carried out for a very careful soil mineralogical classification. The comprehensive laboratory test program completed (Cola & Simonini 2002; Biscontin et al. 2001, 2006) emphasized the very heterogeneous nature of the Venice soils (Figure 6.8): in order to define even the simplest properties with a certain degree of accuracy, a relatively large number of tests was necessarily required. In addition, due to the high silty content and the low-structured nature, the sediments are extremely sensitive to stress relief and disturbance due to sampling, thus affecting a careful the stress history evaluation and a satisfactory stress-strain-time mechanical characterization.

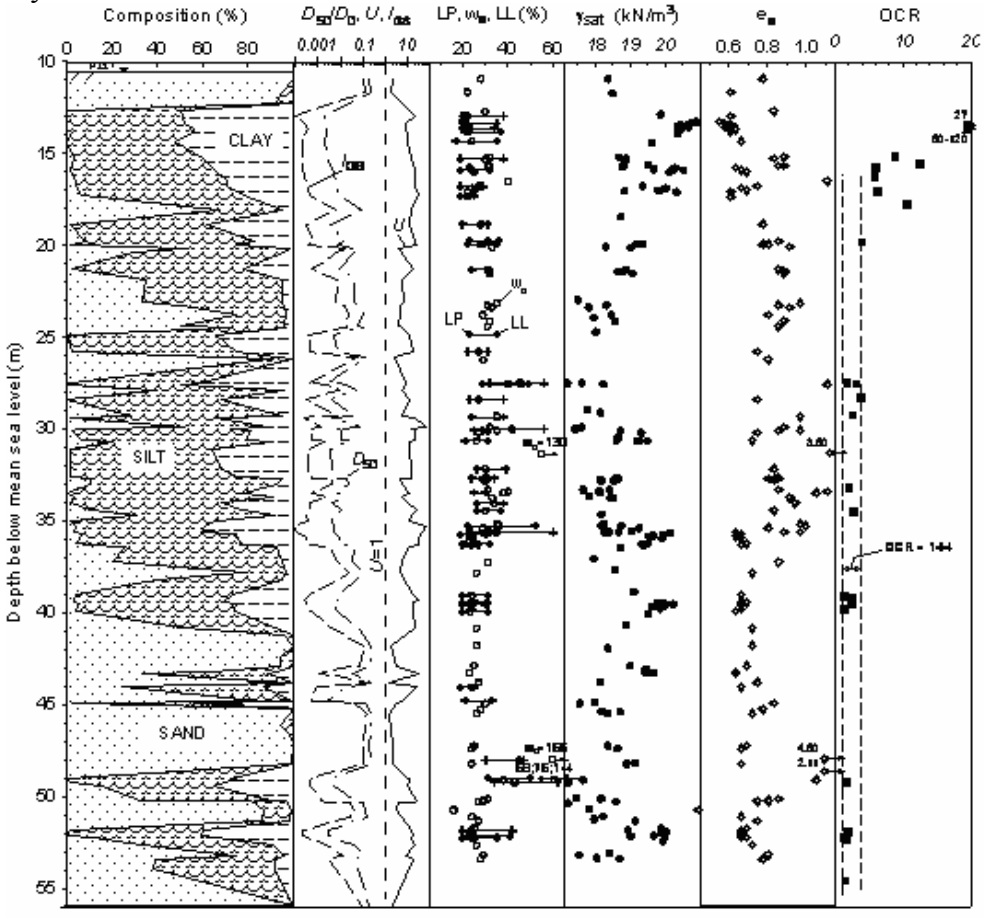

Figure 6.8: Soil profile, basic properties and stress history at the Malamocco Testing Site (Simonini et al., 2006)

Figure 6.9: Treporti embankment at the end of complition

A new test site was therefore selected, namely the *Treporti Testing Site* (Simonini 2006), which is located at the inner border of the lagoon, very close to the inlet of Lido (Figure 6.5). The goal of this campaigns was to measure directly in-situ the stress-strain-time properties of the heterogeneous Venetian soils. In fact a vertically-walled circular embankment whose diameter is 40 meters, loading up the ground to slightly above 100 kPa, was constructed (Figure 6.9), measuring, along with and after the construction, the relevant ground displacements together with the pore pressure evolution. To this end, the ground beneath the embankment was heavily instrumented and also site investigations were carried out to characterize soil profile and estimate the soil properties for comparison with those directly measured in situ. The load was kept for more than four years and then the embankment was removed always monitoring ground displacements in order to catch unloading behaviour. A comprehensive description of the Treporti Test Site is given in the following paragraph.

Treporti embankment: a field test

The location of the testing site was selected in the proximity of the Lido inlet, just outside Treporti, an old fishing village near the Cavallino shoreline, facing the North-Eastern lagoon (Figure 6.5). The exact area was selected throughout a preliminary site investigation carried out by means of penetrometer tests: 7 piezocone tests (CPTU from 1 to 7 in Figure 6.10) and 2 mechanical Begemann-type tip tests (CPT labelled A and B in Figure 6.10). The first task was to find out a test site as representative as possible of such subsoil, especially in relation to the foundation design of the big submersible barriers.

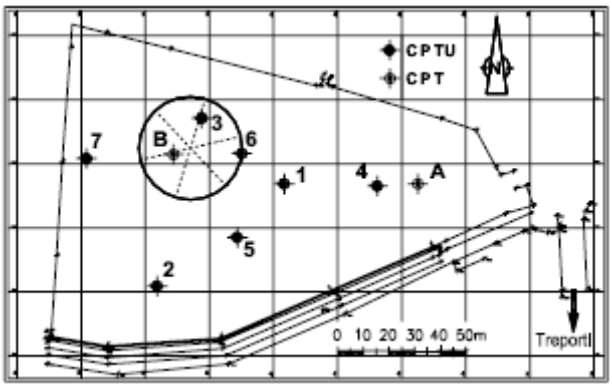

Figure 6.10:plan of the testing site area and location of the first indagine with piezocone (Gottardi and Tonni, 2004)

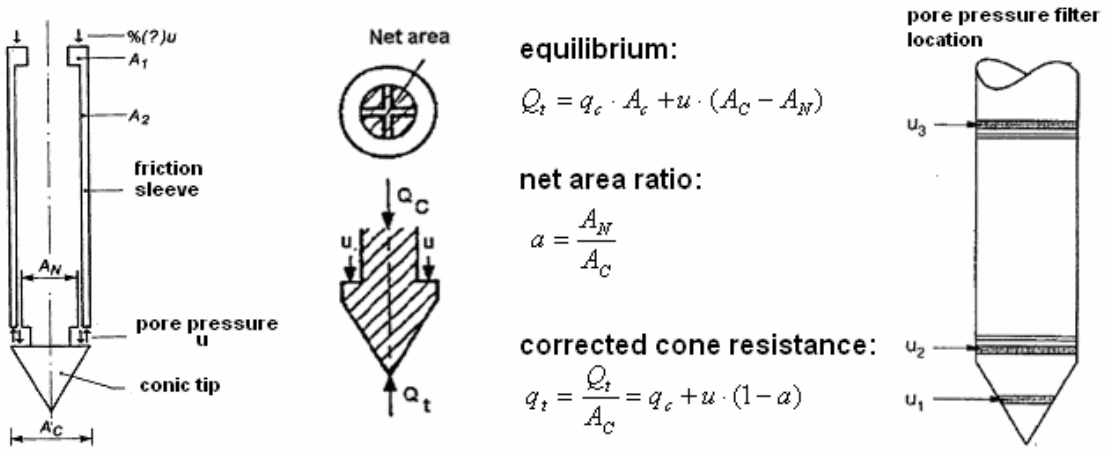

Figure 6.11: scheme of a piezocone with definition of net area ratio, corrected cone resistance and possible locations of pore pressure filter

CPTU tests were performed by the Soil Mechanics Laboratory of the University of Bologna using an integrated electronic piezocone, manufactured by Delft Geotechnics, with 200 kN of nominal thrust. The penetration device is a standard cone, with a net area ratio $a = A_N / A_C = 0.82$. The equipment enables continuous measurement of the cone resistance $q_c = Q_c / A_c$, the sleeve friction $f_s = Q_s / A_S$ and the induced pore pressure u at the cylindrical extension of the cone (u_2 in Figure 6.11). All data were logged at about 1 second intervals, with a standard penetration speed of 20 mm/s. The equipment was also provided with an inclinometer, allowing depth correction according to the possible deviation of push rods.

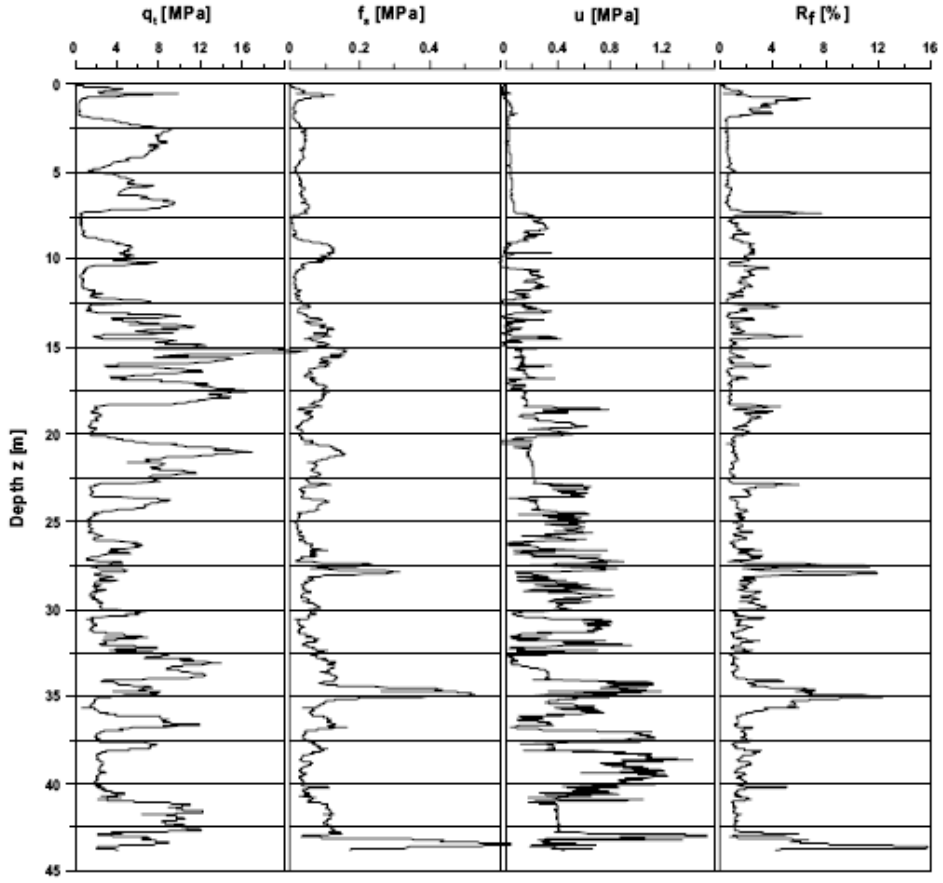

Figure 6.12: piezocone data from the preliminary phase (Gottardi and Tonni, 2004)

A typical result is provided in Figure 6.12 (CPTU N°. 4), showing the profiles of, respectively, the corrected cone resistance $q_t = Q_t / A_C = q_c + u \cdot (1 - a)$ (Figure 6.11), the shaft resistance, f_s, the pore pressure u and the friction ratio $R_f = 100\, f_s / q_c$, vs. the penetration depth z.

The water table was easily found to be very close to the ground level, consistent with the nearby canal height and also subjected to local tidal excursions, about ± 0.5 m twice a day. The presence of a highly stratified subsoil is confirmed, with a well-defined top layer of silty - sand, 6-7 m thick, and then a rather dense alternation of sandy to clayey silts. Such a continuous variation is clearly visible from all logs, in particular from the pore pressure profile, where u rarely follows up the hydrostatic level, often falls below it, but never develops high $\Delta u = u - u_0$ values, typical of pure clays. Occasionally, but consistently throughout the tests, rather large friction ratio values show the presence of thin layers of peat and organic soil. Data are in substantial good agreement with extensive test results from the Malamocco inlet (Figure 6.8), thus confirming the Treporti test site as representative of the Venice lagoon sediments. Between depths of 7-8 m and 20 m, it is detectable the presence of a mainly fine-grained, more compressible, silty unit. However, its thickness is not in the least constant throughout the whole test site area, being often interbedded with a variable clean sand layer. The whole series of penetrometer tests carried out in the first phase enabled to locate the loading bank position in the NW corner (Figure 6.10), where such unit turns out to be thicker.

Once the area for the embankment construction was selected, a thorough in-situ testing programme was carried out for the geotechnical characterization of the soil underneath the bank. It consisted of ten piezocone tests (namely from N° 11 until N° 20) and ten flat dilatometer tests (Marchetti at al., 2004) together with two standard mechanical CPT tests and four 60 meters depth boreholes. Undisturbed sampling was carried in the most cohesive formations out by using the classical Osterberg sampler and a complete laboratory analysis was performed using samples from boreholes N°2. Two CPTU (N° 29 and N° 30) and four DMT have been also performed after completion of the embankment. Furthermore three additional CPTU (N° 34 ,N° 39 and N° 40) were carried out at the end of bank removal, in order to compare results before the construction, after it, and once the soil would have been overconsolidated after the embankment removal. Also a further borehole (SFS) was performed at the end of bank removal, nearby the centreline (so near the boreholes SN before construction).The whole list of tests together with their location is shown in Figure 6.13.

The instrumentation installed at Treporti Testing Site was designed to keep the following main quantities under control:
- surface vertical displacements using 7 settlement plates and 12 bench marks, the latter located outside the embankment area;
- surface vertical displacement by one GPS antenna, located in the centre of the embankment area and fixed to the central settlement plate;
- vertical deep displacements by means of 8 borehole rod extensometers;
- vertical strains, along with four verticals, using 4 special multiple micrometers;
-horizontal displacements by means of 3 inclinometers;
- pore water pressure in fine-grained soils by means of 5 Casagrande as well as 10 vibrating wire piezometers;
- total vertical stress beneath the loading embankment by means of 5 load cells.

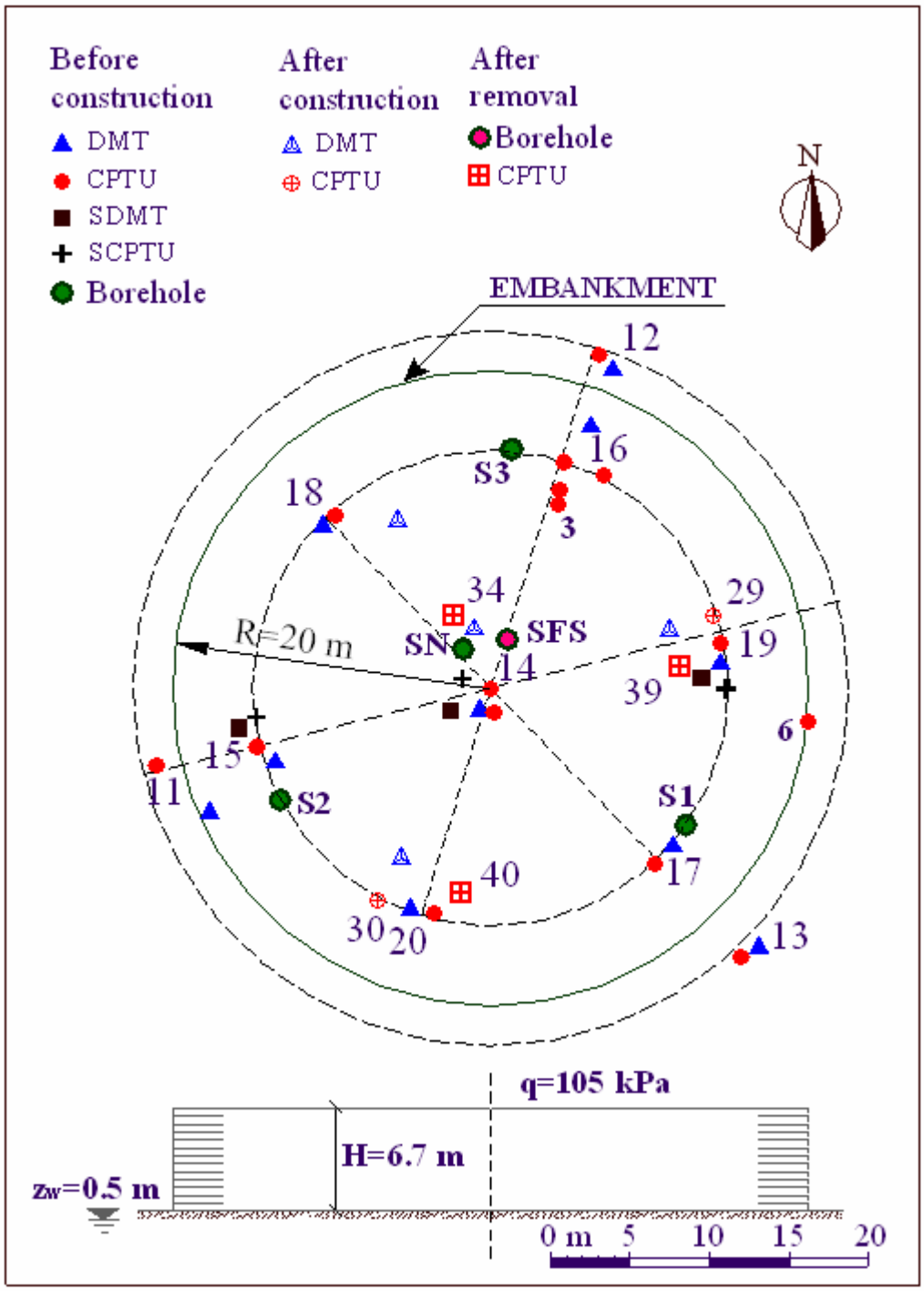

Figure 6.13:Embankment plan with location of site investigation tests (after Simonini et al., 2006)

To measure the vertical displacements throughout the foundation ground very precisely, multiple micrometers " called *sliding deformeters*, capable of measuring vertical displacements at 1 m intervals with an adequate degree of accuracy of 0.03 mm/m (Kovari & Amstad, 1982), were selected. They were developed at the Federal Institute of Technology in Zurich and produced by the Swiss firm "Solexperts" and allow to measure the distribution of the deformation along a line, that in this case was the axis of a borehole: for each borehole a sliding deformeter was installed.

The line along which deformations are to be measured is transformed into a chain of well-defined reference points, thus the continuous deformation measurement is reduced to

observing the movements of the points in the measuring chain, usually the relative displacements of adjacent points. The measuring line is physically a linkage of measuring PVC tubes, which are grouted into the borehole. They contain ring- shaped measuring marks at regular intervals of 1 m. These reference points, made of steel, serve as coupling elements between two adjacent units of tubes and on the other hand as a housing for stop fittings. The latter have the function of holding the two heads of the portable device in position during the short time of a reading. The tube segments are screwed into the ring marks and the stop fittings are fixed in by bolting. If the measuring marks displace relatively to each other due to the deformation of the surrounding subsoil, then the change in distance, i.e. the strain with the base length of 1 m, can be recorded as the difference between two readings. A set of measurements involves the following: beginning at the mouth of the tube, the probe is fixed between two measuring marks and a reading is taken. The probe is then push into the ground in a stepwise manner carrying out readings at each position. After reaching the end of the tube a repetition of the readings is made on retraction of the probe. The two sets of readings allow a valuable check. (Figure 6.15).

In Figure 6.14 the location of the four sliding deformeters is shown, together with the other in situ devices.

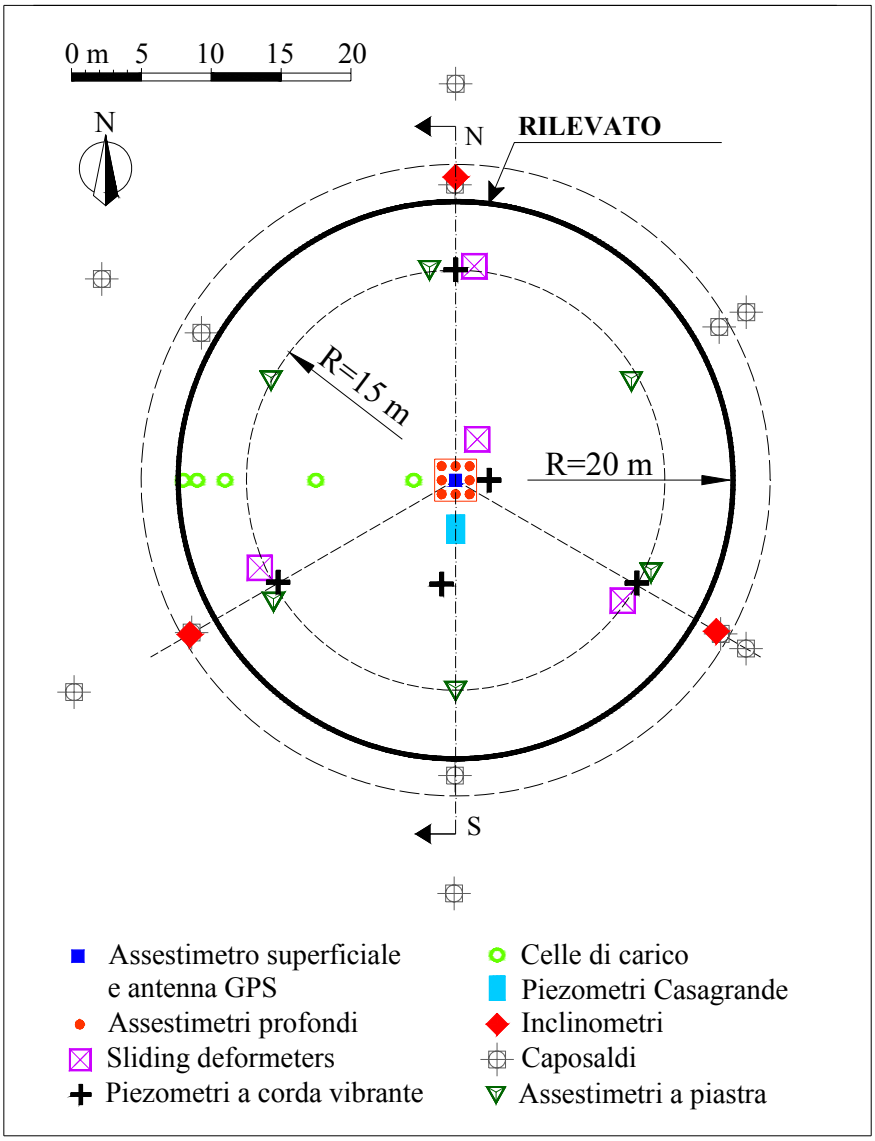

Figure 6.14: in situ testing devices location (Simonini et al., 2006)

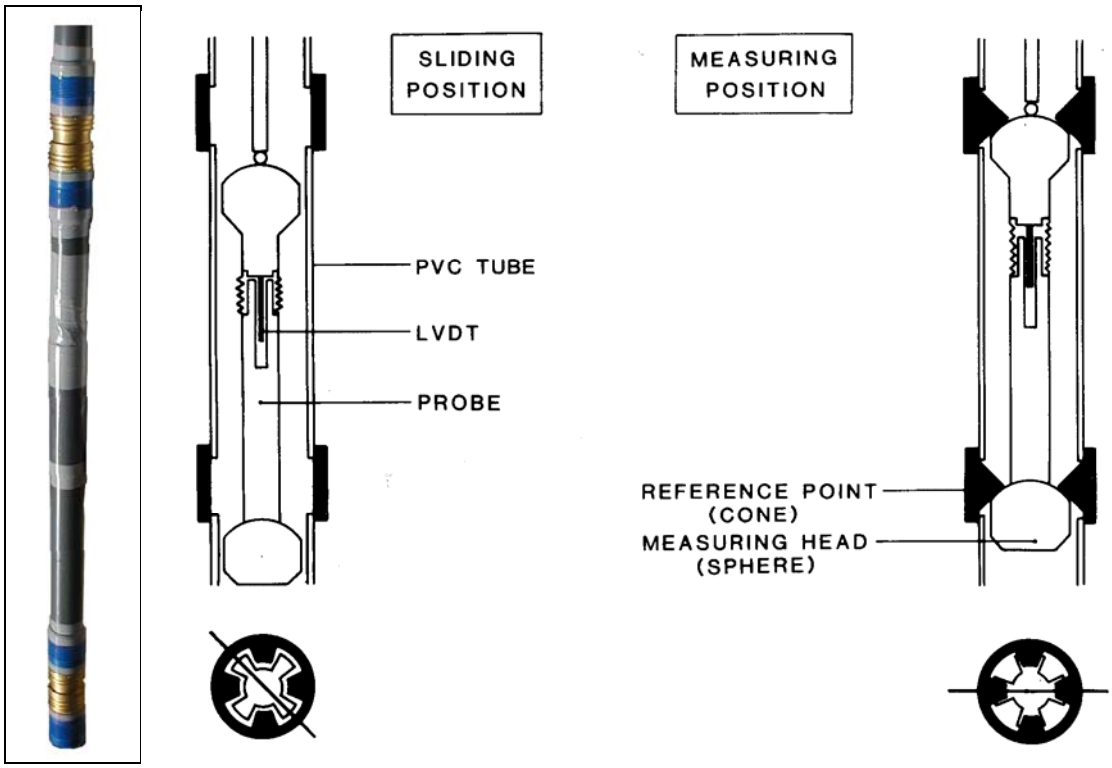

Figure 6.15:a sliding deformeter tube (Kovari, 1985)

The cylindrical sand bank construction started in September, 12th 2002 and ended in March, 10th 2003. The bank is formed by 13 geogrid-reinforced sand layers with 0.5 m thickness. The fill was a medium-fine uniform sand with D_{50}=0.14 mm. As reinforcement a stiff polypropylene geogrid was used; to avoid any sand flow through the holes of the grid, additional sheets of geotextile were placed onto the grids before placing the sand. The fill was dynamically compacted to give an average dry unit weight equal to 15.6 kN/m^3. After completion, the embankment was covered by an impermeable membrane on which 0.2 m of medium-fine gravel was posed, thus reaching a final height of 6.7 m.

Figure 6.16: the first embankment layer with the geogrid

The list of the construction phases and subsequent strain measurements at each meter depth are reported in the following Table 6.1:

measure Nr	date	height (m)	description
measure 0	12 September 2002	0.00	reference measure
phase1	12-17 September 2002	**0.5**	+0.5 sand
measure 1	18 September 2002	0.5	measure
phase2	23-26 September 2002	**1.00**	+0.5 sand
measure 2	27 September 2002	1.00	measure
phase3	1-3 October 2002	**1.50**	+0.5 sand
measure 3	04 October 2002	1.50	measure
phase4	9-14 October 2002	**2.00**	+0.5 sand
measure 4	15 October 2002	2.00	measure
measure 5	29 October 2002	2.00	measure
phase5	7-8 November 2002	**2.50**	+0.5 sand
measure 6	11 November 2002	2.50	measure
phase6	13-18 November 2002	**3.00**	+0.5 sand
measure 7	19 November 2002	3.00	measure
phase7	27-29 November 2002	**3.50**	+0.5 sand
measure 8	02 December 2002	3.50	measure
phase8	16-19 December 2002	**4.00**	+0.5 sand
measure 9	20 December 2002	4.00	measure
phase9	30 December 2002-03 January 2003	**4.50**	+0.5 sand
measure 10	10 January 2003	4.50	measure
phase10	14-16 January 2003	**5.00**	+0.5 sand
measure 11	20 January 2003	5.00	measure
phase11	22-25 January 2003	**5.50**	+0.5 sand
measure 12	27 January 2003	5.50	measure
phase12	04-07 February 2003	**6.00**	+0.5 sand
measure 13	14 February 2003	6.00	measure
phase13	24-27 February 2003	**6.50**	+0.5 sand
measure 14	28 February 2003	6.50	measure
phase14	06-10 March 2003	**6.70**	+0.2 gravel
measure 15	14 March 2003	6.70	measure
measure 16	28 March 2003	6.70	measure
measure 17	18 April 2003	6.70	measure
measure 18	06 June 2003	6.70	measure
measure 19	23 July 2003	6.70	Measure
measure 20	19 September 2003	6.70	Measure
measure 21	03 December 2003	6.70	Measure
measure 22	31 March 2004	6.70	Measure
measure 23	02 September 2004	6.70	Measure
measure 24	15 April 2005	6.70	Measure
measure 25	13 October 2005	6.70	Measure
measure 26	05 May 2006	6.70	Measure
measure 27	17 October 2006	6.70	Measure
measure 28	19 April 2007	6.70	Measure

Table 6.1: Treporti embankment construction phases

The embankment removal has been carried out from June,15th 2007 until March, 31st 2008. in three phases, each of them constituted by more than one sub-phases.
At the end of each three stages the load left was kept for about three months in order to catch secondary compression displacements, if any, even in the unloading phase.
Since the soil has compressed, due to the embankment load increase (from measure 0 until measure 15) and due to creep behaviour (from measure 15 until measure 28:more than four year at constant stress), the measure N°28 is taken as a reference measure for the following ones.
In particular the bench mark chosen as a reference on April, 19th 2007 measures 6.3 m as embankment height. It is placed not exactly in the centreline. In fact under the centreline the total displacement was around 0.5 m and so an embankment height at the end of loading phase was equal to 6.20m.
It clearly appears that on the whole area settlements have been different depending on the place so the unloading phase has been made equating the embankment surface and the height indicated in the following Table 6.2 are indicative.
In Figure 6.18 the whole process of loading, constant load and unloading is shown together with the settlement measurement under the centreline.

Figure 6.17: Treporti embankment (a) on April, 19th 2007 still completed (b) after the first removal phase (c) after the second removal phase (d) after the third removal phase, i.e. completely removed

measure Nr.	date	height (m)	Description
measure 28	19 April 2007	6.30	reference measure
phase1-A	15-29 June 2007	**5.40ca.**	-0.2 gravel-0.70ca. sand
measure 29	04 July 2007	5.40	Measure
phase1-B	08-14 July 2007	**4.60ca.**	-0.80ca. sand
measure 30	26 July 2007	4.60	Measure
measure 31	01 August 2007	4.60	Measure
measure 32	24 September 2007	4.60	Measure
measure 33	18 October 2007	4.60	Measure
phase2-A	22 October-06 November 2007	**3.60ca.**	-1.00ca. sand
measure 34	07 November 2007	3.60	Measure
phase2-B	9-20 November 2002	**2.65ca.**	-0.95ca. sand
measure 35	20 November 2007	2.60	Measure
measure 36	06 December 2007	2.60	Measure
measure 37	22 January 2008	2.60	Measure
measure 38	19 February 2008	2.60	Measure
phase3-A	22 February-04 March 2008	**1.70ca.**	-0.95ca. sand
measure 39	12 March 2008	1.70	Measure
phase3-B	17-21 March 2008	**0.75ca.**	-0.95ca. sand
phase3-C	26-31 March 2008	**0.00**	-0.75ca. sand
measure 40	01 April 2008	0.00	Measure
measure 41	09 April 2008	0.00	Measure
measure42	11 June 2008	0.00	Measure

Table 6.2:Treporti embankment removal phases

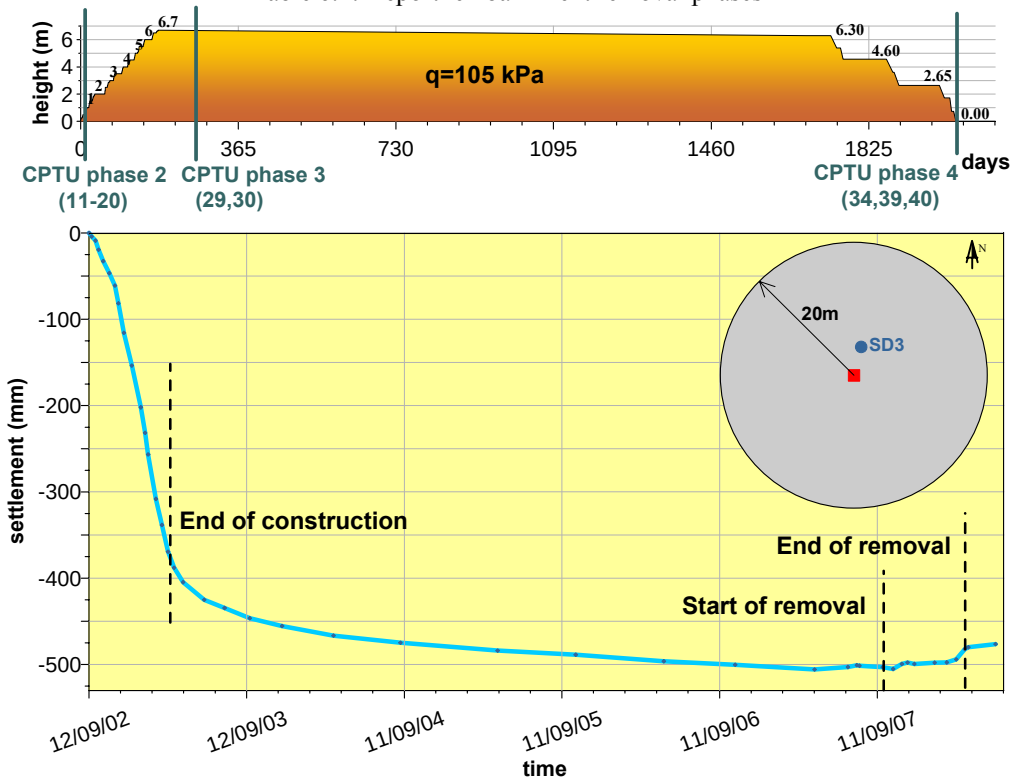

Figure 6.18: Treporti embankment trial- settlement under the centreline

Chapter 7 - Classification and behaviour of Venetian soils

Classification: a big issue

The Venetian subsoil is extremely heterogeneous. From the geotechnical investigations carried out at Malamocco Testing Site and at Treporti Testing Sites, it appears that the main feature of the Venice lagoon soil is the presence of a predominantly silt fraction as a consequence of mechanical degradation of the original sand particles. During the Quaternary period, in fact, the lagoon area underwent alternating periods of marine transgression and regression, as a result of which both marine and continental sediments coexist. More particularly, the deposits forming the upper 50-60 m are characterized by a complex system of interbedded sands, silts and silty clays with some inclusions of peat deposited during the last glacial period of the Pleistocene, when rivers transported fluvial material down from the Alpine glaciers. Holocene is only responsible for the shallowest lagoon deposits.

The depositional pattern is thus rather complex because of a very complex depositional history and varies site to site but in a relatively narrow range due to a unique geological origin and common depositional environment. The silty fraction is therefore always combined with clay and (or) sand without any regular pattern with depth, which leads to highly heterogeneous soil conditions. Sands show two types of mineralogical composition, namely carbonatic and siliceous, the former as detrital calcite and dolomite crystals. When carbonate and quarz-feldspar fractions decrease, the clay minerals increase alongside variation of the grain-size distribution from sands to clays. Clayey minerals, not exceeding beyond 20% are mainly composed of illite or muscovite with chlorite, kaolinite and smectites as secondary minerals.

For classification purposes, the soil types that constitute the Venice Lagoon subsoil have been reduced to three: medium to to fine sand (SP-SM), silt (ML), and very silty clay (CL) according to the Unified Soil Classification System (Figure 7.1). The sands appeared to be quite uniform but moving towards finer material the grain size curves display a larger range of particle diameters, as shown in Figure 7.1

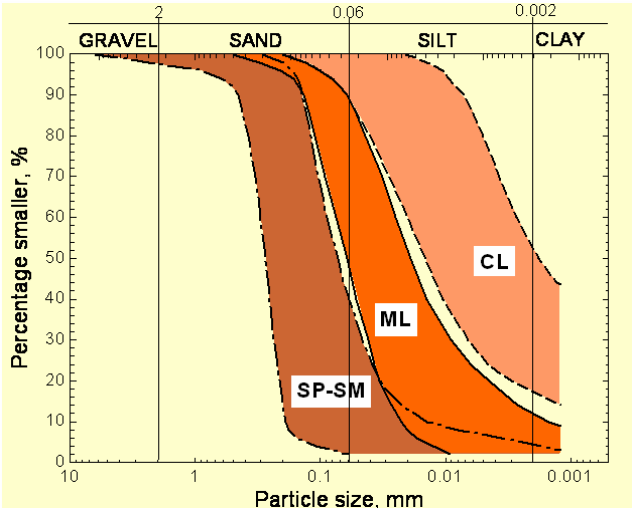

Figure 7.1: typical grain distribution of Venice lagoon soils (Cola and Simonini, 2002)

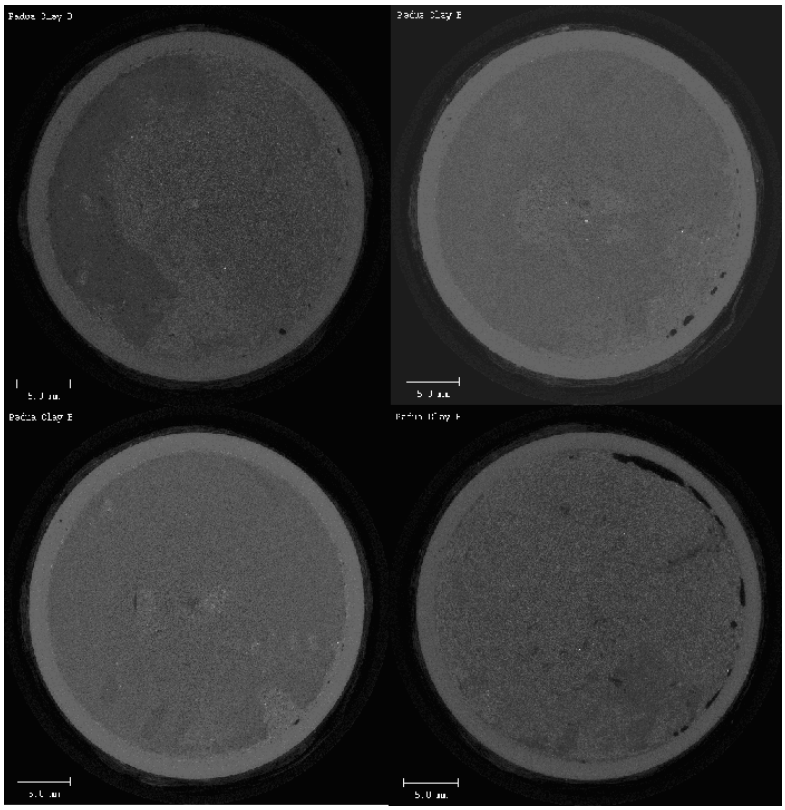

Figure 7.2: microtomography results on Treporti soil sample, at a difference of few centimetres.

However the spatial heterogeneity is so significant that even in the range of a few centimetres soil layering changes so much that it is almost impossible to trim two identical samples in order to perform laboratory tests. In Figure 7.2 the result of a microtomography with X-ray on a Treporti sandy sample taken from SFS borehole are shown. Different colours correspond to different density. It is simple to observe how much the density changes in a section itself and also from section to section, even though they are very close each other.

To define the soil layering is therefore not simple, because one should have a lot of samples on which to perform classification laboratory tests, and also in this case the soil layering obtained would be precise only for that vertical. At Treporti Test site a continuum borehole was performed (S2 in Figure 6.13) in order to define exactly the soil layering and the basic properties, with the results shown in the following. From the soil grading reconstruction, the various types of soil occur up to 60 m, approximately, in the proportion: SM-SP 22%, ML 32%, CL 37% and CH-Pt 9%. Upper and deeper sands are relatively uniform; finer materials are more graded, the coarser the materials, the lower the uniformity coefficient U. I_{GS} coefficient will be described in the next paragraph. Except for the organic soils, Atterberg limits of cohesive fraction are similar to those determined at Malamocco Testing Site and show a quite low plasticity. As regard to the unit weight γ_{sat}, it shows large oscillations with depth, void ratio e_o lies approximately in the range between 0.8 – 1.1, with higher values due to laminations of organic material.

Since the stratigraphy of Venetian subsoil is highly dependent on the specific vertical one refers to, a way to detect this spatial variability is to use the classification through the piezometer cone, performing the test along different vertical lines.

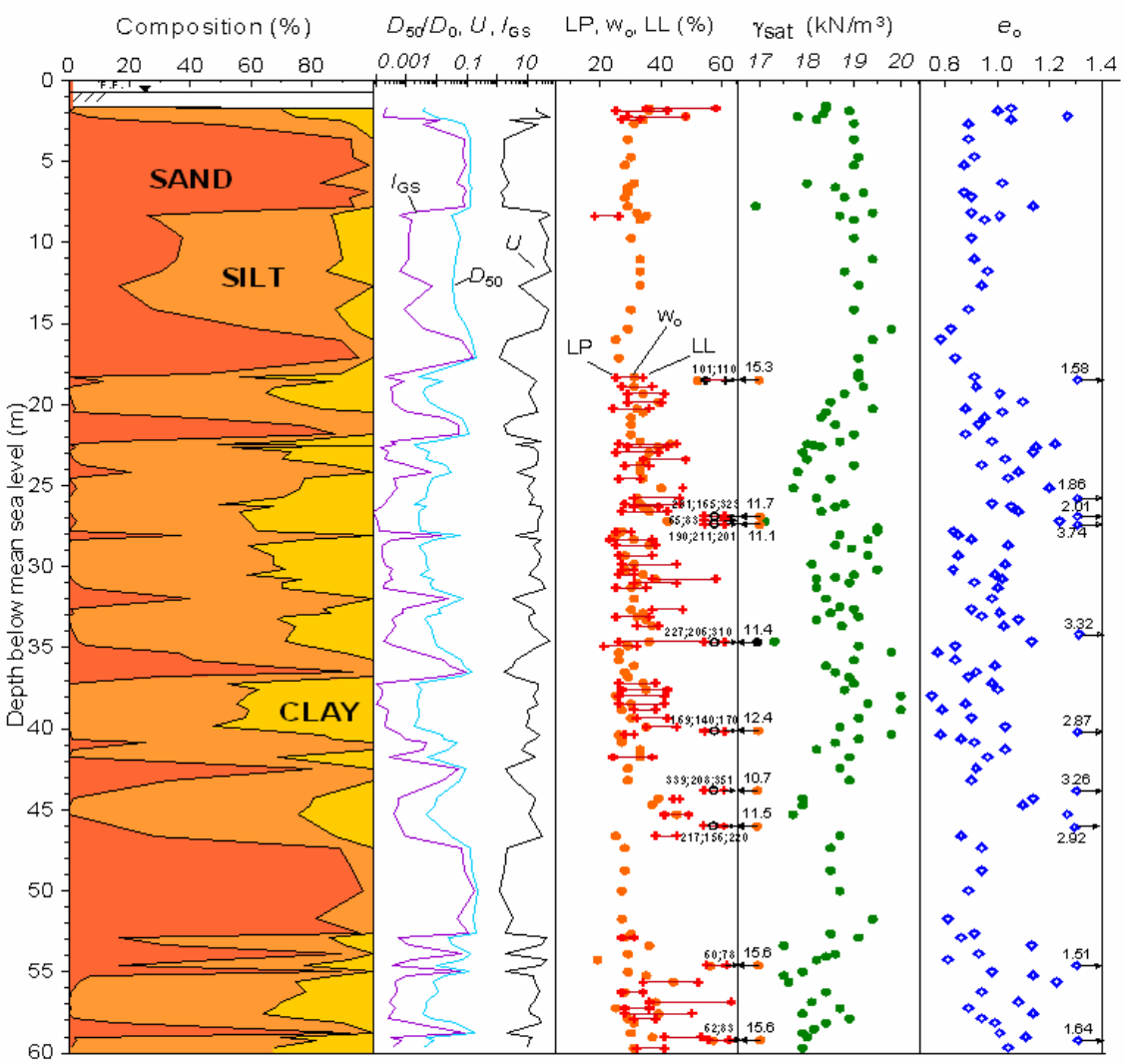

Figure 7.3: Basic properties at Treporti Testing Site (Simonini, 2006)

It is well-known that throughout a piezocone test is possible to retrace the stratigraphic profile of a subsoil, throughout its cone resistance q_t, friction sleeve resistance f_s, and pore pressure development Δu during the penetration. Typically to normally consolidated cohesive soils correspond low tip resistance q_t and high excess pore pressure Δu (sort of undrained behaviour) while for granular soils the cone resistance is quite high and the measured pore pressure coincides with the hydrostatic level. Very high friction resistance is characteristic for peats.

At Treporti Testing Site the use of piezocone before embankment construction allowed to retrace the soil profile along many verticals and demonstrated that there is no spatial uniformity. In Figure 7.4 in fact, the stratigraphic profile along four verticals is shown, drawn along one selected diameters with the corrected cone resistance q_t from CPTU No11, 15, 14 and 19. Moving to Eastwards, unit D (between 14 and 18 m depth) made up of sands, tends to progressively reduce thickness and then disappear under the centreline.
S2 borehole is at the same distance of CPTU N°11 from the centreline and in fact it detects this sandy layer (Figure 7.3). "Taking into account the two stratigraphic sections drawn along the other diameters it can be seen that only a quarter of the loaded circular area is without this sandy unit thus producing a rather marked asymmetry of the subsoil response". (Gottardi and Tonni, 2004).

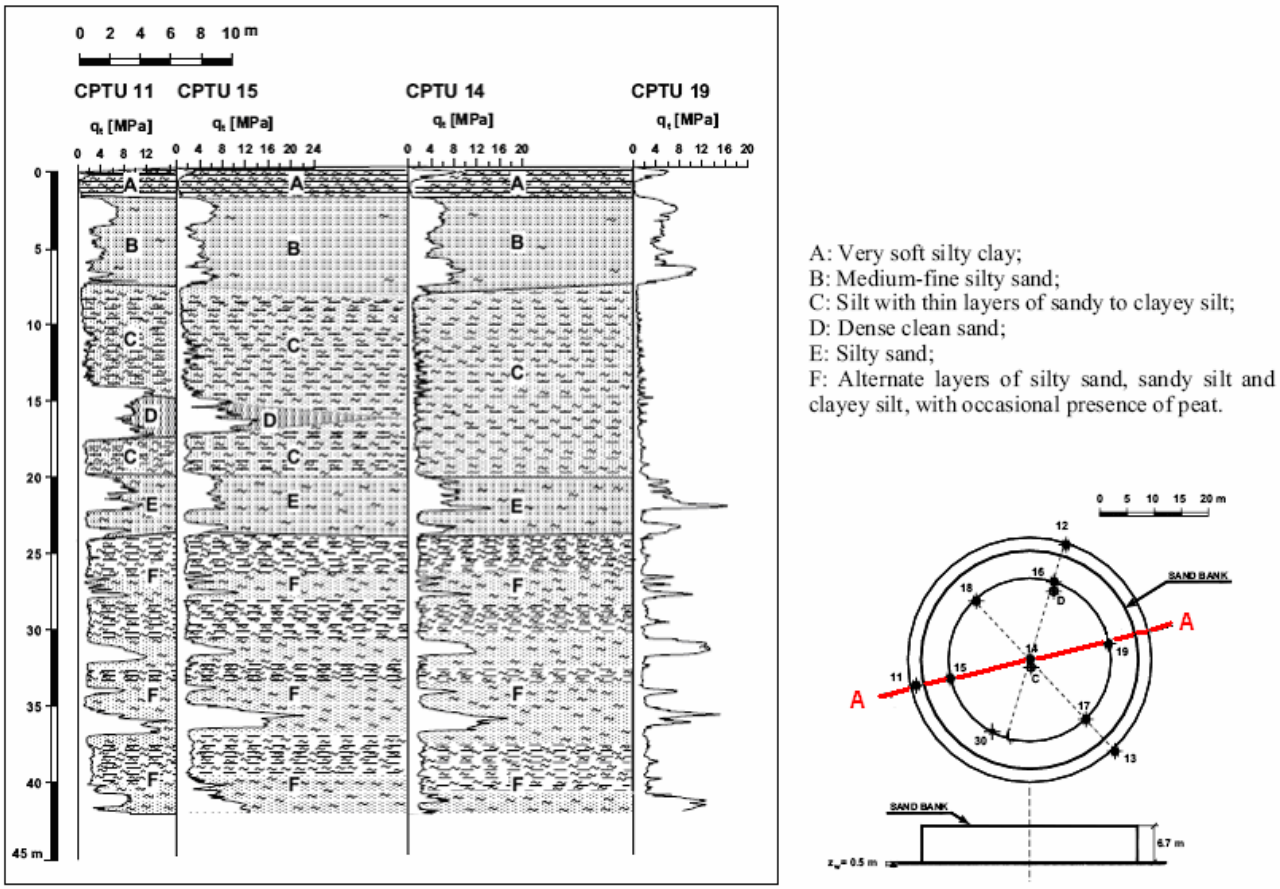

Figure 7.4: stratigraphic section A-A across the loading bank (Gottardi and Tonni, 2004)

To have performed a CPTU test nearby the centreline also after the bank removal (No 34) allow to compare piezocone results between two analogous situations with the only difference being the overconsolidation ratio. In fact soils are almost the same (except for local heterogeneity) and also overburden pressure after embankment removal is the same as before the embankment construction (unless for a thin sandy layer kept into the ground once the embankment has been removed, that corresponds to the displacement due to the embankment load). The only difference between before construction phase and after removal phase is the overconsolidation ratio: since originally the soil was slightly overconsolidated ($OCR = 1.2$ ca., see in the following paragraphs) and the bank loading brought it into normally consolidated conditions, once the embankment has been removed it is overconsolidated.

The overconsolidation ratio can be calculated using elasticity theory to calculate the stress increment due to the embankment load at each depth under the surface. Under a circular uniformly distributed load the stress at a given depth z is:

$$\Delta\sigma_z(z) = \Delta\sigma_z(z=0)\cdot\left(1-\left(\frac{1}{1+\left(\frac{r}{z}\right)^2}\right)^{1,5}\right) \tag{7.1}$$

where r is the radius of the embankment ($r = 20m$) and $\Delta\sigma_z(z=0) \approx 105kPa$ is the stress the embankment transfers to the ground surface.

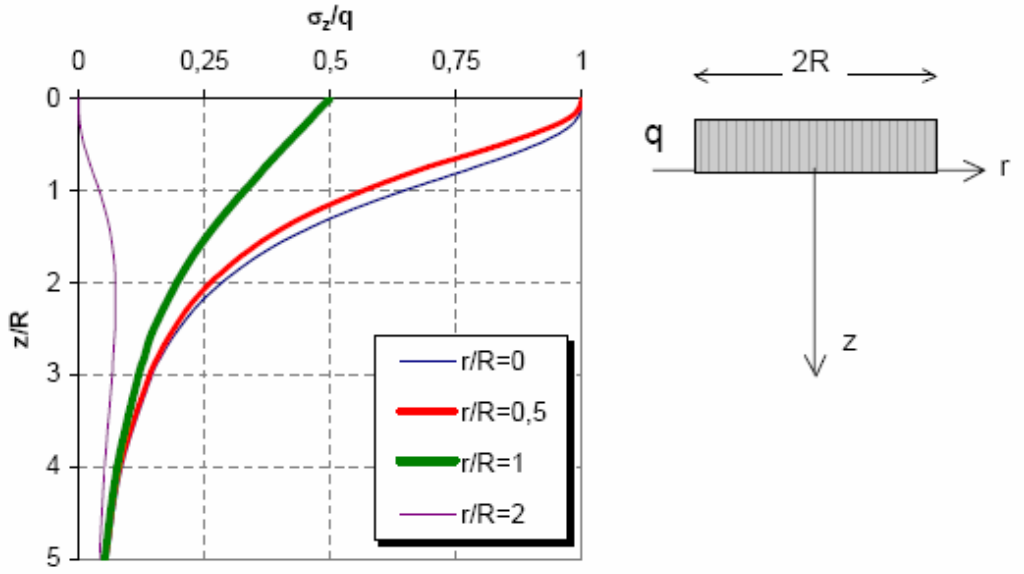

Figure 7.5: stress diffusion under a circular area

Overconsolidation ratio after the embankment removal is therefore:

$$OCR(z) = \frac{\sigma'_{z0} + \Delta\sigma'_z}{\sigma'_{z0}} \tag{7.2}$$

where σ'_{z0} is the effective overburden stress. In Figure 7.6 the OCR profile after removal is sketched.

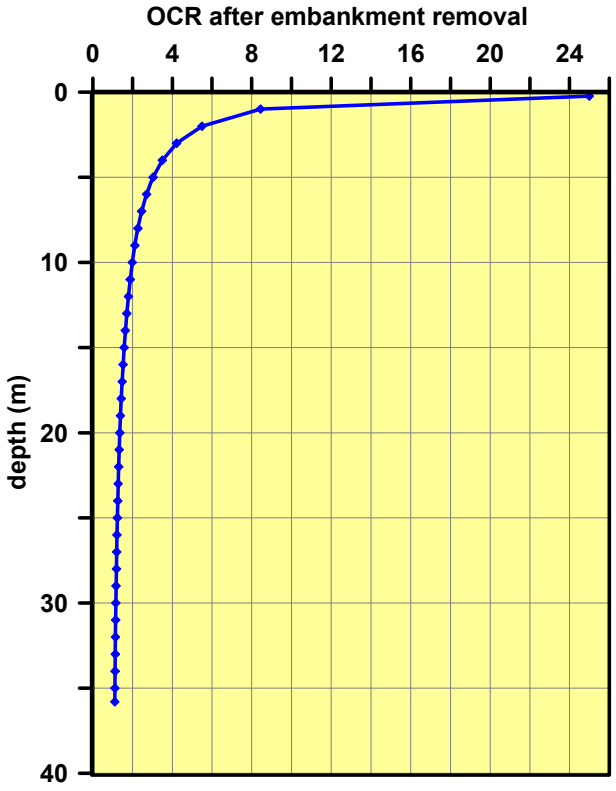

Figure 7.6: OCR profile under the centreline after embankment removal

In Figure 7.7 the cone resistance, friction resistance and pore pressure during penetration under the centreline are plotted for both the CPTU N^o 14 (before embankment construction) and CPTU N^{o}34 (after embankment removal). For seek of comparison the depth coordinates of the latter test have been scaled in order to retrace the "original" coordinates and compare effectively the same layers. This was possible thanks to the strain measurements performed with the sliding deformeters for each meter depth. Knowing settlement for each 1m layer it is possible to retrace the "old" coordinate throughout a proportion:

$$(z_{new} - z_{\text{int}\,new,begin}) : l_{\text{int}\,new} = (z_{old} - z_{\text{int}\,old,begin}) : l_{\text{int}\,old} \tag{7.3}$$

and so:

$$z_{old} = (((z_{new} - z_{\text{int}\,new,begin}) / l_{\text{int}\,new}) \cdot l_{\text{int}\,old}) + z_{\text{int}\,old,begin} \tag{7.4}$$

where z_{new} is the coordinate of the new piezocone test, $l_{\text{int}\,new}$ is the length of the 1m layer that z_{new} belongs to, $z_{\text{int}\,new,begin}$ is the lower limit of this layer and $z_{\text{int}\,old,begin}$ is the lower limit of the same layer before that it settled due to the embankment load and unload and the z_{old} is the coordinate referred to the "old" reference system.

What is expected is that after the removal the soil behaviour will be stiffer due to the higher overconsolidation ratio. What is measured fulfils such a prediction except for the shallow sandy layers (from 2 until 8 m depth) and a possible cause could be the high spatial heterogeneity. In fact, as reported in Figure 6.13 the two tests (CPTU N^{o}14 and N^{o}34) were not performed exactly along the same vertical. A second noticeable feature is the significant negative penetration pore pressure recorded at the shoulder location during piezocone penetration in the latest test (after bank removal). A possible interpretation is a strong overconsolidation of the soil and dilative behaviour. In Mayne's opinion (2008)"the relative magnitude of negative values is primarily a function of instrument behaviour rather soil response" and in those cases he recommends to perform dissipation test: if the soil is a silty sand or a sandy silt full dissipation to hydrostatic pressure u_0 should occur within 5 min.

In Figure 7.8, on the other hand, the piezocone profiles at the toe of the embankment are reported (CPTU 20 and 40 Figure 6.13).
Here, as expected, after the embankment removal, soil appears to harden, especially in terms of cone resistance. However, also in these profiles, negative pore pressure has been detected.

To classify soils by means of piezocone tests results classification charts have been proposed by several authors (Schmertmann 1978, Douglas and Olsen 1981, Robertson and Campanella 1986, Robertson 1990, Mayne 2008 etc.) involving piezocone parameters.

As the effective overburden stress increases with depth, cone penetration tip resistance also tends to increase. This increase in readings with depth may cause errors in the interpreted soil classification using raw piezocone readings (Robertson 1990), particularly in deep soundings such as those from offshore investigation. Therefore normalization of measured parameters is required for evaluation of soil behaviour.

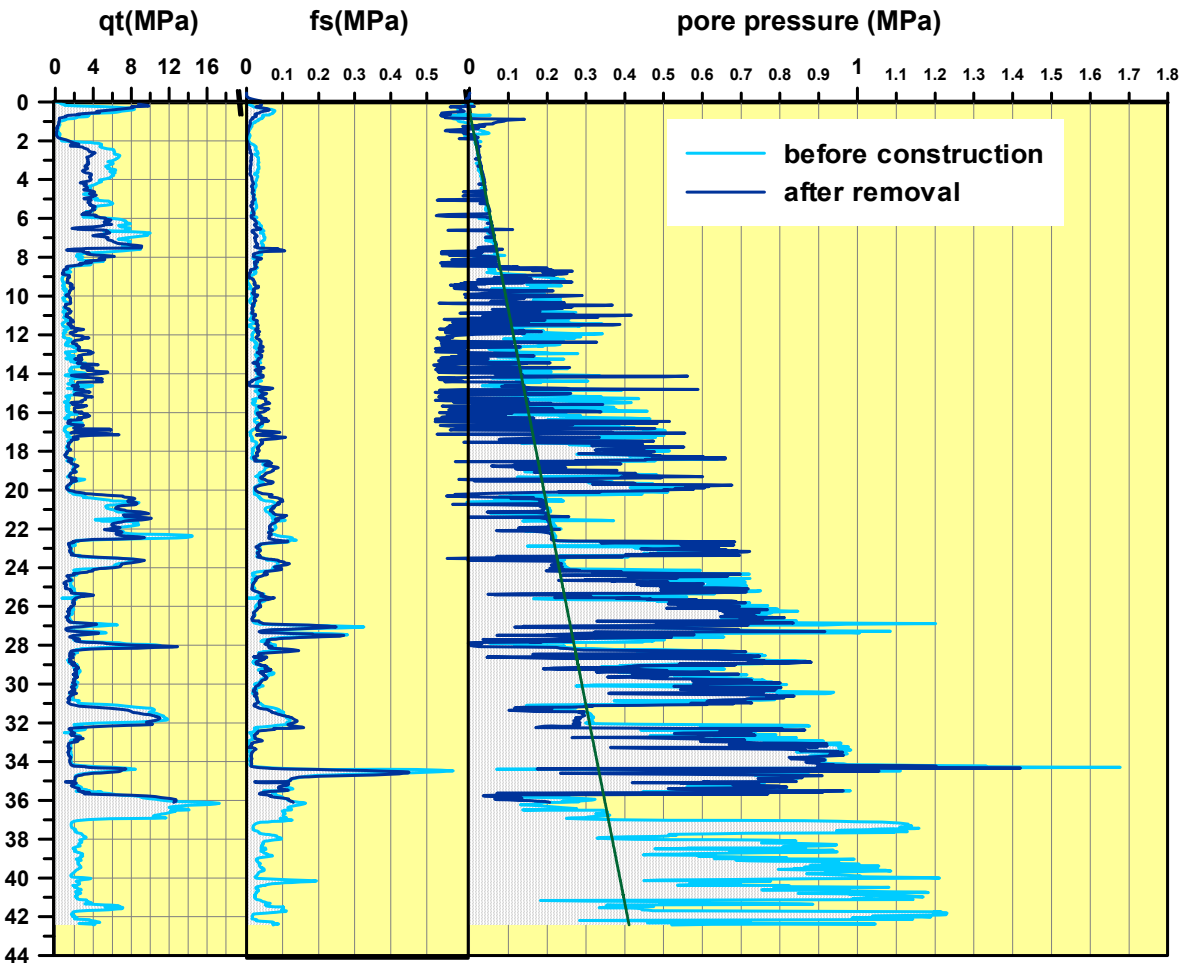

Figure 7.7: CPTU profiles under the centreline before embankment construction and after embankment removal

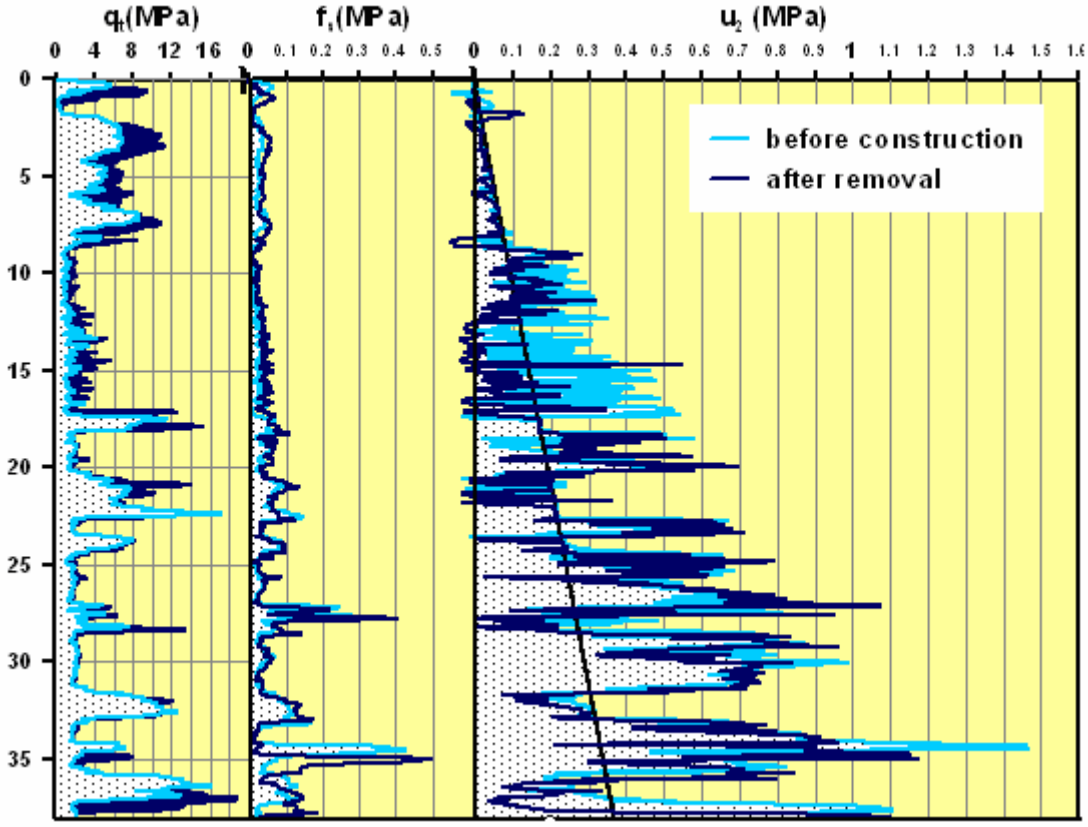

Figure 7.8: CPTU profiles before embankment construction and after embankment removal

With reference to pile bear capacity, in granular soil it holds: $q_c = N_q \sigma'_{z0}$ where q_c is the tip resistance, σ'_{z0} the effective overburden stress and N_q the bear capacity coefficient; for cohesive soil, on the other hand, the bear capacity can be expressed as $q_c = N_c c_u + \sigma_{z0}$ being c_u the undrained shear strength and σ_{z0} the total overburden stress. The bear capacity factors $N_q = q_c / \sigma'_{z0}$ and $N_q = (q_c - \sigma_{z0})/c_u$ can be considered "normalized" cone tip resistances for piezocone tests but, being the test neither completely drained nor undrained, it is necessary to mix the two coefficient.

According to Wroth (1988), normalization of cone tip resistance is typically based on vertical effective stress σ'_{z0} but it accounts also for the total overburden stress deduction and operate on the corrected cone resistance $q_t = q_c + u \cdot (1 - a)$ where a is the net area ratio (see Chapter 6):

$$Q_t = \frac{(q_t - \sigma_{z0})}{\sigma'_{z0}} = \frac{q_{t,net}}{\sigma'_{z0}} \tag{7.5}$$

A similar approach is used for defining the pore pressure parameter (Senneset and Janbu, 1985, Robertson 1986):

$$B_q = \frac{(u_2 - u_0)}{(q_t - \sigma_{z0})} = \frac{\Delta u}{q_{t,net}} \tag{7.6}$$

and also for the friction ratio:

$$F_r = \frac{100 \cdot f_s}{(q_t - \sigma_{z0})} (\%) \tag{7.7}$$

These three parameters are involved in soil classification charts, two or three of them combined together.

Classification of Venetian sediments from *in–situ* measurements has been first performed using the well-known and widely accepted soil behaviour type (SBT) charts proposed by Robertson (1990), based on CPTU data normalized with respect to vertical stress (Q_t, F_r and B_q). The application of these charts to CPTU 20 shows (Figure 7.9 a and b) that most of the relevant points fall in zones 3, 4, 5 and 6, which include soils ranging from clays-silty clays to silty sands. Comparison with classification from laboratory tests reveals certain differences from the Robertson (1990)' SBT approach when applied to silts, which generally fall in both the silt mixtures and clay domains.

Attempts have been made to improve accuracy of Venetian soil classification from piezocone measurements by using the alternative charts recently proposed by Schneider *et al.* (2008), based on the normalized piezocone parameters Q_t and $\Delta u_2/\sigma'_{v0}$ rather than Q_t and B_q. However, the application of the method to CPTU 20 (Figure 7.9 c), does not provide significant additional details to the classification of Venetian sediments but confirms once more the difficulty of separating interbedded clays and silts, which result indistinctly located in the domain of transitional soils.

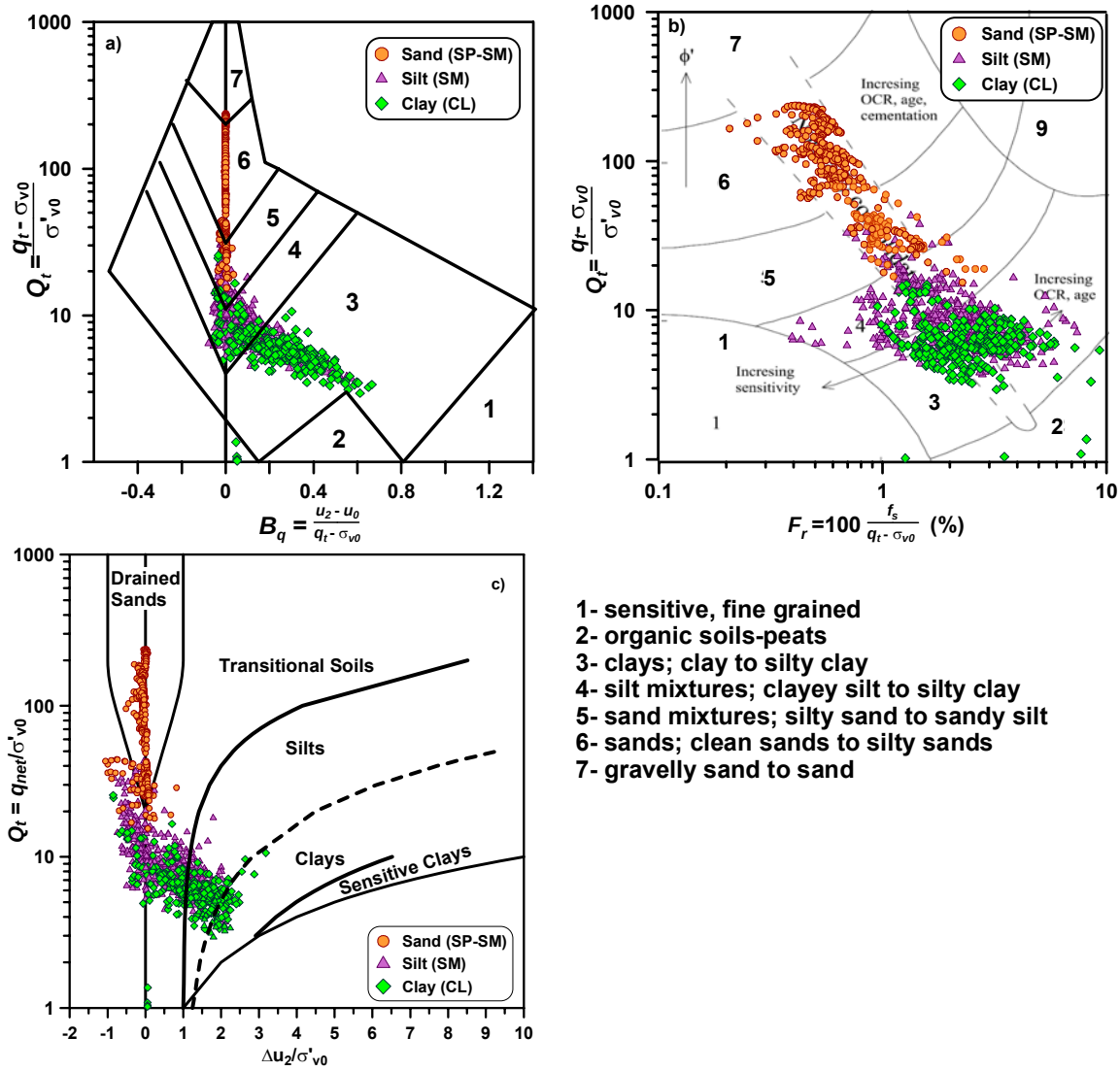

Figure 7.9: Soil classification according to the approaches proposed by: a), b) Robertson (1990); c) Schneider *et al.* (2008) from CPTU 20 (before bank construction).

Reliable *OCR* estimates of Venetian sediments prior to bank construction, based on the interpretation of subsoil strain measurements on loading described in a following paragraph, turned out to range between 1.1 and 1.3, thus confirming that Venetian sediments are in general slightly overconsolidated

Final OCR values, after the bank removal, could be easily back-calculated from the stress history applied with the loading bank (as reported in Figure 7.6).

Interpretation of field OCRs in terms of $(q_t - u_2)/\sigma'_{z0}$ shows that the relevant points defines two different trend lines (Figure 7.10 a), associated to fine (ML, CL) and coarse (SP-SM) sediments respectively. Besides, normalization of OCRs using the friction ratio Fr reveals that all points describe a unique curve, irrespective of the different soil classes. This is given by:

$$OCR = 0.038 \cdot F_r \cdot \left(\frac{q_t - u_2}{\sigma'_{z0}} \right)^{1.21} \quad \text{for } OCR \geq 1 \quad \left(R^2 = 0.92 \right) \tag{7.8}$$

where the two numerical constants were determined as best fit of field-based OCR values from ground surface to 20 m depth.

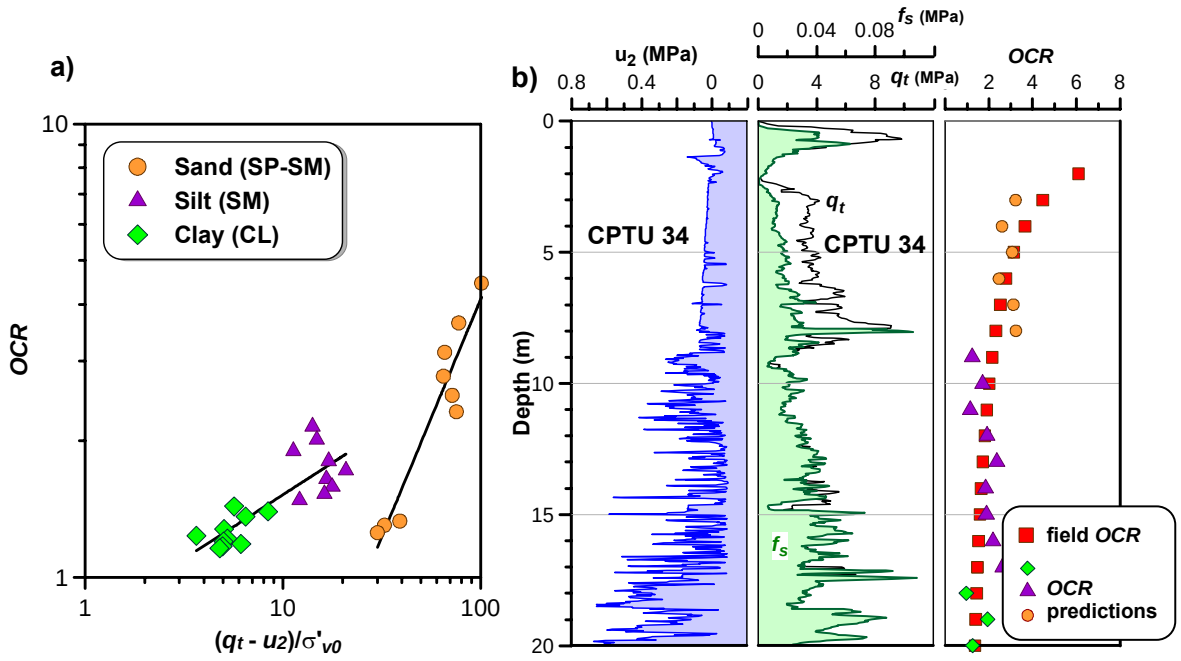

Figure 7.10: a) Interpretation of soil overconsolidation in terms of the normalized tip resistance; b) *OCR* predictions for different soil classes obtained using Equation (7.8)

Unlike existing formulations, which resulted in unrealistic estimates of Venetian sediment *OCR*s (Tonni & Gottardi, 2009), the new approach includes a dependence on the friction ratio F_r, which seems to act as a sort of material index for the different grain-sized Venetian sediments. Predictions of *OCR*s, obtained by applying to the final phase test CPTU 34, are depicted in Figure 7.10 b.

From classification to soil behaviour: Grain size index

Since all the Venetian sediments originated from one common basic material, namely siliceous-calcareous sand, by crushing and sedimentation, Cola and Simonini (2002) proposed an index capable to link mechanical properties to the grading characteristics.

The main feature of the grading characteristics of Venetian soils is that the sands are relatively uniform, but moving towards finer materials, the soils become more graded and the grain-size curve displays a larger range.This feature can be better appreciated by observing the variation of U as a function of D_{50} : the coarser the materials, the lower U, whose range increases with decreasing D_{50}.

To take into account the coupled and opposite variation of D_{50} and U into a single parameter, Cola and Simonini defined the so called *grain size index* :

$$I_{GS} = \frac{\left(D_{50}/D_0\right)}{U} \tag{7.9}$$

where $U = D_{60}/D_{10}$ is the uniformity coefficient and D_0 is a reference diameter, taken equal to 1 mm. In Figure 7.11 profiles of D_{50}/D_0, U and I_{GS} are reported both for the Malamocco Testing Site and Treporti Testing Site.

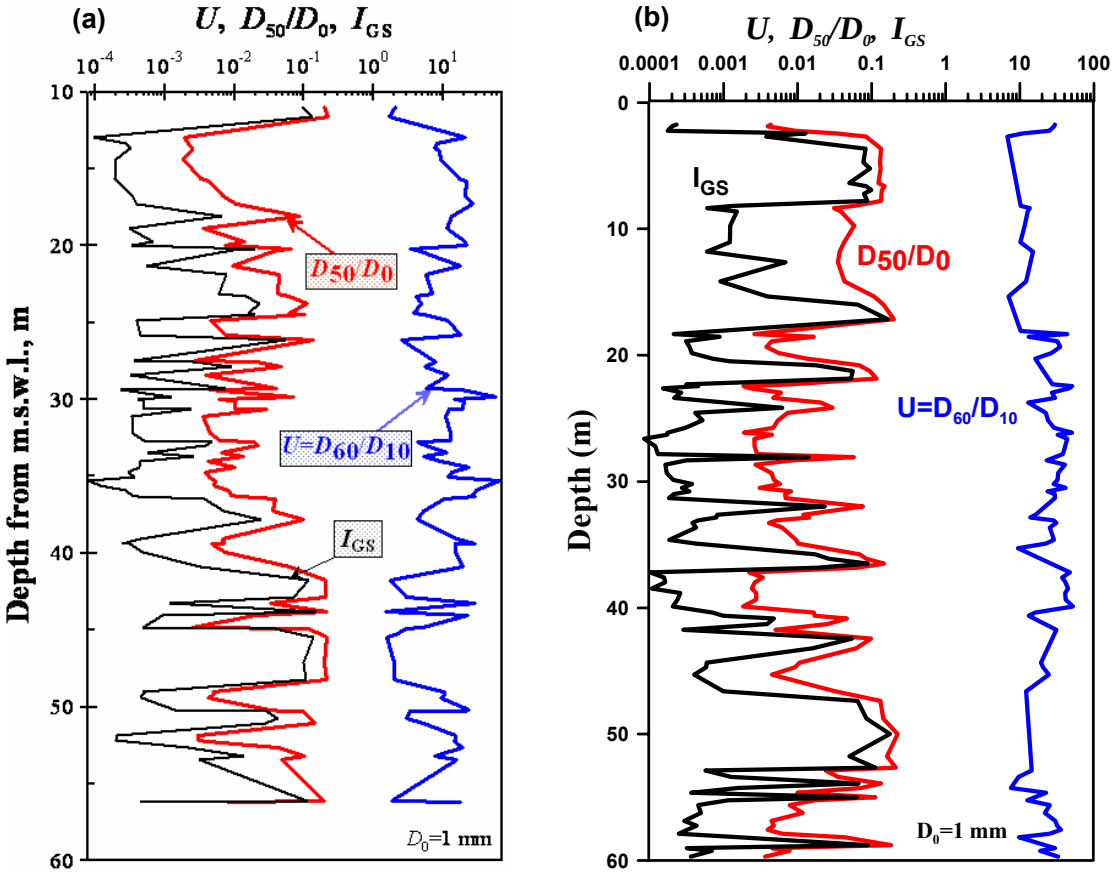

Figure 7.11: profile of mean particle diameter, uniformity coefficient and grain size index (a) at Malamocco Testing Site (b) at Treporti Testing Site

It can be noted that, even if both quantities show oscillations of approximately two orders of magnitude, the profile of D_{50}/D_0 and U are generally characterized by opposite trends with depth, i.e. when D_{50}/D_0 decreases U increases (non-homogeneous silty layers), while when D_{50}/D_0 increases U decreases (homogeneous sandy layers). "The advantage of using I_{GS} as a material index instead of D_{50} or U is due to the fact that I_{GS} associates in an unique expression two soil characteristics that influence the response of a given soil in opposite ways. That is, soil strength and stiffness increase with increasing D_{50} and decreasing U ". (Cola and Simonini, 2002).

From triaxial tests performed on Malamocco Testing Site samples, whose grain size curve was known, trends for critical state variables, such as the critical state friction angle or the critical state line slope can be related to the grain size index (Cola and Simonini, 2002):

$$\varphi_c = 38 + 1.55 \log I_{GS} \tag{7.10}$$

$$\lambda_c = 0.066 - 0.016 \log I_{GS} \tag{7.11}$$

The latter can be used also to evaluate compressibility in oedometric or isotropic condition, since the critical state line and the normally consolidated line are parallel in the stress strain space.

History evaluation from laboratory tests

Estimates of stress history and deformation characteristics are normally made on the basis of oedometer test results. By interpreting the stress-strain curve during initial loading, the preconsolidation pressure p'_{pc} is normally determined using the methods proposed by Casagrande (1936) and Janbu (1969). These methods are based on the assumption that the soil specimen experiences a change in stiffness response at stresses close to p'_{pc}. Experience indicates that the soil specimen will have a relatively stiff response at stresses below p'_{pc} and a softer response at stresses above p'_{pc}. The constrained modulus M is accordingly expected to drop significantly at stresses around p'_{pc} and then increase linearly with increasing stress. If the soil specimen in the oedometer is sufficiently disturbed, however, this ideal situation will be not experienced. In this cases sample disturbance causes the soil to have a soft response at low stresses, which during initial loading results in no measurable change in stiffness, thereby making estimates of p'_{pc} very difficult to obtain. Sample disturbance also causes the measured constrained modulus to show values far below the true in situ soil stiffness. Due to these problems, the oedometer test has limited value on disturbed samples. This is what happen performing such a test on Venetian soil samples.

A brief description of several methods to calculate the preconsolidation pressure will be given in the following and then applied to Venetian soil oedometer tests and CRS tests to show the difficulty in finding p'_{pc}.

In a first approximation, the preconsolidation pressure can be defined as the maximum effective vertical stress that has acted on a clay in the past. This is not a complete description because it can increases without changing the maximum stress that a soil is undergone to due to creep phenomena such as described in the previous chapters. By referencing the current state of the clay p'_0 to the preconsolidation stress p'_{pc} one can determine the OCR which correlates well to many behavioural properties of clay. Preconsolidation stress determined from oedometer test is usually denoted as p'_{pc}, σ'_{pc},or σ'_y. Here we will refer to vertical stresses so we will prefer the second symbol.

In 1936 Casagrande proposed the now classical method to determine preconsolidation stress using an empirical construction from $e - \log\sigma'_z$ curve, where e is the void ratio and σ'_z is the vertical effective stress. To determine the preconsolidation stress σ'_{pc}, the following steps are taken (with reference to Figure 7.12):

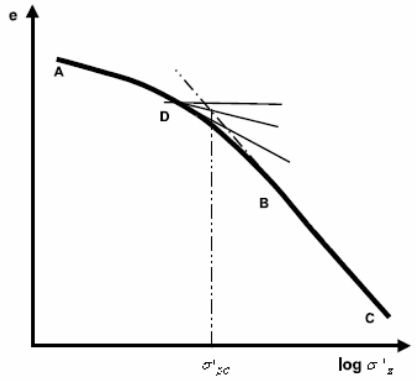

Figure 7.12: Casagrande's method to determine preconsolidation stress.

- produce back the straight line part (BC) of the curve,

- determine the point (D) of maximum curvature on the recompression part (AB) of the curve,

- draw the tangent to the curve at D and bisect the angle between the tangent and the horizontal through D.

The vertical through the point of intersection of the bisector and CB gives the approximate value of the preconsolidation stress.

The Casagrande construction is easy to use and gives good results, provided there is a well-defined break in the $e - \log\sigma'_z$ plot or the $\varepsilon_z - \log\sigma'_z$ plot. Whether it does not happen, results are very subjective depending on which it is chosen as maximum curvature point, especially in an oedometer test where there are few point to draw the compression curve.

In Figure 7.13 an example of oedometer test performed on Treporti soil specimen (borehole S3-see Figure 6.13 – sample S3A, 2.50 m depth) is shown. Results are dependent on interpreter's sensibility, but anyhow a similar value in the end is reached. If smaller load increments were used, or a CRS test performed the inclusion of more data points after the yield stress could facilitate the interpretation of σ'_{pc}.

Let consider a sample taken at 19.5 m depth from the SFS borehole (Figure 6.13) carried out after the Treporti embankment removal. Since the soil was slightly overconsolidated before the embankment construction (see the following paragraph) and the load transferred was enough to bring it into normally consolidated conditions, it is possible to retrace the preconsolidation pressure as the maximum vertical stress that acted on the soil, i.e. the effective overburden pressure. In the case of the specimen SFS16(01) the expected preconsolidation pressure should be: $\sigma'_{z0} + \Delta\sigma'_{z,embankment}(z = 19.5) = 182 + 70 = 252kPa$.

From the Casagrande's procedure applied to a CRS test on it (Figure 7.14), the calculated preconsolidation pressure results in $\sigma'_{pc} = 110kPa$. This demonstrates how unreliable this method can be, and how much Venetian soils loose structure and history memory with sampling.

In a CRS test, where excess pore pressure can be measured, if the sample is well-saturated ($S_r > 92kPa$, at least) and it is enough cohesive to show an excess pore pressure development, the preconsolidation pressure can be detected as soon as the excess pore pressure start increasing, as in Figure 7.14. To use the excess pore pressure development to detect the preconsolidation pressure seems to be more reliable than using the Casagrande's procedure, provided that the sample is well-saturated.

Janbu (1969) showed that for disturbed samples, the zone on the stress-strain curve with the maximum curvature used in Casagrande's procedure may be due solely to the use of a logarithmic scale on the stress axis. Instead, he proposed that the preconsolidation stress could be determined from a plot of constrained modulus M versus the axial stress in a linear scale. A marked drop in the constrained modulus near σ'_{pc} there is expected to be, signifying a breakdown of the structural resistance. The preconsolidation stress is taken as the point just before the constrained modulus levels out.

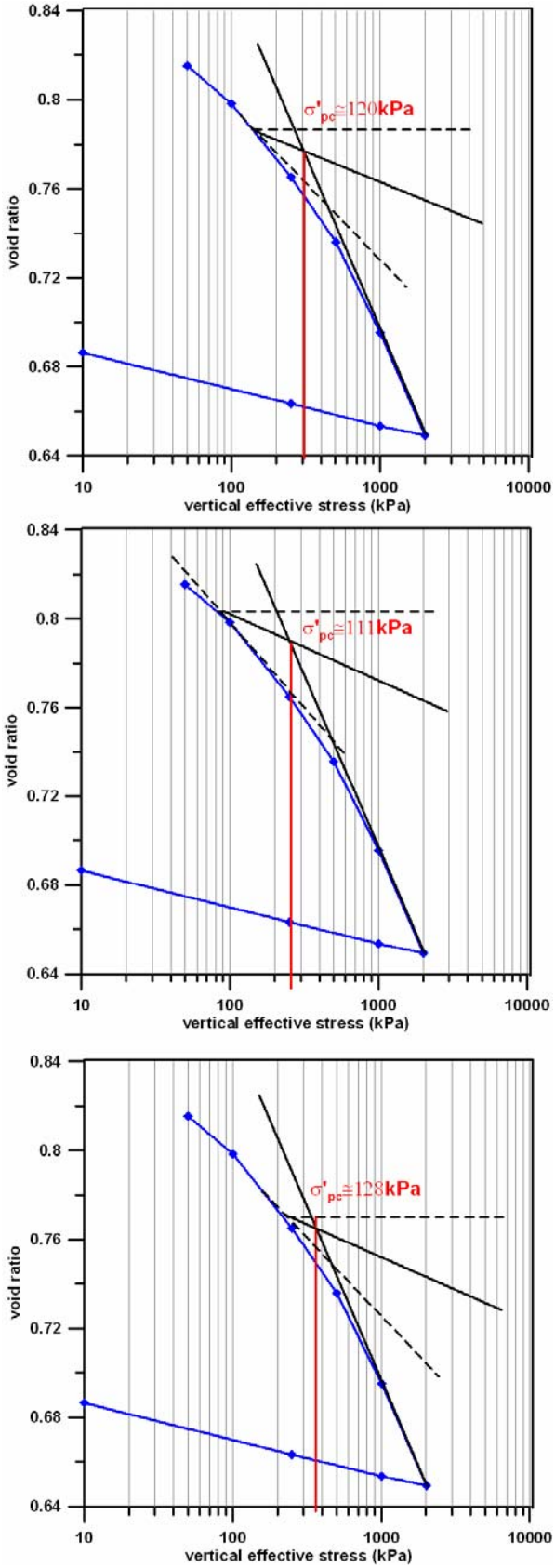

Figure 7.13:Casagrande's methods applied to an oedometer test on Treporti soil specimen (sample S3A)

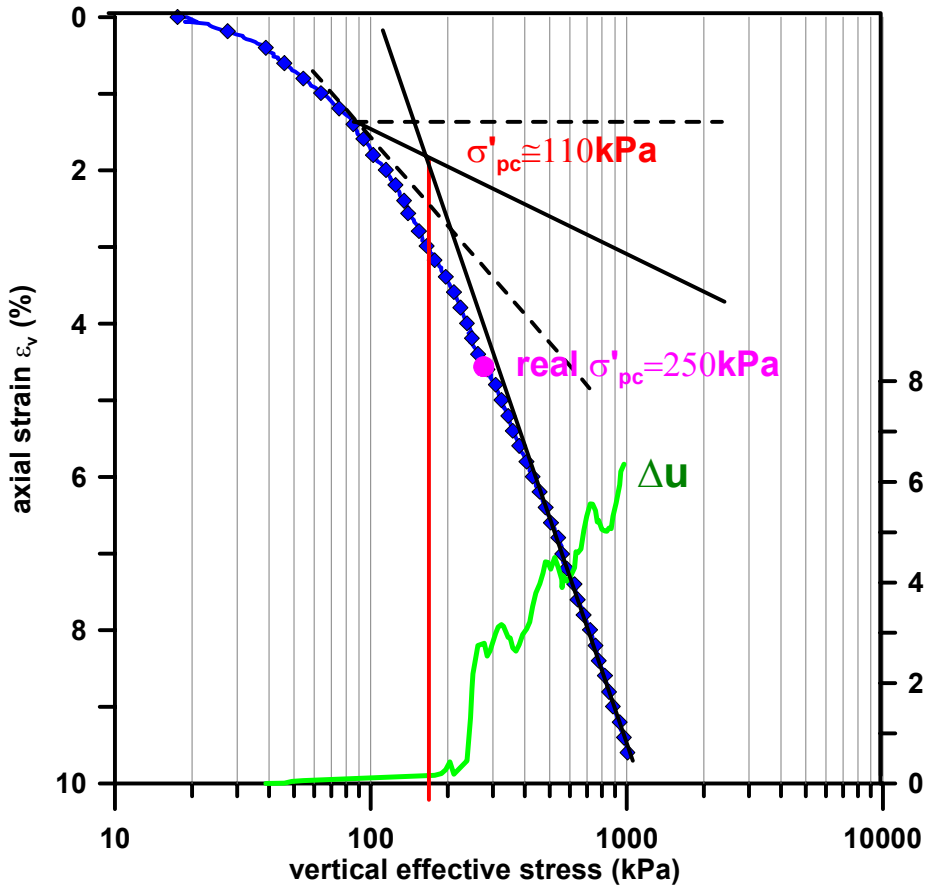

Figure 7.14: CRS test on Treporti soil specimen taken after the embankment removal, sample SFS16(01)

The proposed method is applied both to oedometer test S3A and CRS test SFS16(01) and results are shown in Figure 7.15. No drop in the constrained modulus can be determined since the trend is linear with stress both for the oedometer test and for the CRS test. (Note that in Figure 7.15 the two graphs have different abscissa axis scales).

To evaluate the preconsolidation pressure for more rounded $e-\log\sigma'_z$ curves, Becker et al. (1987) proposed a new method, the so called *work method*. The incremental work is defined as:

$$\Delta W_{oed} = \left(\frac{\sigma'_{z,i+1}-\sigma'_{z,1}}{2}\right)\left(\varepsilon_{i+1}-\varepsilon_i\right) \tag{7.12}$$

where $\sigma'_{z,i+1}$ and $\sigma'_{z,i}$ are the effective stresses at the end of $i+1$ and i loading increments, respectively, and ε_{i+1} and ε_i are the strains at the end of $i+1$ and i loading increments, respectively. Theoretically for overconsolidated samples, data below in situ stress should form a curve that can reasonably approximated with a linear relationship, whereas the post-yield data (above σ'_{pc}) should exhibit a distinctly linear steeper relationship. The intersection of these two fitted lines represents the yield stress, which Becker showed is synonymous of σ'_{pc}.

The procedure does not show the expected change in slope, and whenever one try to find out it, this correspond to a preconsolidation pressure extremely different from that obtained with previous methods.

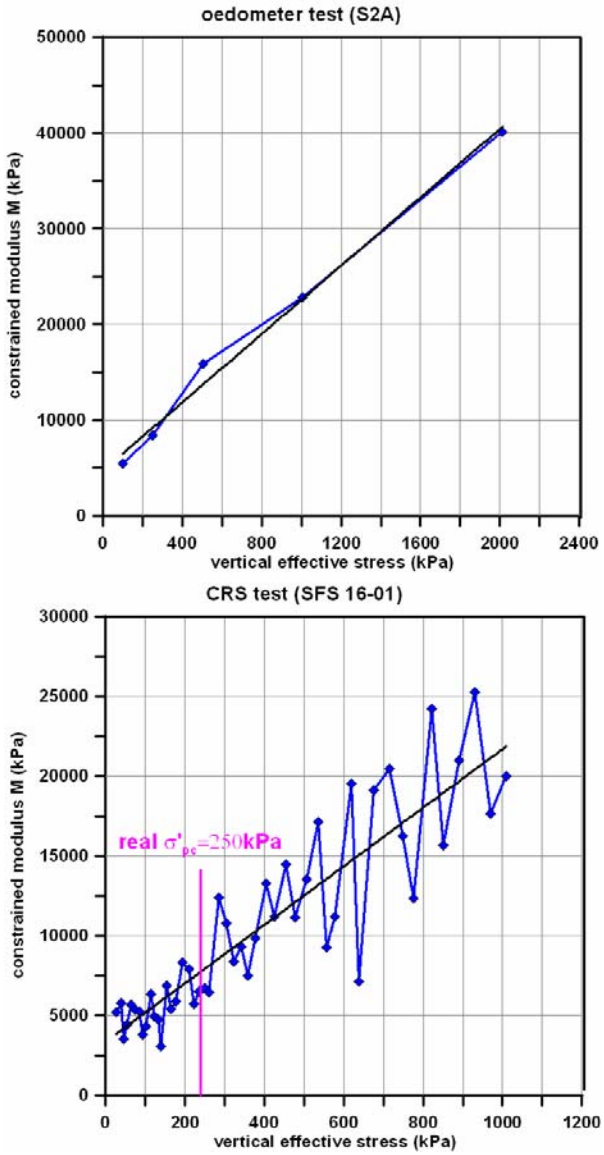

Figure 7.15: Janbu's plot to detect the preconsolidation stress both for S3A oedometer test and for SFS 16(01) CRS test

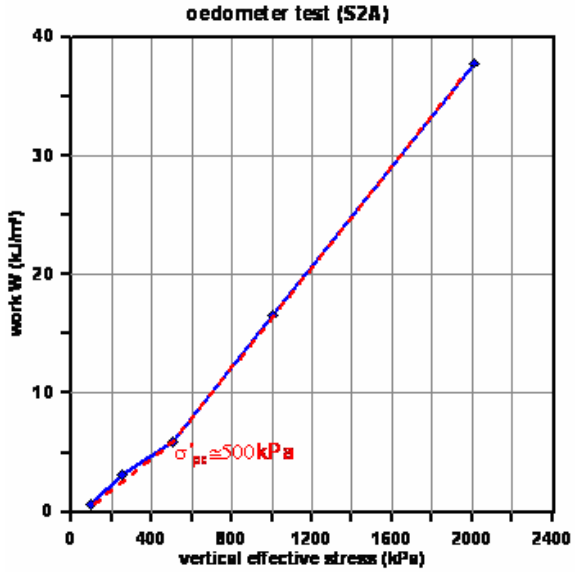

Figure 7.16: Becker methods applied to Treporti oedometer test

Bi-logarithmic approaches have been proposed by Butterfield (1979) and Onitsuka (1995) because they summarize the classical approach and the strain work approach (from whom it can be derived mathematically). In $\ln(1+e)-\log\sigma'_z$ approach the yield stress is defined as the intersection point of two lines representing the pre-yield and post yield stresses.
Once more this not evident in Venetian soils (Figure 7.17) and eventually the preconsolidation pressure identified is very approximated.

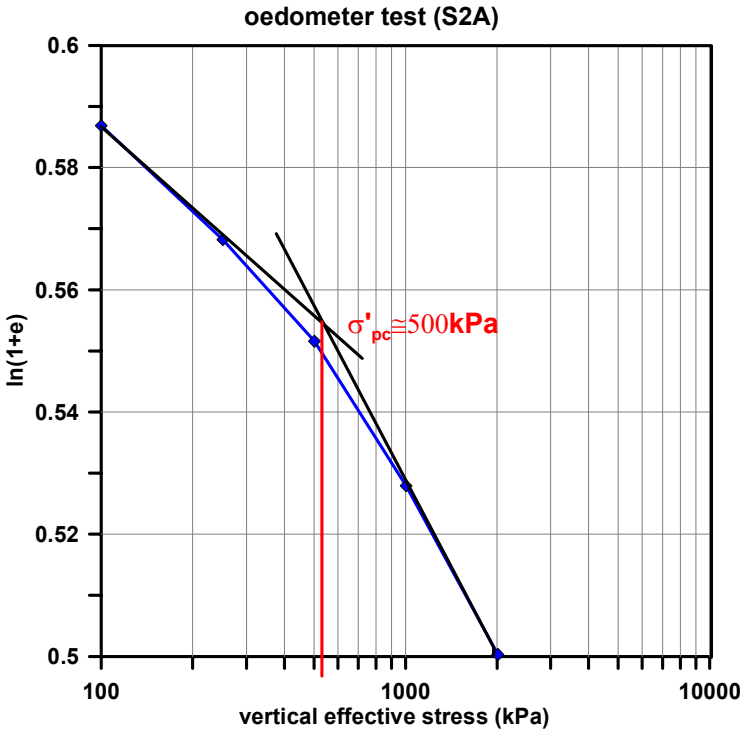

Figure 7.17: bi-logarithmic approach on Treporti specimen oedometer test

History evaluation from in situ stress-strain curve

Venetian soils seem to loose completely history and structure memory when sampled, so that it is almost impossible to retrace preconsolidation pressure and then OCR from laboratory tests. The extreme difficulty in evaluating preconsolidation pressure with classical laboratory tests suggests to refer to in situ experience.

The Treporti embankment, in fact, represents a sort of oedometer tests in a true scale, at least under the centreline where the behaviour can be consider one-dimensional. This is a rough approximation, because soil is not as confined as in an oedometer cell, but, since the embankment diameter is quite large, this approach can be used in estimating soil behaviour.

Thanks to the sliding deformeter devices (see previous Chapter), it has been possible to measure vertical strains each meter depth until 60 m depth and then to reconstruct the strain-time behaviour of each soil layer, and also the total settlement-time curve at each depth. Local vertical displacements (mm/m) under the centreline, i.e. strains corresponding to each depth, are reported in Figure 7.18 at any time, while accumulated displacements for each layer are reported in Figure 7.19. The accumulated displacement is the sum of local displacement from 60 m depth (where there is no displacement at all) until the considered depth: $s_z(z)=\sum_{i=z+1}^{60}\varepsilon_{z,i}$.

The distribution of vertical displacements with depth provided by the multiple extensometers can be use also to double check the soil profile emerged from the piezocone classification. The relevant contribution of the upper silty layer (2 m depth) and particularly of the clayey silt layer from 8 m to 20 m depth are very evident thus confirming the cohesive nature of those layers. The influence of embankment reduces with depth and beyond 35 m the displacements are very small and not appreciable with the sliding deformeters installed. It can be noticed that the maximum vertical deformation does not exceed 4% except for the shallowest silty layer. It is very interesting to note that the complete embankment removal does not reduce so much the displacement, that is, the swelling due to unloading is very little especially compared with the displacement due to the embankment loading and the viscous displacement. Comparing vertical and horizontal displacements measured with inclinometers it has appeared that the total vertical displacement is one order of magnitude greater than the maximum horizontal displacement, that is, the deformation process has developed prevalently in the vertical direction.

Vertical stresses increments at any depth due to the embankment construction, that was performed in 14 phases and resemble to a sort of multiple stage loading test (i.e. an oedometer test), are evaluated with an elastic approach, using Equation (7.1). The derived stress-strain curves are plotted in Figure 7.20 in which also the creep phase and the unloading stages are reported. In brownish colours the sandy layers are reported, while silts and clay are plotted with purple lines.

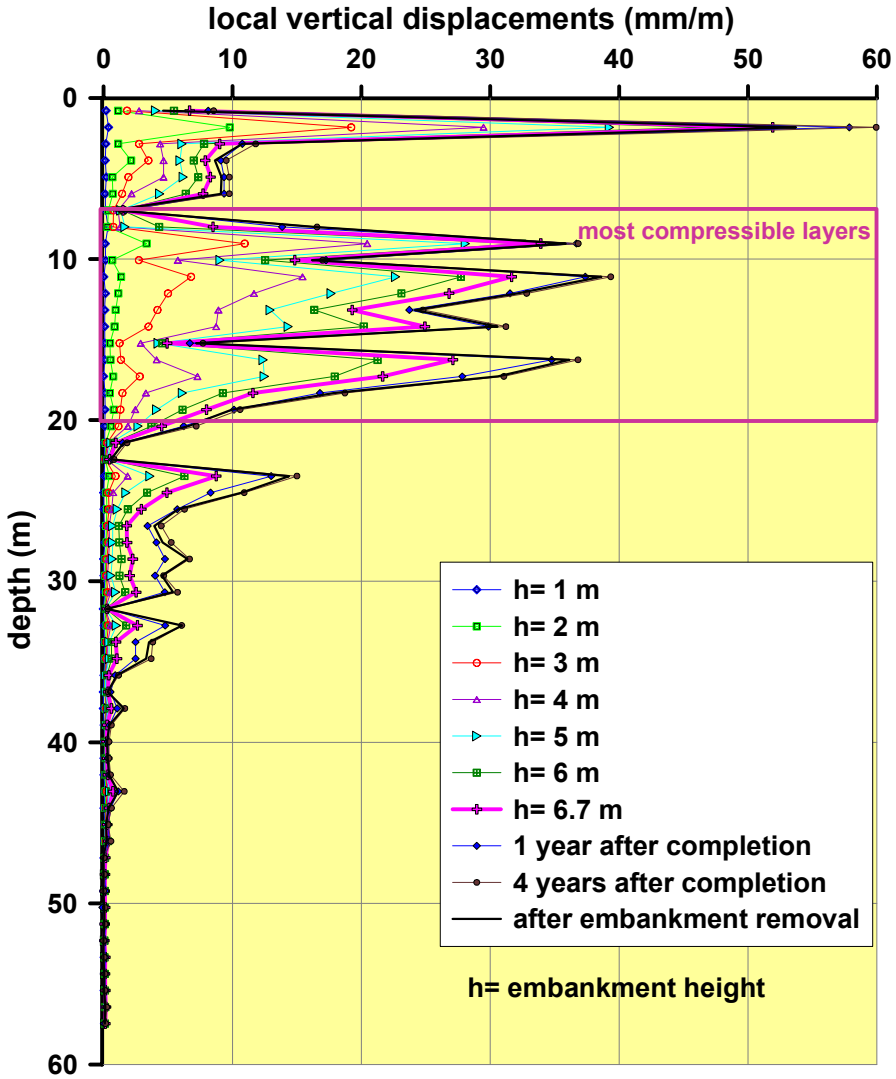

Figure 7.18: local vertical displacements at Treporti Testing Site

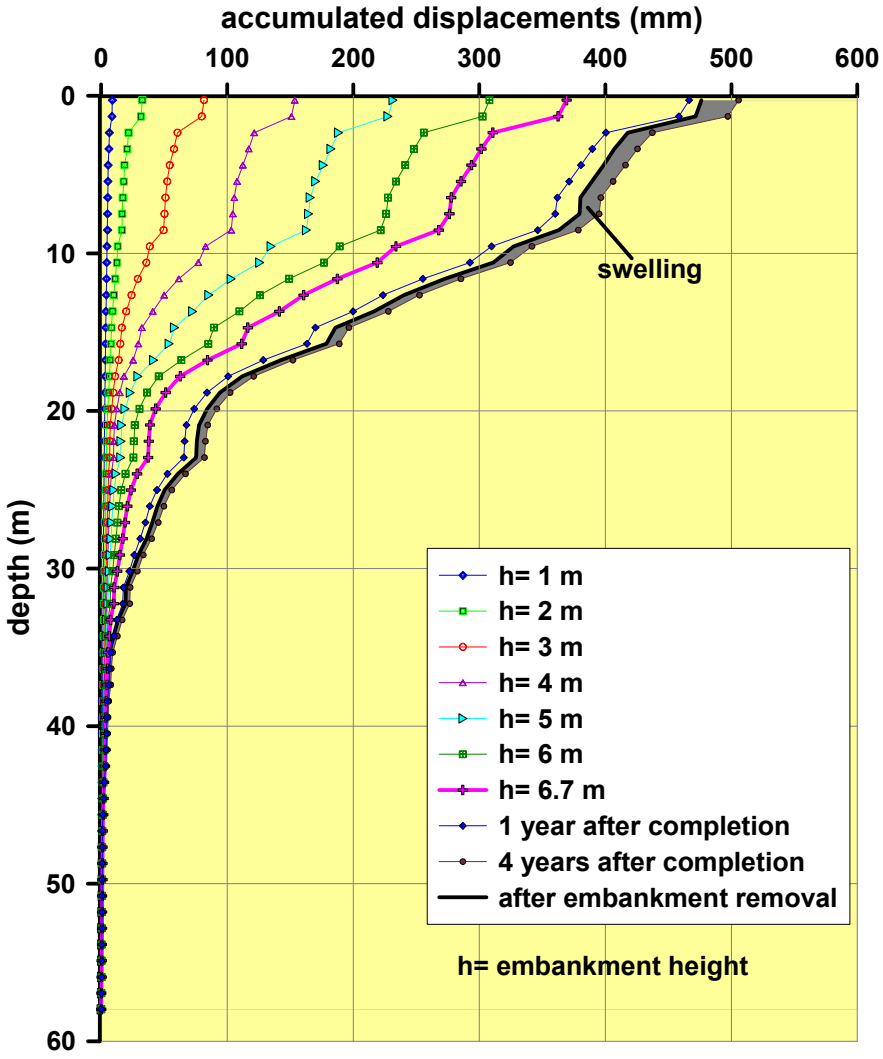

Figure 7.19: accumulated displacements at Treporti Testing Site

It is clearly evident that sandy layers are stiffer than silty ones, since they show little strain even though their stress increments are higher than deeper silty layers subjected to less stress and that show, instead, a noticeable final strain (especially the shallowest sandy layer).

The presence of prefabricated drains in upper silty clay layer (2 m depth) and the relative high soil drainage of all the deeper layers have suggested that primary consolidation has occurred quite rapidly and contemporary with embankment construction also. Therefore, since no delayed deformation due to consolidation process has occurred along with the loading phase, the sharp variation of curvature in stress-strain curves reported in Figure 7.20 has been interpreted in terms of yielding stress σ'_y, and since strains have been prevalently developed in vertical direction, it is assumed that the yielding stress represents the preconsolidation pressure $\sigma'_y \equiv \sigma'_{z,pc}$. Comparing it with the overburden effective stress, the overconsolidation ratio for each layer is given (Figure 7.21).

Using the in-situ measurements provided by the multiple extensometers, it is therefore possible to avoid both the scale effect and the stress-relief and destructuration due to sampling, particularly affecting the mechanical response of these soils.

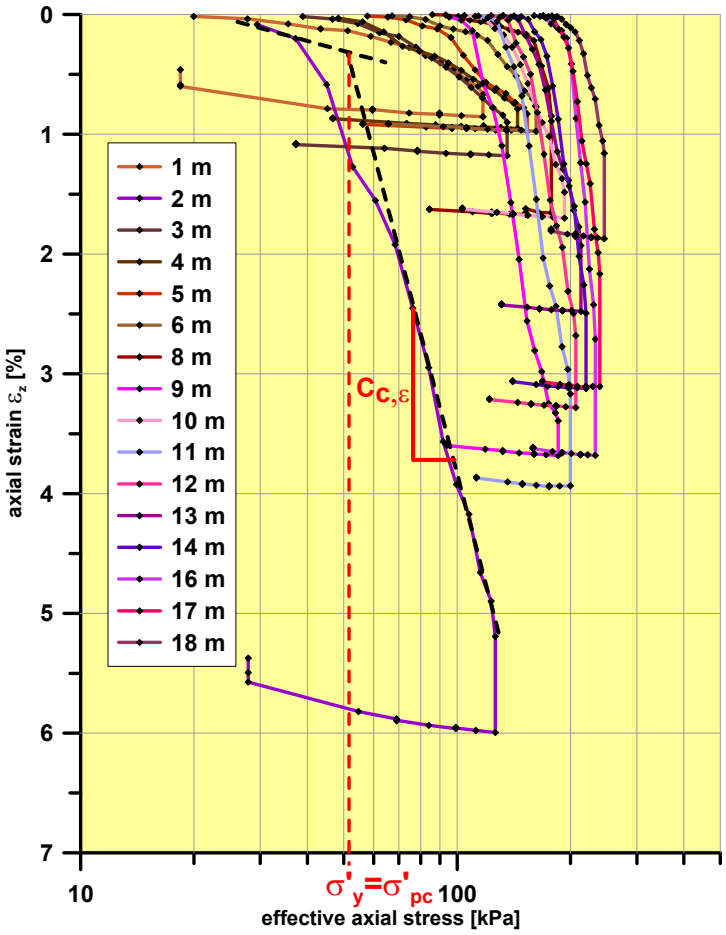

Figure 7.20: stress - strain curves at Treporti Testing Site

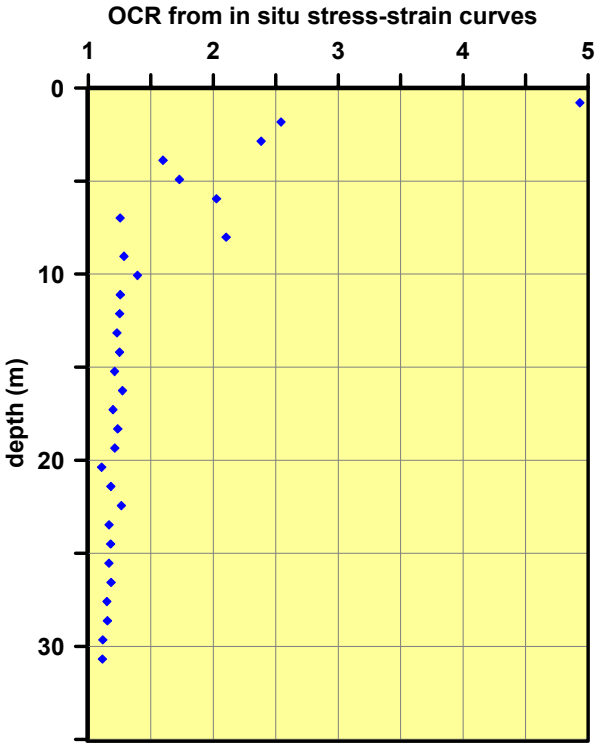

Figure 7.21: OCR profile from in situ stress- strain curve

Stiffness evaluation from in situ stress strain curve

A confirm of the in situ changing behaviour of the subsoil, from a pre-yielding to a post-yielding compressibility behaviour, comes from the analysis of in situ-soil stiffness. A sort of constrained modulus is defined as:

$$M = \frac{\Delta\sigma'_z}{\Delta\varepsilon_z} \tag{3.4}$$

where $\Delta\sigma'_z$ corresponds to 1 meter thickness of the building embankment, in the loading phase, and to 2 meters of embankment removal in the unloading phase. Normalized stiffness with respect to the average vertical stress corresponding to the given stress increment M/σ'_z is plotted against the vertical stress induced by the increasing embankment load, normalized with the site preconsolidation pressure $\sigma'_z/\sigma'_{z,pc,site}$.

Substantially stiffnesses corresponding to overconsolidated state lie on the left part of the graph, while on the right there are stiffnesses corresponding to normalconsolidated state.
A decreasing trend is clearly evident in the loading phase (blue points) both in clayey and silty layers and in sandy layers. In the first case stiffness variation is sharp, while in the latter case sands are characterized by higher values and their variation is less influenced by the overcoming of the in situ yield stress. In any case, after the preconsolidation pressure, stiffness continues decreasing even in the normally consolidated range, thus meaning that the compression behaviour is not truly oedometric, as expected, because there is no real confinement to the lateral soil spreading. As regard to the unloading phase (red points), Figure 7.22 show a recover in stiffness as expected, but to values not as higher as the initial ones, indeed.

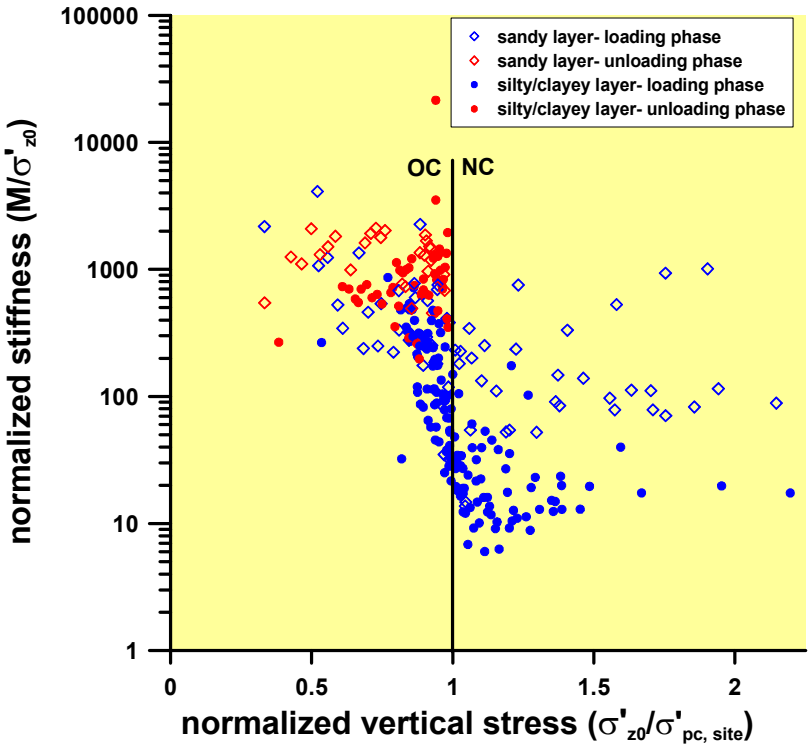

Figure 7.22: normalized stiffness vs. normalized vertical stress

Whereas this representation is extremely useful in highlighting the presence of a yielding stress, guessed from the in situ stress-strain curve, it is not completely legible in terms of stiffness degradation, especially in the unloading phase in which it should be read from left to right, at least. The same data are reported against vertical strain in Figure 7.23 and Figure 7.24. Stiffness normalization with respect to stress makes the modulus stress independent and so it allows to examine its evolution with strain. To compare data from different layers, with different initial state, compressibility parameters and then different strain evolution, a normalization with respect to the maximum vertical strain has been proposed. Figure 7.23 and Figure 7.24 differ only from the scale (logarithmic in the latter). It is evident the stiffness reduction with strain, both in silty layers and in sandy ones. Once again sands show a flatter trend while clayey and silty layers show a deepest decrease. Furthermore, as expected, in the loading phase reduction is sharper than in unloading phase (see Chapter 4).

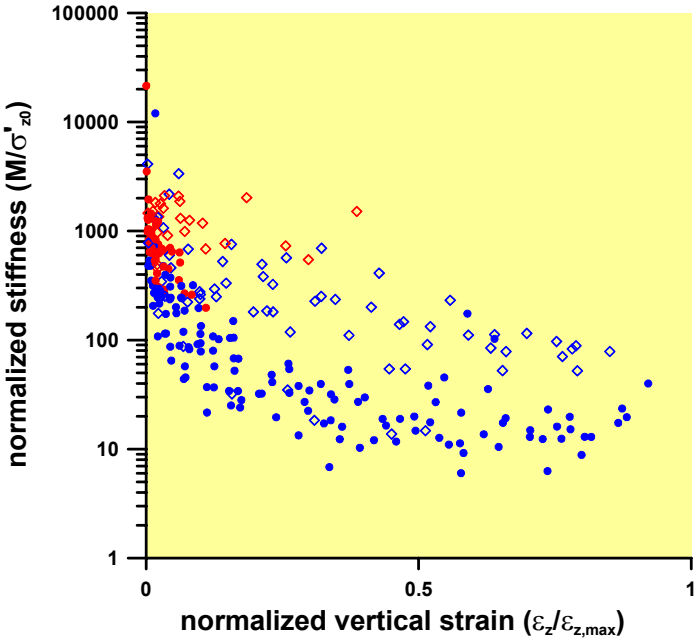

Figure 7.23: normalized stiffness vs. normalized vertical strain

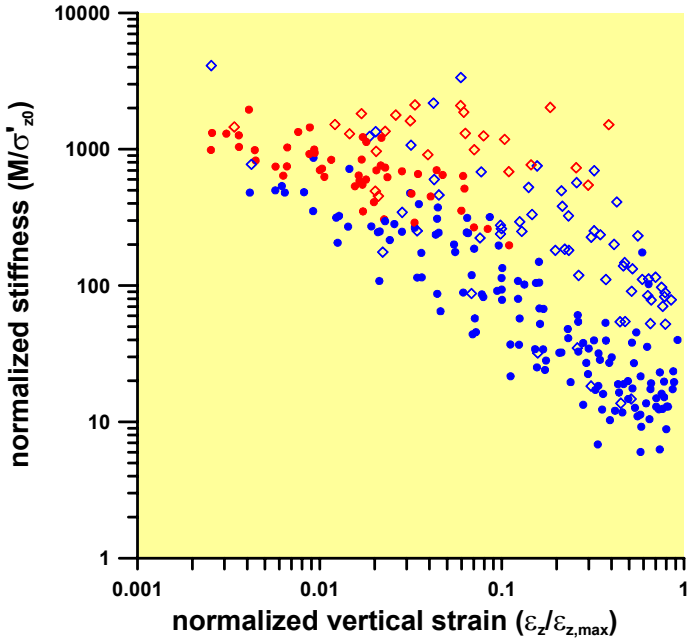

Figure 7.24: normalized stiffness vs. the log of normalized vertical strain

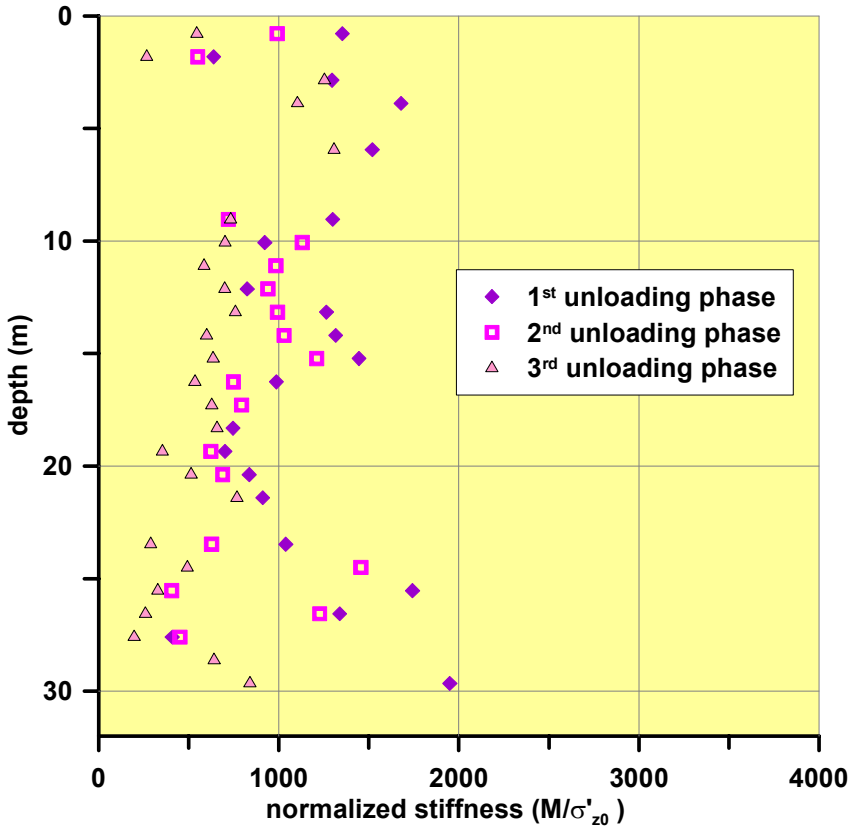

Figure 7.25: stiffness profiles for each unloading phase

In Figure 7.25 a detailed unloading stiffness profile along depth under the centreline is given for each unloading phase thus showing a decrease corresponding to the increasing amplitude strain. At the loading reversal corresponding to the first unloading step, in fact, stiffness gains again a higher value that reduces in the following unloading steps.

In the same framework as that used in the previous paragraph to retrace yielding properties of the Venetian soil from in situ-behaviour, the in -situ compression curve can be interpreted as composed by a recompression line followed by a virgin compression line whose slope can be interpreted as a sort of primary compression coefficient $C_{c,\varepsilon} = \Delta\varepsilon_z / \Delta \log \sigma'_z$ (see Figure 7.20). This is not completely true because the in situ loading trial has not that regularity that is typical in an oedometer test in which load is doubled and kept for the same time interval each step. In the case of Treporti embankment this is not, since the time of construction for each step in different and also time elapsed between one loading phase and the following is not regularly the same. Theoretically, in a multiple stage test, on the normally consolidation line strain rate should be the same for each loading increment, in Treporti trial there are no strain measurements for a same loading step so it is not possible to analyze the strain rate evolution and the strain rate corresponding to the compression line can be calculated only considering a discrete time interval and a discrete strain interval. Comparing this secant strain rate each others, it results that the continue line which we refer to as "compression curve" reported in Figure 7.20 for each 1m thickness layer, intersect many isotache lines and it is thus steeper than the real primary compression coefficient. This is partially confirmed by comparing in situ $C_{c,\varepsilon}$ with values obtained from oedometer tests that are smaller (Figure 7.26). The two series of data are not completely comparable, since the in situ data show an average value for 1 m thickness layer characterized by a very high spatial variability while the oedometer test results refer to a very small sample.

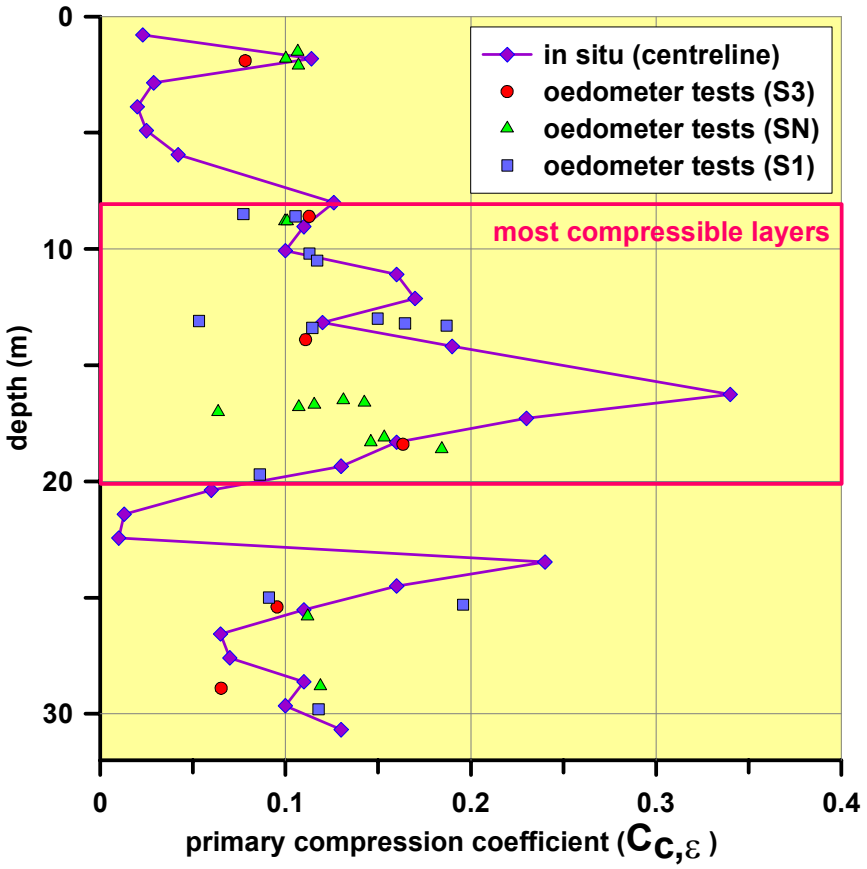

Figure 7.26: primary compression coefficient $C_{c,\varepsilon}$ from in situ curves and from laboratory tests

Creep behaviour of Venetian soil

The completed bank insisted on the soil ground for more than 4 years. The total settlement under the centreline on embankment completion was 381 mm, while at the end of the following four years it reached 505 mm, thus giving 124 mm of secondary compression. (see Figure 7.19). In Figure 7.27 stress-time curve in semi-logarithmic scale are reported for each 1 m thickness layer. The trend is characterized by the classical S-shaped curve, but in this case the first part does nor correspond to a only one load increment but to several ones. The results in term of strain-time curve is the same as the case of one single load increment because in this latter case the first part corresponds to an increase in effective stress as well. The final part of the curves in Figure 7.27 corresponds to deformation occurring after bank construction, fitted in the $\varepsilon_z - \log t$ plane by a straight line whose slope is assumed to be the secondary compression coefficient $C_{\alpha,\varepsilon} = \Delta\varepsilon_z / \Delta \log t$ (Equation 2.5).

$C_{\alpha,\varepsilon}$ profile along with depth is given in Figure 7.28, together with secondary compression coefficients obtained by laboratory oedometer tests referred to normally consolidated states.
As already mentioned in the previous Chapters, secondary compression coefficient is lower for overconsolidated state, that show stiffer behaviour, while it is higher for normally consolidated states.

In Figure 7.29, the evolution of secondary compression coefficient calculated from laboratory oedometer tests (borehole S1, Figure 6.13) is shown with reference to normalized vertical stress. On the left there are $C_{\alpha,\varepsilon}$ referred to overconsolidated states, while higher values are characteristic of normally consolidated.

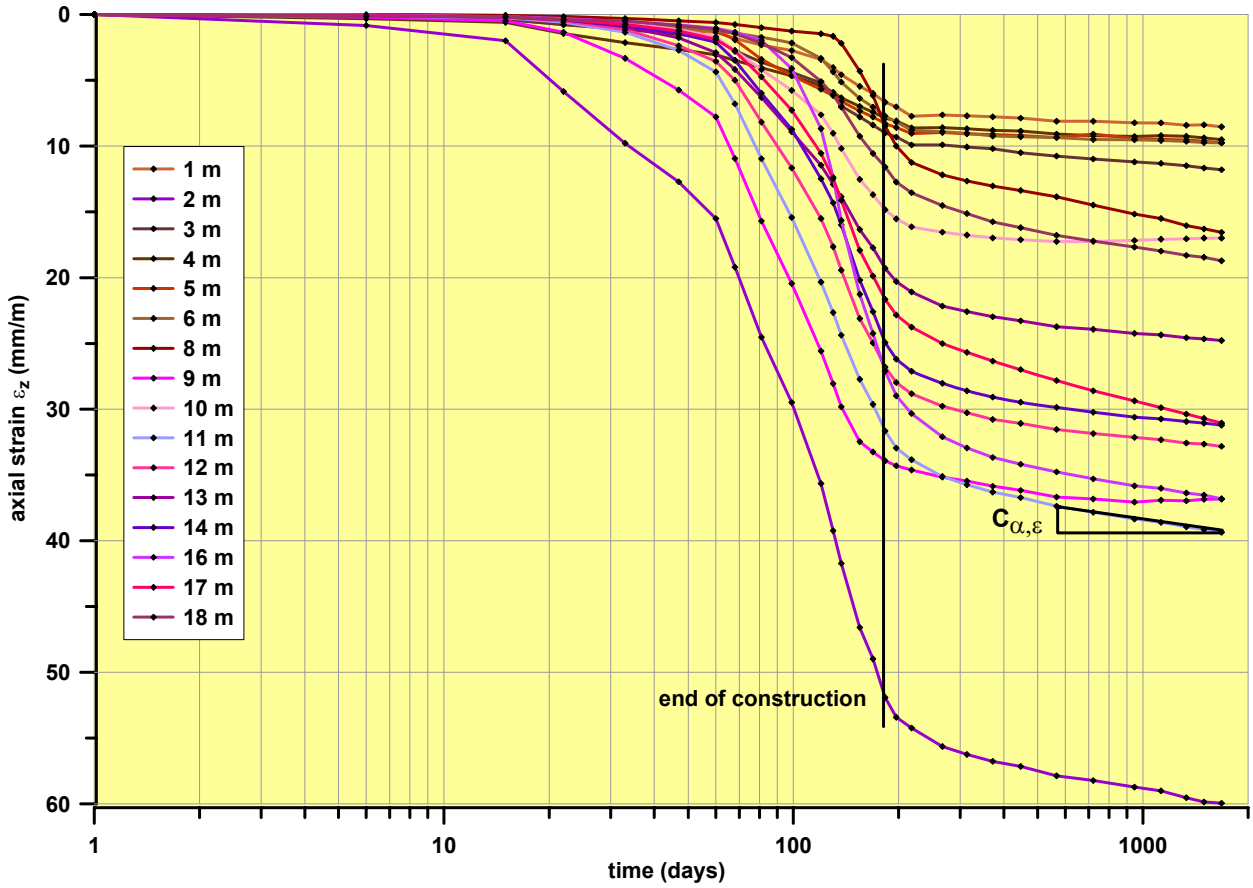

Figure 7.27: stress-time curves in semi-logarithmic scale for 1 m thickness in situ layers

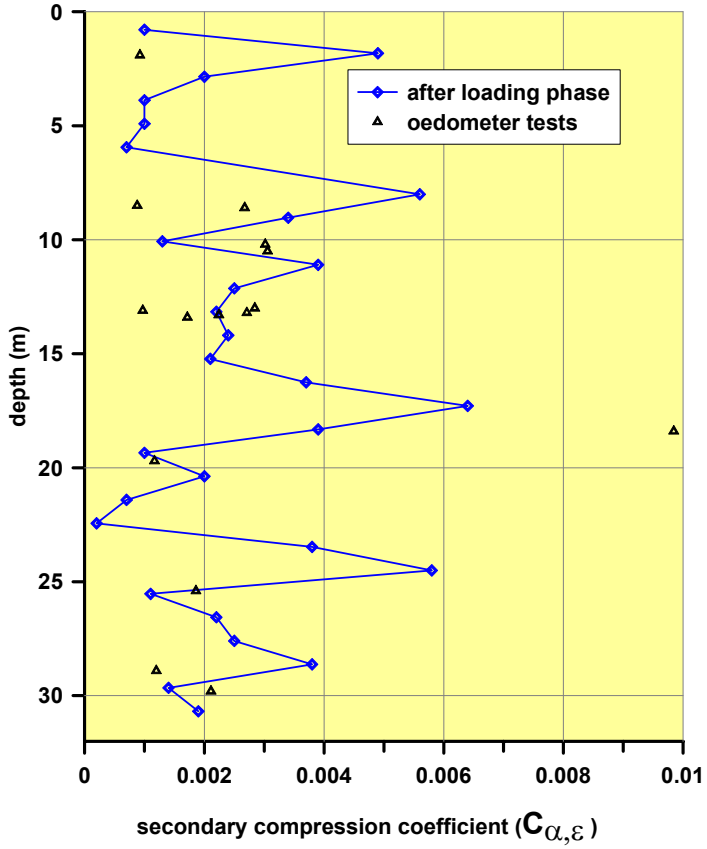

Figure 7.28:in situ secondary compression coefficient for each layer and oedometer secondary compression coefficients

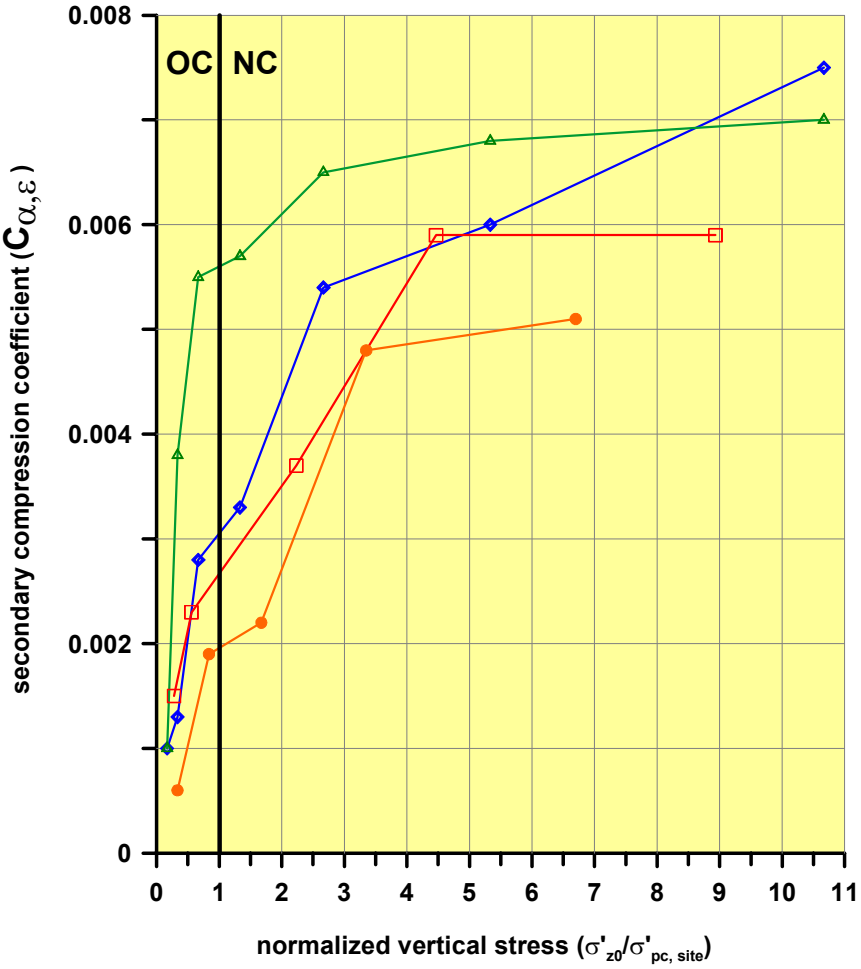

Figure 7.29: secondary compression coefficient vs. normalized vertical stress, from oedometer tests (Treporti, S1)

Creep models that use $C_{\alpha,\varepsilon}$ parameter in general refer to the normally consolidated states' value (like the Soft Soil Creep Model) eventually deriving the overconsolidated values. There is however the influence of the confining stress thus causing the $C_{\alpha,\varepsilon}$ coefficient to increase with σ'_z, as evident in Figure 7.29.

Comparing oedometer and in situ coefficient (Figure 7.28) a good agreement can be observed, and $C_{\alpha,\varepsilon}$ in situ values can be assumed definitely as normally consolidated values. The stress increment due to the embankment load in fact has brought soil layers from a overconsolidated state to normally consolidated conditions and secondary compression coefficients calculated are related to the creeping behaviour after embankment completion.

It has already mentioned that, as postulated by Mesri, the ratio between primary and secondary compression coefficient is constant for a given soil, thus constituting a sort of material parameter. In Figure 7.30 their respective values are plotted both from in situ measurements and laboratory data, in order to detect a possible trend: the ratio $C_{\alpha,\varepsilon}/C_{c,\varepsilon}$ falls between two limits close to those proposed by Mesri, and higher values are characteristic for sandy layers.

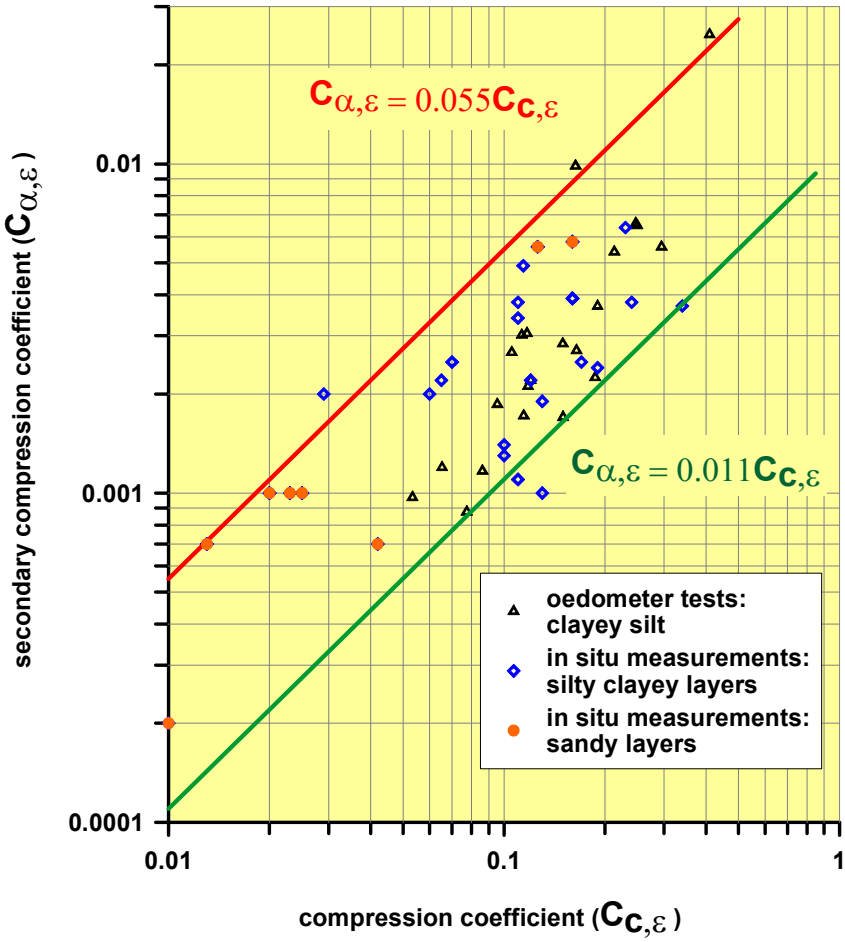

Figure 7.30: primary and secondary compression coefficient from site compression curves and laboratory tests

After four years at constant height, the Treporti test embankment has been removed. The removal has consisted in three phases, each of them has consisted in removing 2 m ca. of sand from the embankment, levelling the surface, and then waiting for three months.

In these period at constant stress, two mechanism coexist, the delayed swelling that follows the instant swelling due to the unloading, and the creep behaviour that, on the other side, tends to make the soil settle. The creep behaviour is negligible when in overconsolidated conditions thus giving a low $C_{\alpha,\varepsilon}$ value. As long as the overconsolidation ratio is still close to the unity, creep behaviour has a not negligible role, and the total balance shows an effective settlement, while, whenever creep behaviour can be neglected, an effective delayed swelling can be appreciated, as evident in Figure 7.33 and even more in Figure 7.34, where local and accumulated vertical swelling strain are plotted, considering as a reference zero strain the last measurement before the first unloading phase.

In Figure 7.31 the strain time behaviour during the unload process is reported for the first eighteen 1 m thickness layers, being the purple ones referred to silty layers and the brownish ones to the sandy layers. It can be noticed that after the first unloading phase soil layers show a creeping behaviour with time, whereas after the second there is a sort of stationary situation, probably a combined effect of the delayed swelling effect and the creep behaviour, and after the last unloading step the soil shows a further delayed swelling. It has to be considered, however, that the accuracy of the multiple extensometers used for the survey is 0.03 mm/m and therefore all the strain interval fall in the range of the measure error.

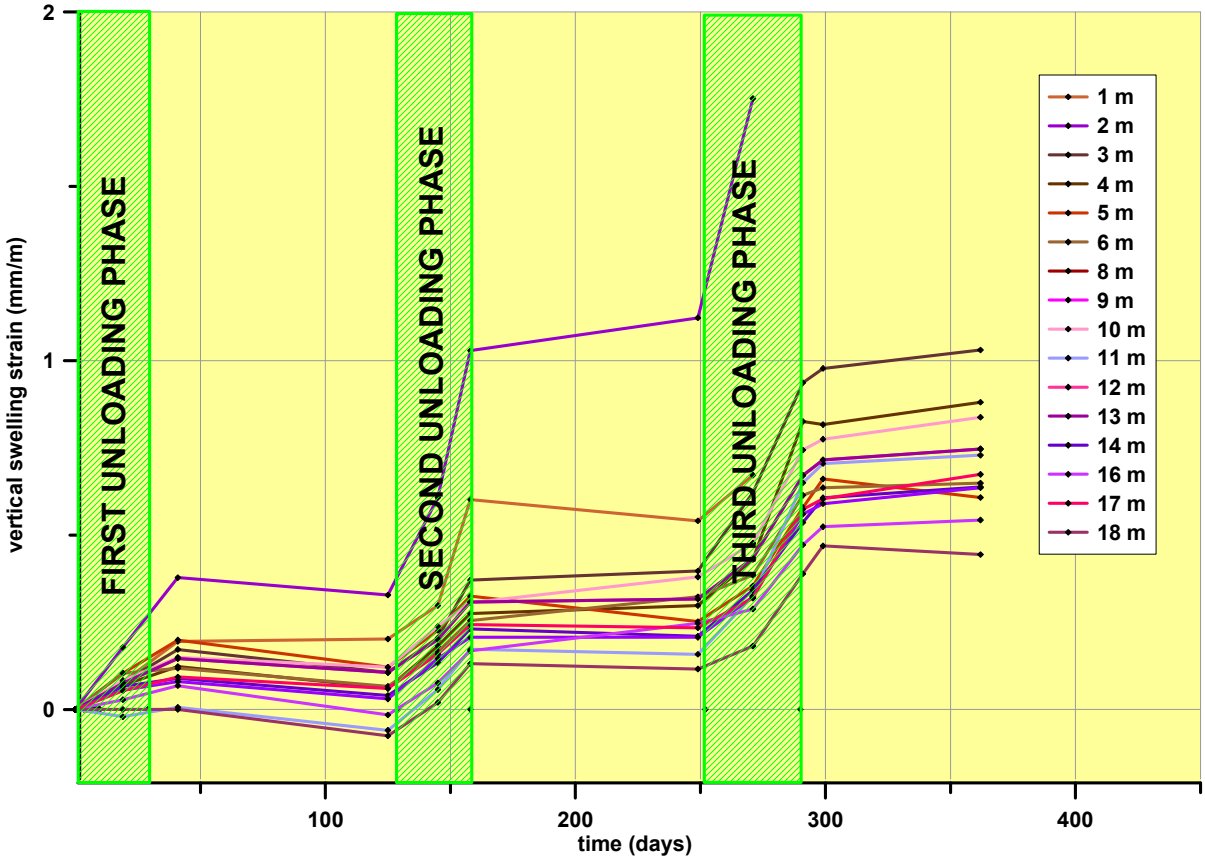

Figure 7.31: swelling behaviour during the Treporti unloading process for each 1m thickness layer

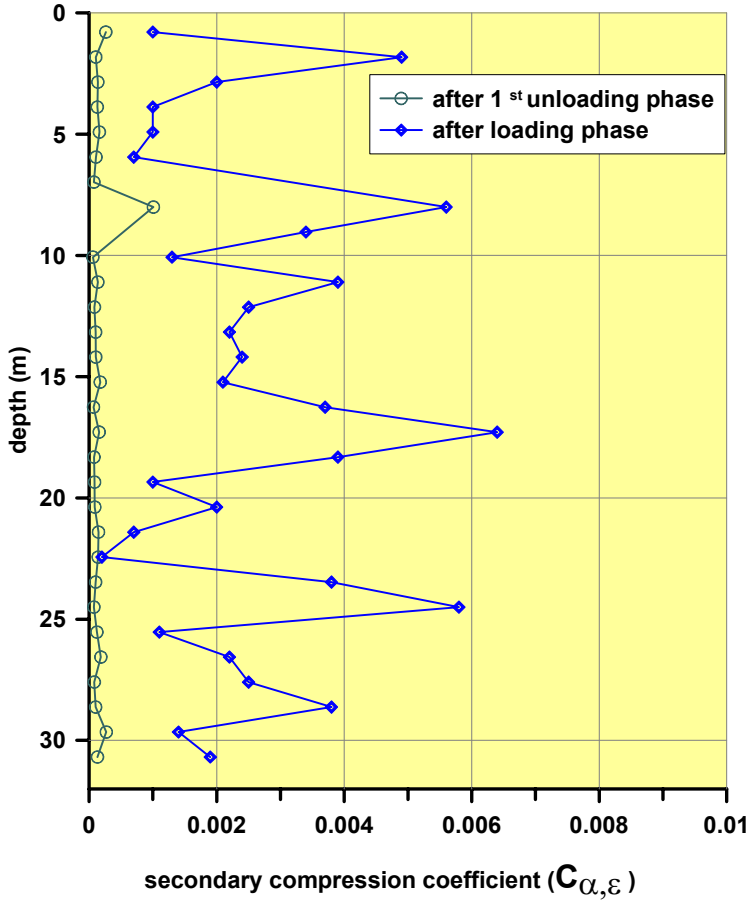

Figure 7.32:secondary compression coefficients along with depth, calculated both in the loading process and after the first unloading stage

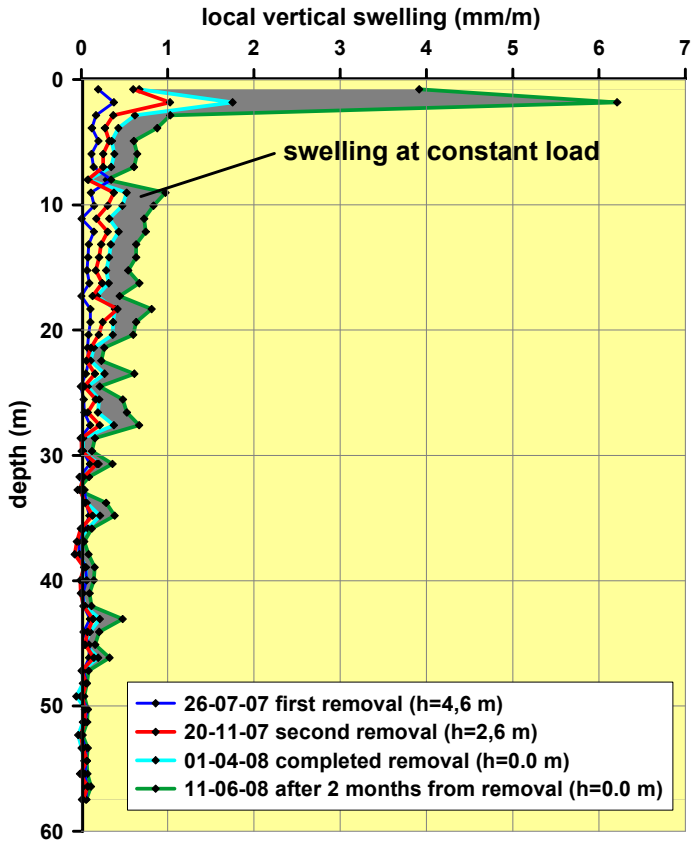

Figure 7.33: local vertical swelling under the centreline corresponding to the three unloading phases

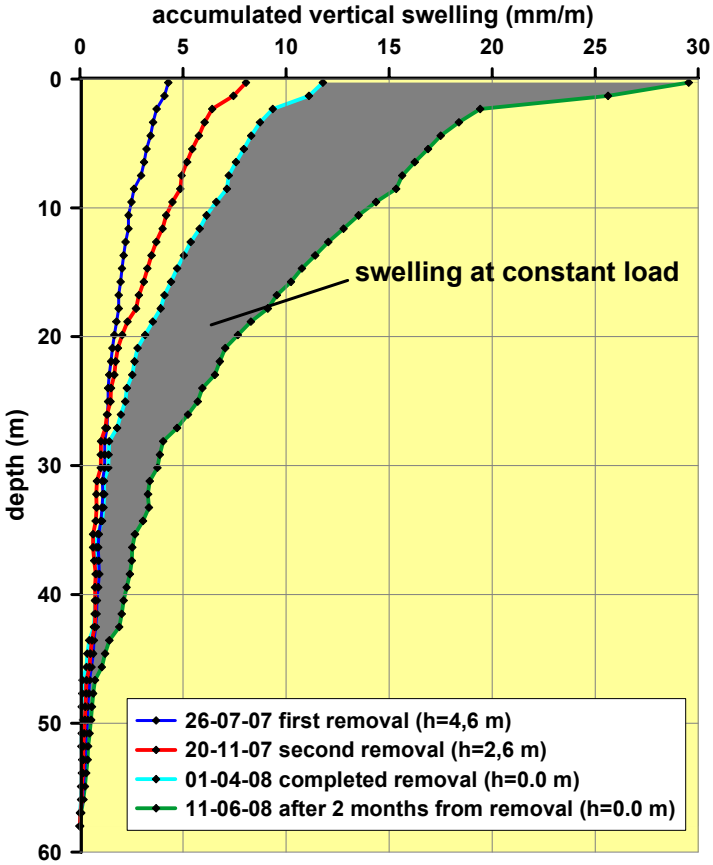

Figure 7.34:accumulated vertical swelling under the centreline corresponding to the three unloading phases

In Figure 7.32 the secondary compression coefficient profile calculated after the first unloading step is shown along with depth: it can be observed that there is a significant reduction in the creep coefficient $C_{\alpha,\varepsilon}$.

In the following Figure 7.35 the ratio between the secondary compression coefficient after the embankment loading and that after the first unloading phase is shown for each soil layer under the centreline. The basic idea is that creep plays an important role in normally consolidated stages and then the higher is the OCR the bigger is its reduction, so that for $OCR = 1$ it holds $C_{\alpha,\varepsilon} / C_{\alpha,\varepsilon NC} = 1$ and then the ratio reduces. This is what happen also in the Treporti embankment case, as shown in the picture: silty layers ratios, indeed, display below sandy layers ones, all decreasing with OCR, as expected.

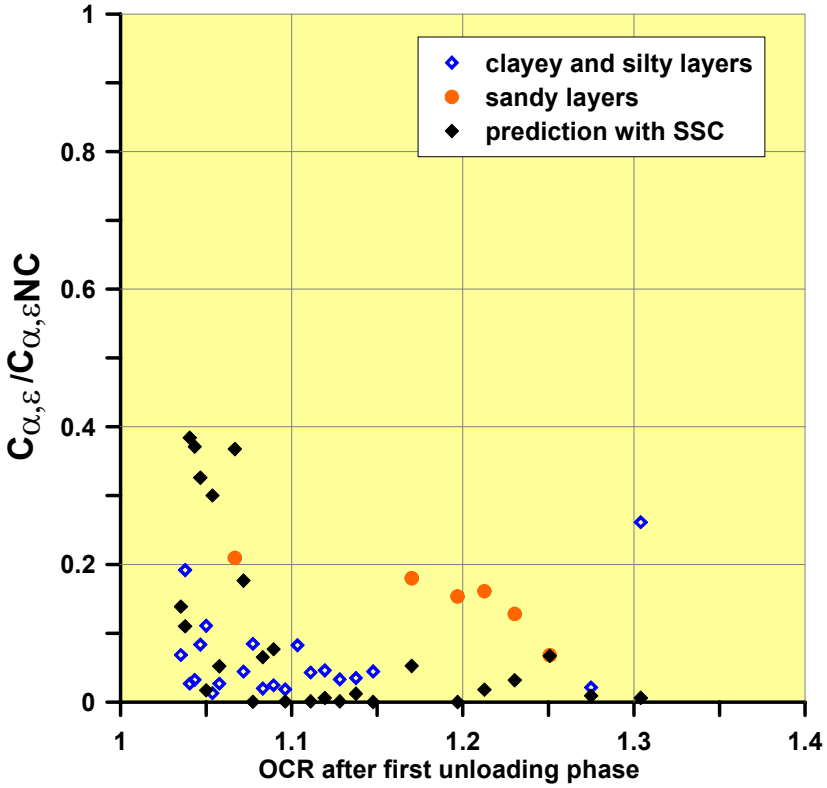

Figure 7.35:creep coefficient ratio between the loading value and the value after the first unloading

Applying the Soft Soil Creep model creep equation, a prediction of the $C_{\alpha,\varepsilon}$ evolution with OCR can be made:

$$\dot{\varepsilon}_v^{creep} = f(OCR) = \frac{\mu^*}{\tau}\left(\frac{1}{OCR}\right)^{\beta} \tag{3.81}$$

with $\beta = \frac{\lambda^* - \kappa^*}{\mu^*} = \frac{C_{c,\varepsilon} - C_{r,\varepsilon}}{C_{\alpha,\varepsilon}}$ and $\mu^* = \frac{C_{\alpha,\varepsilon NC}}{\ln 10}$.

In terms of secondary compression coefficient it can be inferred:

$$C_{\alpha,\varepsilon}(OCR) = C_{\alpha,\varepsilon NC} \cdot \left(\frac{1}{OCR}\right)^{\beta} \tag{7.13}$$

The ratio $C_{\alpha,\varepsilon}/C_{\alpha,\varepsilon NC}$ can be predicted for each site soil layer using this relationship moving from β values calculated on the basis of in situ compression coefficients $C_{c,\varepsilon}$ and $C_{\alpha,\varepsilon}$, and supposing $C_{r,\varepsilon} = C_{c,\varepsilon}/6$. The result is reported in Figure 7.35 (black points) and it is encouraging that prediction points lie close to the measured ones, meaning that measure errors that could affect such small measurements do not have a big influence.

Applicability of isotache framework to Venetian soils

Due to the extreme heterogeneity of Venetian subsoil, the attempt of applying isotache framework to such soils has to be done in a selected way. First of all, it has been chosen to investigate exclusively the most compressible layers, and, among them, those that show a similar compression behaviour.

In Figure 7.36 compression curves are plotted for the 1 m thickness layers most responsible for the creep settlement. In order to compare different layers, strain measurements have been plotted in a normalized way, with respect to the preconsolidation pressure shown in situ by each layer, and also subtracting the overburden effective stress to both the preconsolidation pressure and the actual stress:

$$\sigma'_{norm} = \left(\sigma'_z - \sigma'_{z0}\right) \Big/ \left(\sigma'_{z,pc} - \sigma'_{z0}\right) \tag{7.14}$$

In that way each curve moves from the origin and all of them pass throughout the same point corresponding to the yielding point.

The staged process of embankment construction alters the natural decrease in soil strain rate along time which would appear for a constant stress time interval, and since the embankment has not been built with a regular time schedule, it has been chosen to refer solely to strain rate evolution after the bank completion, as illustrated in Figure 7.37. The trend is a continuous decrease along with time, and the entity of creep strain rate is two order of magnitude lower than in a laboratory oedometer test.

Plotting strain rates along with strain level, it can be seen that curves are shifted depending on the final strain after the end of embankment construction. To retrace an isotache set, in fact, one should work with curves belonging to the same material. In this case each layer is a interbedded mixture of clays-silts and sands in different proportions, and the behaviour measured by the sliding deformeters is an average trend related to 1 meter thickness soil layer. It has been already mentioned, in fact, that $C_{\alpha,\varepsilon}/C_{c,\varepsilon}$ is a sort of material parameter that leads the isotache curves distance, while $C_{c,\varepsilon}$ gives the slope of each isotache in the set. So moving from curves belonging to different layers with different compressibility parameters is theoretically impossible to retrace the isotache set.

An attempt to overcome the heterogeneity can be made using layers with similar $C_{c,\varepsilon}$ and similar $C_{\alpha,\varepsilon}$. The first characteristic imply that in Figure 7.38 curves belonging to such layers are close, while the same secondary compression coefficient makes those curves parallel. In the end it is reliably possible to compare each others layers at 12 and 14 m depth, and with a degree of approximation layers at 11 and 16 m depth, since their primary compression coefficient is different. Compression parameters are reported in Table 7.1.

Normalizing data as described above, curves should converge to a unique stress-strain curve. An attempt is shown in Figure 7.39 for layer at 12 and 14 m depth.

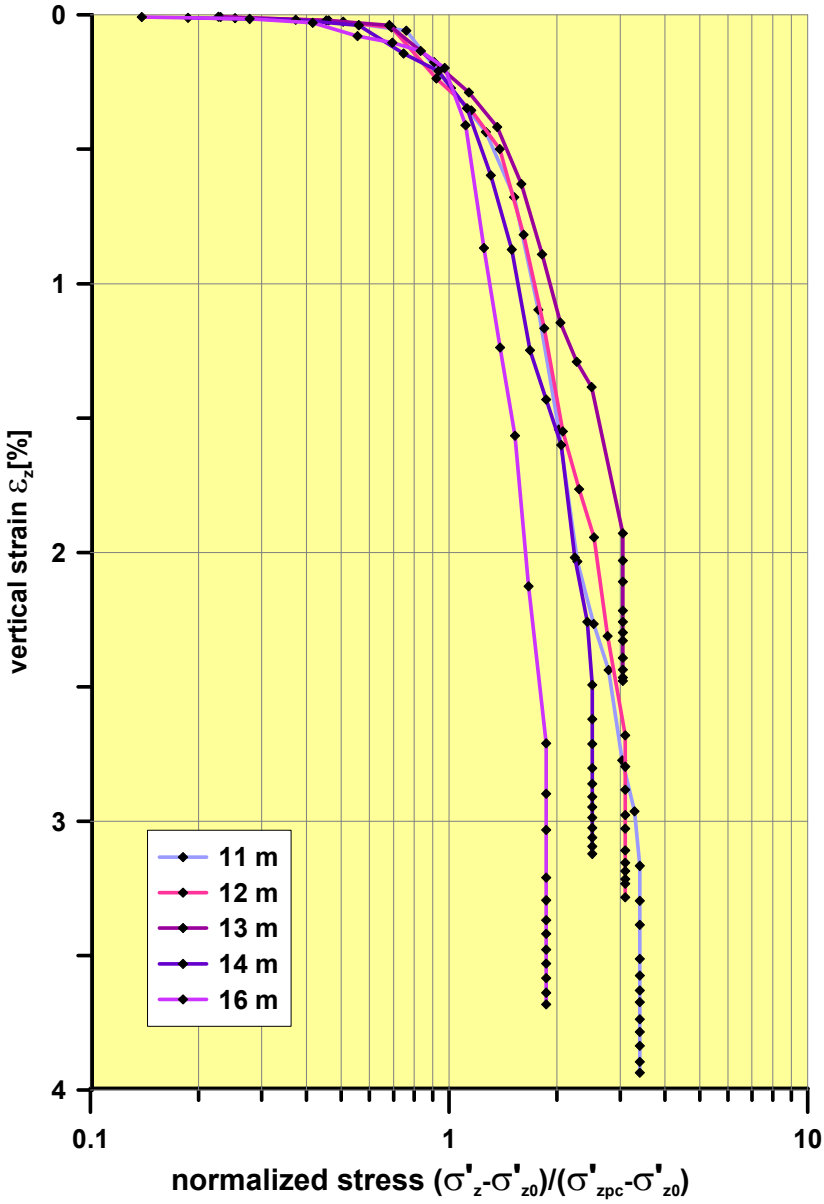

Figure 7.36: normalized compression curve of clayey-silty layers chosen for the isotache analysis

depth(m)	Cc,ε	Cα,ε
11	0,16	0,0039
12	0,17	0,0025
14	0,19	0,0022
16	0,34	0,0037

Table 7.1: compressibility parameters for silty layers at given depth

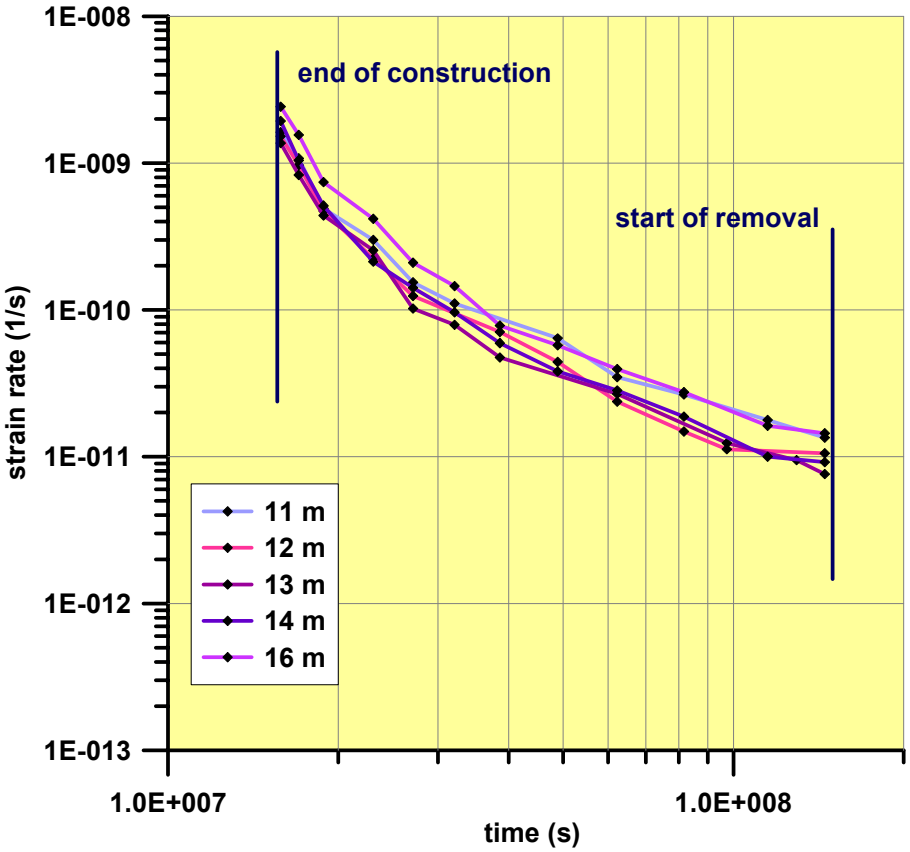

Figure 7.37: strain rate evolution with time

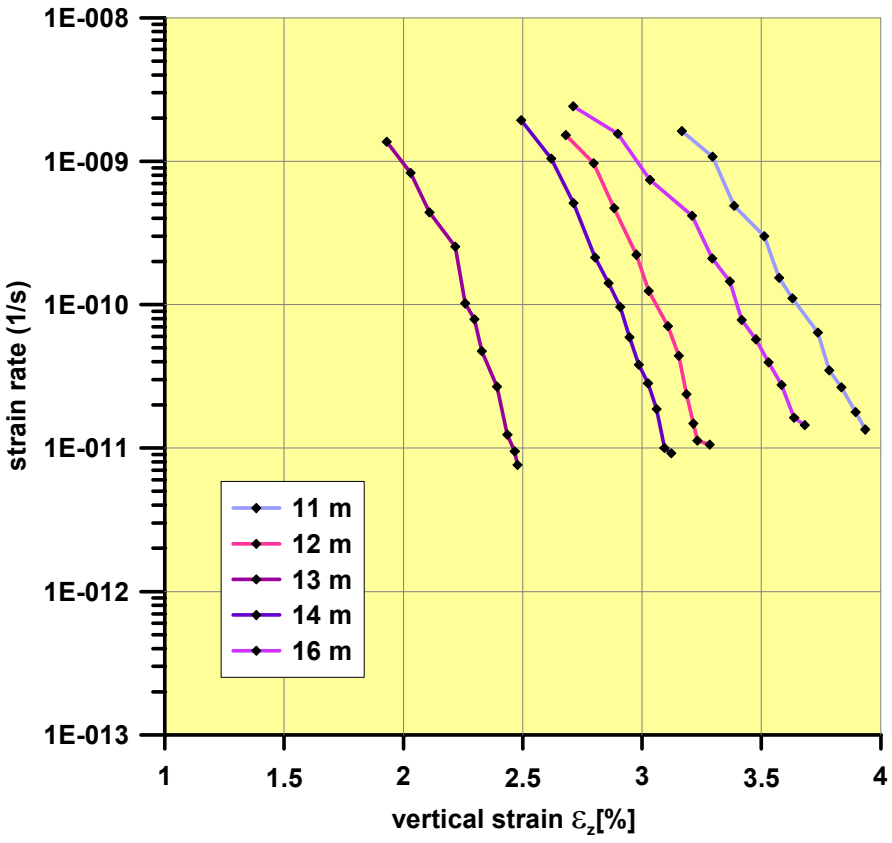

Figure 7.38: strain rate evolution with strain level

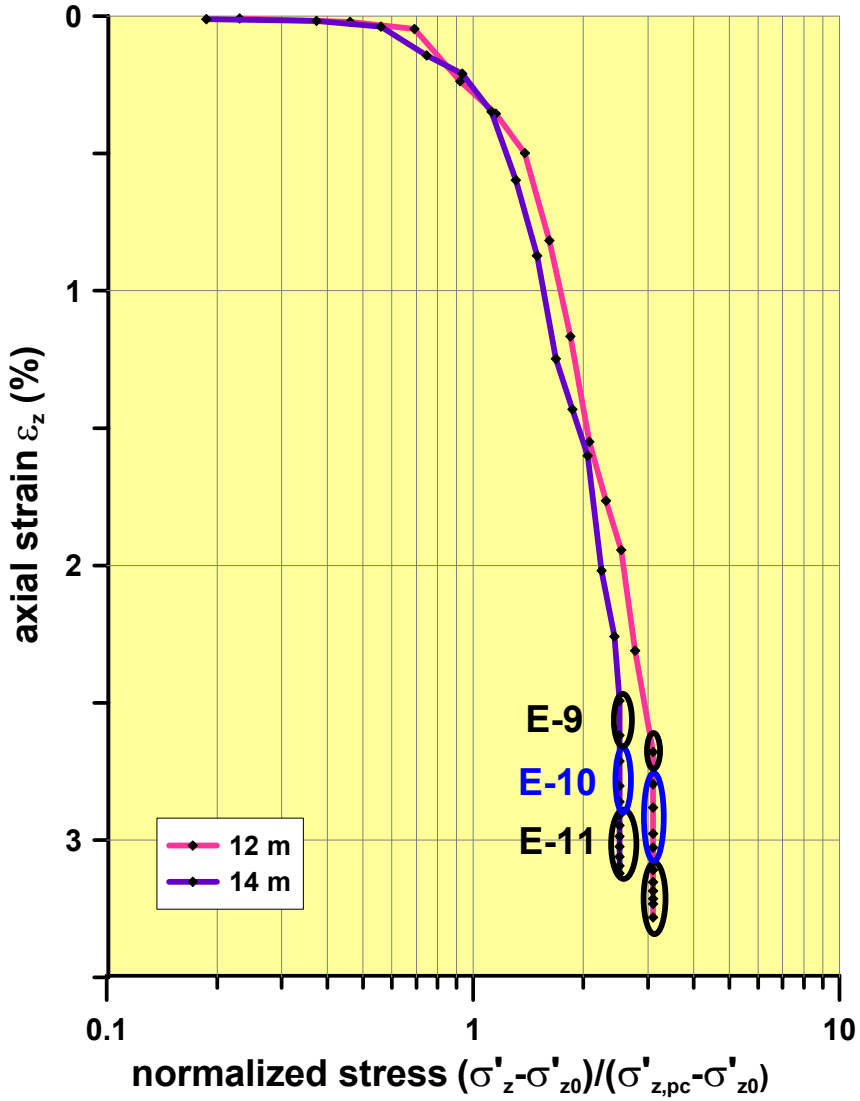

Figure 7.39: isotaches trend for layers at 12 and 14 m depth

Chapter 8 - Constant Rate of Strain laboratory tests

Introduction

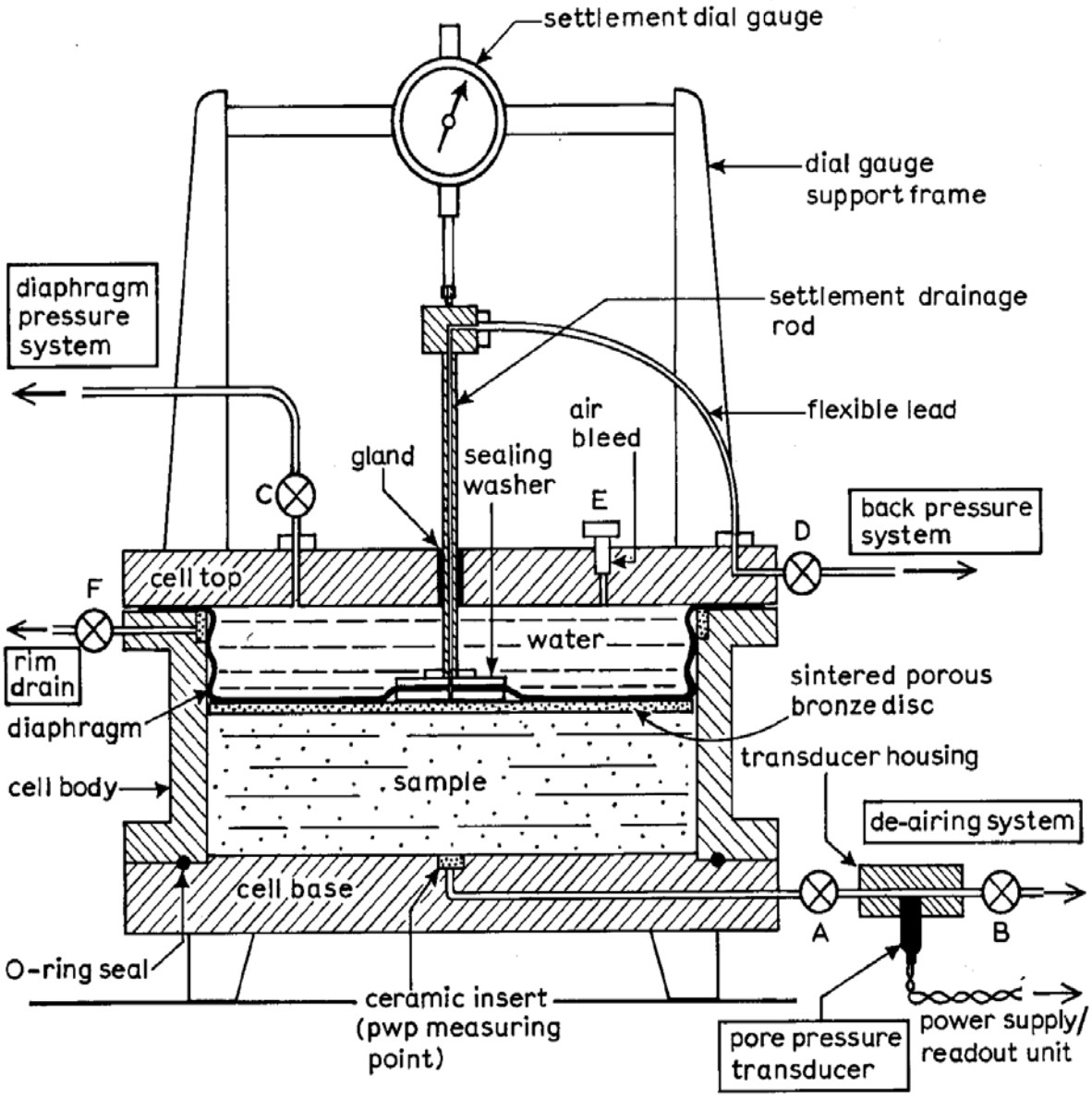

Figure 8.1: the Rowe cell scheme in the original version

The type of consolidation cell herein described (see Figure 8.1), generally known as the Rowe cell, was developed at Manchester University by Professor P.W. Rowe (Rowe and Burden, 1966). The aim was to overcome most of the disadvantages of the conventional oedometer apparatus (for example the impossibility of control drainage), and this cell also allows to perform several kinds of test, among which constant rate of strain tests: this is the main reason why it was chosen to complete the study on Venetian subsoil.

The design of cell differs from a conventional oedometer in the way of loading the sample: in the Rowe cell the test sample is loaded hydraulically by water pressure acting on a flexible diaphragm, instead of by mechanical lever system. This arrangement enables samples of large diameter to be tested and allows for large settlement deformations, to control drainage and to measure pore water pressure during the course of consolidation tests.It is also possible to

apply back pressure. The most important features are the ability of performing a huge variety of test types, among which the constant rate of strain tests (CRS).

The Rowe cell

Three size of Rowe cell are commercially available, based on the 3-6 and 10 inches diameters respectively, originally developed by Rowe, that have the exact following diameter size: 75.7-151.4 and 252.3 mm respectively. The cell available at the University of Padova is the 75.7 mm large and it is produced by the English firm "GDS Instruments".

The cell itself consists in three parts: the body, the cover and the base. In an early commercial design the body was machined from aluminium bronze, the base was made of steel and the top of aluminium alloy for ease of handling. The presence of three different metals in contact with chemical aggressive water in a soil sample sometimes gave rise to serious corrosion, due to chemical reaction and electrolytic effects. The recent design uses an aluminium alloy for all the three components, suitably treated to eliminated porosity, together with a smooth plastic lining bonded on the base and sides, clearly visible in Figure 8.2. Its aim is to avoid friction effects but it does not cover the whole lateral area because, as later explained, the higher space is filled with a rubber membrane that has to seal.

The cell body is clamped between the base and the cover by three long tie bolts, as shown in Figure 8.3. The cell cover is fitted with a convoluted loading jack of natural synthetic rubber, whose outer edge provides a seal between the cover and the upper body flange. The loading jack, also referred to as the diaphragm, transmits a uniform load to the sample by means of water pressure acting on the top. A rim valve (F Figure 8.1) can be used to de-air the zone all around the rubber membrane while water is inserting inside the cell to saturate the sample and to flush behind the jack itself.

Figure 8.2: the Rowe cell (a) the cover (b)the body (c) the base

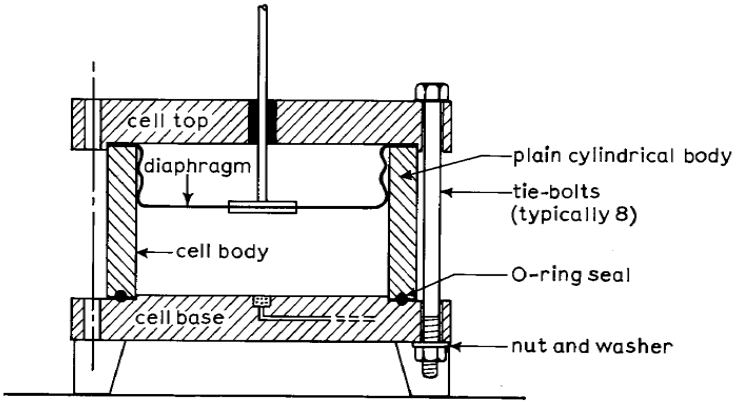

Figure 8.3: assembly details of Rowe cells

Side friction between the walls of the jack and the greased sides of the cell appears to cause very little load reduction on the sample. Rowe and Burden in testing the cell found out a reduction in total stress at the edge of the cell base less than 5% with an average reduction across the entire base of less than 3%. The phenomenon is due both to the side friction of the jack and the side friction on the clay sample, the latter being predominant.

A rigid top platen then may be inserted between the jack and the sample if equal strain condition are required; however a flexible platen and a uniformly distributed load offer the advantage of localizing the effect of side friction and of providing a greater knowledge of the total stress acting on the major part of the sample. In order to obtain a better saturation of the sample at the laboratory of the University of Padova the usual rigid disk (Figure 8.5 A) has been substituted with a disk with much more holes (Figure 8.5 B).

The errors introduced by side friction can be minimize by keeping the diameter-height ratio of the sample as large as possible (as in the case of tests performed at University of Padova, with height=20 mm and diameter=75.7 mm), by coating the walls of the cell with silicone grease and by using a flexible loading plate.

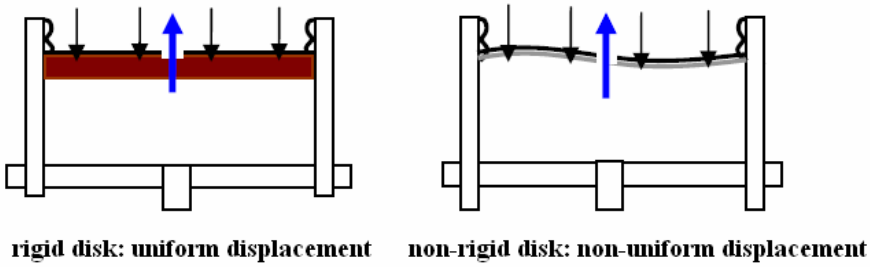

Figure 8.4: displacement with rigid or non-rigid disk

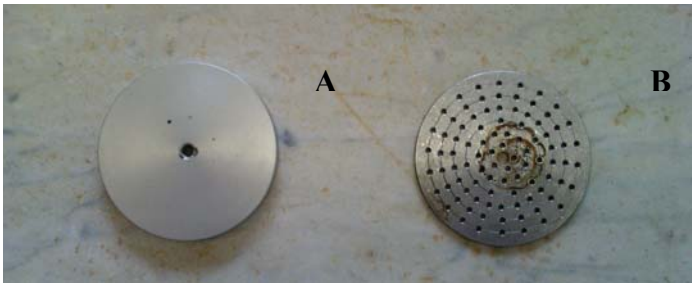

Figure 8.5: classical rigid disk and the one used at Padova University

An aluminium alloy hollow spindle passes through a low friction seal in the centre of the cover. Its lower end passes through the centre of the diaphragm where it is sealed by two metal washers (see Figure 8.2 A and Figure 8.3) that allow to eliminate any error in the settlement readings due to compression of the rubber diaphragm under pressure. The housing in the cell cover contains a 'O' ring which grips the spindle tightly enough to prevent appreciable leakage but not so tightly that the friction affects the settlement readings. The upper end of the spindle is connected by flexible tubing to the drainage valve D in the edge of the cover (Figure 8.1 and Figure 8.6). Through this valve drainage occurs and a back pressure can be imposed to the sample connecting the valve to a pressure water system.
The blanked -off upper end of the spindle provides a bearing for the anvil of the settlement gauge, which is rigidly supported by a bracket assembly bolted to the cover in the original cell (Figure 8.1) while in the cell used at the University of Padova the settlement gauge is kept into position thanks to a cylindrical rigid support as reported in Figure 8.6. The absence of water pressure acting over the area of the spindle results in an average error of about 1.5% in the 75.7 mm diameter cell.

The cover is also fitted with an inlet valve (C Figure 8.1) for connection to a constant pressure water system for applying the vertical load o the sample and an air bleed screw (E Figure 8.1).

The cell base is fitted with a recess for an 'O' ring seal to bear against the tie bolts. At the centre of the base there is a small circular recess containing a porous ceramic or plastic insert bonded in place (Figure 8.2 C). This is the main pore water pressure measuring point, and leads to valve A (Figure 8.1 and Figure 8.6) on the outer edge, to which is connected the electric pressure transducer and valve B that can be connected to a de-airing system. A second and smaller water pressure measuring point is near the bigger one and it is connected to a second valve (Figure 8.2 C and Figure 8.6 G).

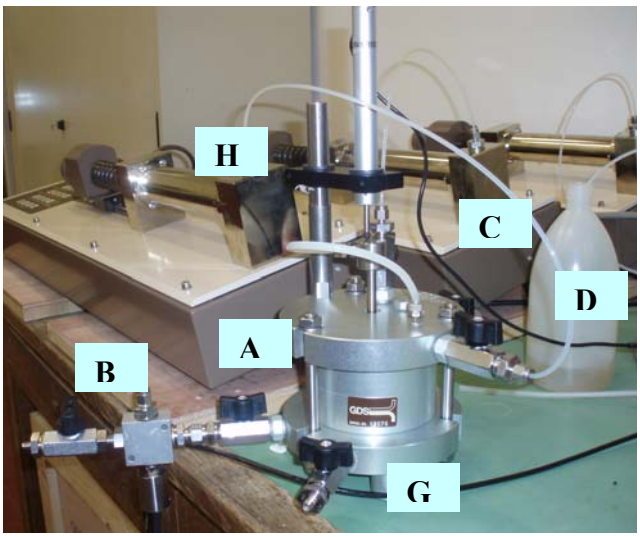

Figure 8.6: the Rowe cell produced by the GDS Instruments used at the University of Padova

Pressure controllers and the whole testing system

Water pressure is applied to the jack of the cell and to the valve D to impose back pressure to the sample by means of two digitals controllers (Figure 8.6 H) linked to the cell as represented in Figure 8.7.

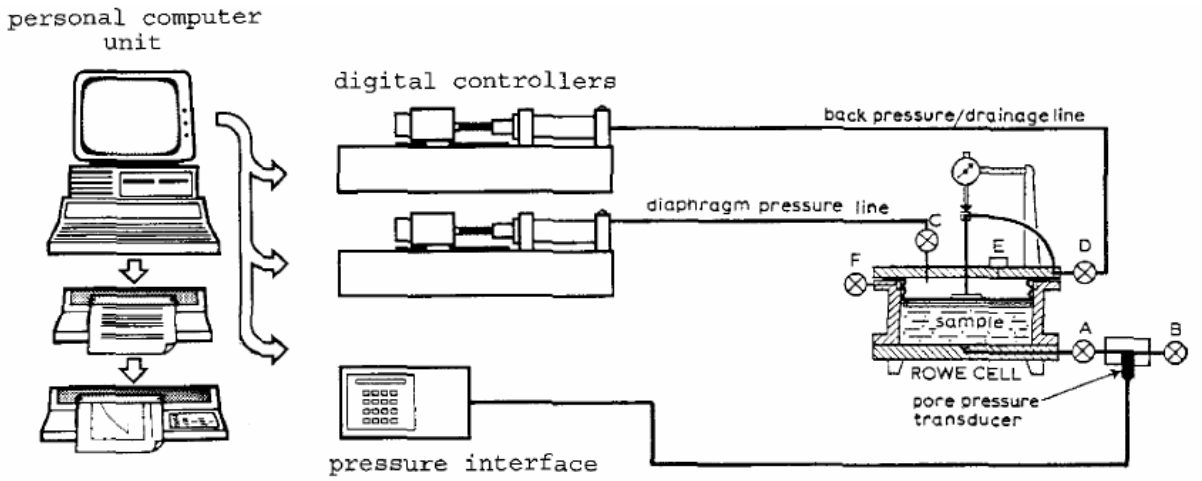

Figure 8.7: layout of GDS Rowe cell testing system

The test cell is linked to a digital controller for back pressure and measurement of volume change and another digital controller for axial stress application while the pore water pressure variation is measured by a pore pressure transducer mounted on the cell.

A digital controller is a microprocessor controlled hydraulic pump for the precise regulation and measurement of water pressure and water volume change. The volumetric capacity of the controller adopter at Padova University is 200 cm^3 and the pressure range is 0-2000 kPa. Pressure measurement is resolved to within 0.2 kPa and the pressure is controlled with deviation les than 0.5 kPa. The scheme of functioning is illustrated in Figure 8.8

De-aired water in a cylinder is pressurized and displaced by a piston pump using a stepper motor. The pressure is detected by means of a solid state pressure transducer. Control mechanism is built to activate the controller either to adjust to achieve a target pressure or to change to attain a target volume change. Volume change is measured by counting the steps of stepper motor: the pump was designed such that one step of the motor will cause a volume change of 1 mm^3.

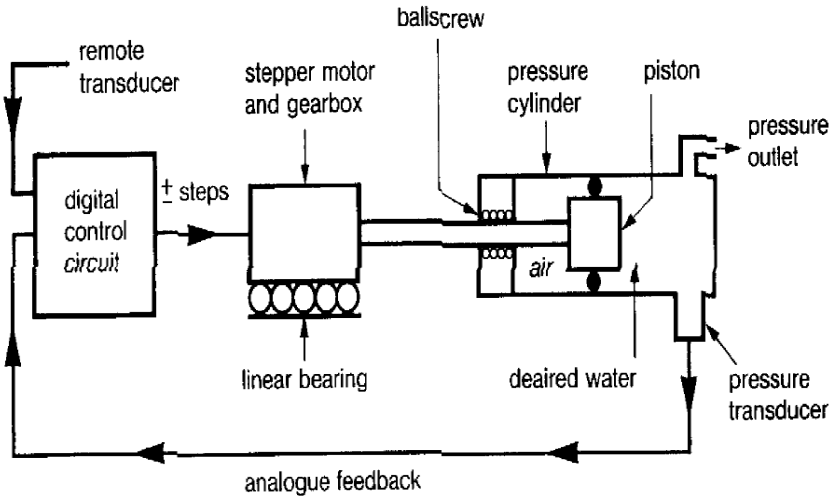

Figure 8.8: scheme of a pressure controller

The system by GDS Instruments, besides cell, controllers and pore water pressure transducer, provides pc automation of test control, data logging and data reduction. Average axial stress is computed from the pressure applied to the top membrane by the axial stress controller. The stress is automatically corrected for the area of the top drainage spindle passing through the top of the Rowe cell. Axial deformation is computed from the volume change of the back pressure controller or from volume change of the axial stress controller . This is the reason why the system has to be fully saturated without air bubbles inside that can deform when water enters without corresponding to sample displacement. Additionally axial deformation can also be measured directly by a digital gauge.

Drainage conditions

As already highlighted, this system enables to perform a lot of test types, from the conventional step loading to the continuous loading tests (like constant rate of strain, constant rate of loading, controlled hydraulic gradient etc., as reported in Figure 8.9).

The continuous loading consolidation testing causes the pore water to flow into or out of the test specimen at a more or less steady rate. This is in direct contrast to the conventional step loading test where the hydraulic gradient causing the flow is itself reduced by the flow thus giving rise to the decaying flow rate.

All of the test types can be performed in different drainage conditions, each of which can be subjected to two types of loading corresponding to free strain or equal strain conditions (on Figure 8.10 left side the first and , right side the latter, respectively).

In the case of the tests carried out within this research, only tests with vertical flow with single top drainage and equal strain loading has been performed (case b in Figure 8.10). The top drainage is provided by a disc of saturated sintered bronze placed between the sample and the jack on which a further rigid disk is placed in order to get uniform displacement. The drainage outlet is via the centre of the settlement spindle and a short length of flexible tube leading to a Klinger valve at the edge of the cell cover, as already mentioned.

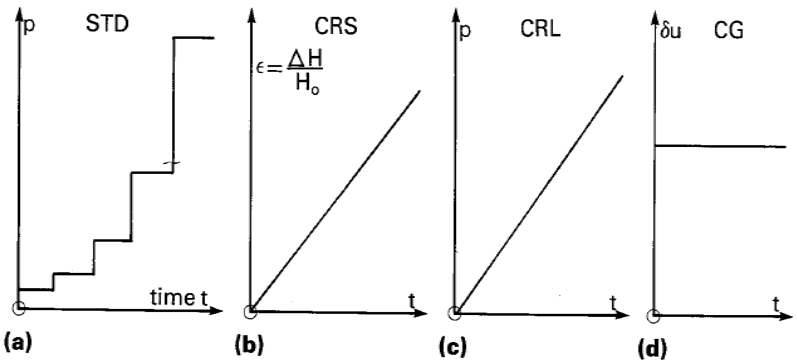

Figure 8.9: types of test: (a) standard incremental loading (b) constant rate of strain (c) constant rate of loading (d) constant pore pressure gradient

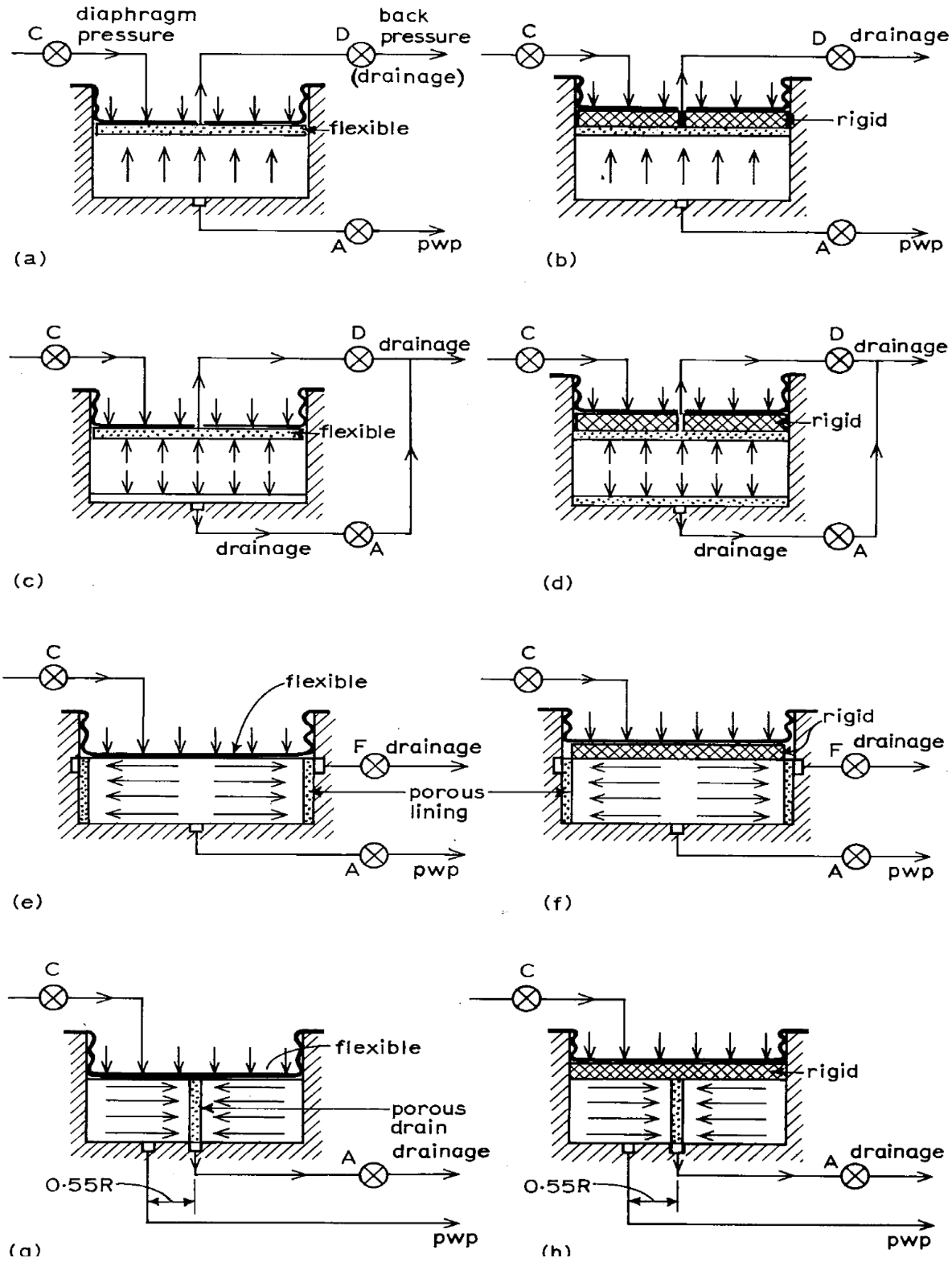

Figure 8.10: drainage and loading conditions for consolidation tests in Rowe cell

For the description of the rest of the drainage conditions the interested reader is referred to Rowe and Burden (1966).The important aspect in all the above arrangements is that full control of drainage, initial pore pressures and back pressures can be achieved.

Advantages of the Rowe cell

The advantages of using the Rowe cell over traditional oedometers can be summarized as follows :

a) minimum vibration effects

b) negligible deformations of the loading system

c) control of various sample drainage conditions

d) measurements of pore water pressure

e) measurement of the volume of water expelled from the sample

f) saturation of sample under back pressure condition

g) application of back pressure to simulate in situ condition

h) variation of load conditions between 'equal strain'(rigid disk) and 'free strain' over the section of the sample

i) control of loading condition, i.e. possibility of performing continuous loading tests

In particular, to perform CRS tests, as in the case of this research, overcomes several disadvantages associated to the conventional oedometer tests, such as:

a) the long time required to perform the test (one or two week)

b) step loading is applied every 24 hours and the amount of secondary compression varies with each loading step

c) test results are widely spaced sometimes making difficult to estimate the preconsolidation pressure value

In a constant rate of strain test, on the contrary, load is applied continuously while keeping the rate of strain constant, so continuous record of stress and strain can be made. With suitable choice of strain rate, indeed, there is little secondary compression and the test can be completed in a few days.

Besides, the preconsolidation pressure can be detected measuring the excess pore pressure developed during the test, if it is fast enough with respect to the permeability of the sample. This is not usually possible in with a conventional oedometer device.

Theoretically, indeed, also the secondary compression C_α coefficient can be evaluated, plotting strain against the logarithm of time establishing the end of primary consolidation from an excess pore pressure-logarithm of time.

In Figure 8.11 the list of plots obtainable from a CRS test are reported.

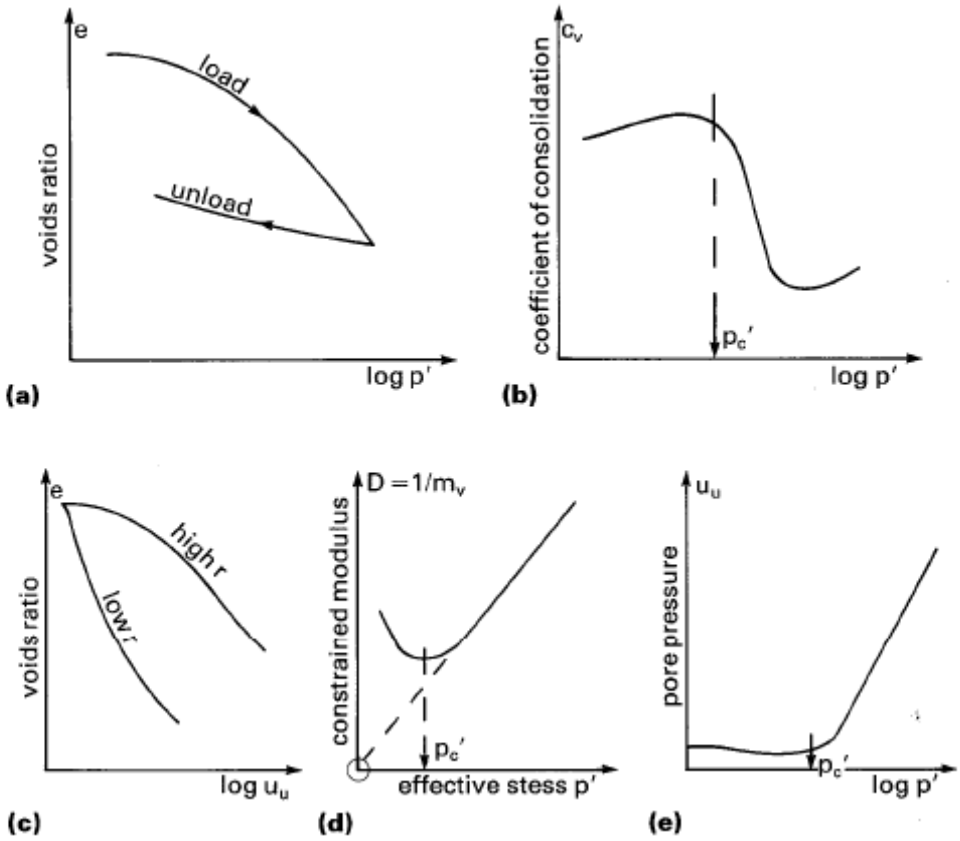

Figure 8.11: typical graphics plot obtained from a CRS test (Head, 1985)

Test procedure

The first phase always consist in preparing the sample. In the case of tests performed in this research, soils samples come from Treporti Testing Site after the embankment removal.
In situ they were taken with an Osterberg piston sampler that produce cylindrical sample 60 cm thick with diameter 10 cm large kept inside an aluminium cylindrical ring . Then it is necessary to extrude the whole soil cylinder and to trim a soil sample to the correct diameter and pushed it into the cell.

Figure 8.12: cylindrical soil samples taken at Treporti Testing Site

Figure 8.13: to trim the sample to bed into the cell

Since the original diameter is larger than the cell diameter, the right dimensions are obtained using a cutting ring driven into the selected soil sample in order to get a sample 20 mm high and with diameter equal to 757mm. Then the sample is extruded into the cell.

With soil material left classification tests have to be performed such as initial moisture content, Atterberg limits and grain size distribution.

The arrangement chosen for the consolidation tests performed on Venetian soils is that with vertical drainage occurring from the top surface of the sample and with pore pressure measurement at the base, as illustrated in Figure 8.14.

Before closing the cover, the space at the top of the cell above the sample has to be flooded with de-aired water. Then a saturated flexible porous disk has to be placed onto the sample, then for an 'equal strain' test as those performed in this research, the holed rigid steel disk has to be lowered into position avoiding trapping air under the plate. The central drainage hole must be left open and aligned with the settlement stem drainage outlet. Both the disks have to be boiled to prevent a gradual build up of fine particles and also they have to be de-aired with the apposite device in order to better guarantee saturation.

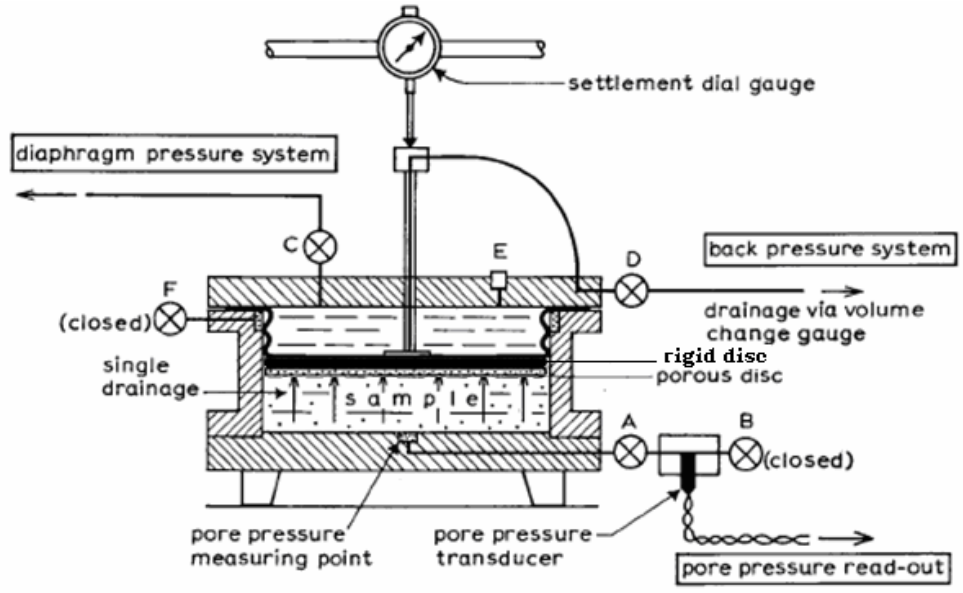

Figure 8.14: cell arrangement for tests performed at the University of Padova on Venetian soils

Then the cell cover with the rubber jack has to be carefully seat to the cell body without entrapping air or causing membrane pinching, as described in Figure 8.15. The long tie bolts have to be tighten to bolting the cell cover and body to the cell base.

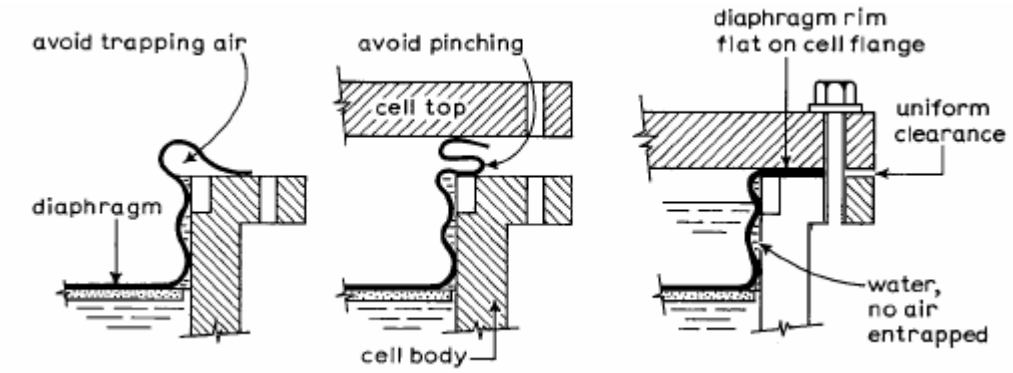

Figure 8.15: seating the diaphragm

The first operation that has to be done at this point is the saturation of the system (cell, valves and connections). To saturate the cell base a de-aired water flux is created connecting a controller to one of the two valves at the base (A in Figure 8.6), and pushing water inside the base keeping the other valve open(G in Figure 8.6) in order to let air exit. Then the space above the diaphragm has to be completely filled through the valve C with bleed screw E removed (Figure 8.1). To ensure complete removal of air E can be connected to a moderate vacuum (using ,for instance a tube).The supply of water at C has to be maintained at C when subsequently replacing the bleed screw.

Before making the diaphragm seal to the cell wall, throughout the back pressure valve D (Figure 8.6) de-aired water is flooded inside the body cell and it goes back up to the upper part all around the membrane, pushing out air trapped throughout the rim valve F (Figure 8.6). The diaphragm is then sealed to the cell wall applying a pressure with the controller throughout C valve inside the membrane, keeping F valve open. This will be close when the membrane will be completely extended. At the same time a back pressure is applied through D. Normally during all the test phases the back pressure should be 10 kPa less then the vertical pressure applied by the membrane.

After saturating the device, the first operation that has to be carried out is the sample saturation, especially for samples taken from above water table. The procedure is similar to that used for saturating triaxial test samples but with diaphragm pressure substituting the cell pressure. The idea is to compress air bubbles remained in the sample by applying a back pressure inside it. At the same time also the diaphragm pressure has to be increased 10 kPa more than the back pressure in order to keep the sample intact. Then the well known 'B check' has to be carried out to control the saturation degree. To perform such a control the back pressure valve D, that is also the way for water to exit when the sample settles, has to be closed. Applying a stress increment through the membrane and the relative controller, an immediate equal response of the pore pressure transducers indicates that saturation is essentially completed. If not, back pressure and so then diaphragm pressure have to be increased again.

The value of B is calculated as the ratio $B = \Delta u / \Delta \sigma$ where $\Delta u = u_{pore} - u_{back}$ is the excess pore pressure development at the base of the cell in response to an increment of total vertical

stress of $\Delta\sigma$ transmitted by the rubber membrane and obtained thanks to the pressure controller connected to the valve C (Figure 8.1). Saturation is generally considered as completed when the pore pressure parameter $B \geq 0.96$.

This parameter has been defined by Skempton, that proposed the following relationship between pore pressure and total stress increment in triaxial conditions:

$$\Delta u = B \cdot \left(\Delta\sigma_3 + A\left(\Delta\sigma_1 - \Delta\sigma_3 \right) \right) \tag{8.1}$$

For oedometric conditions $A = 1$ and so: $\Delta u = B \cdot \Delta\sigma_1$ where the vertical stress can be considered the principal stress ($\Delta\sigma_1 = \Delta\sigma_z$), neglecting friction on the cell walls. If the sample is fully saturated in undrained condition (D valve closed) a stress increment should immediately and completely transfer to the water pressure and then $B = 1$.

After the delicate saturation operation (both for the cell and for the sample) the true test can be performed.

On Venetian soils taken at Treporti Testing Site after the embankment removal, three kinds of constant rate of strain tests have been carried out. All intermediate calculations that take into account sample height or area are carried out by the GDS Instrument tests control software. Simple continuous loading compression tests with given strain rate have been performed imposing a target strain and the time to get it. CRS with unloading reloading cycles have also been performed, being also the unloading and reloading phases strain controlled.
And then CRS test changing strain rate during the test have been performed in order to detect the isotache behaviour. All intermediate changes in a test can be memorized into the software that manages tests, and basically a list of strain target and relative time to get them is required.

As will be later explained, also CRS tests with a previous consolidation phase have been performed in order to give a known preconsolidation pressure to the soil. In this case after the saturation process a stress target has been imposed, in drained condition; once the sample has been consolidated (no more appreciable strain developing) it has been unloaded and only after that the CRS test has been performed. In this latter case the initial sample height that has to be inserted in the software to enables variables calculations is the final value after initial loading and unloading phase.

CRS tests on Venetian soil samples

The samples on which CRS tests have been performed belong to Treporti Testing Site subsoil, as already mentioned. The whole list of tests is reported in Table 8.1. It contains the in situ sample's depth, a brief description of the test, the degree of saturation of the sample at the beginning of the test and the preconsolidation pressure value for each sample.

They were taken after embankment removal, so the preconsolidation pressure can be considered as known along the whole depth and coincident with the maximum stress the soil has been subjected to.

	depth (m)	**test**	**strain rate (s^{-1})**	**S(%)**	**mechanical $\sigma'_{z,pc}$ (kPa)**	**updated $\sigma'_{z,pc}$ (kPa)**
CR 02(01)	9.1-9.7 H	CRS 1 U-R	10^{-5}	96	185	199
CR 02(02)	9.1-9.7 M	CRS 1 U-R	10^{-5}	97	185	199
CR 02(03)	9.1-9.7 L	CRS 1 U-R	10^{-6}	97	185	199
CR 04(01)	10.5-11.1 M	CRS 2 U-R	10^{-5}	95	200	228
CR 05(01)	11.1-11.8 M	CRS	$10^{-4}/4*10^{-7}$	95	204	228
CR 05(02)	11.1-11.8 M	CRS	$10^{-4}/4*10^{-7}$	95	204	228
CR 06(01)	11.8-12.4 H	CRS 2 U-R(P)	10^{-5}	94	207	-
CR 06(02)	11.8-12.4 H	CRS 2 U-R(P)	10^{-6}	97	207	-
CR 06(03)	11.8-12.4 M	CRS 2 U-R(P)	$5*10^{-6}$	97	207	-
CR 06(04)	11.8-12.4 L	CRS 2 U-R(P)	$5*10^{-7}$	96	207	-
CR 07(02)	12.5-13.1 M	CRS	10^{-5}	80	213	241
CR 07(03)	12.5-13.1 L	CRS	$4.5*10^{-6}$	84	213	241
CR 07(04)	12.5-13.1 H	CRS	10^{-4}	78	213	241
CR 07(06)	12.5-13.1 M	CRS 2 sr	$10^{-4}/10^{-5}$	98	213	241
CR 07(07)	12.5-13.1 L	CRS 2 sr	$10^{-4}/10^{-6}$	98	213	241
CR 07(08)	12.5-13.1 L	CRS 2 sr	$10^{-4}/10^{-6}$	87	213	241
CR 08(01)	13.1-13.7 L	CRS 2 U-R(P)	$5*10^{-6}$			
CR 09 (01)	13.7-14.3 H	CRS 2 U-R(P)	10^{-6}			
CR 09 (02)	13.7-14.3 H	CRS 2 U-R(P)	$5*10^{-5}$			
CR 15(01)	18.1-18.7 L	CRS	10^{-5}	89	245	277
CR 15(02)	18.1-18.7 L	CRS	10^{-5}	95	245	277
CR 15(03)	18.1-18.7 L	CRS	10^{-5}	96	245	277
CR 16(01)	18.8-19.4 H	CRS	10^{-5}	94	252	266
CR 16(02)	18.8-19.4 H	CRS	10^{-5}	75	252	266
CR 16(03)	18.8-19.4 H	CRS	10^{-5}	82	252	266
CR 16(04)	18.8-19.4 H	CRS	10^{-5}	75	252	266
CR 19(01)	23.0-23.6 L	CRS	10^{-5}	58	280	300
CR 19(02)	23.0-23.6 L	CRS	10^{-5}	69	280	300
CR 19(03)	23.0-23.6 L	CRS	10^{-5}	92	280	300
CR 19(04)	23.0-23.6 L	CRS	10^{-5}	97	280	300

Table 8.1: list of CRS tests on Venetian soils, L=low, M=medium, H=high, U-R=unloading-reloading, P=preconsolidated, 2sr=two different strain rates

Considering the creep behaviour shown by the soil in four year standing ,the preconsolidation pressure should be updated, since it increases with time, as explained in Chapter 2.
To evaluate the preconsolidation pressure increase the equation proposed in the Soft Soil Creep model can be used; it depends on the creep strain, as follows:

$$p'_{pc} = p'_0 \exp\left(\frac{\varepsilon_v^{creep}}{\lambda^* - \kappa^*}\right) \tag{3.80}$$

For each sample, the preconsolidation pressure, as estimated from in situ measurements, is reported in the fifth and sixth columns, as the maximum stress value and taking into account the creep strain respectively.

Besides the mechanical tests, classification procedures are carried out in order to classify the material. Natural moisture content, Atterberg limits and plasticity index together with the USCS classification are reported in Table 8.2. Grain size curves for some of those tests are displayed in Figure 8.16.

	depth (m)	**w(%)**	**w_L(%)**	**w_P(%)**	**I_P**	**G_S**	**USCS**
CR 02(01)	9.1-9.7 H	30	27	23	4	-	SP
CR 02(02)	9.1-9.7 M	26	26	24	2	-	SP
CR 02(03)	9.1-9.7 L	29	-	-	-	-	SP
CR 04(01)	10.5-11.1 M	28	26	24	2	-	SP
CR 05(01)	11.1-11.8 M	28	26	24	2	-	ML
CR 05(02)	11.1-11.8 M	28	26	24	2	-	ML
CR 06(01)	11.8-12.4 H	30	26	21	5	-	SP
CR 06(02)	11.8-12.4 H	31	37	22	15	-	ML
CR 06(03)	11.8-12.4 M	29	34	25	9	-	ML
CR 06(04)	11.8-12.4 L	32	30	26	4	-	SM
CR 07(02)	12.5-13.1 M	31	33	21	12	2,802	ML
CR 07(03)	12.5-13.1 L	26	27	22	5	2,799	ML
CR 07(04)	12.5-13.1 H	33	35	25	10	2,795	ML
CR 07(06)	12.5-13.1 M	26	28	-	-	2,783	ML
CR 07(07)	12.5-13.1 L	29	30	25	5	2,778	ML
CR 07(08)	12.5-13.1 L	23	25	21	4	2,782	ML
CR 15(01)	18.1-18.7 L	30	41	28	13	2,811	ML
CR 15(02)	18.1-18.7 L	26	37	25	12	2,770	ML
CR 15(03)	18.1-18.7 L	30	48	28	20	2,725	ML
CR 16(01)	18.8-19.4 H	31	34	25	9	2,786	ML
CR 16(02)	18.8-19.4 H	30	35	25	10	2,804	ML
CR 16(03)	18.8-19.4 H	29	35	24	11	2,786	ML
CR 16(04)	18.8-19.4 H	30	37	25	12	2,764	ML
CR 19(01)	23.0-23.6 L	33	40	24	16	2,730	ML
CR 19(02)	23.0-23.6 L	31	37	22	15	2,739	ML
CR 19(03)	23.0-23.6 L	28	33	21	12	2,749	ML
CR 19(04)	23.0-23.6 L	30	-	-	-	2,753	ML

Table 8.2: classification of samples used for CRS tests

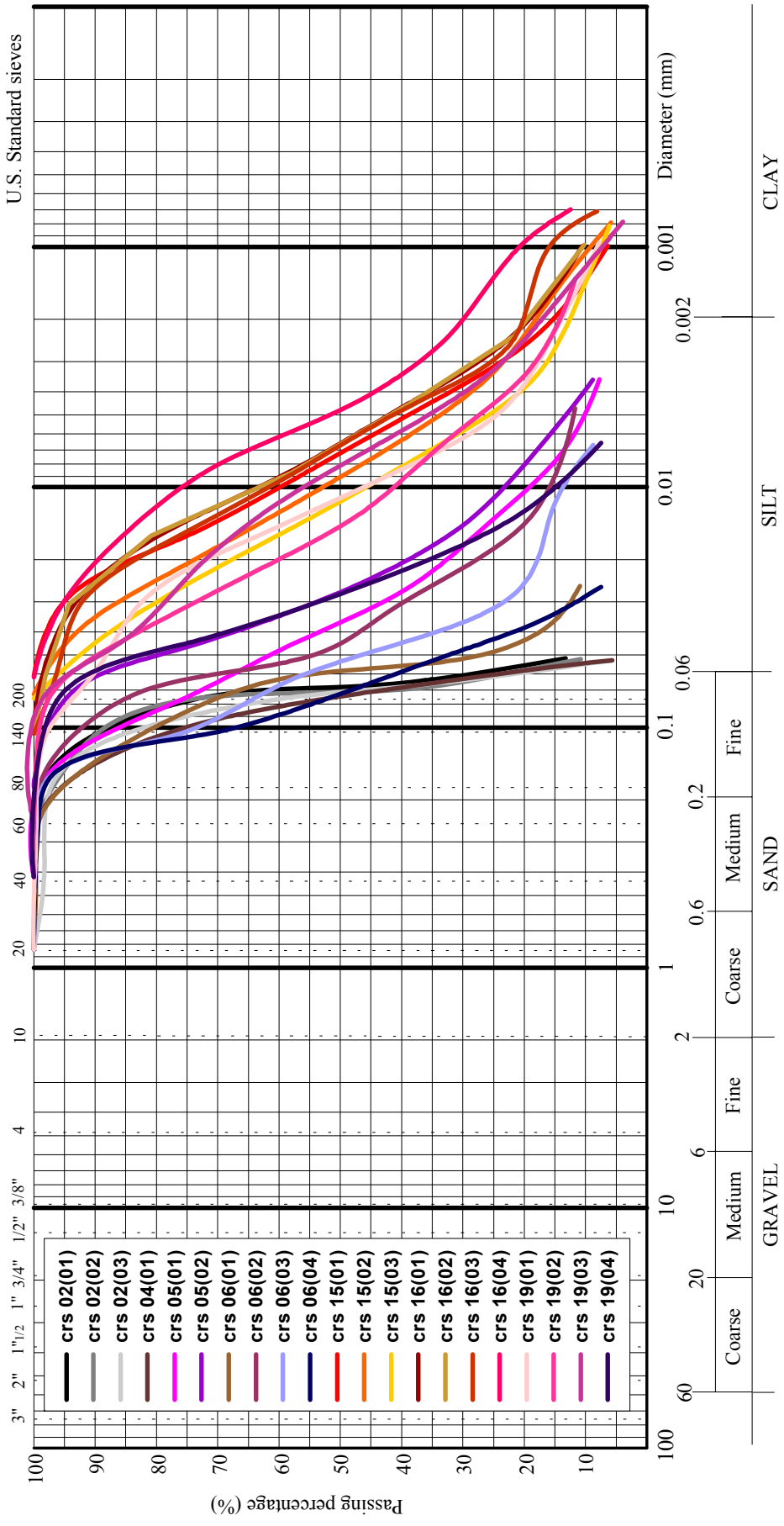

Figure 8.16: grain size curves

As it can be clearly seen from Figure 8.16, most of the samples are silty sands with low plasticity, while a few of them are fine sands or silty sands. The extreme heterogeneity of Venetian subsoil makes difficult to get two similar samples, so there is no expectation of identical or comparable results in performing CRS tests on such samples.

Besides the intrinsic material differences, in some cases samples have not been completely saturated. The reason can be retraced in the compression system: the convoluted membrane can trap air inside its bends, and also air has only one way escaping from the sample. This was the reason why the rigid platen with only one hole has been substituted with a disk with many holes, as described in a previous paragraph (see Figure 8.5). On the other hand a saturation ramp could be performed, but since the Rowe cell at the University of Padova supports 1000 kPa at most, it is better to not to use this method, otherwise there would be a small range of stresses that can be used in the test itself.

For seek of completeness the grain size index $I_{GS} = (D_{50}/D_0)/U$ has been calculated for each samples, showing, once more, that sands are quite uniform while the finer the material, the more graded it is.

	D_{10}	D_{50}	D_{60}	$U = D_{60}/D_{10}$	$I_{GS} = \frac{(D_{50}/D_0)}{U}$	USCS
CR 02(01)	0,0490	0,0680	0,0670	1,37	0,0497	SM
CR 02(02)	0,0560	0,0690	0,0660	1,18	0,0585	SM
CR 02(03)	0,0551	0,0718	0,0882	1,60	0,0449	SM
CR 04(01)	0,0548	0,0711	0,0828	1,51	0,0471	SM
CR 06(01)	0,0278	0,0592	0,0646	2,32	0,0255	SM
CR 06(02)	0,0044	0,0457	0,0588	13,36	0,0034	ML
CR 06(03)	0,0079	0,0528	0,0648	8,21	0,0064	ML
CR 06(04)	0,0289	0,0591	0,0643	2,22	0,0266	SM
CR 15(01)	0,0012	0,0063	0,0101	8,47	0,0007	ML
CR 15(02)	0,0010	0,0097	0,0128	12,82	0,0008	ML
CR 15(03)	0,0014	0,0116	0,0166	12,18	0,0010	ML
CR 16(01)	0,0010	0,0067	0,0091	9,09	0,0007	ML
CR 16(02)	0,0010	0,0070	0,0091	9,09	0,0008	ML
CR 16(03)	0,0007	0,0071	0,0096	12,82	0,0006	ML
CR 16(04)	0,0007	0,0050	0,0069	10,61	0,0005	ML
CR 19(01)	0,0011	0,0112	0,0147	13,04	0,0009	ML
CR 19(02)	0,0014	0,0120	0,0200	14,14	0,0008	ML
CR 19(03)	0,0011	0,0079	0,0116	10,25	0,0008	ML
CR 19(04)	0,0082	0,0274	0,0331	4,04	0,0068	ML

Table 8.3: grain size index I_{GS} value and uniformity coefficient U of samples for CRS tests

The opposite trend of the grain size index and uniformity coefficient is reported in Figure 8.17.

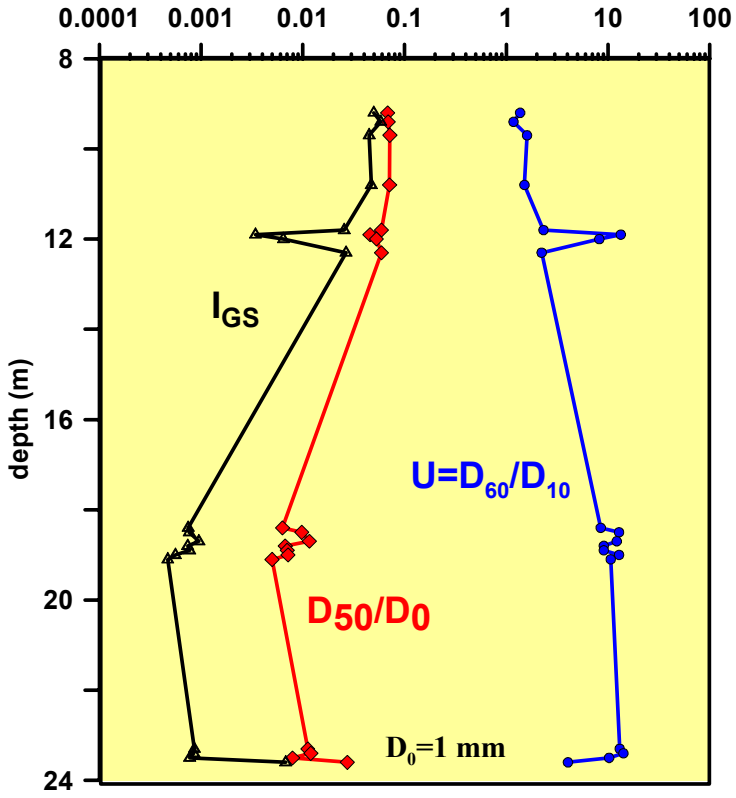

Figure 8.17: grain size index, average diameter and uniformity coefficient profiles

Preconsolidation pressure determination

The preconsolidation pressure should be almost known, since before embankment construction soil was slightly overconsolidated and the embankment load brought it into normally consolidated conditions. In Table 8.1 supposed values are reported.

However from compression tests on Venetian soil is extremely difficult to retrace the preconsolidation pressure, since it is very sensitive to sampling. The result is a rounded curve in which it is almost impossible to apply the Casagrande construction, as described in the previous chapter (see Figure7.19). On the other hand the constrained modulus is always increasing as it is clearly evident plotting data in linear scale, as reported for example in Figure 8.18.

A further technique already mentioned is to assign to the preconsolidation pressure the value corresponding to the excess pore pressure increase, whether the strain rate is enough fast with respect to the soil permeability to cause a pore water pressure development in drained tests. In Figure 8.19 results are shown for those tests in which excess pore pressure development has been measured. In Table 8.4 results are summarized.
It can be noted that in order to get a reliable result from such a method the soil has to be well-saturated and also in this case the excess pore pressure does not mark a precise stress value but it gives only an indication.

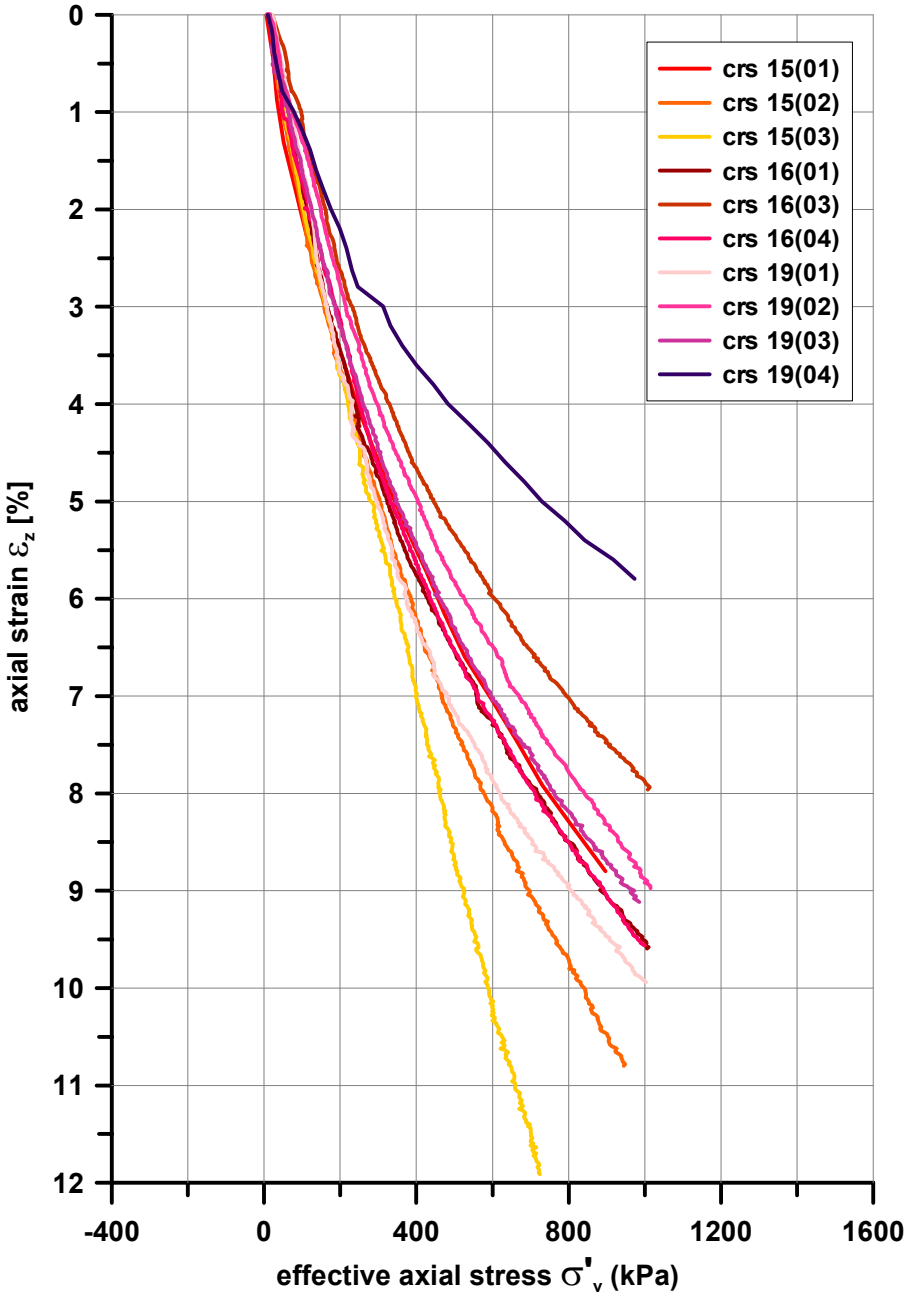

Figure 8.18: CRS test at $10^{-5}s^{-1}$ plotted in linear scale

	test	mechanical $\sigma'_{z,pc}$ (kPa)	creep $\sigma'_{z,pc}$ (kPa)	S(%)	measured $\sigma'_{z,pc}$ (kPa)
CR 07(02)	CRS 10^{-5}	213	241	80	300
CR 07(04)	CRS 10^{-4}	213	241	78	400
CR 15(02)	CRS 10^{-5}	245	277	95	270
CR 15(03)	CRS 10^{-5}	245	277	96	270
CR 16(04)	CRS 10^{-5}	252	266	75	220
CR 19(01)	CRS 10^{-5}	280	300	58	110

Table 8.4: preconsolidation pressure as from excess pore pressure measurements

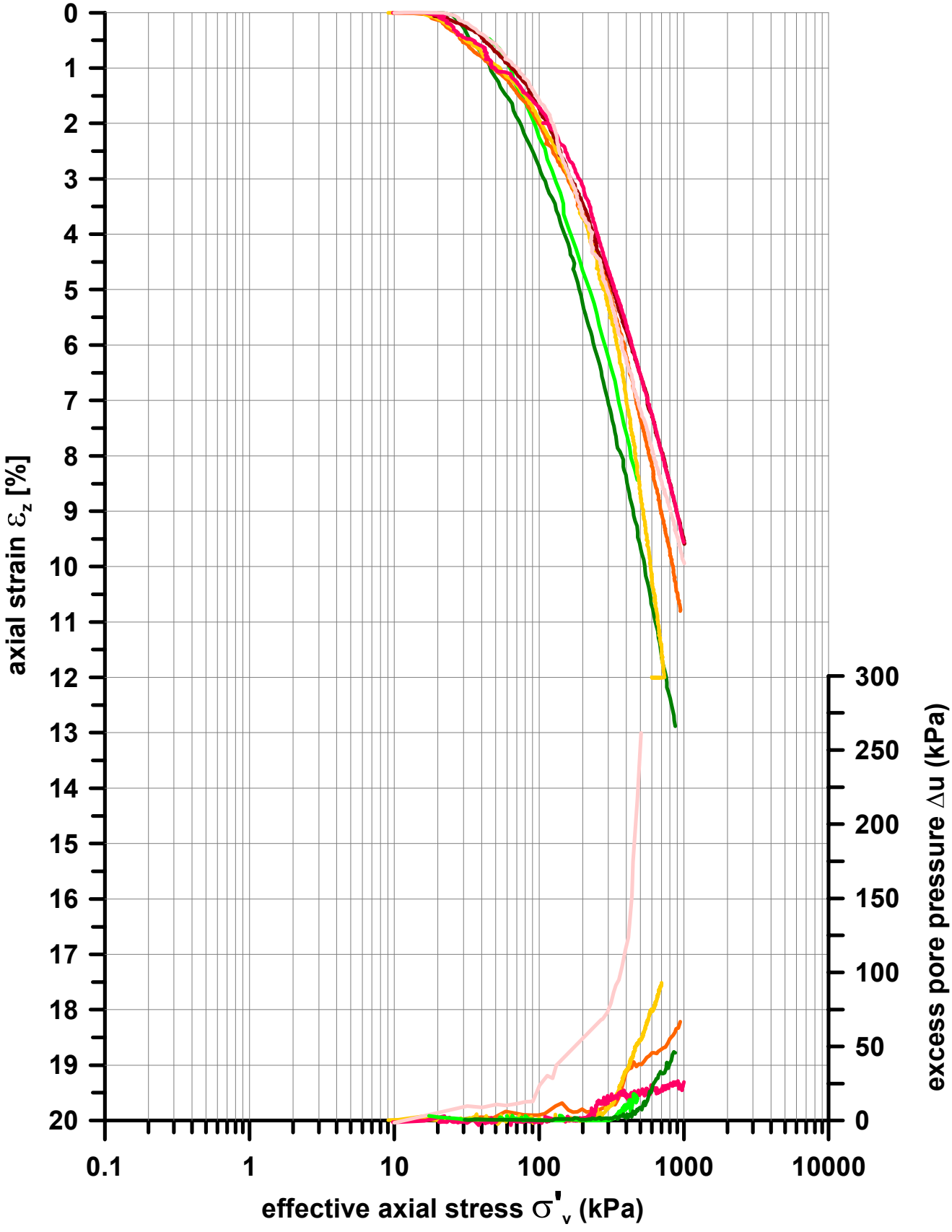

Figure 8.19: CRS tests with excess pore pressure development

Compressibility curves' slope and isotache approach

In Figure 8.20 CRS tests performed at the same strain rate equal to $\dot{\varepsilon}_z = 10^{-5} s^{-1}$ are reported. It can be noticed that the slope of the continuous loading compression curve strongly depends on the material. It is clearly evident, in fact, that sandy samples have to show stiffer behaviour than silty ones, and even among silty layers there are differences in slope, even though they display in a beam. This spread of slopes is certainly due to the high heterogeneity of the Venetian subsoil. Slope values for each test are reported in Table 8.6.

A correlation with the I_{GS} index has been proposed:

$$\lambda^* = \frac{d\varepsilon_z}{d\ln\sigma'_z} = \frac{0.046 - 0.007\ln(I_{GS})}{1+e_0} \tag{8.2}$$

and its application is shown in Figure 8.21.

The looseness of the preconsolidation pressure memory and the spread of slopes make almost impossible to retrace the isotache behaviour comparing different CRS tests. In fact, the preconsolidation pressure and the compression slope are the two elements that bound the compression curve on the stress-strain plane. If the first is not identifiable and the second is different for each layer, the visualization of the isotache curves' set cannot be expected.

Two solutions have been found in order to visualize the isotache behaviour of Venetian soil. It is already well-known, in fact, that this framework apply for a large variety of soils, especially in oedometric conditions, so it is realistic that it applies also to Venetian silts. This hypothesis has been confirm applying the two solution proposed, as below described.

The first solution has been to change strain rate during the same test and, as expected, compression curve has moved from an isotache curve to another, being the faster on the right side of the compression plane. In this way the relative position of the curves corresponding to different strain rates is fixed while the right positioning of the whole curve is not completely exact because the preconsolidation pressure is not well identified. An example is reported inFigure 8.22.

The second solution acts on the preconsolidation pressure. A given preconsolidation pressure has been imposed in a first consolidation phase, imposing a stress target with the Rowe cell system ($\sigma'_z = 145kPa$), then the sample has been unloaded to a given stress ($\sigma'_z = 115kPa$), more or less corresponding with the in situ overburden pressure. Then the CRS test has been performed. Results have been compared in Figure 8.23.

It can be observed that even imposing the same preconsolidation pressure for the three sample, they actually show a different value, depending on the strain rate, as expected, the faster showing an higher value than the slower.

Comparing the first three tests, one can notice that the sample 06(02) and 06(03), indeed, have also the same slope, thus being in the expected relative position one with reference to the other. Not the same can be inferred for the third sample (crs 06(04)), that, being much sandier show a stiffer behaviour and its compression curve cross the other two.

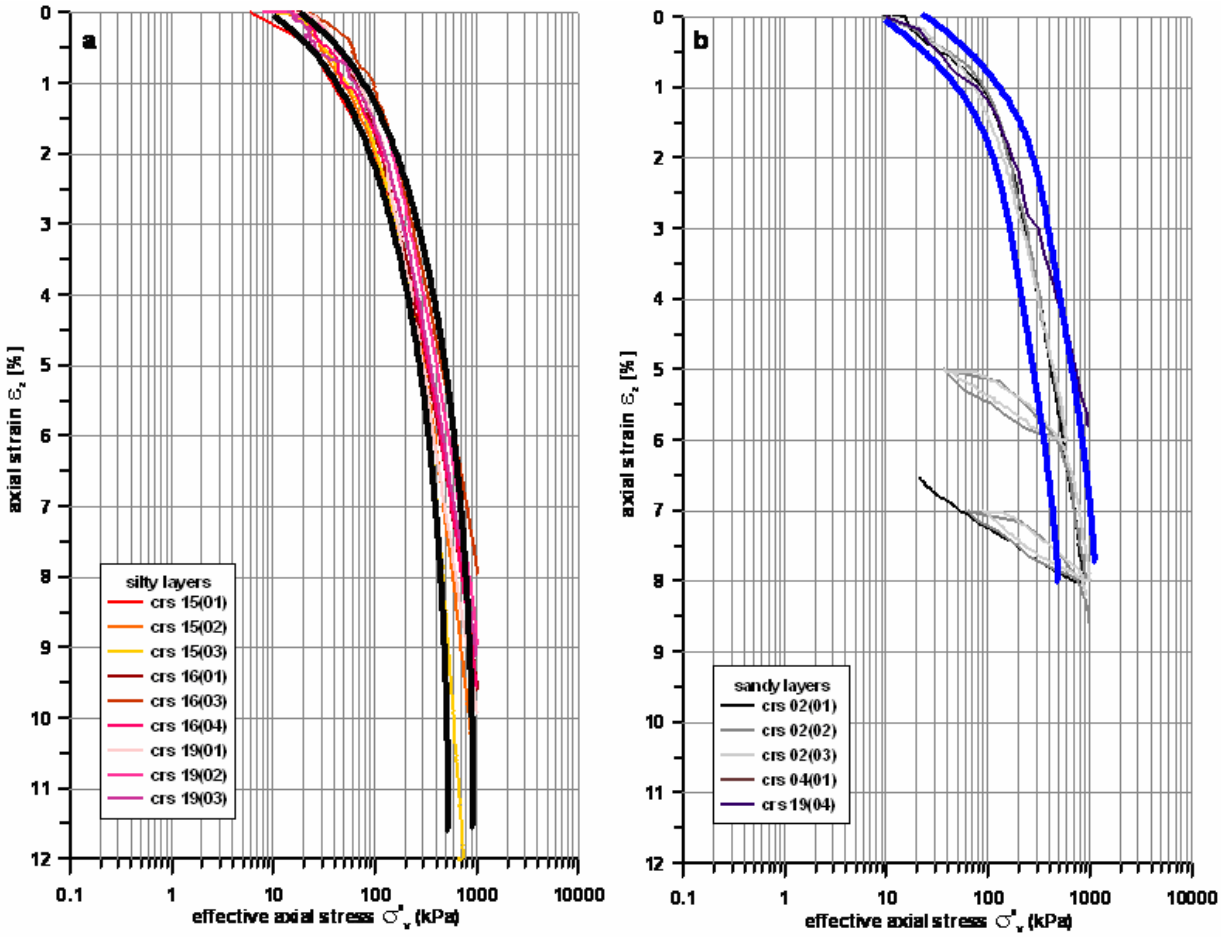

Figure 8.20: CRS tests at $10^{-5}s^{-1}$ plotted in semi-logarithm scale a) silty layers, b) sandy layers

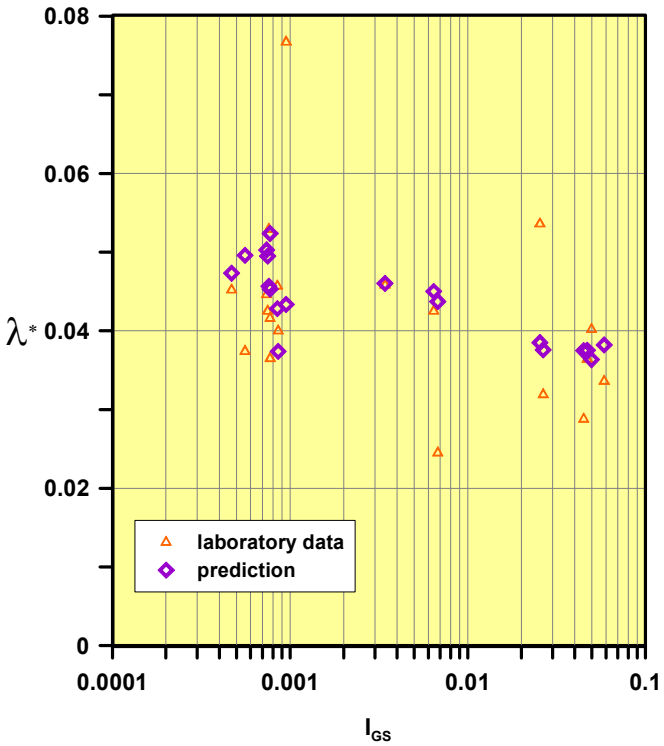

Figure 8.21: CRS tests slope versus grain size index (experimental data and prediction)

	G_S	w(%)	S(%)	e_0	λ^*
CR 02(01)	-	30	96	0,84	0,0402
CR 02(02)	-	26	97	0,72	0,0336
CR 02(03)	-	29	97	0,81	0,0288
CR 04(01)	-	28	95	0,80	0,0364
CR 06(01)	-	30	94	0,86	0,0536
CR 06(02)	-	31	97	0,86	0,0431
CR 06(03)	-	29	97	0,81	0,0425
CR 06(04)	-	32	96	0,90	0,0319
CR 15(01)	2,811	30	89	0,95	0,0425
CR 15(02)	2,770	26	95	0,76	0,0529
CR 15(03)	2,725	30	96	0,85	0,0767
CR 16(01)	2,786	31	94	0,92	0,0446
CR 16(02)	2,804	30	75	1,12	0,0365
CR 16(03)	2,786	29	82	0,99	0,0374
CR 16(04)	2,764	30	75	1,11	0,0452
CR 19(01)	2,730	33	58	1,55	0,04
CR 19(02)	2,739	31	69	1,23	0,0457
CR 19(03)	2,749	28	92	0,84	0,0416
CR 19(04)	2,753	30	97	0,85	0,0245

Table 8.5: compression curves' slope for CRS tests on Venetian soils

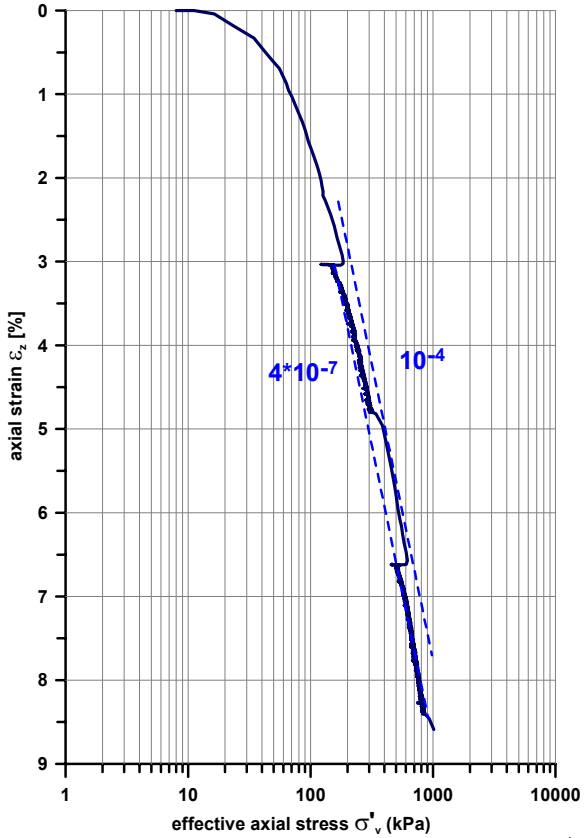

Figure 8.22: CRS 05(01) in which strain rate changes from 10^{-4} s^{-1} to $4*10^{-7}$ s^{-1}

The same happens for sample 08(01) and 09(01) in Figure 8.24: they have the same slope and being preconsolidated to the same stress value and then performing two different strain rate tests, they display in the correct order. If one chose to plot the four tests with the similar slope the result would be that showed in Figure 8.25, in which at the very beginning curves displayed in the right sequence. Then slope affects results.

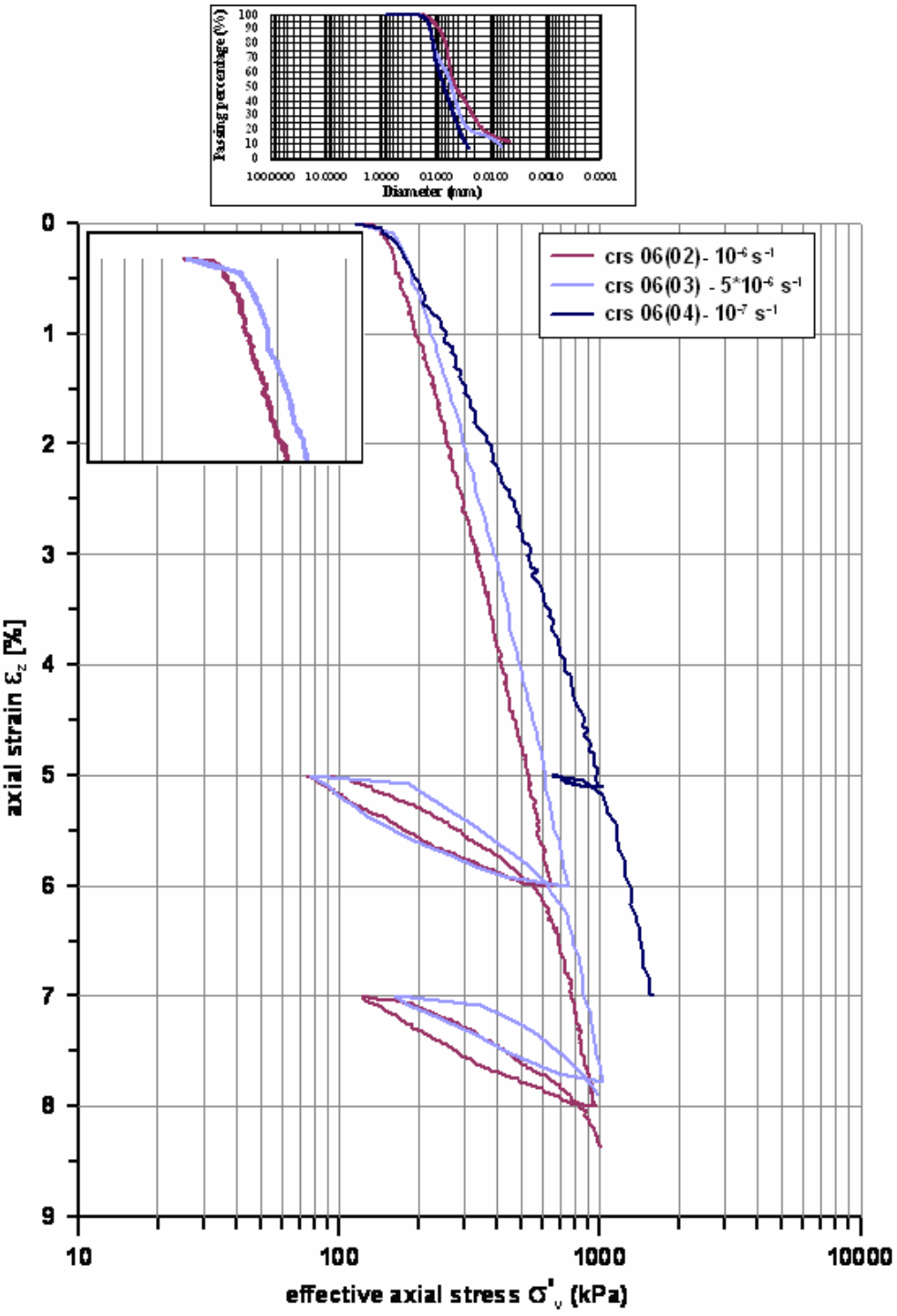

Figure 8.23: CRS tests on Venetian soil samples pre-imposing a preconsolidation pressure

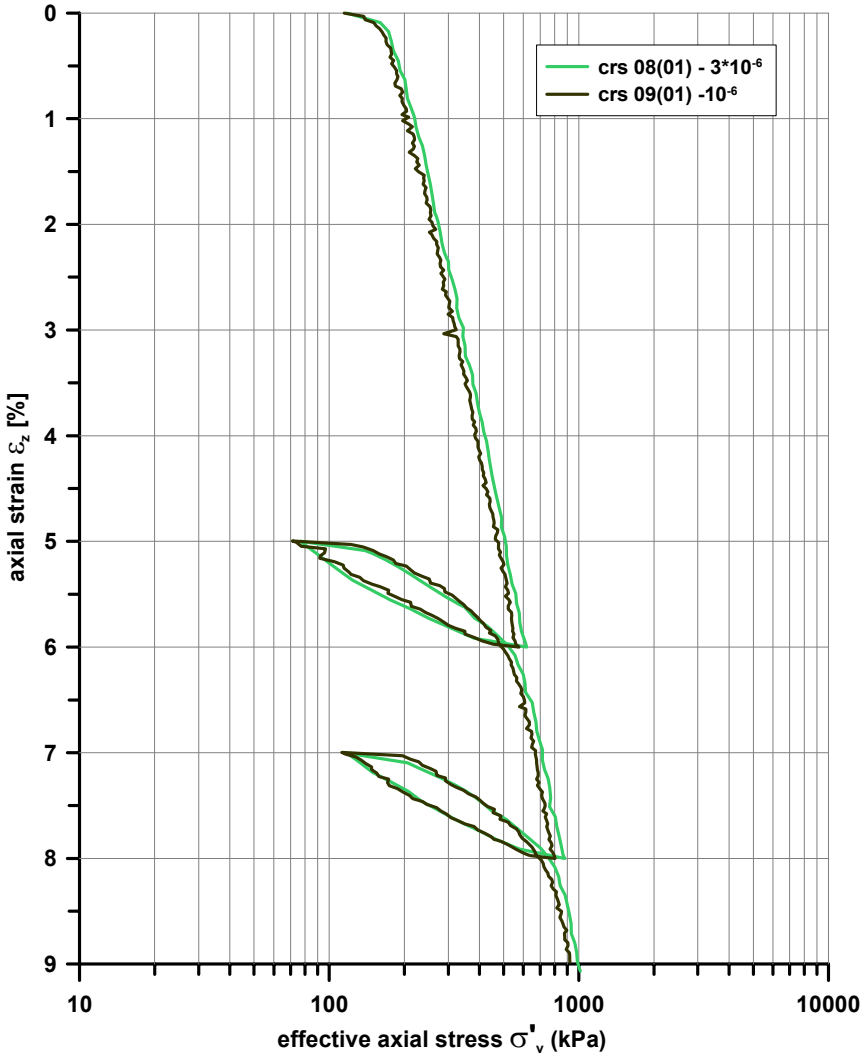

Figure 8.24: CRS tests on Venetian soil samples pre-imposing a preconsolidation pressure

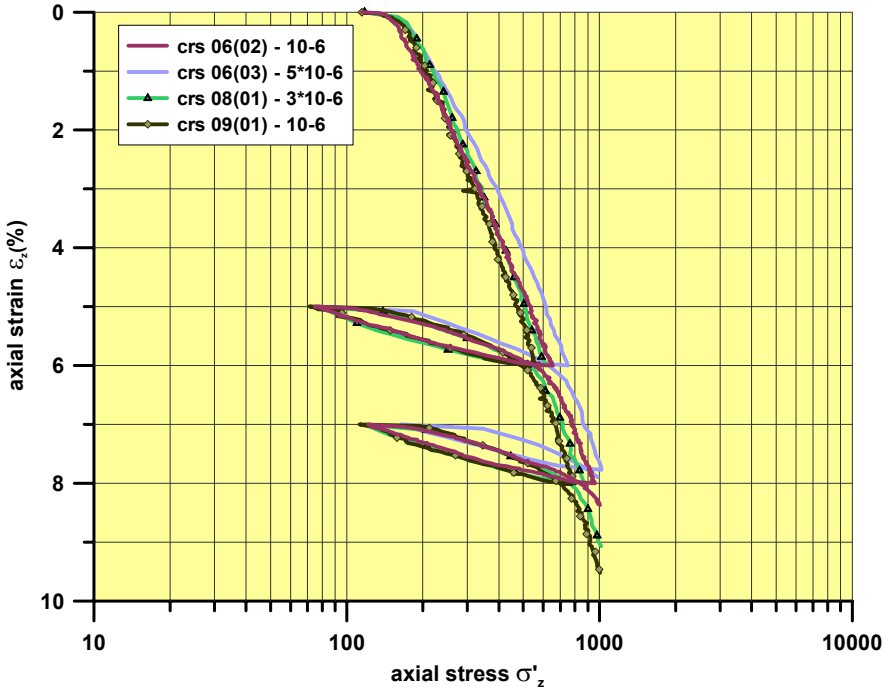

Figure 8.25: CRS tests with similar slope

Unloading reloading cycles

Some of the CRS tests have been performed with unloading-reloading cycles just to investigate small strain behaviour, that affects mainly the unloading reloading behaviour ,as previously described. The main effect of varying stiffness along with strain amplitude is the formation of hysteresis loops in stress-strain space, performing unloading-reloading paths. This behaviour is experimentally observed as reported, for example, in Figure 8.26 and in Figure 8.20b.

CRS tests with unloading-reloading cycles were carried out just imposing a strain target with a correspondent time to reach it, then imposing a new strain target in unloading, that is lower than the first, and the correspondent time and so on. Unloading-reloading cycles were performed both in tests with imposed preconsolidation and in tests without it. A detail of one of the first category is given in Figure 8.26.

It is interesting to notice that the two cycles are almost identical, and clearly show an initial stiff phase just after the direction reversal, followed by a progressive softer one. In Table 8.6 slope values are reported identifying also the strain amplitude at which the stiff behaviour start changing into a softer one. It can be noticed that, the trend is almost the same for loading and unloading in a same cycle and also comparing the two cycles.

It is worthy highlighting that cycles close not exactly at the initial reversing point (see Figure 8.26), and reach the normal compression line a bit below the expected point as if the cycles closed at the initial reversing point. This feature has already been described for the creep model that accounts for small strain stiffness, in the dedicated chapter, but here the aim is to highlight that this is not only a modelling feature but an experimental observation.

		slope	strain amplitude at change
1st unloading	**small strain**	0,00122	0,000319
	large strain	0,00508	
1st reloading	**small strain**	0,00099	0,000372
	large strain	0,00596	
2nd unloading	**small strain**	0,00145	0,000319
	large strain	0,00524	
2nd reloading	**small strain**	0,00121	0,000372
	large strain	0,00595	

Table 8.6: unloading-reloading slopes (crs06(02))

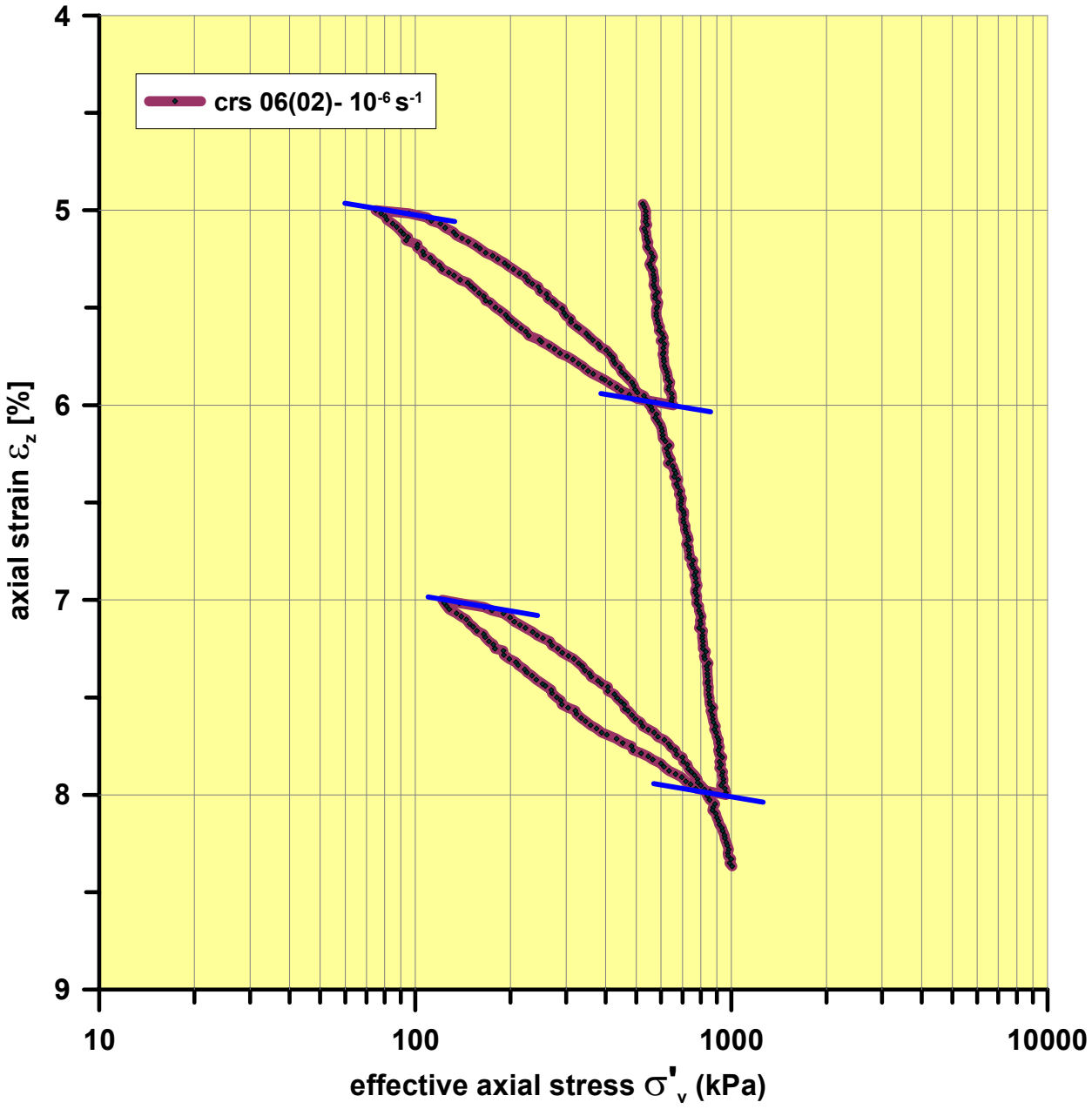

Figure 8.26: detail of unloading reloading cycles in crs test 06(02), at 10^{-6} s^{-1}

Chapter 9 - Modelling Venetian soils

Suitability of the creep model

The Venice lagoon soil, as widely highlighted, is a strongly heterogeneous interbedding of sands, silts and clayey or sandy silts. The mineralogical origin is the same but they display different grain size curves, as discussed in Chapter 7. As noticed from the Treporti embankment subsoil settlement measures, creep strains develop both for silty/clayey layers and sandy ones (see Figure 7.27). The internal mechanism is different, indeed, since sands generally show a deviatoric creep, while softer material is characterized by a volumetric creep.

The Soft Soil Creep model has been designed to model the pretty soft material, and in this case can be applied to silty and clayey layers. One of the interesting features of the model is the capability to take into account the behaviour showed by the Venetian soil for long time creeping. As described in Berengo (2006), in fact, long time oedometer tests have been carried out on silty samples taken from Treporti Testing Site before the embankment construction. Instead of keeping the load for 24 hours as in a traditional oedometer test, it has been kept for longer periods (7 days) and results have been then compared with those obtained in a standard oedometer test.

A slope change in overconsolidated step has been noticed, from a low value until (at the 7th day), the C_α value characteristic of normally consolidated steps (Figure 9.1). This feature is well captured by the Soft Soil Creep model. It in fact predicts a low slope in overconsolidated steps, for creep time lower than the reference time $t' << \tau_c$:

$$\frac{\varepsilon_v^{creep}}{d\ln t} = \mu^* \frac{t'}{\tau_c + t'} \approx 0 \tag{3.86}$$

being the reference time the quantity described in Figure 3.11 and directly connected with the OCR.

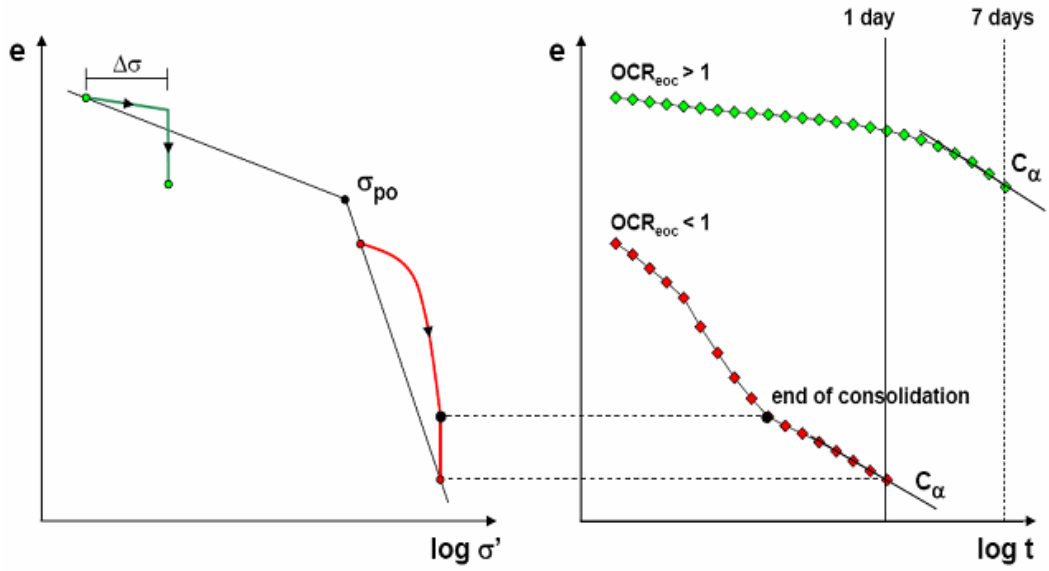

Figure 9.1: long oedometer test on Venetian silt sample

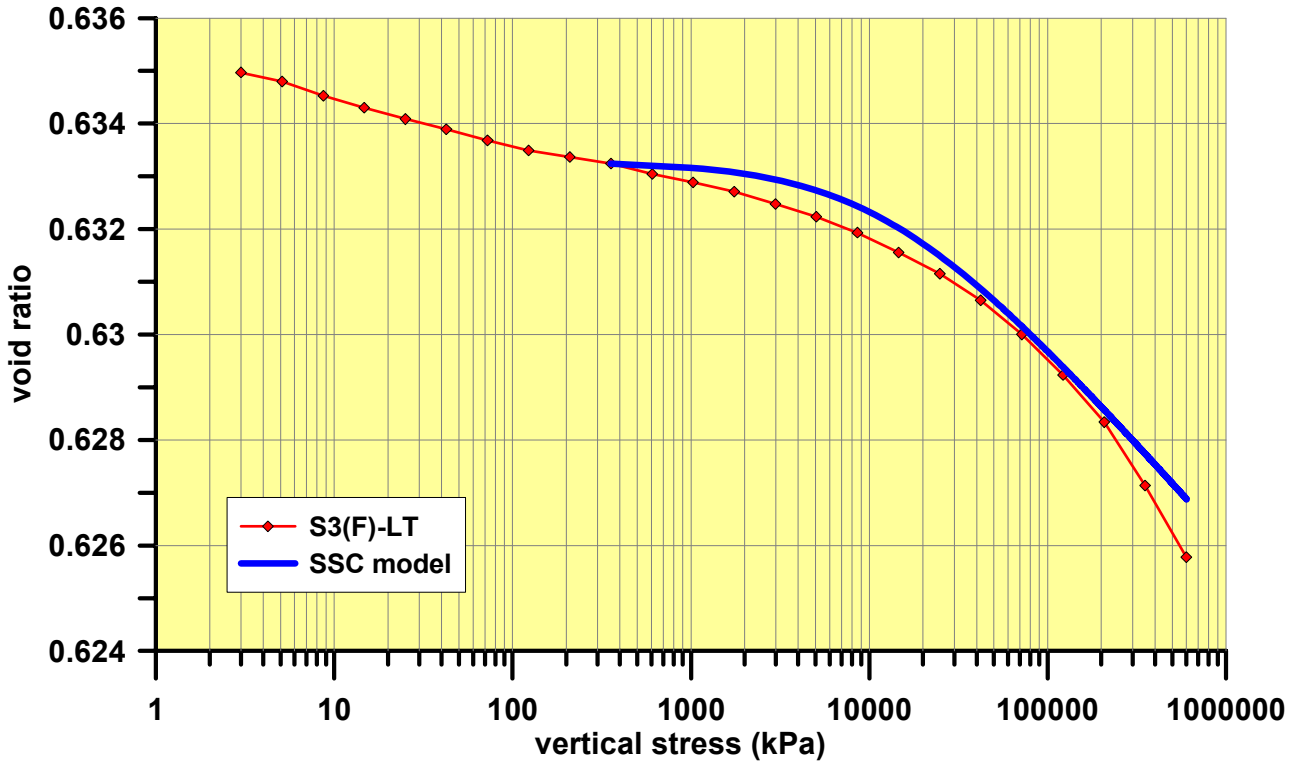

Figure 9.2: long term oedometer test S3(F) in an overconsolidated step modelled with SSC

On the other hand, whenever $t' >> \tau_c$ the previous equation becomes:

$$\frac{\varepsilon_v^{creep}}{d\ln t} = \mu^* \frac{t'}{\tau_c + t'} \approx \mu^* \tag{3.87}$$

In other words, if the creep time is enough long to overcome the time reference τ_c, even overconsolidated sample has a slope equal to μ^* in semi-logarithmic scale. Experimental data for an overconsolidated step with long time creep are shown together with the predicted behaviour in Figure 9.2.

This capability is one of the reasons why the Soft Soil Creep model has been chosen in order to model Venice lagoon soils' behaviour. It needs being aware that the soil is so heterogeneous that any possible model would have intrinsic limitations in describing such a peculiar soil.

Unloading behaviour: neediness of small strain stiffness formulation

The swelling behaviour shown by the subsoil under the Treporti embankment in the unloading phase was relatively small compared to the settlement occurred during the loading phase. Under the centreline, in fact, soil has exhibited settlement for a total of 505 mm circa after four years creep; at the removal completion the recover has been less of 30 mm. Besides, it occurred mainly in the final removal stage, while as regard to the first removing phases, the swelling was very small (see Figure 6.18 and Figure7.19).

This observation suggested to introduce the small creep behaviour to the creep model in order to account for the stiff behaviour registered during the unloading phase. However the strain

dependency of stiffness is a general feature for soils, and to take it into account results as a general improvement in a creep model.

As regard specifically Venice lagoon soils, an analysis of stiffness reduction along with strain has been carried out by Cola and Simonini (1999). In Figure 9.3 trends of secant shear stiffness G determined in undrained tests are displayed against shear strain. In order to appreciate the presence of a critical value of shear strain, beyond which rapid changes in secant modulus occur, data are provided in the log-log scale. Together with the experimental data, the prediction with Hardin and Drnevich hyperbolic law described in Chapter 5 is displayed:

$$G = G_0 \frac{1}{1 + 0.385 \frac{\gamma}{\gamma_{0.7}}} \tag{4.18}$$

where the maximum shear stiffness has been taken as $G_0 = 100MPa$ and the strain amplitude corresponding to a reduction to the 70% of the initial value has been assumed to be $\gamma_{0.7} = 0.0001$.

As one can see from Figure 9.3, the hyperbolic law formulated by Hardin and Drnevich well describes the experimental trends, so the choice of using that relationship to introduce the stiffness' strain dependency in the creep model results indicated for Venetian soils.

In the following simulations, very small stiffness value and reference strain amplitude will be taken as evaluated in Figure 9.3 or with very close values.

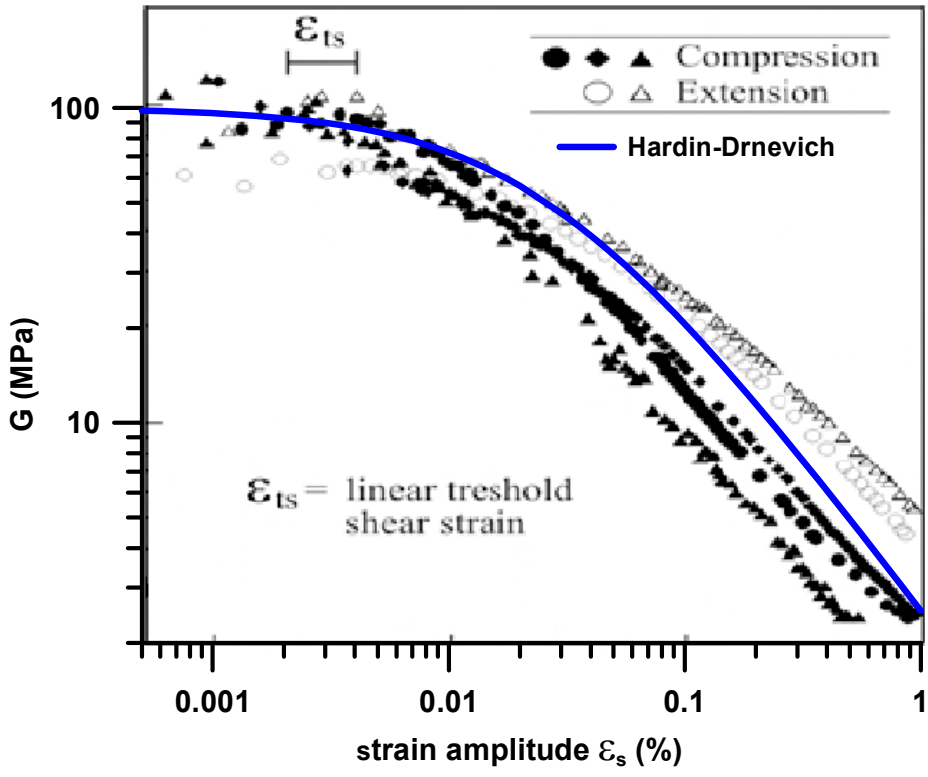

Figure 9.3: shear modulus versus shear strain in undrained tests on Venetian soils

Modelling oedometer and CRS tests with one-dimensional formulation

The one-dimensional version of the creep model with small strain stiffness behaviour has been tested in modelling one-dimensional tests. The attention has been paid mainly in observing unloading-reloading response. As already highlighted, in fact, in primary loading differences are expected to be negligible with respect to the pure creep model.

Since the one-dimensional formulation here proposed enables to simulate CRS tests only, the oedometer tests have been modelled imposing the final strain rate, that coincides with μ^*. To be precise for $OCR = 1$ (when stress-strain state lies on the normally consolidated line) what is coincident with μ^* is not the total $\dot{\varepsilon}_v$ but $\dot{\varepsilon}_v^{creep}$, in fact:

$$\dot{\varepsilon}_v^{creep} = \frac{\mu^*}{\tau}\left(\frac{p'}{p'_{pc}}\right)^{\frac{(\lambda^*-\kappa^*)}{\mu^*}} = \frac{\mu^*}{\tau}\left(\frac{1}{OCR}\right)^{\beta} \tag{3.81}$$

but the idea is to reproduce just the final state in which the local strain rate is $\dot{\varepsilon}_v = \dot{\varepsilon}_v^{creep}$

In Table 9.1 and Table 9.2 parameters used in the simulation of two oedometer tests on Venetian soils are listed, in the second row derived parameters are reported.

In Figure 9.4 and Figure 9.5 the relative compression curves are shown. As regard to the primary compression curve, the small gap between the modelling and the experimental data is due to the fact that data points do not display exactly along a line in semi-logarithmic scale, while the model framework is based on this assumption. The difference is so small to be considered negligible. In the case of S3(H), however, the model show a sharp slope change in correspondence of the preconsolidation pressure. Venetian soils, on the contrary, as many times highlighted, loose memory of the preconsolidation pressure, showing a rounded shape. In the specific case the Casagrande method has been used to retrace it, and the value has been used in modelling. This procedure, as already explained, can lead to wrong results in terms of retracing OCR value, because laboratory samples feel the effect of sampling.

S3(E)	G_0	$\gamma_{0.7}$	κ^*	λ^*	μ^*	OCR	$\dot{\varepsilon}_{axial}$
oedometer	100000	0.0001	0.0062	0.031	0.001	6.6	0.001
		γ_{cutoff}	G_{ur}	β			τ
		0.000705	7017.976	24.8			1.25

Table 9.1: S3(E) oedometer tests' parameters

S3(H)	G_0	$\gamma_{0.7}$	κ^*	λ^*	μ^*	OCR	$\dot{\varepsilon}_{axial}$
oedometer	100000	0.0001	0.006	0.044	0.002	1	0.002
		γ_{cutoff}	G_{ur}	β			τ
		0.000705	7251.908	19			1.15

Table 9.2: S3(H) oedometer tests' parameters

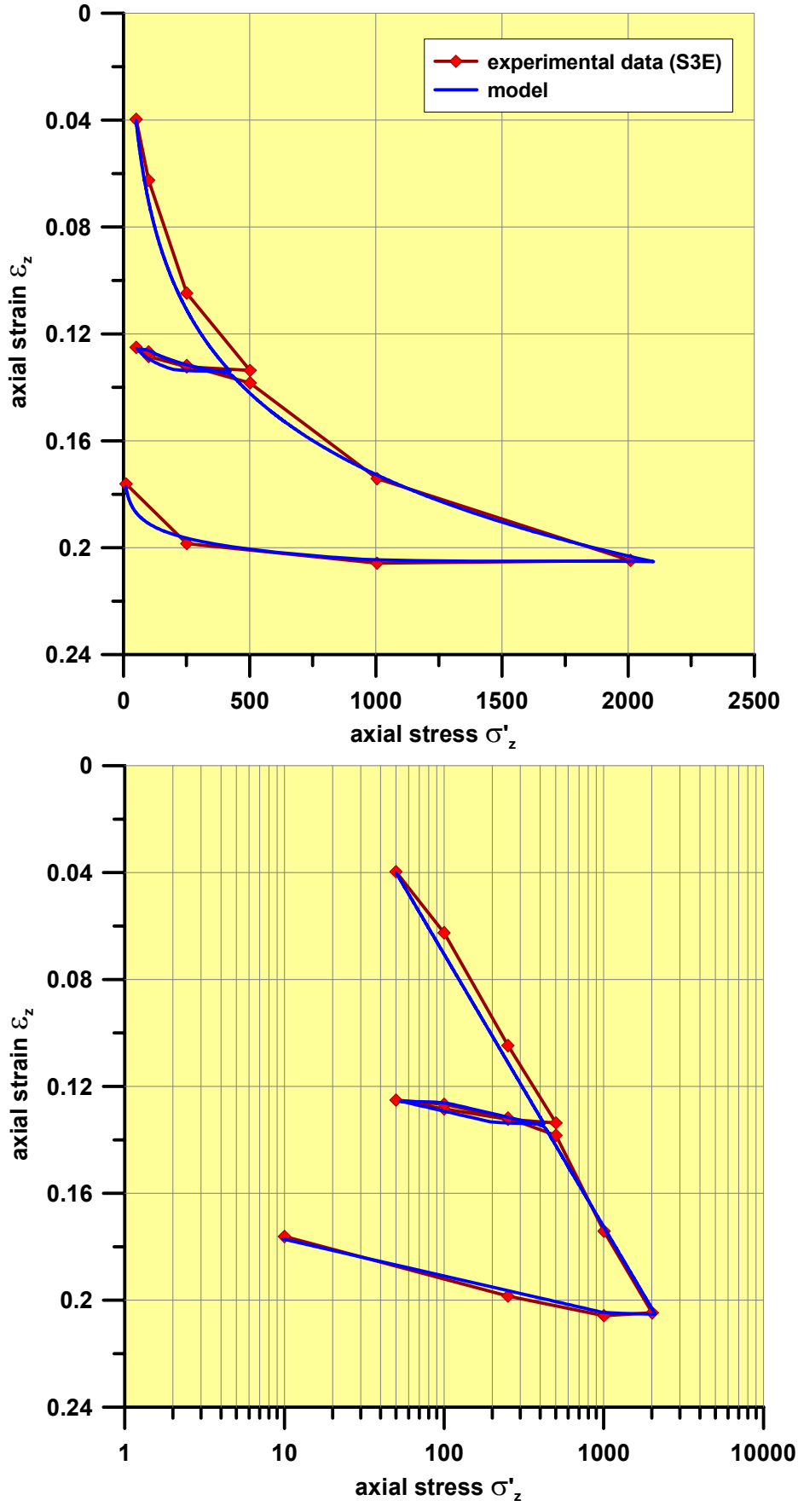

Figure 9.4: S3(E) oedometer test data and modelling

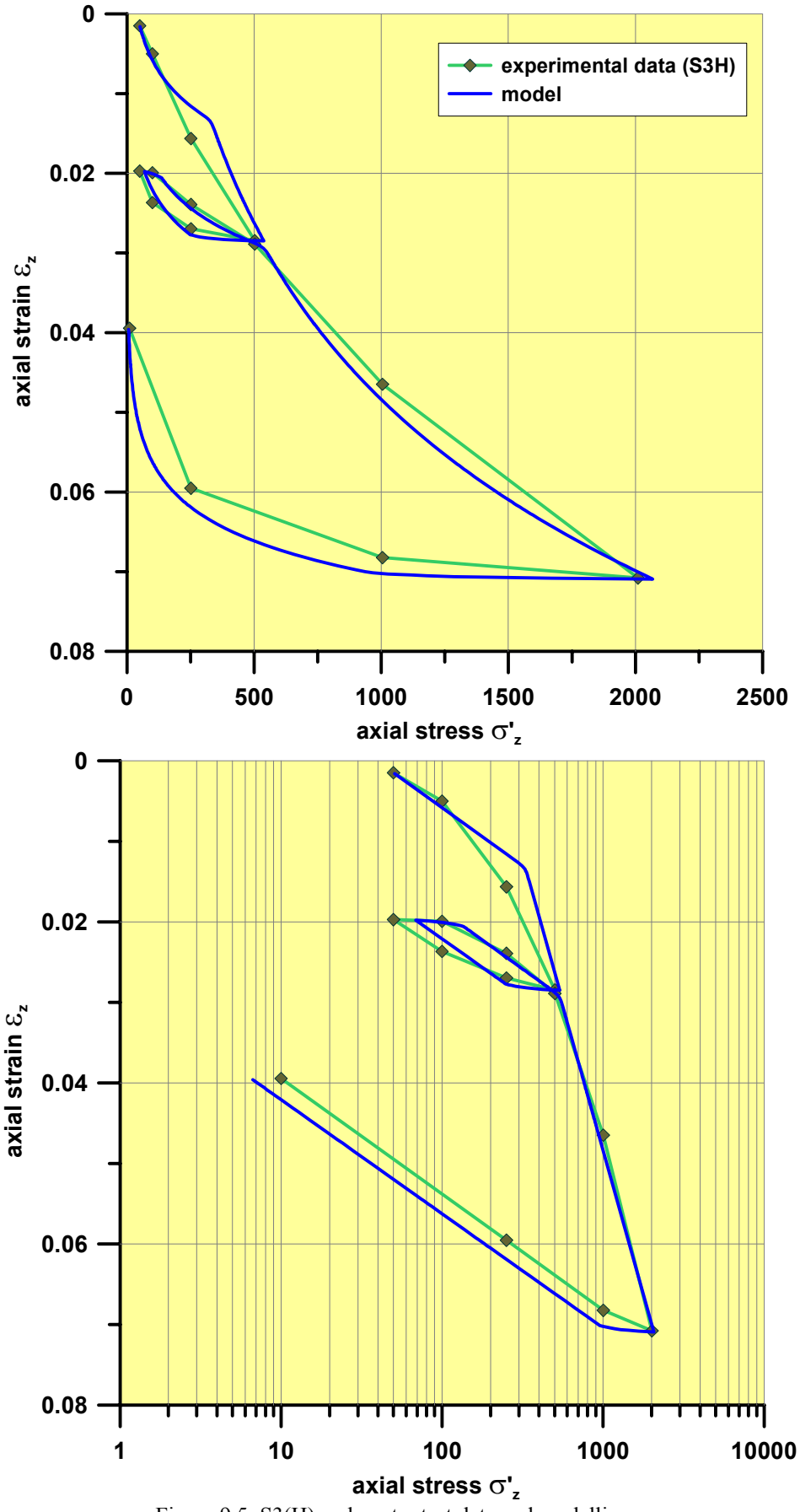

Figure 9.5: S3(H) oedometer test data and modelling

In the specific case the aim is to reproduce the compression curve, especially the unloading part, so preconsolidation can be assumed as a fictitious parameter, just to model the compression curve shape. This is not intrinsically wrong because it has been shown that in situ soil has a compression curve shaped as the model predicts, with a recompression part and a virgin compression part. As regard to the unloading behaviour the model predictions fit well with laboratory data, following almost the same path.

The CRS tests modelled with the 1d CRS creep model accounting for small strain stiffness reduction are reported in Figure 9.6. They have been already described in the previous chapter. Here it is worthy of highlighting that all of them have been preconsolidated to the same stress value, showing then a different value depending on the strain rate. The four tests display in the right order (on the right-side the faster ones, on the left-side the slower ones), at least at the very beginning. Then the even slightly different slope affect the results.

In order to best describe and model the isotache behaviour shown in these laboratory tests, it is convenient do divide them into two groups, each of them made of two tests with the same slope and different strain rates.The first test of each group is taken as the reference, the OCR is evaluated and the relative τ parameter (described in Chapter 3). The second of each group, on the contrary, uses the same OCR and τ values as the first, obtaining a different preconsolidation pressure depending on the strain rate.

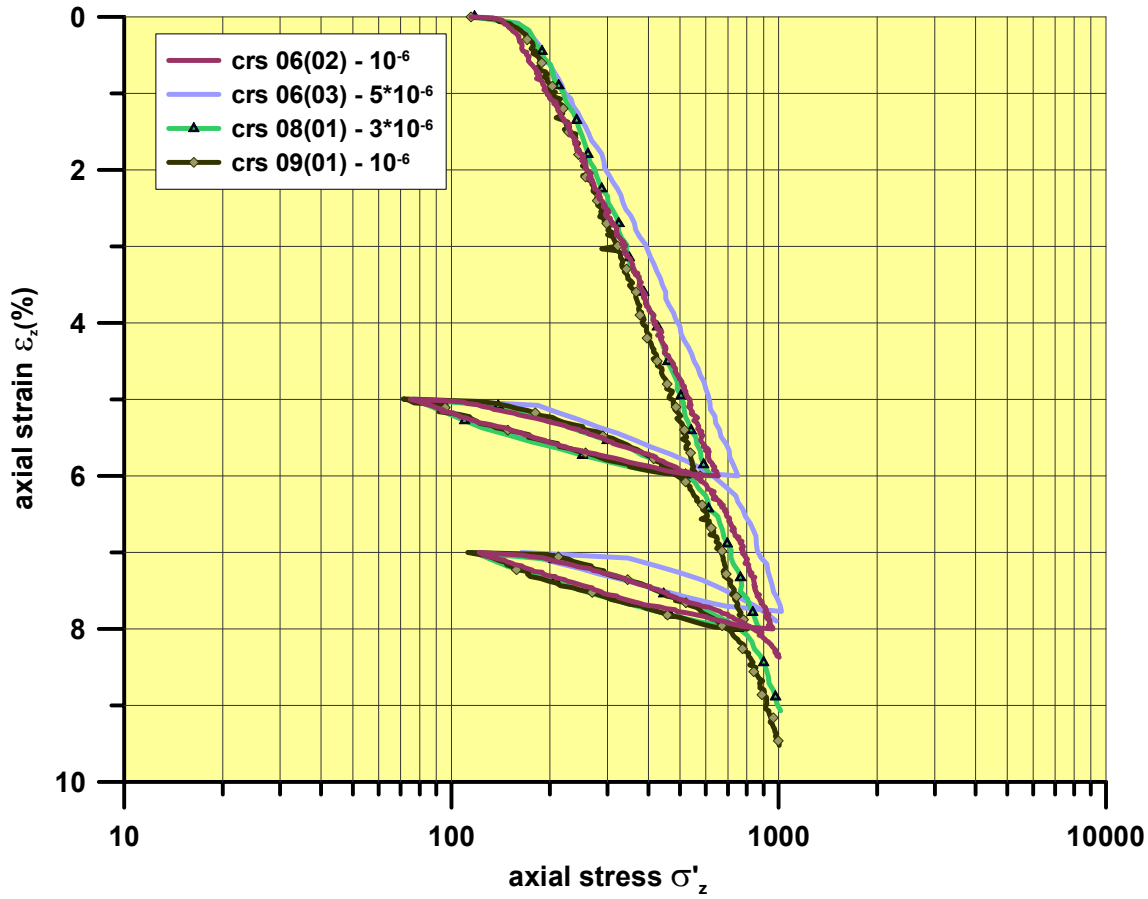

Figure 9.6:CRS tests on Venetian soil

Model parameters are listed in Table 9.3, Table 9.4, Table 9.5 and Table 9.6. Strain-stress curves are reported in Figure 9.7 and Figure 9.8.

Results are very satisfactory, both in strain rate dependent preconsolidation pressure prediction and especially in describing the unloading reloading cycles. Slopes are not perfectly fitted, since experimental data do not display exactly along a line, as in oedometer tests, but the approximation is quite good.
As regard to the unloading-reloading cycles the results it is almost excellent using the initial stiffness value come from the Hardin and Drnevich calibration reported in Figure 9.3 and a reference strain amplitude based on the value found in that calibration, a little bit modified to better fir results.

crs06(02)	G_0	$\gamma_{0.7}$	κ^*	λ^*	μ^*	OCR	$\dot{\varepsilon}_{axial}$
CRS-2 UR $\sigma'_{z,pc} = 145kPa$	100000	0.00005	0.0062	0.042	0.0021	1.336	10^{-6}
		γ_{cutoff}	G_{ur}	β			τ
		0.00036	7017.97	17.04			2463.68

Table 9.3: crs06(02) tests' parameters

crs06(03)	G_0	$\gamma_{0.7}$	κ^*	λ^*	μ^*	OCR	$\dot{\varepsilon}_{axial}$
CRS-2 UR $\sigma'_{z,pc} = 145kPa$	100000	0.00001	0.0062	0.042	0.0021	1.336	$5*10^{-6}$
		γ_{cutoff}	G_{ur}	β			τ
		0.0007	7017.97	17.04			2463.68

Table 9.4: crs06(03) tests' parameters

crs09(01)	G_0	$\gamma_{0.7}$	κ^*	λ^*	μ^*	OCR	$\dot{\varepsilon}_{axial}$
CRS-2 UR $\sigma'_{z,pc} = 145kPa$	100000	0.00005	0.007	0.048	0.0021	1.336	10^{-6}
		γ_{cutoff}	G_{ur}	β			τ
		0.00039	6215.92	19.52			2458.53

Table 9.5: crs09(01) tests' parameters

crs08(01)	G_0	$\gamma_{0.7}$	κ^*	λ^*	μ^*	OCR	$\dot{\varepsilon}_{axial}$
CRS-2 UR $\sigma'_{z,pc} = 145kPa$	100000	0.00005	0.007	0.048	0.0021	1.336	$3*10^{-6}$
		γ_{cutoff}	G_{ur}	β			τ
		0.00039	6215.92	19.52			2458.53

Table 9.6: crs08 (01) tests' parameters:

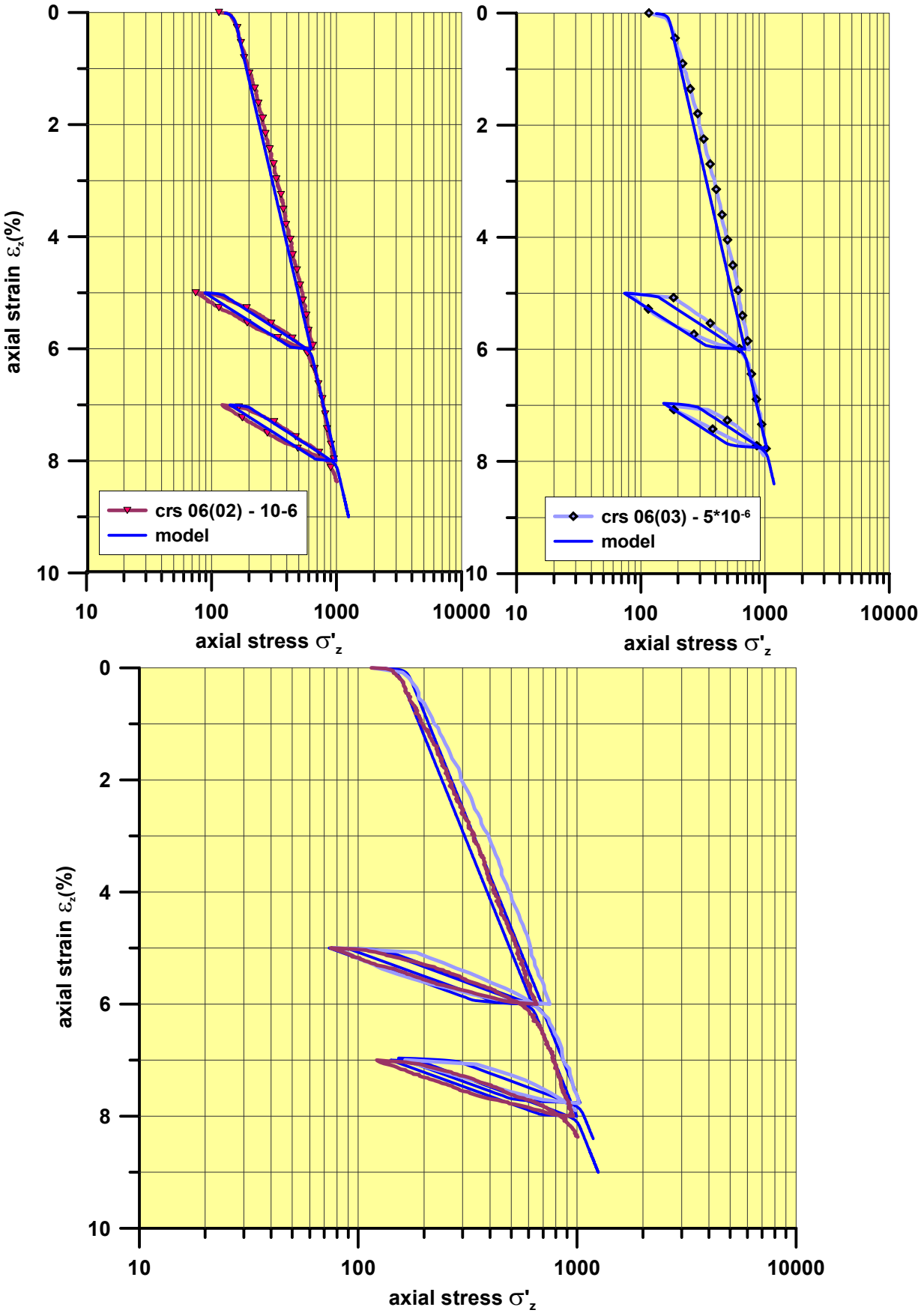

Figure 9.7: crs06(02) and crs06(03) tests data and modelling

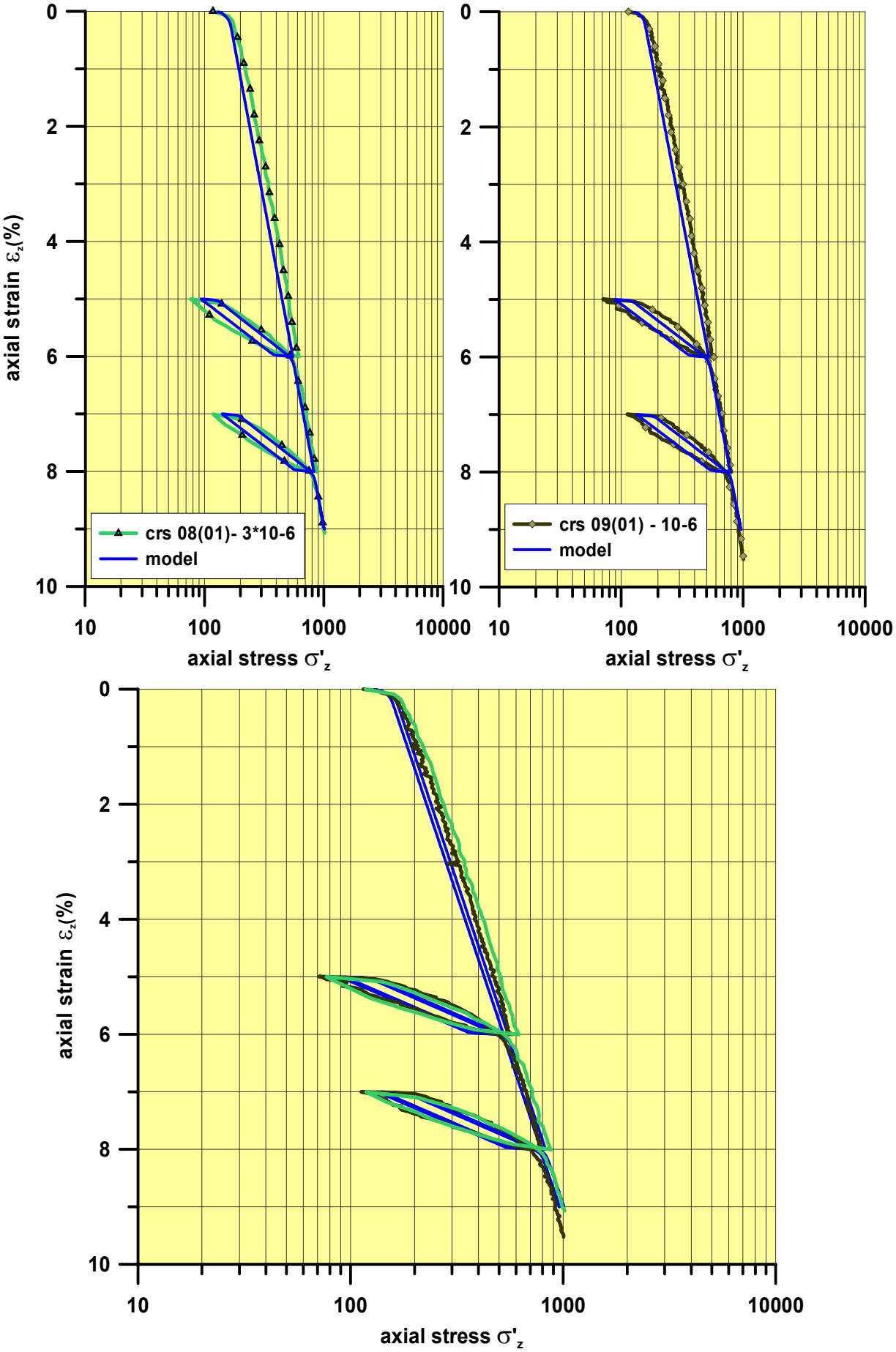

Figure 9.8: crs09(01) and crs08(01) tests data and modelling

Modelling Treporti embankment trial

The three-dimensional formulation of the creep model accounting for the stiffness' strain dependency (SSC small) was formulated by Benz and Leoni on the basis of the one-dimensional one.

It has been used to simulate the Treporti embankment trial, in the framework of the Plaxis 2D finite element code. It was applied to the most silty and clayey layers (C in Figure 9.8), whilst for pretty sandy layers (S in Figure 9.9) the elasto-plastic inviscid Hardening Soil model was chosen. The soil layers distribution assumed in this study for numerical analysis is shown in Figure 9.9.

It was retraced according to the CPTU profiles described in Chapter 7. Since only one soil profile for the whole area has to be defined, the sandy lamination that is present on the border of the embankment has been extended until the centreline, choosing a little bit smaller thickness, however. In Berengo et al.(2008) a slightly different soil profile was chosen on the basis of the horizontal displacement profile measured at the toe of the embankment: the sandy layers were identified as the stiffest ones, so in correspondence of small horizontal displacement a sandy lamination was introduced. This constitutes a sort of back analysis, that, obviously, provides very good results in terms of horizontal displacements. In this following study the soil profile was based exclusively on the laboratory and in situ classification tests.

An axisymmetric mesh of 6-noded triangular elements was chosen. Horizontal displacements were prevented along the symmetry axis at the left side of the mesh and at the right side, whilst horizontal and vertical displacements were prevented at the bottom of the mesh. As for the hydraulic boundary conditions, the water table was assumed to be 0.5 m below ground surface and horizontal water flow was prevented along the symmetry axis.

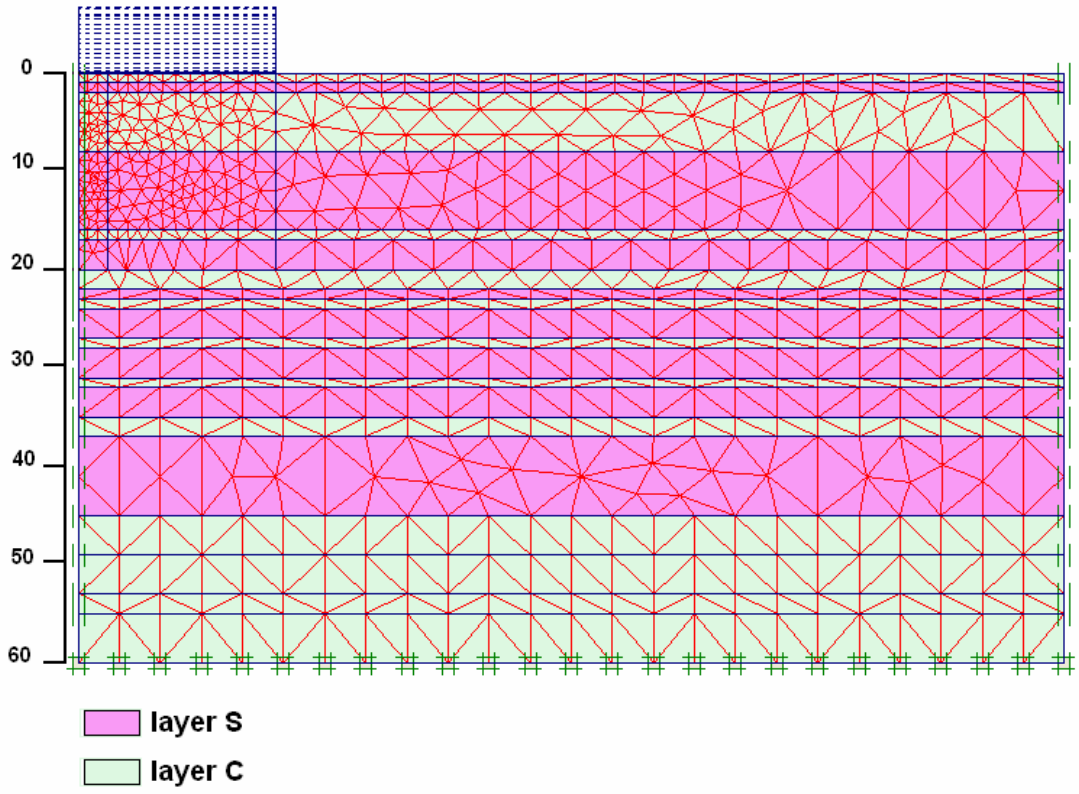

Figure 9.9: soil profile and finite element mesh

The construction phases of the test embankment were simulated by activating the soil layers according to the real construction sequence. Each construction stage was simulated by undrained phase followed by consolidation.

As for the constitutive law's parameters, the use of the SSC-small model requires the identification of the critical state friction angle φ and of the so-called modified compression, swelling and creep indexes (λ^*, κ^* and μ^* respectively) together with the initial shear stiffness G_0 and the reference strain amplitude $\gamma_{0.7}$ corresponding to the strain amplitude at which stiffness reduces to the 70% of its initial value.

These latter two parameters were calibrated on the basis of the shear stiffness reduction curve shown in Figure 9.3. As regard to the compression index it has been evaluated on the basis of oedometer tests results (see Chapter 7), choosing an average value characteristic for the silty layers. The swelling index, then, has been taken as $\kappa^* \approx \lambda^*/10$. This can be considered already an underestimated value, but the aim is to show that even with a low value the swelling displacement would be overestimated. As regard to the creep index it was evaluated according to oedometer tests normally consolidated loading steps. The average value chosen results in good agreement with the creep index values calculated from in situ measurements for silty layers. Those values in fact are representative of normally consolidated soils since the embankment load brought the subsoil form a slightly overconsolidated to the normalconsolidated conditions. The stiffness parameters of the Hardening Soil used for sands soils were set to typical values. The complete set of material parameters used for FE analyses is summarized in Table 9.7 and Table 9.8. The embankment was modelled with a simple linear elastic constitutive law, and the Young's modulus was set to E=3*10^4 kPa.

As regard to the OCR profile, it has been imposed in terms of $POP = \sigma'_{z,pc} - \sigma'_{z,0}$, from which:

$$OCR = \frac{POP + \sigma'_{z,0}}{\sigma'_{z,0}} \tag{9.1}$$

For $POP = 30$ the OCR profile estimated in situ as described in Chapter 7 is well captured, as shown in Figure 9.10.

layer	model	γ_{sat} (kN/m^3)	φ	G_0 (kPa)	$\gamma_{0.7}$	κ^*	λ^*	μ^*	ν	POP	c	ψ
C	SSCsmall	18	33	100000	0.0001	0.0048	0.050	0.0012	0.2	30	0	0

Table 9.7: SSC-small parameters for C layers

layer	model	γ_{sat} (kN/m^3)	φ	E_{50} (kPa)	E_{oed} (kPa)	E_{ur} (kPa)	m	ν	POP	c	ψ
S	HHS	18.5	35	3*10^4	3*10^4	1.2*10^5	0.5	0.2	30	1	0

Table 9.8: HS parameters for S layers

To compare the numerical results with in situ measurements, the vertical settlement versus time under the centre of the embankment is plotted (Figure 9.11).

The total vertical settlement, measured with the sliding micrometer near the embankment centreline in the middle of the first layer was compared to the total vertical settlement predicted by numerical analysis, both with the pure SSC and the SSC small models. The overall stiffness of the subsoil is slightly larger than the calculated one, but the final settlement is well-captured by the two creep models, that in loading phase give exactly the same results.

The big difference occur in the unloading phase where the pure creep model overestimates the swelling displacements while the modified version that accounts for small strain behaviour well captures the real trend.

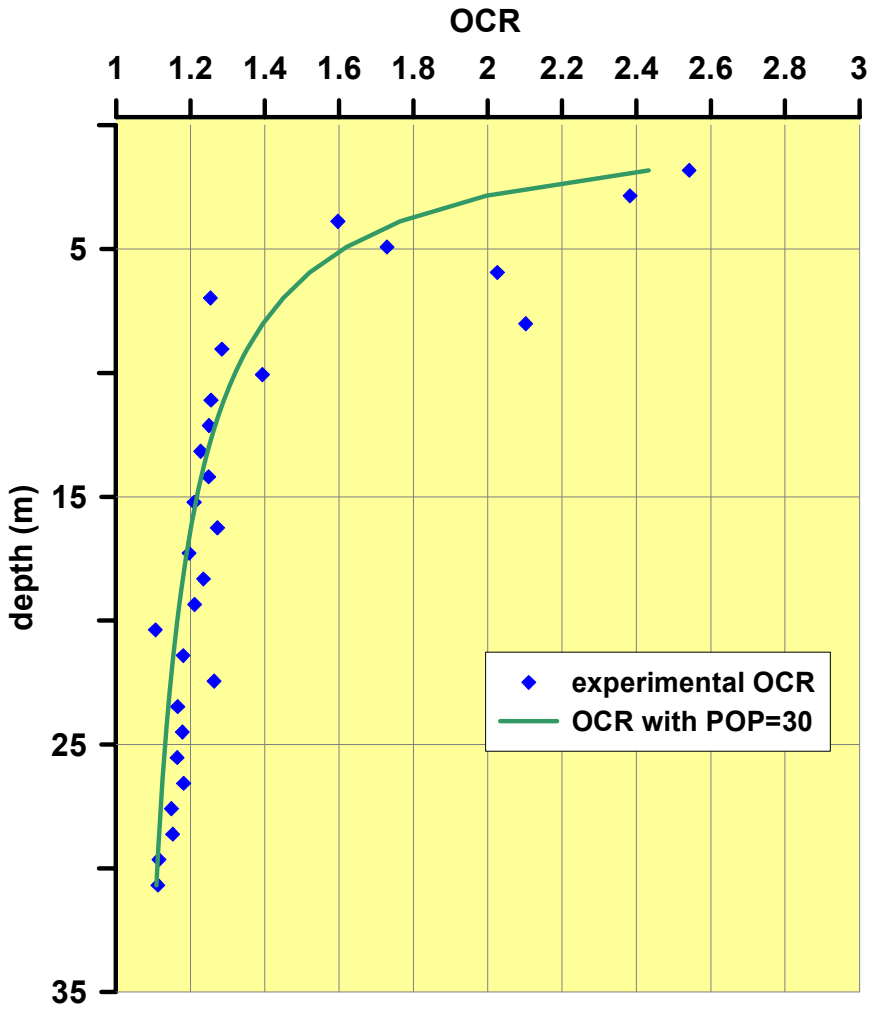

Figure 9.10: OCR profile at Treporti Testing Site before embankment construction and OCR profile calculated form POP=30

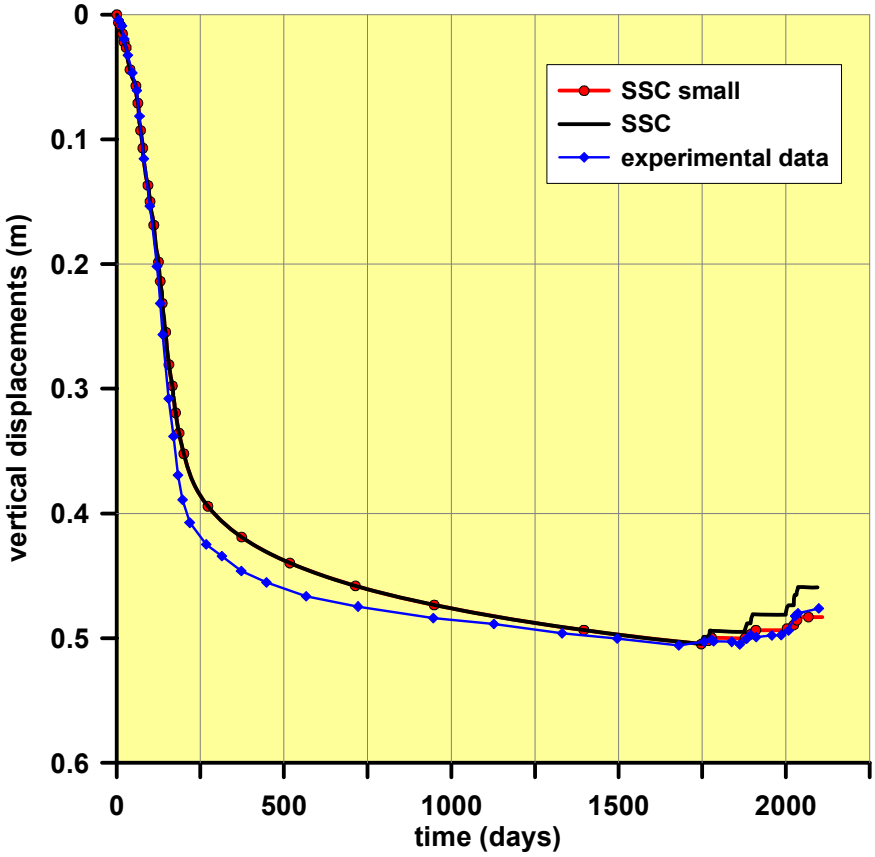

Figure 9.11:vertical displacement at the embankment centre

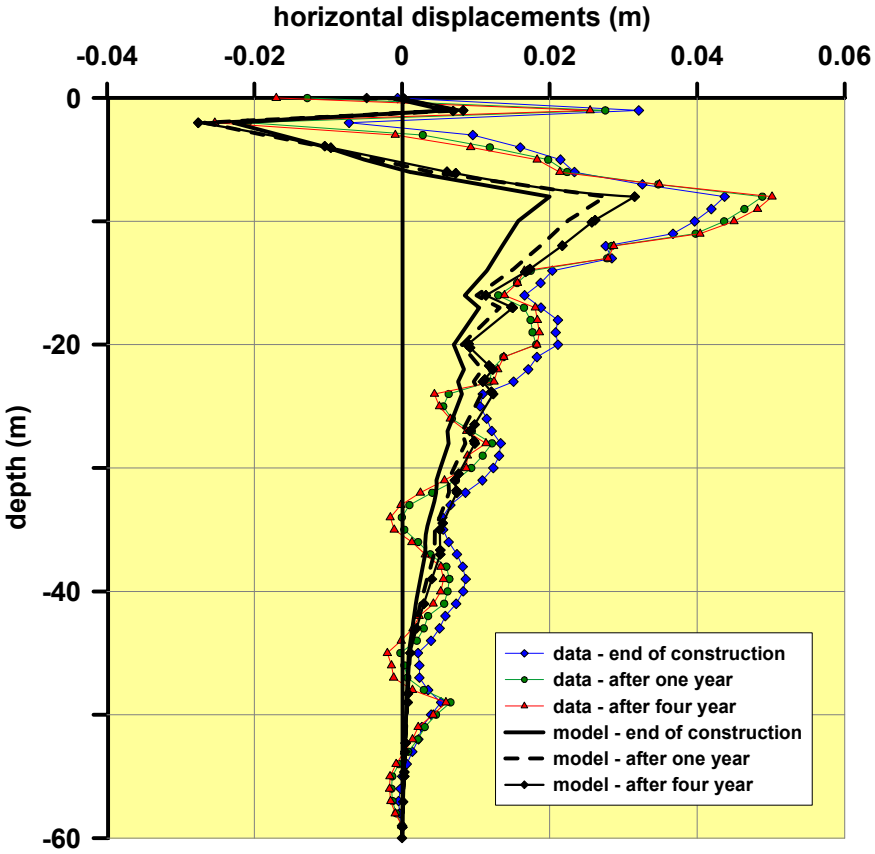

Figure 9.12: horizontal displacements at the embankment toe

Both the version, indeed, underestimate the small creep displacement shown after the fist unloading phase, since the OCR value is already too high so that the models could give important creep strain, and, on the other hand, they do not capture the delayed swelling shown after the complete embankment removal.

The improvement brought introducing the small strain stiffness formulation can be however considered very good.

In Figure 9.12 horizontal displacement just after the end of construction, after one year and four years respectively from the embankment construction are shown. The two models in loading phase show identical results, that in this case underestimate real soil response. The trend is however well captured.

Unlikely horizontal displacement measures during the embankment removal and after it are not available, so it is not possible to compare them with numerical results.

Bibliography

Abed, A. (2008) 'Numerical modelling of expansive soil behaviour'. Institut fuer Geotechnik Stuttgart, PhD Thesis.

Alonso, E.E., Gens, A. & Lloret, A. (2000) 'Precompression design for secondary settlement reduction'. *Géotechnique*, 50 (6), 645-656.

Atkinson, J.H. & Little, J.A. (1988) 'Undrained triaxial strenght and stress- strain characteristics of a glacial till soil'. *Canadian Geotechnical Journal*, 25, 428-439.

Atkinson, J.H. (2000) 'Non- linear soil stiffness in routine design'. *Géotechnique*, 50 (5), 487-508.

Augustesen, A., Liingaard, M. & Lade, P.V. (2004) 'Evaluation of Time-Dependent Behavior of Soils'. *International Journal of Geomechanics*, ASCE 4 (3), 137-156.

Belloni, L.G., Rizzo, A., Caielli, A. & Mayerle, G. (2007) 'Influenza sedimentologica sulle caratteristiche dei terreni della laguna veneta'. *Proceedings of the AGI - XXIII Convegno Nazionale di Geotecnica*, Padova- Abano Terme, 147-159.

Benz, T. (2007) 'Small- strain stiffness of soils and its numerical consequences'. Institut fuer Geotechnik Stuttgart, PhD Thesis.

Benz, T., Vermeer, P.A., Schwab, R. (2009) 'A small- strain overlay model'. *International Journal for Numerical and Analytical Methods in Geomechanics*, 33, 25-44.

Berengo, V. (2006) 'Modellazione costitutiva del comportamento viscoso dei terreni di Venezia'. Padova, Degree Thesis (in italian).

Biscontin, G., Cola, S., Pestana, J.M. & Simonini, P. (2007) 'Unified compression model for Venice lagoon natural silts'. *Journal of Geotechnical and Geoenvironmental Engineering*, n.133 (8), 932-942.

Biscontin, G., Pestana, J.M., Cola, S.& Simonini, P. (2001) 'Influence of grain size on the compressibility of Venice Lagoon soils'. *Proceedings of the XV International Conference on Soil Mechanics and Foundation Engineering*, Istanbul, Turkey, Vol. 4, 2801-2804.

Bjerrum, L. (1967). 'Engineering geology of Norwegian normally- consolidated marine clays as related to the settlements of buildings'. *Géotechnique*, 17 (2), 83-119.

Bjerrum, L. (1973). 'Problems of soil mechanics and construction on soft clays and structurally unstable soils'. *Proceedings of the VIII International Conference on Soil Mechanics and Foundation Engineering,* Moscow, Vol.3, 111-159.

Bowman, E. T. & Soga, K. (2003) 'Creep. Ageing and microstructural change in dense granular materials'. *Soils and Foundations*, 43 (4), 107-117.

Briaud, J.L & Gibbens, R. (1999) 'Behaviour of five large spread footings in sand'. *Journal of Geotechnical and Geoenviromental Engineering*, ASCE 125 (9), 787-796.

Brinkgreve, R.B.J. & Vermeer, P.A. (1992) 'On use of Cam-Clay models'. *Numerical Models in Geomechanics*, Pande & Pietruszczak, Balkema, Rotterdam, 557-565.

Burland, J.B. (1989) 'Ninth Laurits Bjerrum memorial lecture:'small is beautiful'- the stiffness of soils at small strains'. *Canadian Geotechnical Journal*, 26, 499-516.

Cola, S., Ricceri, G. & Simonini, P. (1998) 'Small stiffness of Venetian soils from field and laboratory tests'. *Proceedings of the XI Danube- European Conference on Soil Mechanics and Geotechnical Engineering*, 679-687.

Cola, S. & Simonini, P. (1999) 'Some remarks on the behaviour of Venetian silts'. *Proceedings of the II Inernational Symposium on the Pre-failure Deformation Characteristics of Geomaterial*, Torino, 167-174.

Cola, S. & Simonini, P. (2002) 'Mechanical bahaviour of silty soils of the Venice lagoon as a function of their grading characteristics'. *Canadian Geotechnical Journal*, n.39, 879-893.

Cola, S., Sanavia, L., Simonini, P. & Schrefler, B., A. (2008) 'Coupled thermohydromechanical analysis of Venice lagoon salt marshes'. *Water Resources Research*, Vol.44.

Cortellazzo, G., Ricceri, G. & Simonini, P. (2007) 'Analisi retrospettiva del comportamento del terreno di fondazione di un rilevato sperimentale ubicato nella laguna di Venezia'. *Proceedings of* the *AGI - XXIII Convegno Nazionale di Geotecnica*, Padova- Abano Terme, 515-522 (in italian).

Dei Svaldi, A. & Simonini, P. (1997) 'Static and cyclic deformation properties of Toyoura sand from triaxial tests'. *Memorie e Studi dell'Istituto di Costruzioni Marittime e di Geotecnica*, Padova.

Den Haan, E. J. (1994) 'Stress- independent parameters for primary and secondary compression'. *Proceedings of the XIII International Conference on Soil Mechanics and Foundation Engineering,* New Delhi, 65-70.

Deng, J., Tatsuoka, F. & Zhang, X. (2007) 'Viscous effects on deformation of kaolin clay in drained 1D compression with cyclic loading'. *Journal of Central South University of Technology*, 14 (1), 405-408.

Einav, I. & Puzrin, A.M. (2004) 'Pressure- dependent elasticity and energy conservation in elastoplastic models for soils'. *Journal of Geotechnical and Geoenvironmental Engineering*, 130 (1), 81-92.

Gottardi, G. & Tonni, L. (2004) 'Use of piezocone tests to characterize the silty soils of the Venetian lagoon (Treporti test site)'. *Proceedings of the II International Conference on Site Characterization*, Porto, Vol.2, 1643-1649.

Gottardi, G & Tonni, L. (2005) 'The Treporti test site: Exploring the behaviour of the silty soils of the Venetian lagoon'. *Proceedings of the XVI International Conference on Soil Mechanics and Geotechnical Engineering*, Osaka, Japan, Vol.2, 1037-1040.

Grozic, J.L.H., Lunne, T. & Pande, S. (2003) 'An oedometer test study on the preconsolidation stress of glaciomarine clays'. *Canadian Geotechnical Journal*, 40, 857-872.

Hardin, B.O. & Black, W.L. (1968) 'Vibration modulus of normally consolidated clay'. *Journal of the Soil Mechanics and Foundations Division*, Proceedings of the ASCE, Vol. 94, SM2, 353-369.

Hardin, B.O. & Richart, F.E. (1963) 'Elastic wave velocities in granular soils'. *Journal of the Soil Mechanics and Foundations Division*, Proceedings of the ASCE, Vol. 89, SM1, 33-65.

Hardin, B.O. & Drnevich, V.P. (1972) 'Shear modulus and damping in soils: design equations and curves'. *Journal of the Soil Mechanics and Foundations Division*, n.98, Proceedings of the ASCE, SM7, 667-691.

Hardin, B.O. & Drnevich, V.P. (1972) 'Shear modulus and damping in soils: measurement and parameter effects'. *Journal of the Soil Mechanics and Foundations Division*, Proceedings of the ASCE, Vol. 98, SM6, 603-624.

Head, K., H. (1985). 'Rowe cell consolidation and permeability tests'. *Manual of soil laboratory testing*, Wiley & Sons Ltd, Vol.3, 1129-1225.

Houlsby, G.T. (1985) 'The use of a variable shear modulus in elastic- plastic models for clays'. *Computers and Geotechnics*, 1, 3-13.

Jamiolkowski, M., Ricceri, G. & Simonini, P. (2009) 'Safeguarding Venice from high tides: site characterization and geotechnical problems'. *Proceedings of the XVII International Conference on Soil Mechanics and Geotechnical Engineering*, Alexandria, Egypt.

Janbu, N. (1969) 'The resistance concept applied to deformations of soils'. *Proceedings of the VII International Conference on Soil Mechanics and Foundation Engineering,* Mexico, Vol.1, 191-196.

Janbu, N. (1994) 'In- situ creep behaviour obtained from long- term settlement observations'. *Proceedings of the XIII International Conference on Soil Mechanics and Foundation Engineering,* New Delhi.

Kabbaj, M., Oka, F., Leroueil, S. & Tavenas, F. (1986). 'Consolidation of natural clays and laboratory testing'. *Proceedings of the Conference on Consolidation of Soils: Testing and Evaluation*. *American Society for Testing and Materials*, STP 892, 378-404.

Kabbaj, M., Tavenas, F. & Leroueil, S. (1988). 'In situ and laboratory stress-strain relations'. *Géotechnique*, 38 (1), 83-100.

Kim, Y., T. & Leroueil, S. (2001). 'Modelling the viscoplastic behaviour of clays during consolidation: application to Berthierville clay in both laboratory and field conditions'. *Canadian Geotechnical Journal*, 38 (3), 484-497.

Kuhn, M.R. & Mitchell, J.K. (1993). 'New perspectives on soil creep'. *Journal of Geotechnical Engineering*, 119 (3), 507-524.

Lade, P.V. & Abelev, A.V. (2005) 'Characterization of cross- anisotropic soil deposits from isotropic compression tests'. *Soils and Foundations*, 45 (5), 89-102.

Lade, P.V. & Nelson, R.B. (1987) 'Modelling the elastic behaviour of granular materials'. *International Journal for Numerical and Analytical Methods in Geomechanics*, 11, 521-542.

Lancellotta, R. (2004) 'Geotecnica'. Zanichelli Editore, Bologna (in italian).
Leoni, M., Karstunen, M. & Vermeer, P., A. (2008) 'Anisotropic creep model for soft soils'. *Géotechnique,* 58 (3), 215-226.

Leroueil, S. (2006) 'The Isotache Approach. Where are we 50 years after its development by Professor Šuklje? - 2006 Prof. Šuklje's Memorial Lecture'. *Proceedings of the XIII Danube-European Conference on Geotechnical Engineering*, Ljubljana, Slovenia.Vol. 1, 55–88.

Leroueil, S., Kabbaj, M. & Tavenas, F. (1988) 'Study of the validity of a $\sigma'_v - \varepsilon_v - \dot{\varepsilon}_v$ model in in situ conditions'. *Soils & Foundations*, 28 (3), 13-25.

Leroueil, S., Kabbaj, M., Tavenas, F. & Bouchard, R. (1985). 'Stress-strain-strain rate relation for the compressibility of sensitive natural clays'. *Géotechnique*, 35 (2), 159-180.

Leroueil, S., Tavenas, F., Brucy, F., La Rochelle, P. & Roy, M. (1979). 'Behavior of destructured natural clays'. *Journal of the Geotechnical Engineering Division*, ASCE, 105 (6), 759-777.

Liingaard, M. , Augustesen, A., & Lade, P.V. (2004) 'Characterization of Models for Time-Dependent Behavior of Soils'. *International Journal of Geomechanics*, ASCE 4 (3), 157-177.

Mesri, G. (2003) 'Primary compression and secondary compression'. *Geotechnical Special Pubblication*, 119, 122-166.

Muir Wood, D. (1990) 'Soil behaviour and critical state soli mechanics'. *Cambridge University Press*, Cambridge.

Muir Wood, D. (2004) 'Geotechnical modelling'. Spon Press, London.

Neher, H., P., Wehnert, M., Bonnier, P., G. (2001). 'An evaluation of soft soil models based on trial embankments'. *Proceedings of the X International Conference on Computer Methods and Advances in Geomechanics* (Eds Desai et al.), Vol.1, 373-378.

Nordal, S. (2008) 'Lecture notes: PhD course BA8304 – Soil modelling'. Trondheim, Norwegian University of Science and Technology – Geotechnical Division.

Nova, R. (2002) 'Fondamenti di meccanica delle terre'. McGraw-Hill, Milano (in italian).

Premchitt, J. & Evans, N.C. (1996). 'Conventional and CRS Rowe cell consolidation test on some Hong Kong clays'. *Geo Report*, n.55.

Pyke, R. (1979) 'Nonlinear soil models for irregular cyclic loadings'. *Journal of the Geotechnical Engineering Division*, Proceedings of the ASCE, Vol.105, GT6, 715-726.

Ricceri, G., Simonini, P. & Cola, S. (2002) 'Applicability of piezocone and dilatometer to characterize the soil of Venice lagoon'. *Geotechnical and Geological Engineering*, 20, 89-121.

Rosenblueth, E. & Herrera, I. (1964) 'On a kind of hysteretic damping'. *Journal of the Engineering Mechanics Division, Proceedings of the American Society of Civil Eneinners*, EM4, 37-48.

Rowe, P., W. & Barden, L. (1966). 'A new consolidation cell'. *Géotechnique,* 16 (2), 162-170.

Schmertmann, J.H. (1991) 'The mechanical aging of soils'. *Journal of Geotechnical Engineering*, ASCE 117 (9), 1288-1327.
Schuurman, E. (1966) 'The compressibility of an air/water mixture and a theoretical relation between the air and water pressure'. *Géotechnique,* 16 (4), 269-281.

Simonini, P. (2004) 'Characterisation of the Venice lagoon silts from in- situ tests and the performance of a test embankment'. *Proceedings of the II International Conference on Site Characterization*, Porto, Vol.1, 187-207.

Simonini, P., Ricceri, G. & Cola, S. (2006) 'Geotechnical characterization and properties of Venice lagoon heterogeneous silts'. *Proceedings of the II International Workshop on Characterization and Engineering Properties of Natural Soils*, Singapore, Vol. 4, 2289-2328.

Skempton, A., W. (1954) 'The pore- pressure coefficients *A* and *B*'. *Géotechnique,* 4 (4), 143-147.

Stolle, D., F., E., Vermeer, P., A., Bonnier, P., G. (1999). 'Time Integration of a Constitutive Law for Soft Clays'. *Communications in Numerical Methods in Engineering*, 15, 603-609.

Stolle, D.F.E., Bonnier, P.G., Vermeer, P.A. (1997) 'A soft soil model and experience with two integration schemes'. *Numerical Models in Geomechanics*, Pande & Pietruszczak, 123-127.

Stolle, D.F.E., Vermeer, P.A., Bonnier, P.G. (1999) 'A consolidation model for a creeping clay'. *Canadian Geotechnical Journal*, 36 (4), 754-759.

Svano, G., Christensen, S. & Nordal, S. (1991) 'A soil model for consolidation and creep'. *Proceedings of the X European Conference on Soil Mechanics and Foundation Engineering*, Firenze, 1, 269-272.

Tatsuoka, F. & Ishihara, K. (1974) 'Drained deformation of sand under cyclic stresses reversing direction'. *Soils & Foundations*, 14 (3), 51-65.

Tonni, L. & Gottardi, G. (2009) 'Partial drainage effects in the interpretation of piezocone tests in Venetian silty soils'. *Proceedings of the XVII International Conference on Soil Mechanics and Geotechnical Engineering*, Alexandria, Egypt, Vol.2, 1004-1007.

Uzielli, M., Simonini, P. & Cola S. (2008) 'Statistical identification of homogeneous soil units for Venice lagoon soils'. *Proceedings of the III International Conference on Site Characterization*, Taiwan.

Vermeer, P., A. & Neher, H., P. (1999) 'A soft soil model that accounts for creep'. *Proceedings of the Inernational Symposium 'Beyond 2000 in Computational Geotechnics'*, Amsterdam, 249-261, Balkema, Rotterdam.

Vermeer, P., A., Stolle, D., F., E. & Bonnier, P., G. (1998). 'From the classical theory of secondary compression to modern creep analysis'. *Proceedings of the Conference on Computer Methods and Advances in Geomechanics*, Wuhan, China, 2469–2478.

Vermeer, P.A., Leoni, M., Karstunen, M., Neher, H.P. (2007) 'Modelling and numerical simulation of creep in soft soils'. *Proceedings of the IV International Conference on Soft Soil Engineering*, Vancouver, 57-71.

Viggiani, G. & Atkinson, J.H. (1995) 'Stiffness of fine- grained soil at very small strain'. *Géotechnique*, 45 (2), 249-265.

Wheeler, S., J., Näätänen, A., Karstunen, M. & Lojander, M. (2003) 'An anisotropic elastoplastic model for soft clays'. *Canadian Geotechnical Journal*, 40, 403-418.

Zytynski, M., Randolph, M.F., Nova, R. & Wroth, C.P. (1978) 'Short communications on modelling the unloading- reloading behaviour of soils'. *International Journal for Numerical and Analytical Methods in Geomechanics*, Vol. 2, 87-94.